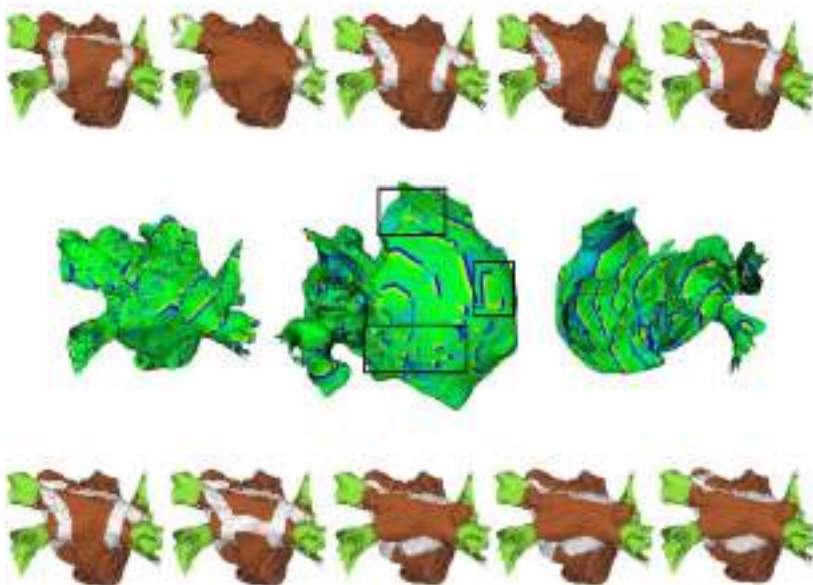


Matthias Reumann

# Computer Assisted Optimisation of Non-Pharmacological Treatment of Congestive Heart Failure and Supraventricular Arrhythmia





Matthias Reumann

**Computer Assisted Optimisation of Non-Pharmacological  
Treatment of Congestive Heart Failure and Supraventricular  
Arrhythmia**

**Vol. 2**  
**Karlsruhe Transactions on Biomedical Engineering**

Editor:  
Universität Karlsruhe (TH)  
Institute of Biomedical Engineering

# **Computer Assisted Optimisation of Non-Pharmacological Treatment of Congestive Heart Failure and Supraventricular Arrhythmia**

von  
Matthias Reumann



---

universitätsverlag karlsruhe

Dissertation, Universität Karlsruhe (TH)  
Fakultät für Elektrotechnik und Informationstechnik, 2007

## **Impressum**

Universitätsverlag Karlsruhe  
c/o Universitätsbibliothek  
Straße am Forum 2  
D-76131 Karlsruhe  
[www.uvka.de](http://www.uvka.de)



Dieses Werk ist unter folgender Creative Commons-Lizenz  
lizenziert: <http://creativecommons.org/licenses/by-nc-nd/2.0/de/>

Universitätsverlag Karlsruhe 2007  
Print on Demand

ISSN: 1864-5933  
ISBN: 978-3-86644-122-4







# Computer Assisted Optimisation of Non-Pharmacological Treatment of Congestive Heart Failure and Supraventricular Arrhythmia

Zur Erlangung des akademischen Grades eines  
DOKTOR-INGENIEURS

an der Fakultät für  
Elektrotechnik und Informationstechnik  
der Universität Fridericiana Karlsruhe  
genehmigte

DISSERTATION

von

MEng (Trip. Dipl.) Matthias Reumann  
geboren in Frankfurt am Main

Tag der mündlichen Prüfung: 8. Februar 2007

Hauptreferent: Prof. Dr. rer. nat. Olaf Dössel

Korreferentin: PD Dr. med. Brigitte Osswald



*“Why are the things that you write for yourself always so much better than the things that you write for others.”*

Sean Connery alias William Forrester in the movie “Finding Forrester”



---

# Contents

<b>Preface - a personal note</b> .....	VII
--	-----

---

## Part I Introduction

---

<b>2 Introduction</b> .....	3
2.1 Motivation .....	3
2.2 Aim of this Thesis .....	5
2.3 Structure of the Thesis .....	6

---

## Part II Medical Background

---

<b>3 Anatomy and Physiology</b> .....	9
3.1 Macroscopic Structures of the Heart .....	9
3.1.1 Anatomy of the Heart and the Cardiovascular System .....	10
3.1.2 Atrial and Ventricular Anatomy .....	12
3.2 Myocardial Cells .....	16
3.2.1 Cellular Anatomy and Electrophysiology .....	17
3.2.2 Working Myocardium, Pacemaker Cells and Cells of the Conduction System .....	26
3.2.3 The Electrocardiogramm .....	27
<b>4 Pathology</b> .....	29
4.1 Supraventricular Arrhythmia .....	29
4.1.1 Atrial Fibrillation .....	30
4.1.2 Maintenance of Atrial Fibrillation .....	32
4.1.3 Atrial Flutter .....	33
4.1.4 Clinical Classification of Atrial Fibrillation .....	34
4.1.5 Atrial Fibrillation after Surgical Intervention .....	34

4.2	Congestive Heart Failure .....	35
4.2.1	Hypertensive Heart Disease .....	35
4.2.2	Ischemic Heart Disease .....	35
4.2.3	Blockage in the Cardiac Conduction System .....	36
4.2.4	Ventricular Remodelling .....	37
4.2.5	Diastolic Heart Failure .....	39
4.2.6	Ventricular Dyssynchrony .....	39
4.2.7	Clinical Classification of Congestive Heart Failure .....	39
4.2.8	Congestive Heart Failure Related to Atrial Fibrillation .....	40
<b>5</b>	<b>Therapy .....</b>	<b>41</b>
5.1	Therapeutical Options in Atrial Fibrillation .....	41
5.1.1	Interventional and Surgical Therapies in Atrial Fibrillation .....	42
5.1.2	Atrial Antitachycardial Pacing .....	56
5.1.3	Other Therapeutical Options in Atrial Fibrillation .....	61
5.1.4	Unresolved Issues in Atrial Antitachycardial Pacing .....	61
5.2	Therapeutical Options in Congestive Heart Failure .....	63
5.2.1	Cardiac Resynchronisation Therapy .....	63
<b>6</b>	<b>The role of computer models in cardiac research .....</b>	<b>67</b>

---

### Part III Modelling Cardiac Electrophysiology

---

<b>7</b>	<b>Modelling the Anatomy of the Heart .....</b>	<b>73</b>
7.1	Anatomical Image Data .....	73
7.2	Digital Representation of the Image Data .....	74
7.2.1	Image Segmentation and Classification .....	75
<b>8</b>	<b>Electrophysiological Model .....</b>	<b>77</b>
8.1	Mathematical Description of Cellular Electrophysiology .....	77
8.1.1	Transmembrane Voltage $V$ .....	78
8.1.2	Membrane Currents .....	78
8.2	Atrial and Ventricular Cell Models of the Human Cardiomyocyte .....	80
8.3	Excitation Propagation .....	82
8.3.1	Poisson's Equations to determine Excitation Propagation .....	82
8.3.2	Cellular Automata .....	84

---

### Part IV Modelling Cardiac Pathologies and Therapies

---

<b>9</b>	<b>Modelling the Pathologies of the Heart</b>	89
9.1	Computer Model of Supraventricular Arrhythmia	89
9.2	Characterisation of Atrial Fibrillation	92
9.2.1	Segmentation and Classification of Excitation Patterns	93
9.3	Computer Model of Congestive Heart Failure	96
9.3.1	Anatomical Model of Patients with Heart Failure	96
9.3.2	Modelling Blockages in the Cardiac Conduction System	97
9.3.3	Modelling Ventricular Dyssynchrony	97
9.3.4	Summary of Pathologies in Heart Failure Simulated	98
<b>10</b>	<b>Modelling Interventional and Surgical Therapies</b>	99
10.1	Computer Model of Ablation Therapy	99
10.2	Computer Model of Atrial Antitachycardial Pacing	102
10.3	Computer Model of Cardiac Resynchronisation Therapy	104
10.3.1	Electrode Positions in Cardiac Resynchronization Therapy	105
10.3.2	Optimisation Strategy	105

---

## Part V Results and Conclusions

---

<b>11</b>	<b>Results: Pathology</b>	113
11.1	Simulation of Supraventricular Arrhythmia	113
11.1.1	Macro Re-entries	114
11.1.2	Driving Rotor	114
11.1.3	Break-up of Stable Excitation Wave Fronts	115
11.1.4	Local Excitation Pattern	117
11.1.5	Chaotic Excitation of the Atria	119
11.1.6	Location of the Ectopic Focus	119
11.1.7	Results of Excitation Pattern Classification	122
11.2	Simulation of Congestive Heart Failure	132
11.2.1	Simulation of Blockages in the Cardiac Conduction System	132
11.2.2	Simulation of Ventricular Dyssynchrony	132
<b>12</b>	<b>Results: Therapy</b>	135
12.1	Simulation of Ablation Therapy	135
12.1.1	Simulation Results vs. Clinical Studies	138
12.1.2	Simulation of Linear Ablation Lesions	139
12.1.3	Simulation of Circumferential Ablation Lesions around each Pulmonary Vein	141
12.1.4	Simulation of Circumferential Ablation Lesions around both Left and Right Pulmonary Veins	141

12.1.5	Simulation of Circumferential Ablation with Two Additional Linear Lesions	144
12.1.6	Simulation of Circumferential Ablation of Left and Right Pulmonary Veins Including Separation of Inferior and Superior Pulmonary Veins . . . . .	146
12.1.7	Simulation of Isolation of Each Pulmonary Vein Including Two Additional Linear Lesions . . . . .	149
12.1.8	Simulation of Isolation of Each Pulmonary Vein Including Three Additional Linear Lesions . . . . .	151
12.1.9	Simulation of Circumferential Ablation Lesion around All Pulmonary Veins Including One Additional Linear Lesion . . . . .	152
12.1.10	Simulation of Circumferential Ablation Lesion around All Pulmonary Veins Including Two Additional Linear Lesion . . . . .	155
12.1.11	Simulation of Circumferential Ablation Lesion of All Pulmonary Veins with Additional Lesions to the Left Atrial Appendage and the Mitral Annulus . . .	157
12.2	Results: Atrial Antitachycardial Pacing . . . . .	159
12.2.1	Simulation of Atrial Antitachycardial Pacing to Prevent Atrial Fibrillation..	159
12.2.2	Simulation of Atrial Antitachycardial Pacing to Terminate Atrial Fibrillation	161
12.3	Results: Cardiac Resynchronisation Therapy . . . . .	162
12.3.1	Optimization of CRT on the Visible Man Data-Set . . . . .	166
12.3.2	Optimization of CRT on the Patient Data-set . . . . .	171
12.3.3	Optimization of CRT using the Downhill Simplex Algorithm . . . . .	178
<b>13</b>	<b>Discussion . . . . .</b>	<b>191</b>
13.1	Computer Model of Atrial Fibrillation . . . . .	191
13.2	Classification Methods of Excitation Patterns in AF . . . . .	193
13.3	Evaluation of Ablation Strategies . . . . .	194
13.3.1	Comparison of Ablation Strategies . . . . .	194
13.3.2	Comparison with Clinical Studies . . . . .	195
13.3.3	Limitations . . . . .	196
13.4	Investigation of Atrial Antitachycardial Pacing . . . . .	196
13.5	Optimisation of Cardiac Resynchronisation Therapy . . . . .	197
13.5.1	Sequential Search versus Downhill Simplex Search Algorithm . . . . .	198
13.5.2	Comparison with Clinical Studies . . . . .	198
13.5.3	Limitations . . . . .	199
<b>14</b>	<b>Conclusion . . . . .</b>	<b>201</b>
14.1	General Conclusion . . . . .	201
14.2	Concluding Remark . . . . .	203
<b>15</b>	<b>Perspective . . . . .</b>	<b>205</b>



---

15.1 Future Research Issues .....	205
15.2 Final Remark .....	207
<b>16 Postscript - a personal note</b> .....	<b>209</b>
<b>References</b> .....	<b>215</b>
<b>Curriculum Vitae</b> .....	<b>236</b>



## Preface - a personal note

*“Alles ist schon gesagt - nur nicht von jedem!”*

*All has been said - but not by everyone!*

Karl Valentin, German comedian (1882-1948)

When I began my work on this thesis, I believed that I had to say many things that were already said. Now, at the end of this thesis, I am happy that most of what I wrote has not been said yet, apart from my publications. The last three and a half years have been exhilarating for my personal development. It was interesting and exciting to work in this field. Therefore, I would like to thank Prof. Olaf Dössel for his support. His door has always been open for any discussion - academically or concerning my personal professional development. Olaf Dössel gave me the opportunity to carry out my own projects, to explore teaching and research and always supported my sometimes ‘crazy’ ideas. He has followed my personal development and gave me the liberty to develop. I owe thanks to Mrs. PD Dr. Brigitte Osswald who has tirelessly read my papers and conference contributions. She has taken care of the medical aspects and has checked that my work was focussed in the right direction. But I would also like to thank my colleagues and students without who I would not have been able to finish this thesis. There is a long list to name and I am grateful to all since they ‘forced’ me to carry on my work and gave me the opportunity of ‘change of methods’ in my daily routine. I would especially like to thank Anke, Antoun, Julia, Matthias and Oleg for their support and friendship.

My father said once that he believed when one has finished his/her PhD thesis, one should be *the* expert in the field. Modeling cardiac function is a pretty large field. I hope I have acquired the expertise in at least one corner of this field to help advance cardiac modelling with respect to its integration in clinical routine. I would like to thank my parents for all the inspiration and support. This thank has to be extended to my parents-in-law whose domicile on the country side has always offered a welcoming break from daily life and a place where to acquire physical strength. But most supportive was my wife who had to bear all the ups and downs of my mood. It is to her that I dedicate this work.



## Part I

---

### Introduction



## Introduction

*“Der Geist ist kein Schiff, das man beladen, sondern ein Feuer, das man entfachen muss.”*

*The spirit is not a vessel that has to be loaded but a fire that has to be lighted.*

Plutarch

Greek biographer and moralist (46 AD - 120 AD)

### 2.1 Motivation

Cardiac disease is the most common disease worldwide. Atrial fibrillation (AF) and congestive heart failure (CHF) are two frequently encountered conditions in clinical practice [260]. In fact, AF is the most common sustained cardiac arrhythmia [197, 114]. It causes the highest number of hospitalization and is associated with higher mortality, major clinical complications, such as heart failure, acute myocardial infarction and stroke, and impaired quality of life [164, 243, 3, 242, 159, 100, 89, 69, 66, 71]. Congestive heart failure leads to an asynchronous contraction of the ventricles and poses a high risk factor for sudden death [1]. Both pathologies can occur independently. However, CHF is often developed in patients with AF due to its adverse effect on cardiovascular haemodynamics. On the other hand, AF can be induced by an asynchronous contraction of the ventricles as may be developed in CHF. The latter has become the most important risk factor of AF in developed countries, as a result of ageing populations. An increase in the prevalence of both atrial fibrillation and congestive heart failure is occurring in part because of the demographic shift toward an aging population [272]. Approximately two thirds of patients with CHF are > 65 years of age. They are likely to have AF as a coexistent complication. Epidemiological surveys and large clinical trials in CHF provide strong evidence that AF is a marker of increased mortality [255]. AF by itself is not leading to death, mostly. The increased risk of thromboembolism and stroke, however, leads to most complications that then increase morbidity and mortality [241, 186, 179]. It is approximated that this arrhythmia will reach epidemic proportions over the next two decades [12]. In fact, AF is gaining in clinical and economic importance even today [164]. It has great impact on quality of life especially related to complications such as stroke

and heart failure as well as functional status and the cost of chronic treatment [295]. By 2004, AF represented the most common dysrhythmia in North America [127]. AF affected an estimated 2.8 million individuals and was associated with 1 billion dollars in healthcare costs each year in the United States.

The patho-physiology of AF remains unclear to date [114, 71]. Although the association with structural cardiac diseases such as mitral valve regurgitation, aortic valve stenosis and any circumstances leading to pressure and volume overload of the atria is obvious, the exact mechanisms underlying AF initiation and maintenance are not completely understood. In general, AF is described by very fast and chaotic excitation of the atria, resulting in a loss of mechanical contraction and a turbulent blood flow through the atria. Many other factors such as age, diet, fluid homeostasis, electrolyte status, neurohormones and inflammation as well as cardiovascular diseases, structural and physiological changes, genetics and the autonomic nervous system have been associated with the initiation and maintenance of AF [159, 210, 211]. It is unlikely that a single pathophysiology is operative in all or even a majority of cases [114]. Thus, atrial fibrillation remains one of the most challenging arrhythmias for the clinician and basic researcher [30]. Further to the epidemiological development of AF, its incidence postoperatively is common with an occurrence in 25 % to 60 % of patients after cardiac surgery [267, 55, 221].

Since new-onset AF occurs frequently after cardiac surgery, prophylactic atrial antitachycardial pacing (AATP) following cardiac surgery is a preventive measure to suppress the onset of AF. Its utility as therapy has been investigated in clinical trials. However, its role with respect to preventive measures and its technique remains to be validated [170]. Also, clinical guidelines for its use are lacking [171]. Perhaps, the association of different techniques evaluated - the site of pacing, the prevention algorithms, respect of the ventricular rhythms, reduction by anti-tachycardia stimulation - will provide multifunction devices capable of best managing atrial arrhythmias which do not require "curative" therapy, and in particular, endocavitary ablation [170]. However, setting transmural lesions either surgically or by ablating the cardiac tissue still represents the gold standard in AF treatment. A manifold of ablation strategies exists and it remains unclear which strategies lead to the best results. Thus, treatment of AF is mostly challenging for the clinician and tools for an optimised therapy that assist the clinician in choosing the most appropriate application do not exist.

In contrast to atrial fibrillation, the epidemiology of congestive heart failure is mostly understood. However, despite progress in the management of heart failure (HF) using pharmacotherapy, the mortality and morbidity associated with this condition remain unacceptably high. Cardiac resynchronization therapy (CRT), a left-sided pacing therapy for drug-refractory and highly symptomatic CHF patients with ventricular conduction delay, has been shown to improve left ventricular (LV) systolic function, myocardial oxygen consumption, and New York Heart Association functional class and to inhibit or reverse LV chamber dilation and remodelling [92]. Nevertheless, about one



third of patients receiving CRT do not respond to the therapy [175]. Also, the adjustment to the individual patient is not optimised so far. The atrio-ventricular and the interventricular delays, i. e. the time difference between the stimulus of the physiological excitation of the atria to the stimulus on the ventricle and the time difference between the stimuli of the two ventricular electrodes, have to be adjusted to the individual patients patho-physiology. This adjustment, however, is too time consuming so that it is not carried out in clinical practice. Automatic algorithms to make this adjustment are not known to the author. In the end, CRT can also be seen as a preventive measure against AF. Since the ventricles will contract synchronously, the atrial stress is reduced which in turn reduces the risk of developing atrial fibrillation.

Thus, the motivation for the presented thesis is to advance the understanding of the interventional therapies against atrial fibrillation and the optimisation of cardiac resynchronisation therapies for patients with congestive heart failure.

## 2.2 Aim of this Thesis

Pharmacological therapies as well as non-pharmacological therapies of congestive heart failure and atrial fibrillation as supraventricular arrhythmia require an optimisation to achieve better success rates. On one hand, clinical studies are carried out to investigate the underlying mechanisms so that the therapies can explicitly target the cause of the disease. Especially the pharmacological approach requires the input of these results. Since a clinical trial is not subject to this work, pharmacological strategies will not be outlined and treated in detail in this thesis. Concerning non-pharmacological strategies, the procedure itself is based on a certain understanding of the pathology. However, the pathology of each individual patient differs and the effects of the therapies are not yet clear. While success rates around 70 % are achieved, the strategies are not optimal.

The limitations of clinical studies are:

1. Only one therapy can be tested on one patient - other therapies cannot be applied to do a direct comparison on an individual basis.
2. To overcome the above issue, a large patient collective with similar, ideally exactly the same patho-physiology is required to be statistically valid. A limited number of patients is counter-acting this approach.
3. Mortality as an endpoint for clinical trials [18, 303, 204].

Computer models of the heart can overcome these problems. Given a patients anatomical and patho-physiological data in a computer model, a multitude of therapies can be tested leading to an optimal therapy. Thus, the aim of this thesis can be formulated as follows:

*To produce a computer model with which non-pharmacological therapies can be evaluated and optimised with respect to realistic anatomical structures leading to an individual patient therapy planning in the future.*

So far, the algorithms to model the electrophysiology of the heart have been mostly applied to patches of cardiac tissue and simplified anatomical structures. Simulation on anatomically detailed models of the heart are few and not yet applicable to an evaluation of therapies, therapy optimisation and planning. Therefore, this thesis deals with the following issues:

- To model initiation and maintenance of atrial fibrillation on an anatomically detailed data set.
- To evaluate ablation lesion sets on an anatomically detailed data set.
- To investigate the mechanisms of atrial antitachycardial pacing.
- To develop an automatic optimisation algorithm with respect to pacemaker parameters in cardiac resynchronisation therapy for an individual patient anatomy.

## 2.3 Structure of the Thesis

Current research and the methods used to produce the results will be presented as follows:

Part II “Medical Background” gives an overview of atrial anatomy and electrophysiology (chapter 3) as well as the pathologies discussed in this work (chapter 4). Current state-of-the-art therapy will be described in chapter 5 and the role of computer models in cardiac research will be displayed at the end of part II in chapter 6.

Part III and IV will present the methods used to create a computer model with respect to anatomy and electrophysiology (chapter 7), pathology (chapter 9.1) and its therapies (chapter 10). The chapters “Modelling the Pathologies of the Heart” and “Modelling Interventional and Surgical Therapies” are structured according to part II by describing atrial fibrillation first, then congestive heart failure, followed by the therapies of ablation strategies, atrial antitachycardial pacing and cardiac resynchronisation therapy, respectively.

The results of this thesis (chapter 11 - 12) will be presented in part V, followed by a discussion (chapter 13), conclusion (chapter 14) and an outlook on future work (chapter 15).

## Part II

---

### Medical Background



## Anatomy and Physiology

*“Die Natur steht unter dem Zwange der vernünftigen Ursache des Gesetzes, das in ihr eingeschmolzen lebt. Die Natur bricht ihr Gesetz nicht.”*

*Nature underlies the obligation of the reason of the law that lives within her. Nature does not break its law.*

Leonardo da Vinci

Italian engineer, painter and sculptor (1452 - 1519)

The constant need of oxygen and nutrients of any organ in the body as well as the transport of carbon dioxide and cellular waste from these organs demands a constant blood circulation. To hold this circulation up is the heart's only task. The heart contracts on average over 100,000 times a day and has a throughput of roughly 8,000 litres of blood. To keep a constant flow, the heart never rests.

The heart's structure (anatomy) has evolved according to its functional (physiological) requirements. Anatomy and physiology can be well separated as the anatomical structures can be described without considering its function and its inner working. Nevertheless, how the heart works depends on the structure of the heart and the cells that make up this special organ. But the structure of the cells and the heart has formed according to the task the heart has to perform. Since anatomy and physiology are much interlinked, this chapter takes the approach of considering both, anatomy and physiology at organ level and microscopic, cellular level at the same time to deliver the whole picture of the hardest working organ in the human body.

### 3.1 Macroscopic Structures of the Heart

The heart is situated frontally in the middle of the chest (thorax) behind the breast bone (sternum). Its size is about the same as a person's fist; its weight ranges from 230 g to 350 g. About two thirds of its volume is lying on the human's left side with the apex, the heart's pointed bottom, tilted to the left front. Thus, the heart's base is shifted to the top left following the heart's main axis. The

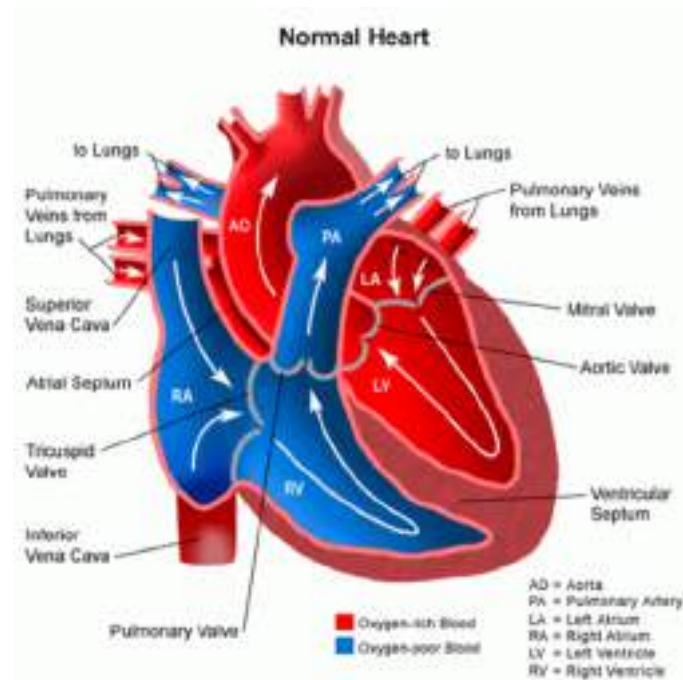


**Figure 3.1.** The oxygenated blood flows into the left atrium through the pulmonary veins, and fills the left ventricle. The left ventricle ejects the blood through the aorta to the body. The deoxygenated blood reaches the heart through the venous system back into the right atrium through the venae cavae. The right ventricle propels the blood to the lungs through the pulmonary arteries. Figure downloaded from <http://www.childrenscentralcal.org/images/healthimages/ei175.gif> (accessed 18.12.2006).

pericardial sac is keeping the heart in its place. It surrounds the heart completely and is connected to the epicardium (the outside wall of the heart) by connective tissue that allows the heart to move smoothly within the given boundaries.

### 3.1.1 Anatomy of the Heart and the Cardiovascular System

The heart is a hollow organ according to its function as a pump. The constant contraction (systole) and relaxation (diastole) causes the blood to flow through the hearts chambers into the body and back to the heart. Respective the pulmonary circuit and the systemic circuit, the heart can be split in two halves, the right and left side which is separated by the septum (see fig. 3.1). Also, to keep up a constant blood flow, the hearts main chambers (ventricles) have an antechambre, the atria. While the ventricles are pumping their contents into the body through the aorta (left ventricle) and to the lungs through the pulmonary artery (right ventricle), the atria are filled by blood through the pulmonary veins (left atrium) and the vena cava superior and vena cava inferior (right atrium). They store the blood until the ventricles relax and can be filled again.

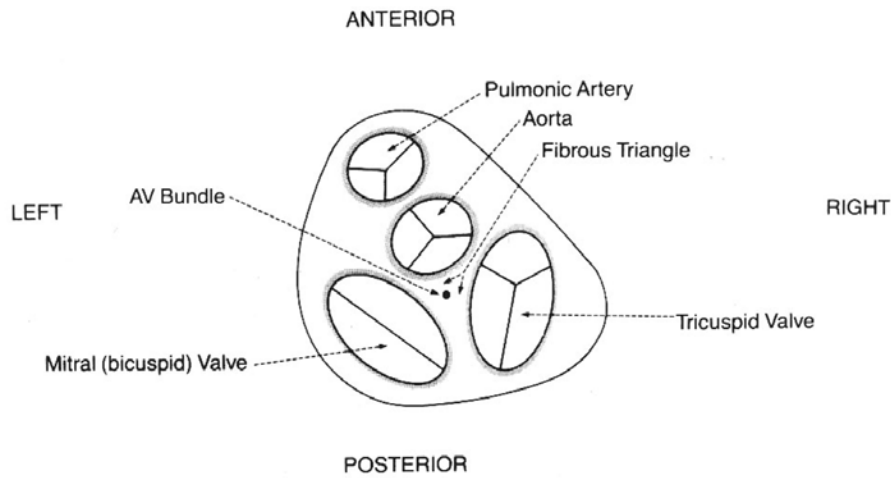


**Figure 3.2.** This figure shows a schematic view of the valve plane [144]. It shows the mitral valve and the tricuspid valve which connect the left and right atrium to the ventricles. The atrio-ventricular (AV) node is situated between these two valves and the aorta. The AV node is surrounded by fibrous tissue and is the only electrophysiologic connection between the atria and the ventricles.

The pulmonary arteries lead the deoxygenated blood to the lungs where the carbon dioxide is exchanged with oxygen. The oxygenated blood flows through the pulmonary veins to the left atrium which delivers a preload to the left ventricle. The filling volume of the left ventricle is smaller than the right but the ejection fraction of the right ventricle is smaller than in the left ventricle (around 50 % vs. 70 %) [88] and the aortic pressure is higher than the pressure in the arteria pulmonalis (end diastolic: 80 mmHg vs. 10 mmHg; max. systolic: 125 mmHg vs. 25 mmHg)[7]. Therefore, the left ventricle has to be stronger than the right. Thus, its size is greater (three times the mass of the right ventricle [88]) and its muscles are thicker (20 mm compared to 10 mm). The aorta, beginning with the aorta ascendens, first branches into the arteria coronaria dextra and sinistra (see section 3.1.2.4, figure 3.6) that supply the heart with oxygen <sup>1</sup> [246]. The oxygenated blood is flowing through arteries to the limbs and organs where the metabolism takes place and the oxygen is replaced by carbon dioxide. The blood carries the carbon dioxide through the veins back to the right atrium through the venae cavae. Thus, the circulation of blood flow is complete.

The blood flow inside the heart is regulated by mainly four valves. The mitral (bicuspid) and tricuspid valve separate the left and right atria from the left and right ventricle, respectively. They open towards the ventricles during the inflow of blood into the ventricles and close during the contraction phase. This is the time when the aortic valve and the pulmonary valve open to give

<sup>1</sup> Interestingly, the brain is the next part that will receive fresh oxygen: Branching off from the arcus aortae, the truncus brachiocephalicus supplies the right brain, neck and arm. The arteria carotis communis sinistra carries the blood to the left brain and neck while the arteria subclavia sinistra supports the left arm with oxygen. The pars thoracica aortae and pars abdominalis aortae lead to the chest and the lower body. The arteria sacralis mediana forms the end of the aorta [246].

way to the ejection of blood into the body. They close to prevent the backflow of blood during diastole (see fig. 3.1). These four valves are situated in the so called valve plane (see fig. 3.2). As part of the fibrous skeleton of the heart, the valve plane separates the atria from the ventricles not only structurally but also electromechanically. Still, the excitation of the atria causes the ventricles to be excited through the atrio - ventricular node (see fig. 3.2) in the physiological case which causes the contraction of the hearts main chambers.

### 3.1.2 Atrial and Ventricular Anatomy

The hearts muscle (myocardium) contracts due to an electrical excitation of each myocardial cell (cardiomyocyte). First, the atria contract simultaneously, then - after a short delay, the ventricles contract. For the cardiomyocytes to contract simultaneously, each myocyte has to be excited rather simultaneously. A special network of fast conducting cells spreads across the ventricles so that they also are stimulated at the same time. The atrial structure has developed so that the regions of the left and right atrium are stimulated closely together.

#### 3.1.2.1 Excitation Initiation and Conduction System

The heart beat is initiated in the sino - atrial node (SA node) which is an area of cardiac tissue of about 10 – 30 *mm* length and 5 *mm* width situated at the ostium of the vena cava superior in the right atrium. Its cells have the ability to self-depolarise, i. e. they are excited with a certain variable frequency<sup>2</sup>. The SA node is setting the heart rate with an average 60 - 80 beats per minute during rest. Thus, its cells are also called primary pacemaker cells. The excitation is spreading across the atria to the atrio - ventricular node (AV node). The excitation propagates through atrial working myocardium. There are no special isolated, fast conducting pathways that explicitly link the SA node and the AV node (see fig. 3.3). The AV node is an area located in a fibrous triangle in the hearts center between the mitral and tricuspid valve and the aorta.

The excitation of the ventricles happens slightly differently: The AV node, once excited, propagates the excitation to the bundle of His with a short delay. They connect with each other at the distal part of the AV node through connective tissue. The bundle of His (fasciculus atrioventricularis) is the only electrical link between atria and ventricles through the Pars membranacea septi. This bundle branches into the left and right Tawara branches along the septal wall. The left in turn splits into the fasciculus posterior and fasciculus anterior [246]. These bundles lead into the Purkinje fibres that form a network of conduction pathways across the ventricles. While the bundle of His and the Tawara branches are completely isolated electrically from the ventricular working myocardium, the Purkinje fibres connect to the subendocardial cells. The working myocardium is only excited at the end of these pathways.

<sup>2</sup> The frequency is variable due to the fact that the heart has to adjust the heart rate according to the required situation, i. e. faster if the human being is doing exercise or slower if the body is relaxed and calm.



Overall, these two different approaches to excite the cardiac tissue make sense. The atria contract pushing the blood downwards through the mitral and tricuspidal valve into the ventricles. The ventricles in contrast have to push the blood upwards into the pulmonary artery and the aorta. Thus, the excitation of the ventricles requires a slightly different setup than the excitation of the atria.

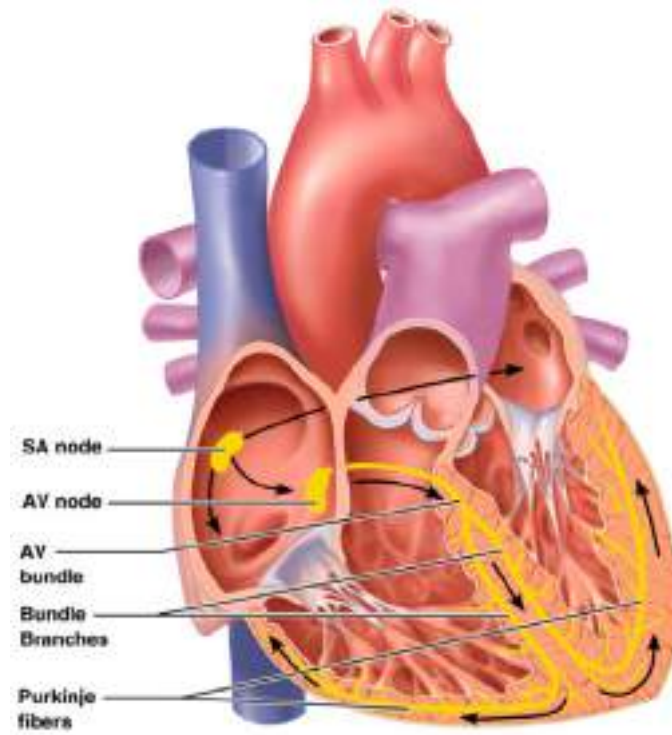


**Figure 3.3.** This figure shows the hearts excitation-conduction system and the pathways of excitation [279]. The excitation of the heart will be initiated by the sino-atrial (SA) node and spreads across the atria. The atrio-ventricular (AV) node delays the excitation before initiating the excitation of the ventricles which is carried forward through the bundle branches to the Purkinje fibres. Only at the end of the Purkinje fibres the working myocardium is excited.

### 3.1.2.2 Atria

The atria do not show conduction pathways as necessary for ventricular contraction. Instead, the excitation spreads along fast conducting muscle fibres that are not isolated from the working myocardium. The crista terminalis and the pectinate muscles cause the right atrium to be excited, the Bachmanns bundle carries the excitation from the right to the left atrium. The crista terminalis is connected to the SA node and stretches across the right atrium from the anterior side of the

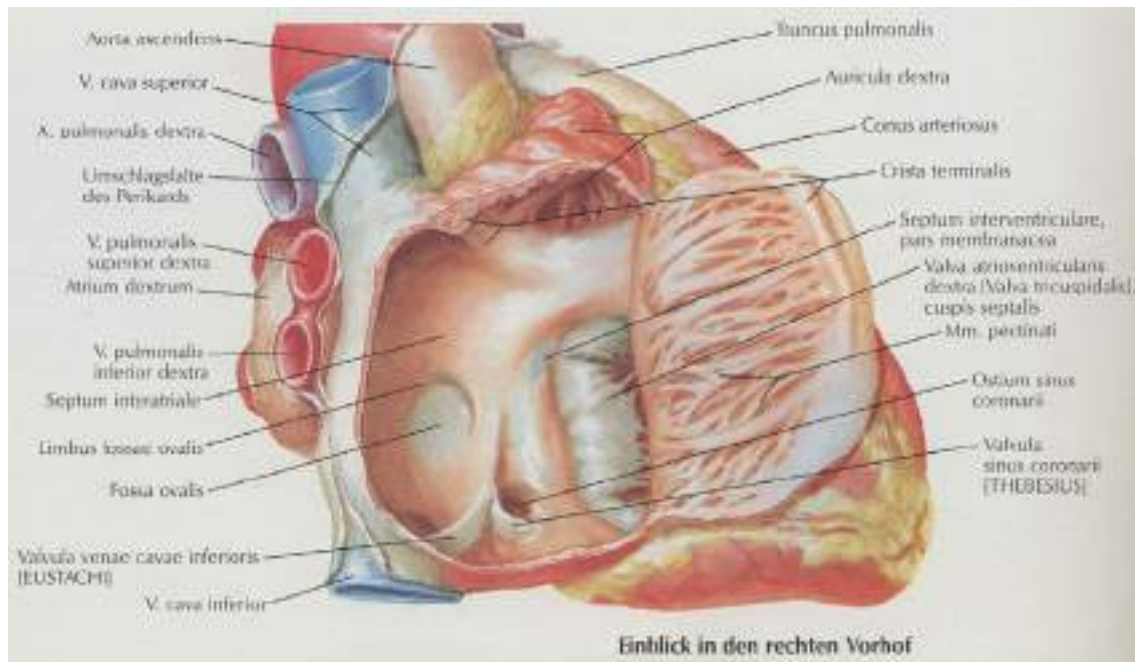


**Figure 3.4.** This figure shows the atrial anatomy looking onto and into the right atrium. Figure adapted from Netter [203].

atrial septum via the orifice of the vena cava superior towards the vena cava inferior and ends near the orifice of the sinus coronarius. Its thickness is about  $5 - 8 \text{ mm}$ . The pectinate muscles reach perpendicular across the right atrium. The excitation is conducted fast along these muscle structures.

Bachmanns bundle reaches across towards the left atrium. It is situated near the SA node and stretches right up to the left atrial appendage. This fast conducting channel, next to the limb of the fossa ovalis and the coronary sinus, causes the left atrium to be excited. The muscle structure of the left atrium does show the same build up as in the right atrium with pectinate muscles leading from Bachmanns bundle across the left atrium. But in contrast to the right atrium, the pectinate muscles are not strongly developed and the endocardial surface is rather smooth. Further, landmarks in the left atrium are given by the four pulmonary veins<sup>3</sup> (PV) compared to the two venae cavae in the right atrium. The ostium of these veins is surrounded by myocardial tissue which reaches about  $0.6 - 25 \text{ mm}$  deep into the veins showing a gradual transition from myocardium to vein [196, 31, 119, 118].

<sup>3</sup> Five pulmonary veins have also been observed as well as common trunks [119, 118, 83]. Still, this is not the general rule and disregarded in this thesis.

### 3.1.2.3 Ventricles

Structurally, the ventricles include not only the excitation conduction network of His bundle, Tawara branches and Purkinje fibres, it also contains papillary muscles and the working myocardium, which takes up most of the hearts muscle mass. The myocardial wall shows a transmural distribution of different cell types: endocardial, midmyocardial and epicardial cells. They have slightly different electrophysiological properties (see section 3.2.2). An apico - basal distribution in different cell types has also been observed. Thus, working myocardium does not behave homogeneously but heterogeneously. The contraction is carried out along the muscle fibre whose orientation varies greatly depending on the cells location in the heart, making the heterogeneity of the hearts wall even more complex. While the contraction of the ventricles is similar to a wringing movement, the contraction in general begins apically. The valve plane is pulled downwards when the ventricles contract [7].

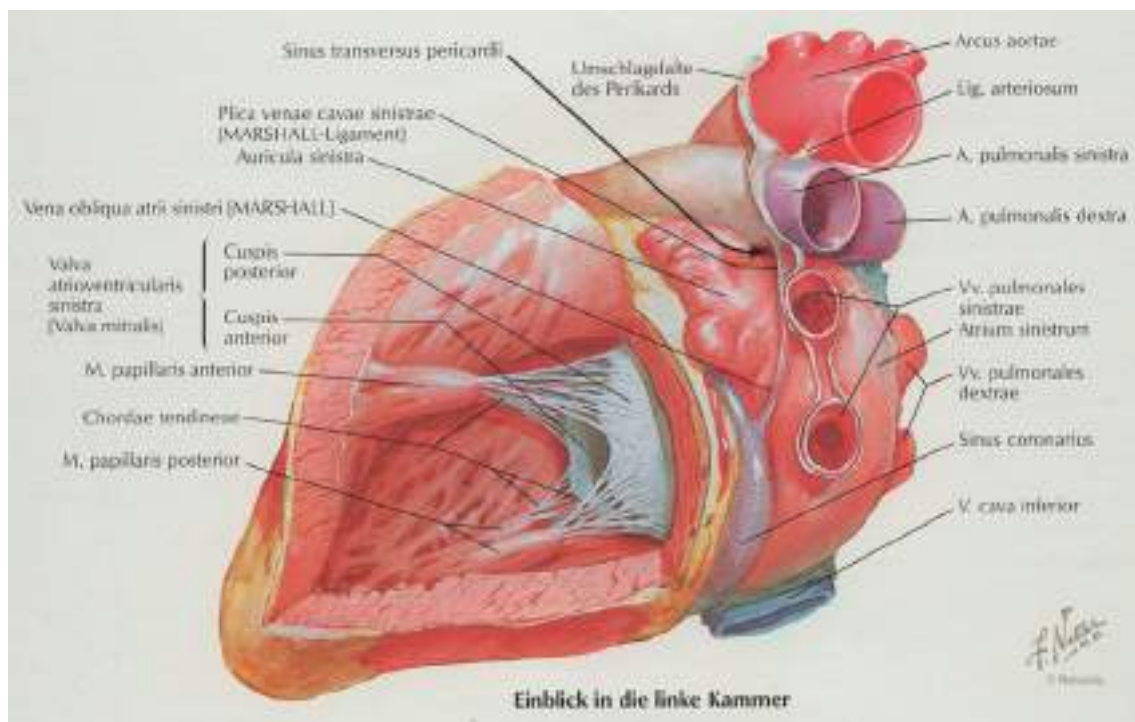


**Figure 3.5.** This figure shows the ventricular anatomy looking into the left ventricle. Figure adapted from Netter [203].

#### 3.1.2.4 Coronary Vessels

The heart's oxygen supply is delivered through the coronary vessels. They follow the natural gaps between atria and ventricles (sulcus coronarius) and between the left and right ventricle (sulcus interventricularis). The arteria coronaria sinistra and arteria coronaria dextra are the first vessels to branch off the aorta ascendens.

The arteria coronaria sinistra (see figure 3.6) is situated between the truncus pulmonalis and the left atrial appendage and splits into the Ramus (R.) interventricularis anterior and the R. circumflexus. The R. interventricularis anterior follows the frontal gap between the ventricles downwards, around the apex and slightly back up the sulcus interventricularis posterior. Its branches supply the anterior cardiac wall, the anterior papillary muscles of the right ventricle, the frontal and middle part of the septum, the anteroapical areas of the left ventricle. The bundle of His and the Tawara branches are supplied with oxygen and nutrients by the R. interventricularis anterior as well. The R. circumflexus is situated in the sulcus coronarius. The blood flow goes to the left atrium as well as the posterior wall of the left ventricles.

The arteria coronaria dextra is located between the truncus pulmonalis and the right atrial appendage. It is directed downwards through the right side of the sulcus coronarius. The right ventricular wall is supplied with blood by its branches. The R. nodi sinuatrialis as well as the R. nodi atrioventricularis lead from the arteria coronaria dextra to the SA and AV node to take care of their oxygen supply.

The backflow of deoxygenated blood through the coronary veins follows the structure of the coronary arteries described above. They all end in the sinus coronarius which leads into the right atrium.

### 3.2 Myocardial Cells

The macroscopic structures of the heart are made up of millions of myocardial cells. Respective their function in the heart, different structural build ups can be distinguished between them. While the working myocardium's main task is the contraction, the cells of the conduction system take care of the fast excitation pathways. The cells in the SA node have the property to trigger an excitation and therefore show a different structure again. The differences are in the build up of the cell membrane or the contractile elements inside the cell. Ion channels, pumps and exchangers as well as gap junctions vary within the different cell types. These differences cause different ion currents through the cells membrane and thus different action potentials if the cells are excited. A resting potential can be observed in all myocardial cells. It results from constant ion movement and differing ion concentrations inside and outside the cell.

Working myocardium, pacemaker cells and the cells of the conduction system are the three main types of cardiomyocytes. A heterogeneous distribution of cells can be even found in these groups

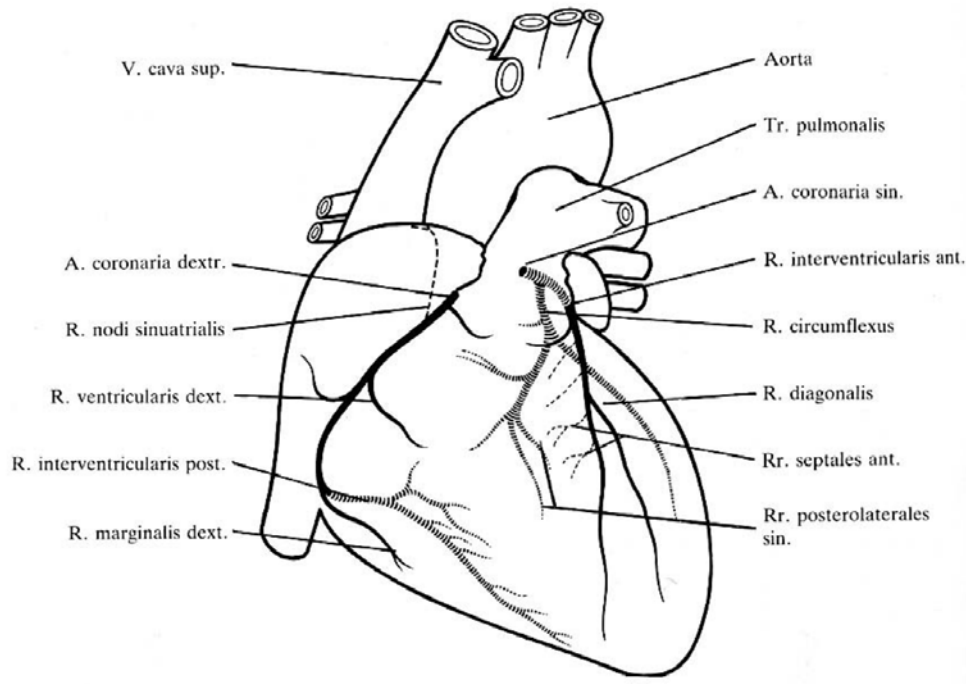


**Figure 3.6.** The figure shows a schematic drawing of the heart and its coronary vessels by H. J. Kretschmann and M. Kaltenbach [246] looking onto the right ventricle.

leading to many different cell types in the myocardium. The structural differences of cardiomyocytes of the working myocardium, the conduction system and pacemaker cells will be outlined in this section, giving an insight into the differences in cell types. First, the principal structure of a cardiomyocyte will be given. The processes and mechanism that lead to a resting potential and an action potential will be explained. The contraction of the myocardial cells will be briefly touched leading back to a structural description of the myocardium via an explanation of the interrelationship of ionic currents, action potential and contraction.

### 3.2.1 Cellular Anatomy and Electrophysiology

A cardiomyocyte of the working myocardium has a cylindrical shape of  $50 - 120 \mu m$  length and  $5 - 25 \mu m$  diameter. While each cell is linked to other cells of the myocardium, it is also linked to the capillary system which is required for the metabolism. The cells “skin” is a membrane separating the inside (intracellular space) from the outside (extracellular space) of the cell. The intracellular space incorporates the nucleus that holds all genetic information for the function of the cell. The mitochondria are responsible for carrying out the metabolism and thus delivering the energy required for the cells processes. The sarcoplasmatic reticulum is storing calcium ions needed for the contraction of the cell which is carried out by thousands of myofibrills.

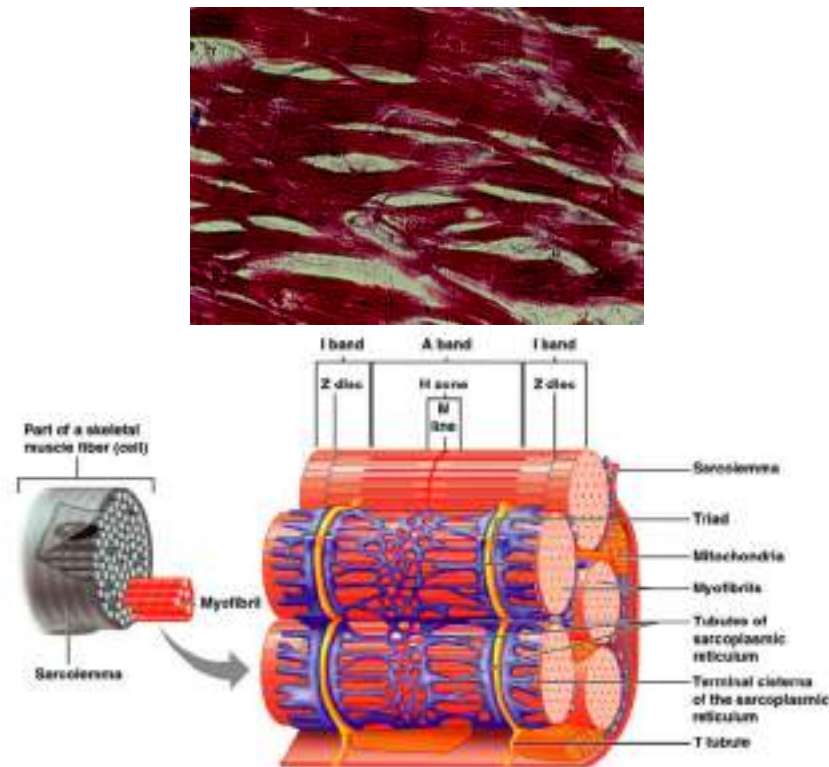


**Figure 3.7.** The figure shows a microscopic image of myocardial cells (top) [195]. The branching fibres are clearly visible. The laminar structure can be recognized, also. The bottom figure is a schematic drawing of a part of skeletal muscle fibre showing the structures responsible for the contraction of a muscle cell [279].

### 3.2.1.1 The Membrane of the Cell

The cell membrane (sarcolemma) causes differences in ion concentration which lead to a potential difference between the inside and the outside of the cell. This potential difference can be measured and is called transmembrane voltage  $V_m$ . An excitation of the cell causes changes in ion concentration which in turn triggers the contraction of a cell.

Mainly sodium ( $Na^+$ ), potassium ( $K^+$ ), calcium ( $Ca^{2+}$ ) and chloride ( $Cl^-$ ) ions can be found in the aqueous milieu of the cell. Their different concentrations inside the cell and extracellularly are held up due to the structure of the cells membrane. It is a selective permeable phospholipid bilayer of thickness  $4 - 5 \text{ nm}$  where ions can only pass between the intra- and extracellular space through their respective channels, i. e. a  $Ca^{2+}$  ion cannot pass through a  $Na^+$  ion channel (see fig. 3.8). But the membrane also incorporates proteins that actively work against the ion concentration gradient and the electrochemical gradient of ions: ion pumps and exchangers. Finally, gap junctions - existing only in cardiac cells - make up channels between cells, connecting the intracellular spaces where all particles can pass through freely. They are therefore called non-selective.



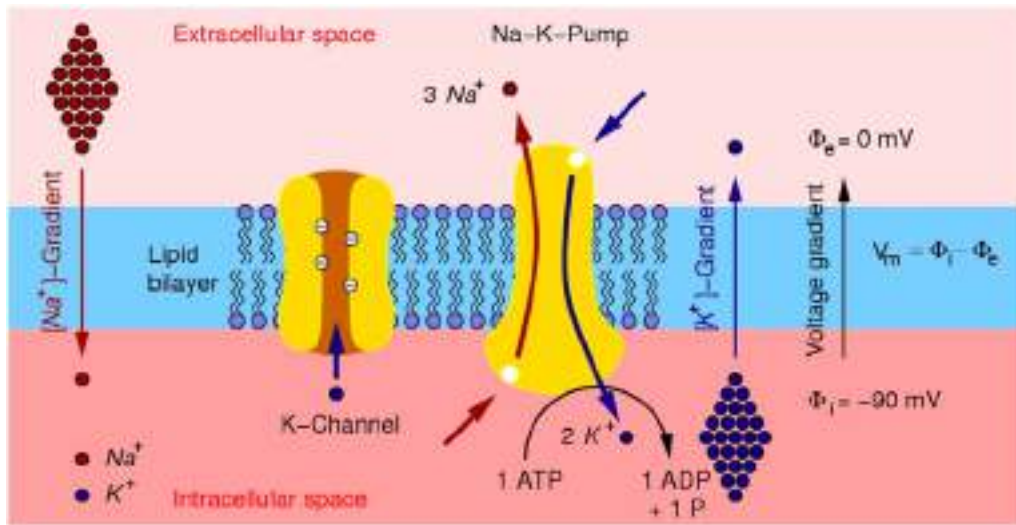


**Figure 3.8.** The figure shows the principle components of a cell membrane including a potassium ( $K^+$ ) channel, a sodium ( $Na^+$ ) - potassium pump and the ion channel concentrations with their respective gradients [70]. The voltage gradient points from the intracellular space to the extracellular space making the transmembrane voltage  $V_m$  negative in the resting phase.

### *Ion Channels*

The channels diameter is about 1 nm. Ion channels do not allow all ion types to pass through freely. Mainly three different ion channel types can be observed:  $Na^+$  channels,  $K^+$  channels and  $Ca^{2+}$  channels. Their structure cause a selection of ions, i.e. a specific ion can only pass through a specific channel. Since the ions are in an aqueous milieu, they are hydrated:  $H_2O$  molecules are bound to the ions since the water molecule is polarized. The binding energy of the hydrated ion has to be broken so that the ion can pass the channel. Since this dehydration is specific for each ion type, a specific selection of ions can be seen. Also, the size of ions varies, too. Thus, some ions simply do not fit through the ion channels of a different type.

Ion channels are not open all the time. Gating processes allow the ions either to pass the membrane or force the ions to stay on one side of the membrane. A gating process depends on several parameters. It can be voltage dependent (see figure 3.9), which means that the opening and closing of the channel depends on the transmembrane voltage  $V_m$ . These voltage sensitive channels have an electrical sensor which controls the conformation state of the protein and thus the opening and closing of the channel. Neurotransmitter (e.g. adrenaline) or ligands (e.g. ATP) can be found as gating mechanism. In these cases, the channel incorporates binding sites where the ligand or neurotransmitter can dock in and open the channel. These specialized binding sites can be situated intracellularly working with ligands or extracellularly for neurotransmitters. Even mechanical activation triggers the gating in some proteins. Since

the ion flow through these channels is controlled only by gating, the transport of ions is passive, i.e. no energy is required for the transport and the ions follow the electrochemical gradient and diffuse through the membrane (see section 3.2.1.2).

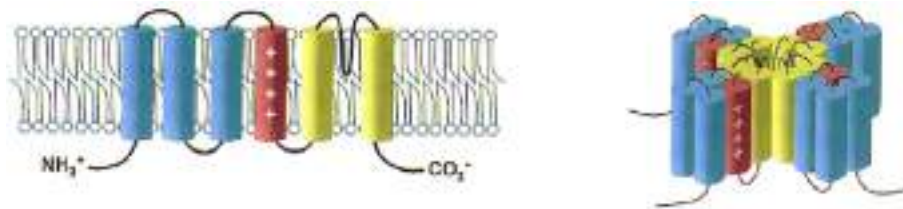


**Figure 3.9.** This figure shows the structure of a voltage gated  $K^+$  channel. Figure from [10].

### ***Ion Pumps***

Ion pumps work against the electrochemical gradient, i.e. they help to maintain it (see section 3.2.1.2). They therefore require energy. The hydrolysis of ATP (adenosine triphosphate) into ADP (adenosine diphosphate) and phosphate ions  $P$  delivers this energy that can be directly used by the cell. Hence, the ion pumps are also called ATPase. They are the primary active transport of ions through the sarcolemma. Three different types of pumps can be observed:  $Na^+ / K^+$  pumps, which transport three  $Na^+$  ions out of the cell and two  $K^+$  ions into the cell in once cycle (see figure 3.10),  $Ca^{2+}$  pumps that support the  $Ca^{2+}$  reservoir in the sarcoplasmic reticulum and  $Ca^{2+}$ -ATPase pumps, which functions as a maintainer of low intracellular  $Ca^{2+}$  ion concentration during the resting phase. The  $Na^+ / K^+$  pumps are most prominent. They are mainly responsible for holding up the transmembrane voltage through keeping the ion concentration gradient stable between intra- and extracellular space.

### ***Ion Exchanger***

Ion exchanger are a secondary active transport for ions through the cells membrane: The exchange of ions is coupled to the passive transport along the electrochemical gradient of a specific ion type (see figure 3.11). Hence, the electrochemical gradient is the driving force of the exchanger. Thus, the passive transport of one molecule along the gradient causes the exchange of ions against the gradient of another molecule. The  $Na^+ / Ca^{2+}$  exchanger swaps three  $Na^+$  (from extracellular to intracellular space) for one  $Ca^{2+}$  ion, which moves through the cell membrane into the extracellular space, in forward mode. During depolarisation, the  $Na^+ / Ca^{2+}$  exchanger operates in reverse mode, i.e. the direction of ion flow changes both for  $Na^+$  ions and  $Ca^{2+}$  ions. This specific exchanger is called antiport because the exchange of ions is carried out in opposite direction to the driving force (in this case generated by the  $Na^+$  ion gradient). If the exchange of ions is carried out in the same direction to the driving molecule, the exchanger is called symport: The  $Na^+$  -glucose exchanger transports a glucose



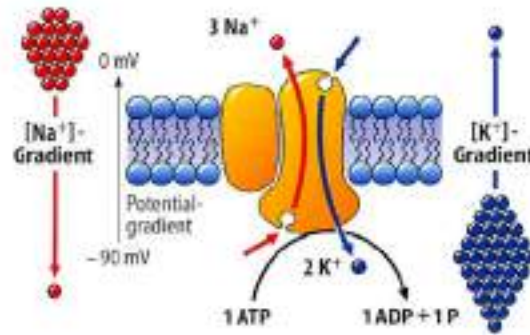


**Figure 3.10.** Schematic description of a  $\text{Na}^+ / \text{K}^+$  pump [70]. Three  $\text{Na}^+$  ions are pumped against the chemical gradient to the outside of the cell in one cycle. At the same time, two  $\text{K}^+$  ions will be transported from the extracellular space into the cell against the  $\text{K}^+$  ion concentration gradient. The pumping process requires energy which is gained by the hydrolysis of ATP (adenosine triphosphate) into ADP (adenosine diphosphate) and phosphate ions  $P$ .

molecule against its electrochemical gradient into the cell as the inflowing  $\text{Na}^+$  ions delivers the energy for this transport.

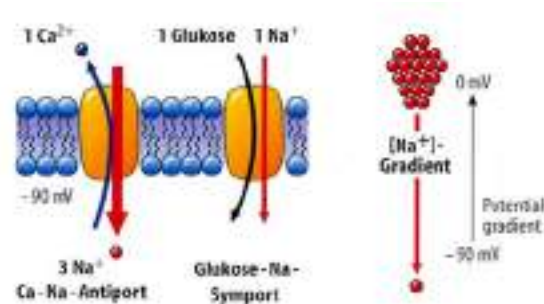


**Figure 3.11.** Schematic description of an ion exchanger [70]. The  $\text{Na}^+ / \text{Ca}^{2+}$  exchanger swaps as an antiport three  $\text{Na}^+$  for one  $\text{Ca}^{2+}$  ion from extracellular to intracellular space and vice versa. The  $\text{Na}^+$  - glucose exchanger transports a glucose molecule against its electrochemical gradient into the cell as the inflowing  $\text{Na}^+$  ions delivers the energy for this transport.

### Gap Junctions

With a channel diameter of  $1.5 - 2 \text{ nm}$ , the gap junctions cause a low electrical resistance between adjacent cells. These channels form the interconnection between cardiomyocytes not only electrically but also mechanically. They are mostly located at the intercalated discs, the coupling region of cells, which are mainly situated at the ends of the myocyte. The gap junctions transverse a gap of  $2 - 3 \text{ nm}$  between the membranes of adjacent cells. Their length is between  $2 - 12 \text{ nm}$ . Their barrel shaped structure is held up by two connexons, one of each cell. The

connexon is a hexamer of six proteins called connexins (see figure 3.12). Since the diameter of a gap junction is large compared to the size of ions and metabolites, they can diffuse freely inside the intracellular space of several cardiomyocytes.

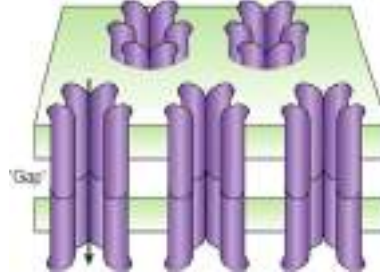


**Figure 3.12.** Schematic drawing of gap junctions [103]. Gap junctions form an electromechanical inter-connection between cardiac cells. A gap junction is barrel shaped and made up of two connexons which is a hexamer of six connexins.

Ion channels, pumps and exchangers are pores and each cell type has a different set of their sacrolemmal distribution. The multitude of gating mechanisms lead to a multitude of ionic currents even of the same kind through the membrane. Thus, each cell type shows different changes of transmembrane voltage  $V_m$  when excited (see section 3.2.1.3).

### 3.2.1.2 Resting Potential

Due to the selective permeability of the sacrolemma, its ion channels, pumps and exchangers, the intra- and extracellular space show different concentrations for each ion type (see table 3.1). While the concentration of  $Na^+$  ions is higher extracellularly ( $144.0 \text{ mmol/kgH}_2\text{O}$  vs.  $7.0 \text{ mmol/kgH}_2\text{O}$ ), the  $K^+$  ion concentration is lower extracellularly than inside the cell ( $4.5 \text{ mmol/kgH}_2\text{O}$  vs.  $160.0 \text{ mmol/kgH}_2\text{O}$ ). This results not only in different ion concentration gradients: since the ions have an electric charge associated with them, their different concentrations causes a potential difference across the membrane leading to an electrochemical gradient. Ion movement occurs through diffusion along the concentration gradient and the electrochemical gradient. Once a balance has been reached between these driving forces, the cell is in equilibrium and the potential difference between the intracellular and extracellular space is called resting potential. The transmembrane voltage  $V_m$  is defined as

$$V_m = \Phi_i - \Phi_e \quad (3.1)$$

where  $\Phi_i$  and  $\Phi_e$  are the intracellular and extracellular potentials, respectively. Changes in the transmembrane voltage push the resting potential out of balance and an action potential is triggered (see section 3.2.1.3). But first the definition and calculation of the resting potential will be discussed.

### ***Diffusion of Ions***

Diffusion is defined as the random thermal movement of particles. Although random, the movement can become directed if a concentration difference between two subspaces can be observed. Hence, a diffusion rate can be defined as described by Ficks Diffusion Law:

$$J_D = AD \frac{\Delta C}{\Delta x} \quad (3.2)$$

It states that the diffusion rate  $J_D$  acts proportional to the area  $A$  of the membrane, the diffusion coefficient  $D$  and the concentration gradient  $\Delta C$  but inversly proportional to the thickness of the membrane  $\Delta x$ . The diffusion coefficient is defined by the Stokes-Einstein Equation including the absolute temperature  $T$ , the viscosity of fluid  $\eta$ , the radius of the particle  $r$  as well as the gas constant  $R = 8,3144 \frac{J}{K_{mol}}$ .

$$D = \frac{RT}{6\pi r \eta} \quad (3.3)$$

Ficks Diffusion Law (eq. 3.2) describes diffusion due to a concentration gradient only. Since ions are associated with a certain charge  $q$  or valence of the ion and the concentration differences on both sides of the cell membrane cause the potential difference  $V$ , a force  $F_E$  can be defined that also acts on the ions causing directed movement along the forces direction through the membrane with thickness  $\Delta x$ :

$$F_E = q \frac{V}{\Delta x} \quad (3.4)$$

Thus, the total ion flux through the membrane  $j_{Ion}$  is the sum of ion fluxes due to the concentration gradient  $j_D$  and the electrical force  $j_E$ :

$$j_{Ion} = j_D + j_E \quad (3.5)$$

### ***Equilibrium Voltage $E_{Ion}$***

Equation 3.5 leads to a description of the equilibrium voltage  $E_{Ion}$  called the Nernst Equation via the Nernst-Planck Equation. The total flux  $j_m$  can be written as

$$j_{Ion} = j_D + j_E = -D_{Ion} \nabla [Ion] - D_{Ion} \frac{[Ion] z_{Ion} F}{RT} \nabla \phi$$

resulting in the Nernst-Planck Equation for the total ionic flux of ion type  $[Ion]$ :

$$j_{Ion} = -D_{Ion} \left( \nabla [Ion] + \frac{[Ion] z_{Ion} F}{RT} \nabla \phi \right) \quad (3.6)$$

where the concentration of ion type  $[Ion]$  is taken into account. The valence number and thus charge of the ion  $z_{Ion}$  together with the gas constant  $R$ , the absolute temperature  $T$  as well as the Faraday constant  $F = 9,6510^4 \frac{As}{mol}$  and the electrical potential  $\phi$  are included. The diffusion constant  $D_{Ion}$  taking into account the ion mobility  $\mu$  for the specific ion type is given by

$$D_{Ion} = \frac{\mu RT}{|z_{Ion}| F} \quad (3.7)$$

Given  $j_{Ion} = 0$ , an electrochemical equilibrium state is reached. In this state, no diffusion and no overall ion flux passes through the membrane resulting in a resting potential. It can be determined by the Nernst Equation that follows from equation 3.6 including the intra- and extracellular ion concentration  $[Ion]_i$  and  $[Ion]_e$ , respectively:

$$E_{Ion} = \frac{RT}{F z_{Ion}} \ln \frac{[Ion]_e}{[Ion]_i} \quad (3.8)$$

$E_{Ion}$  is called the equilibrium or Nernst voltage across a membrane for a specific ion of type  $[Ion]$  provided the membrane is only permeable for just one single ion type. Table 3.1 shows the Nernst voltages for  $K^+$ ,  $Na^+$ ,  $Ca^{2+}$  and  $Cl^-$  ions.

Ion type	Extracellular space $[X]_e [mmol/kgH_2O]$	Intracellular space $[X]_i [mmol/kgH_2O]$	Nernst voltage $[mV]$
$K^+$	4,5	160,0	-95,4
$Na^+$	144,0	7,0	80,8
$Ca^{2+}$	1,3	$10^{-5} - 10^{-4}$	126,5 – 157,3
$Cl^-$	114,0	7,0	-74,5

**Table 3.1.** Typical ion concentration and their associated Nernst voltages of skeletal muscle [266].

### Goldman-Hodgkin-Katz Equation

While the Nernst Equation takes care of only one ion type, the Goldman-Hodgkin-Katz Equation includes principally all ion types. It is an extension of the Nernst Equation where each ion concentration  $[Ion]$  is associated with the respective permeability of the membrane  $P_{Ion}$  which in turn no longer requires the valence number  $z_{Ion}$ . The membrane potential  $E_m$  is therefore determined by

$$E_m = \frac{RT}{F} \ln \frac{P_{K^+} [K^+]_e + P_{Na^+} [Na^+]_e + P_{Cl^-} [Cl^-]_i}{P_{K^+} [K^+]_i + P_{Na^+} [Na^+]_i + P_{Cl^-} [Cl^-]_e} \quad (3.9)$$

with

$$P_{Ion} = \frac{\mu_{Ion} RT}{\Delta x F} = D_{Ion} \frac{\beta_{Ion}}{\Delta x} \quad (3.10)$$

including the diffusion constant  $D_{Ion}$  (eq. 3.7), the water membrane partition coefficient of the ion  $\beta_{Ion}$  and  $\Delta x$ , the thickness of the membrane respective equations 3.2 and 3.4.

The Goldman-Hodgkin-Katz Equation (eq. 3.9) can be extended by any ion type if its intra- and extracellular concentration and its permeability is known. Thus, the transmembrane voltage of a repolarized cell, i.e. a cell in its resting state, can be determined by  $V_m = E_m$ . The resting potentials for a selection of cell types is given in table 3.1.

### 3.2.1.3 Action Potential

Cells of the nervous system carry forward information through triggering action potentials that are carried to the respective part in the brain or back to the body. Cardiac cells can also be excited and show an action potential which in turn causes a shift in ion concentration and thus a contraction. The change of transmembrane voltage  $V_m$  over time  $t$  defines the action potential:

$$\frac{dV_m}{dt} = -\frac{1}{C_m} (I_m - I_{inter}) \quad (3.11)$$

$C_m$  is the membrane capacitance and the membrane current  $I_m$  is due to the change of charge through the membrane, i.e. ion flow through the sacrolemma, and can be determined by

$$I_m = \frac{dQ}{dt} = g_m (V_m - E_{ext}) \quad (3.12)$$

An external stimulus  $E_{ext}$  carried forward by neighbouring cells or by artificially stimulating causes a change of membrane potentials above a certain threshold triggers the action potential. The “all or nothing” principle can be applied meaning that any stimulus causing  $V_m$  to reach the threshold leads to an action potential. The course of action potential is determined by the opening and closing of different ion channels and thus of different ion currents through the membrane (see figure 3.13). The currents charge or discharge the membrane capacitor leading to a change of  $V_m$  (eq. 3.11). Many ionic currents are involved in forming the action potential. But fast sodium channels, slow calcium channels and slow potassium channels are the most predominant and therefore define the principal shape of the action potential (see figure 3.13). The fast upstroke of the action potential is controlled by a fast inflowing sodium current  $I_{Na}$ . The fast  $Na^+$  channels open when the threshold voltage is reached causing the  $Na^+$  ions to flow into the cell in an avalanche-like fashion. This change in the electrical gradient between intra- and extracellular space is called depolarisation. The transient outward flow of  $K^+$  ions creates the so called “spike-and-dome” morphology. The spike is created by the fast sodium current followed by a little notch due to the inactivation state of  $Na^+$  channels and the opening of the  $Ca^{2+}$  and  $K^+$  channels (repolarisation phase 1). The  $K^+$  current gives way to a dominion of the  $Ca^{2+}$  current to create the “dome” in the plateau phase (repolarisation phase 2). The slow  $Ca^{2+}$  channels are responsible for keeping the transmembrane

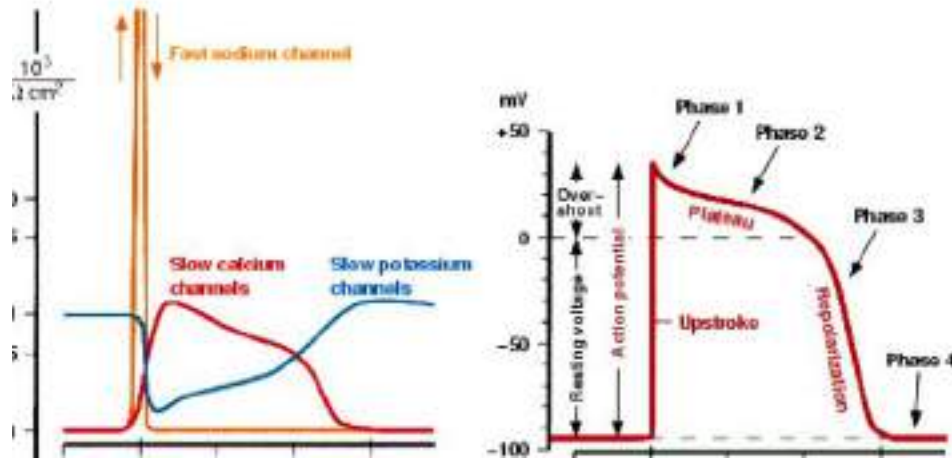


**Figure 3.13.** This figure depicts the elements of an action potential [258]. The sum of different transmembrane currents (left) make up the action potential (right).

voltage  $V_m$  at almost a constant level, slowly decreasing. During the repolarisation phase 3, a transient outward flux of  $K^+$  ions results in a steep repolarisation of the cell. The early resting phase in which the transmembrane voltage  $V_m$  has reached its resting potentials is called repolarisation phase 4. During this phase a hyperpolarisation can be observed sometimes due to other outward currents turning  $V_m$  more negative than the resting voltage.

### 3.2.2 Working Myocardium, Pacemaker Cells and Cells of the Conduction System

Since the cardiac cells have to fulfill the task of excitation initiation, fast excitation conduction and contraction, their respective structure is slightly changed. While different ion channel distributions cause the cells of the sinus node to self-depolarise, the amount of gap junctions between cells of the conduction system is increased compared to other areas. The working myocardium is responsible for the contraction of the heart. Thus, its contraction apparatus is strongly developed. The different structures lead to different action potentials seen in figures 3.14 and 3.15. Also, the action potential differs depending on the frequency with which the cell is stimulated. The hearts pumping frequency has to increase if a faster blood flow is required, e.g. during exercise. The faster the frequency, the shorter the action potential. Its shape is also slightly modified (see figure 3.15).

Thus, the cardiomyocytes adapt to the required needs. Also, if a cell is stimulated while the repolarisation is not finished, another action potential can be initiated having a different course again. This does not happen if the  $Na^+$  channels are still in their inactive state. They are voltage sensitive and only open again after the transmembrane voltage  $V_m$  falls below  $-50 \text{ mV}$ . This period is called absolute refractive period since no action potential can be triggered within this

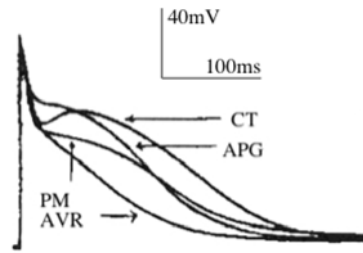


**Figure 3.14.** This figure shows the action potentials for different atrial myocytes: the crista terminalis (CT), the pectinate muscles (PM), the atrial appendage (APG) and the atrio-ventricular ring (AVR) [81].

time. Afterwards, during relative refractoriness (repolarisation phases 3 - 4), the fast  $Na^+$  channels could be opened again by an external stimulus which would lead to another overshoot and action potential. But since the resting phases ion concentrations of  $K^+$  and  $Ca^{2+}$  will not have been reestablished, the action potential shows a different morphology, which is mainly characterised by short action potentials with lower amplitude. Under physiological circumstances, the cells will not be excited during their relative refractive periods, though, while the adaptation to frequency change is obligatory physiologically.

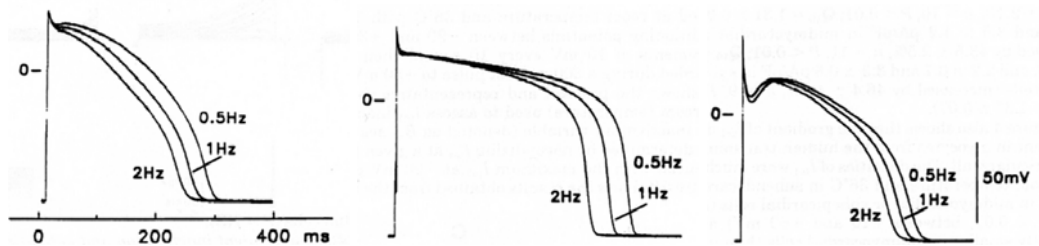


**Figure 3.15.** Different action potential morphologies are shown for ventricular myocytes that were stimulated with different frequencies. The action potentials were measured on isolated cells from the subendocardium (left), the midmyocardium (middle) and the subepicardium (right) [162].

### 3.2.3 The Electrocardiogramm

All different action potentials of the myocardium add to a changing electric field created by the excitation propagation. The signal of the excitation of cardiac cells is conducted to the body surface. There, the electrical activity of the heart can be measured by electrodes giving an electrocardiogramm (ECG) [150]. The ECG shows which part of the heart is depolarising, which repolarising. While the excitation of the atria is clearly visible in the P wave of the ECG (see figure 3.16), its

repolarisation is overshadowed by the depolarisation of the ventricles. The heterogeneity of the ventricular wall cause a positive T wave which represents the repolarisation phase of the ventricles.

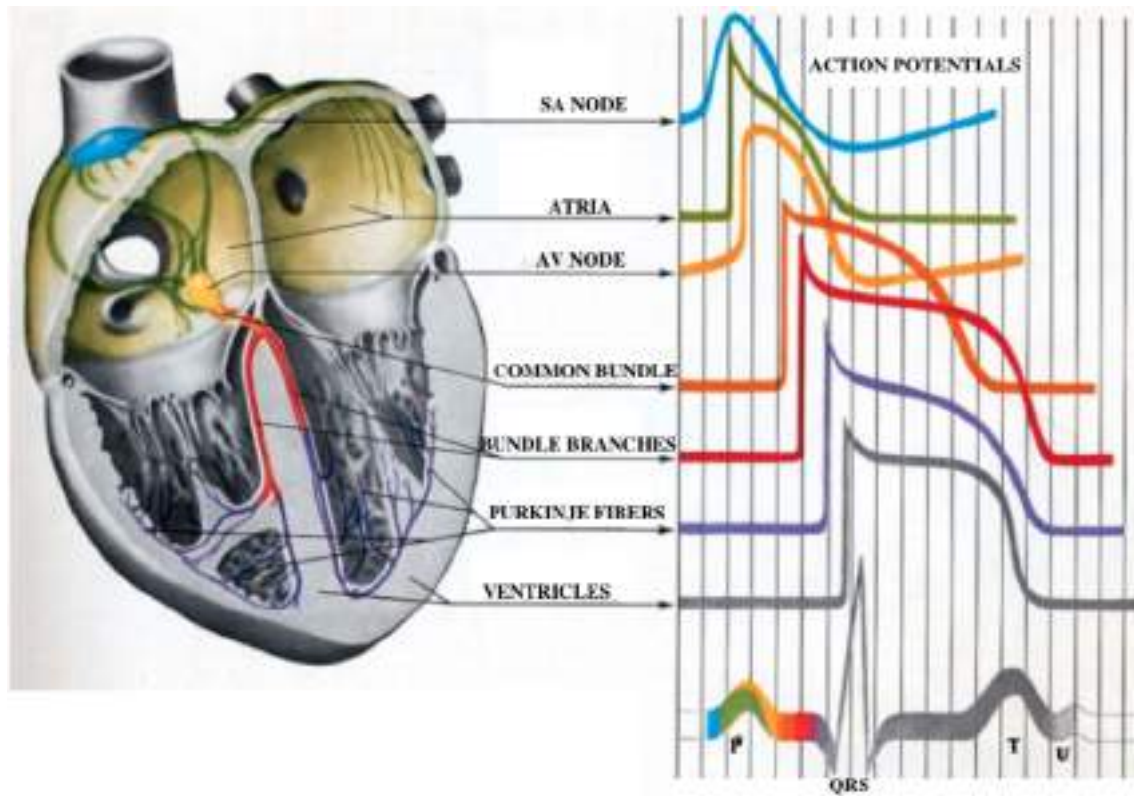


**Figure 3.16.** The excitation of the myocardial cells give rise to different action potential shapes at different times in the cardiac cycle (left). They contribute to the morphology of the electrocardiogram (right) [202].



## Pathology

*“The art of medicine consists in amusing the patient while nature cures the disease.”*

Voltaire

French author, humanist, rationalist and satirist (1694 - 1778)

The understanding of the pathological genesis and behaviour in heart failure and in supraventricular arrhythmia is of vital importance not only in choosing the correct form of therapy but also in designing algorithms to optimise therapeutical strategies in a computer model. The computer model has to realistically represent the pathological behaviour. Only then can the simulation of the therapy predict likely outcomes of the intervention. Therefore, the following chapter will describe the pathological basis of supraventricular arrhythmia (4.1.1) and congestive heart failure (4.2) according to current clinical studies and analysis. The interrelationship between congestive heart failure and atrial fibrillation will be briefly highlighted in section 4.2.8.

### 4.1 Supraventricular Arrhythmia

An arrhythmic heart is given if the heart rate differs from the physiologic rate mostly not showing a constant beating frequency. Bradycardia is present if the heart rate is very slow (less than 60 beats per minute (bpm)), which can lead to re-entrant circuits and thus to atrial flutter and fibrillation (see section 4.1.1.1). Tachyarrhythmia are defined by an abnormally fast heart rate from 100 bpm in an adult up to 400 bpm. This work focuses on supraventricular tachyarrhythmia whose initiation, mechanisms and classification will be discussed below. The therapeutical strategies (see section 5.1) are based on these mechanisms. Therefore, the distinct knowledge of the initiation and mechanisms of atrial fibrillation (AF) is required for the simulation and optimisation of therapeutical approaches (see section 10.1). Many factors contribute to the development and progression of AF [124, 159, 210, 211, 114, 71]. The pathophysiology is described in this section. Its relevance for modelling AF in a computer simulation is discussed in section 9.1.

### 4.1.1 Atrial Fibrillation

Atrial fibrillation is described by very fast and chaotic excitation of the atria which leads to a loss of mechanical contraction of the atria and non-physiological contraction of the ventricles. Age, diet, neurohormones and inflammation as well as cardiovascular diseases, structural and physiological changes, genetics and the autonomic nervous system have an influence on the initiation and maintenance of AF [159, 210, 211]. While age, diet and inflammation may coincidentally occur, cause changes and therefore contribute to AF instances, structural and physiological changes (maybe supported by the underlying genetics) as well as the autonomic nervous system are mainly responsible for atrial fibrillation<sup>1</sup>.

#### 4.1.1.1 Initiation of Atrial Fibrillation

##### *Initiation through bradycardia*

Bradyarrhythmia are due to sinus or AV nodal dysfunction [251] or develop due to reduced blood circulation in the tissue [216]. Bradycardia can induce areas of heterogeneous refractoriness [217]. But also, relative bradycardia can trigger paroxysmal AF. The slower heart rate results in the tissue not being excited timely. Areas of slower conduction will cause the atria to be vulnerable to AF due to re-entrant mechanisms.

##### *Initiation through re-entrant circuits*

The pulmonary veins (PVs) have been mostly targeted as the source of arrhythmogenic activity involved in the initiation of atrial fibrillation. This activity appears to be localized in the myocardial sleeves of the vessels [147, 47]. The anatomic pattern of these sleeves indeed seems to correlate with the relative distribution of PV ectopy [119, 118] compared with the seminal findings in [108] where 31 foci were located in the left superior PV, 17 in the right superior PV, 11 in the left inferior PV and 6 in the right inferior PV. The myocardial sleeves have a greater extend in the superior PVs and the left PVs show larger sleeves compared to the right PVs [196, 31]. Further, myocardial gaps composed of fibrous tissue have been found [118]. The meshlike arrangement of muscle fascicles, which is made up of circular-oriented bundles that are interconnected by longitudinally oriented myocardial bundles, indicates the complexity of the anatomical structures at the PV ostia. These structures do not seem to be influenced by neither age nor histological appearance [83]. The fibre orientation

<sup>1</sup> “Many factors have been identified as being associated with postoperative AF, but the most consistent variable across studies is increasing patient age [124].” - Many studies mentioned in the following sections state that age is a parameter that correlates greatly with the incidence of AF: The older the patient the more likely the incidence of AF. This correlations is a fact although age itself does not seem to present any mechanism to cause AF. The changes of the substrate due to age is rather what causes AF in elderly patients. The older a person gets, the more likely will be changes in the electrophysiological behaviour, structural and anatomical changes as well as changes in the contraction properties of myocytes. These changes contribute to AF as described below.

also seems to play a vital role in the initiation of AF: The greater the degree of fibre orientation the longer the conduction delay [121] which facilitates re-entry in the PVs. A conduction block was also associated with the sudden change of fibre orientation and secondary to gaps of connective tissue. This behaviour seems to be further exacerbated by fibrosis and aging [121]. Hence, evidence from these studies indicates that the anatomical structures and a non-uniform anisotropy is the key to re-entry and therefore to AF [110, 121]. This can be supported by other studies: Decremental conduction between PVs and LA and slow conduction between PVs was also noted to be far more frequent in patients with AF [134]. Conduction delay and short refractory periods have also been identified suggesting a re-entrant mechanism [275, 259]. Different repolarisation times in the myocardium ( $APD_{80}$ <sup>2</sup> is significantly longer in the endocardium than in the epicardium; it is even longer in the PVs [5]) and the influence of atrial stretch on maintaining re-entries in the PVs [142] support the theory of re-entrant circuits at least for the maintenance of AF. In fact, heterogeneous conduction velocities leave the atria vulnerable to re-entries and thus to AF. Increased dispersion of atrial refractoriness and long intra-atrial conduction timing leaves the atrium vulnerable to AF due to the possibility of re-entrant circuits [153, 77, 83]

#### *Initiation through foci in the pulmonary veins*

Although no evidence of abnormal automaticity or triggered activity were observed in [121], a tight coupled extrastimulus within the PV would result in unidirectional conduction block and re-entry. Several studies have measured abnormal automatic activity mostly in the pulmonary veins [83]. It was proposed that a focal trigger may be maintained as a rapid re-entrant circuit in the PVs [5]. Studies in experimental models and in patients have demonstrated that a rapidly firing focus or a reentrant circuit of very short cycle length can cause AF by producing fibrillatory conduction to the rest of the atria [290]. Other findings suggest that the PVs are capable of automaticity [83]. Repetitive focal discharges of about 340 bpm [108] with a cycle length of 108 – 280 ms [194] have been measured. Their occurrence with respect to the sinus beat is  $216 \pm 34$  ms (time from sinus beat to begin of ectopic beat). While the foci in atrial tachycardia seem to be situated ostially [149], they originate rather distally in the PVs [108, 133]. A single trigger most often is present although multiple foci in multiple veins have been observed. Especially rapid firing activity in one vein could induce firing in another vein [155]. These triggers can be recurrent, especially in patients with paroxysmal<sup>3</sup> AF [256]. The ectopic or premature activation of the atria renders them vulnerable to re-entrant circuits. The time between a premature atrial complex due to ectopic activity to the following physiologic sinus beat is often longer than the intrinsic rate. These so called short - long - short cycles [187, 65, 243] are an indicator for a likely occurrence of AF.

<sup>2</sup> The action potential duration (APD) at 80 % repolarisation is denoted by " $APD_{80}$ ". In other studies, the APD is set to 90 % of repolarisation. Often this is not explicitly clarified.

<sup>3</sup> see section 4.1.4

### *Influence of the autonomic nervous system*

The underlying mechanisms of abnormal automatic foci remains uncertain to date. It has been suggested that the electrical properties of PVs are modulated by autonomic tone. Anatomic studies have revealed that the LA and PVs are innervated by adrenergic and cholinergic nerve fibres [83]. The autonomic nervous system (ANS) can alter refractory period properties of myocytes, atrial conduction and can affect automaticity, reentry, triggered automaticity and fibrillatory conduction. It is even implicated that the ANS may be the prime cause of AF which influences its initiation, perpetuation and termination [210]. However, it can be certain that the ANS plays a potentially important role in AF [198].

### *Atrial remodelling*

Atrial remodelling is known as a series of processes leading to change in atrial structure and function. These changes include alterations in atrial electrophysiology (ionic remodelling), atrial dimensions, contraction and atrial (ultra-) structure (structural remodelling) [260, 199]. It is an important factor in providing the substrate that supports the maintenance of AF. The shortening of atrial refractory periods and atrial action potentials may be caused by a net decrease of inward ionic currents ( $Na^+$ ,  $Ca^{2+}$ ), a net increase of outward currents ( $K^+$ ), or a combination of both. Shortening of refractoriness in combination with a reduced conduction velocity results in a shorter atrial wavelength which in turn favours AF [260]. But it has been shown, that the remodelling process is not the initiator of AF but occurs as a consequence of AF [300]. This process is known as “AF begets AF” since the remodelling process due to AF favours the maintenance of AF. But the remodelling process can also be initiated by haemodynamic overload. Nevertheless, its role in triggers such as PV ectopy and the initiation of AF is less clear. But the interrelationship between triggers and substrate can be also taken into account for the genesis and maintenance of AF [83].

#### **4.1.2 Maintenance of Atrial Fibrillation**

Although some claim ectopic foci to be the cause of AF in 80 % to 95 % of cases [250], re-entrant circuits are also still regarded to initiate AF [83, 183] possibly through a unidirectional conduction block. While pulmonary vein firing appears to be more dominant in the initiation of AF, driving rotors and multiple re-entrant circuits seem to maintain AF.

The multiple wavelet theory [188] hypothesis states that AF is sustained by multiple randomly wandering wavelets that either divide into daughter wavelets or collide and get extinguished. Consequently, the atria are re-excited in a chaotic and non-linear fashion. More recent studies have shown that a single source of stable re-entrant activity can also maintain AF [137, 172, 173, 190].

The PVs and the left atrium seem to have a critical role in maintaining rotors and re-entrant circuits in AF. It has been observed that the cycle length in the PV differs compared with the

cycle length in the left atrium. The cycle length was recorded in over 90 % to be shorter in the PVs than in the adjacent atrium [212]. The opposite was found after 5 s in another study where the posterior left atrium was proposed to be responsible in the maintenance of AF [200]. It can be concluded that the results from mapping electrical activation during AF may differ from that at AF onset.

The change in substrate contributes to the maintenance of AF. Brief refractory periods and decremental conduction as well as structural changes in the anatomy can be noted in patients with AF [52] which is favourable for the initiation of wavelets. The maintenance of these wavelets seems to be determined by local atrial refractoriness and excitability which sets their pathways rather than anatomical influences [153]. It was also observed that the minimum size of an atrial macro-reentrant circuit is determined by the duration of the local refractory period [50].

However, the multiple rotor theory has been challenged by Allesie's group [4]: measurements of the activation of the left atrium showed an excitation pattern whose paths seemed to follow the atrial fibre bundle structure. They did not measure a uniform excitation front but many small wavefronts exciting the tissue in a disorderly fashion. This excitation is due to the snake-like excitation pattern.

Whether the arrhythmogenicity of AF is a re-entrant or focal phenomenon, or possibly both, remains unclear. Also, the role of rotors or snakes in AF has to be determined. The underlying mechanism by which the PVs cause AF stays also incompletely characterised. The complex interplay of anatomy and electrophysiology in the PVs and the left atrium as well as their changes can be held to be responsible for the initiation and maintenance of AF. To conclude, among mechanisms recognised for having a role in atrial fibrillation stay primarily pulmonary vein focal triggers, rotors and re-entrant circuits, a critical mass to sustain fibrillatory conduction and vagal ganglia that can initiate spontaneous activation [223]. It is unlikely that a single pathophysiology is operative in all or even a majority of cases of AF.

#### 4.1.3 Atrial Flutter

Atrial fibrillation (AF) and atrial flutter (AFL) have a close clinical interrelationship [290]. Its understanding differs since the underlying mechanisms including arrhythmogenic substrate are very familiar [290, 32, 256]. Recent electrophysiological studies, especially mapping studies, have significantly advanced our understanding of this interrelationship. While the initiation of AF is mostly associated with ectopic triggers in the left atrium, AFL is most commonly arising from a macro re-entrant circuit in the right atrium or around scar tissue in case of previous cardiothoracic surgery [256]. The functional components of the macro re-entry are believed to be established during atrial fibrillation which precedes the onset of AFL in almost all instances [290]. Apparently, a block between the venae cavae is the major determinant whether AF persists or AFL develops. If this block is not present or small, classical AFL does not appear [290].

A driving rotor wave which causes a stable re-entrant circuit of very short cycle length can be seen

as a fast form of AFL. If only a small part of the atria are excited by this rotor wave causing rapid, irregular activity in the atria, AFL turns into AF. The regular excitation conduction during AFL will be replaced by fibrillatory excitation. Thus, AF can be distinguished from AFL by the atrias property of regular or fibrillatory conduction [290].

#### 4.1.4 Clinical Classification of Atrial Fibrillation

Clinical classification takes four classes of AF into account: first episode, recurrent paroxysmal, recurrent persistent, permanent AF<sup>4</sup> [114].

##### *First episode*

The first episode is an initial event that occurs only once.

##### *Paroxysmal AF*

Recurrent paroxysmal AF describes episodes of AF lasting from a few seconds up to a few days. Most episodes are self-terminating and convert back into sinus rhythm within seven days. AF events may appear once a year or more frequently.

##### *Persistent AF*

Persistent AF does not spontaneously convert back into sinus rhythm. It lasts longer than seven days by definition. The first occurrence of AF may be persistent or episodes of paroxysmal AF may have preceded persistent AF. Cardioversion (either pharmacological or electrical) is successful treatment in persistent AF. Nevertheless, it is recurrent and cardioversion is not a cure.

##### *Permanent AF*

Permanent AF or chronic AF is constantly present. Cardioversion does not show signs of success. Permanent AF may be interrupted but comes back within 24 hours.

Clinical classification can be helpful in treatment decisions and the most widely accepted classification scheme as described above is found in the ACC/AHA/ESC guidelines [114].

#### 4.1.5 Atrial Fibrillation after Surgical Intervention

AF is one of the most frequent complications of cardiac surgery affecting up to 40 % of patients [124, 53, 55, 60]. Its incidence is high despite advances in surgical techniques and major advances in anaesthetics. Its precise mechanism is still totally unknown [267]. However, the etiology of post-operative AF is most likely multifactorial [53, 77] and the mechanism is believed to be re-entry [124].

<sup>4</sup> “Lone” AF is often discussed in literature. It is not a classification of AF but describes patients who do not appear to have any underlying heart disease after a careful evaluation.

Surgery might alter the substrate electrophysiologically and structurally due to heterogeneity of refractoriness after surgery. Multiple perioperative factors have been proposed to contribute to the latter, including operative trauma, inflammation, elevations in atrial pressure, autonomic nervous system imbalance, metabolic and electrolyte imbalances, or myocardial ischemic damage occurred during the operation [124].

## 4.2 Congestive Heart Failure

Heart failure in general describes a dysfunction of the heart. The pathological behaviour shows a reduced cardiac output [45]. Due to the dysfunction, the heart does not pump out the blood as quickly as it flows back, the venous system congests. Thus, this kind of heart failure is known as congestive heart failure (CHF). Hypertensive heart disease, coronary or ischemic heart disease, cardiomyopathy and valvular heart diseases all cause a change in the cardiovascular system leading to CHF which in turn can lead to sudden cardiac death.

### 4.2.1 Hypertensive Heart Disease

Hypertension can be diagnosed in 75 % of patients with heart failure [140]. Systemic hypertension induces an increased demand to the heart which reacts with the development of hypertensive heart disease. The result is hypertrophy in the ventricles due to pressure overload. In the case of no other injuries to the heart, ventricular hypertrophy mostly leads to a ventricular wall thickness which equally gets larger in the ventricle. The result is myocardial dysfunction, CHF, cardiac dilation and can lead to sudden death [45].

### 4.2.2 Ischemic Heart Disease

Ischemic Heart Disease (IHD) causes 80 - 90 % of deaths from patients with heart disease [45]. Myocardial ischemia describes an imbalance of the demand for oxygenated blood and nutrients to the supply (perfusion) and waste removal. In over 90 % of IHD, the coronary arteries are blocked to a certain extent which reduces bloodflow and perfusion. Thus, IHD can also be termed coronary artery disease (CAD). Clinical manifestations include myocardial infarction, angina pectoris, chronic ischemic heart disease with heart failure and sudden cardiac death. The affected tissue will cease to function with physiological behaviour. Conduction and contraction properties will diminish. Myocardial cells will also die rendering the tissue to become necrotic. Figure 4.1 shows the progression of myocardial necrosis after coronary artery occlusion [45].

Not only working myocardium suffers from IHD. The conduction pathways can be disturbed by IHD as well since the reduced perfusion also leaves the conduction system at decreased supply of oxygen and metabolic substrate delivery. Indeed, a blockage of the conduction system is present in many patients with severe heart failure which can cause asynchronous contraction of the ventricles which reduces the cardiac output even further.

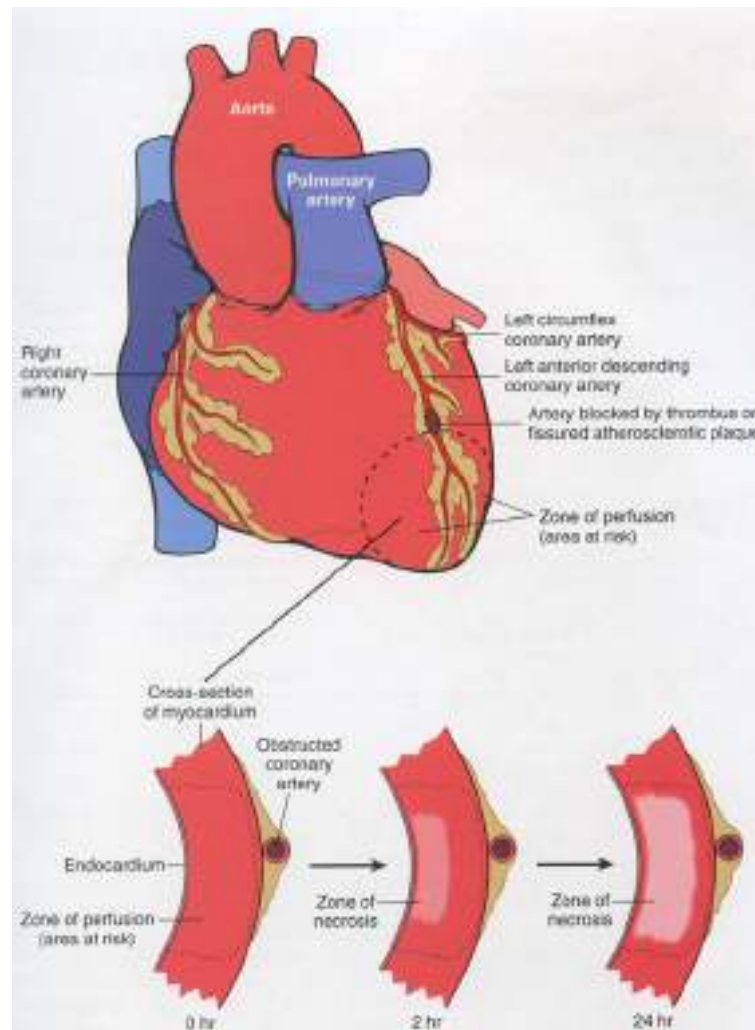


**Figure 4.1.** The figure shows a possible site of cardiac infarction [45]. The top figure shows the heart with a blockage in the left anterior descending coronary artery. The dashed circle at the apex around the artery indicates the area at risk where an infarction could develop due to lack of oxygen. The bottom three drawings show the effect of an obstructed artery: The necrotic area gets larger the longer the obstruction lasts. The result is an infarction leading to ischemic heart disease.

#### 4.2.3 Blockage in the Cardiac Conduction System

The cardiac conduction system (see section 3.1.2.1) can be disturbed at different stages leading to different pathologies. If the conduction system is blocked right after the atrio-ventricular (AV) node, the excitation does not propagate to the bundle of His (see figure 4.2). The result is hardly any excitation of the ventricles. If the block exists further down the conduction pathway, either ventricle gets excited through the respective other: A right bundle branch block (RBBB) causes the



left ventricle to be excited first. The excitation wave front then moves through the myocardium to the right ventricle which then contracts irregularly and delayed. Respectively, a left bundle branch block (LBBB) (see figure 4.2) causes the left ventricle to be excited after the right ventricle through myocardial conduction and not through the physiologic pathways.

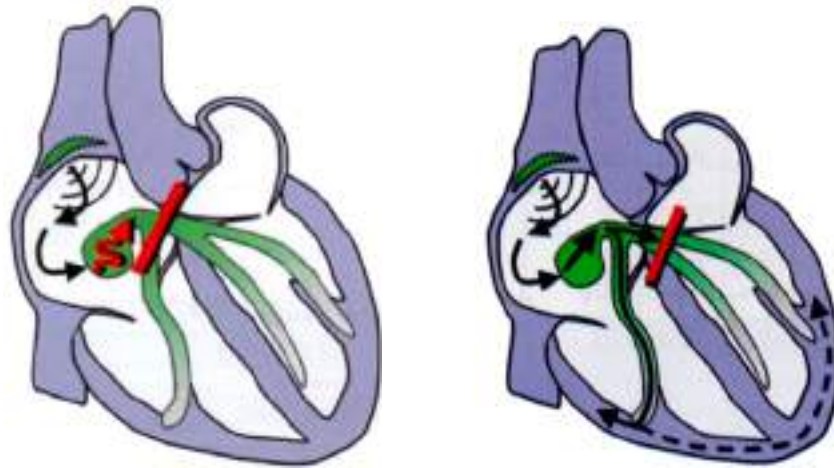


**Figure 4.2.** The left schematic drawing shows the excitation propagation in an atrio-ventricular (AV) block III [74]. The conduction block is right at the AV node which leads to no excitation of the ventricles through atrial excitation. The right figure shows a left bundle branch block. The atrial excitation gets propagated via the AV node to the right ventricular myocardium. The left ventricle will not be excited by physiological conduction but through the right ventricular excitation.

These interruptions in conduction pathways show many variations due to the underlying cardiomyopathy. They may be complete conduction blocks or incomplete. However, a synchronous contraction of the ventricles is not given. Abnormal conduction leads to delays in ventricular conduction. Mechanical events of the cardiac cycle are influenced by this behaviour and lead to abnormal ventricular activation and contraction, dyssynchrony, delayed opening and closure of mitral and aortic valves and abnormal diastolic function. Haemodynamically, cardiac output and ejection fraction are decreased as well as arterial pressure [140].

#### 4.2.4 Ventricular Remodelling

Ventricular remodelling is due to the previously mentioned pathological conditions as well as valvular heart disease [140]. It describes the process by which the size, shape and function of the ventricles changes due to mechanical, neurohormonal and maybe genetic factors. The remodelling characteristics are a loss of cardiac myocytes, hypertrophy and augmented interstitial fibrosis. Remodelling in cardiomyopathy can be recognised in hypotrophic or dilatated hearts without initial event (see figure 4.3), or after a myocardial infarction. The latter leads to a loss of myocytes, changes the

mechanical and electrophysiological properties of the ischemic region which causes an abnormal load condition on the ventricle. The remodelling process then continues over a period of month rendering the heart in a hypertrophic state and a more spherical state [140].

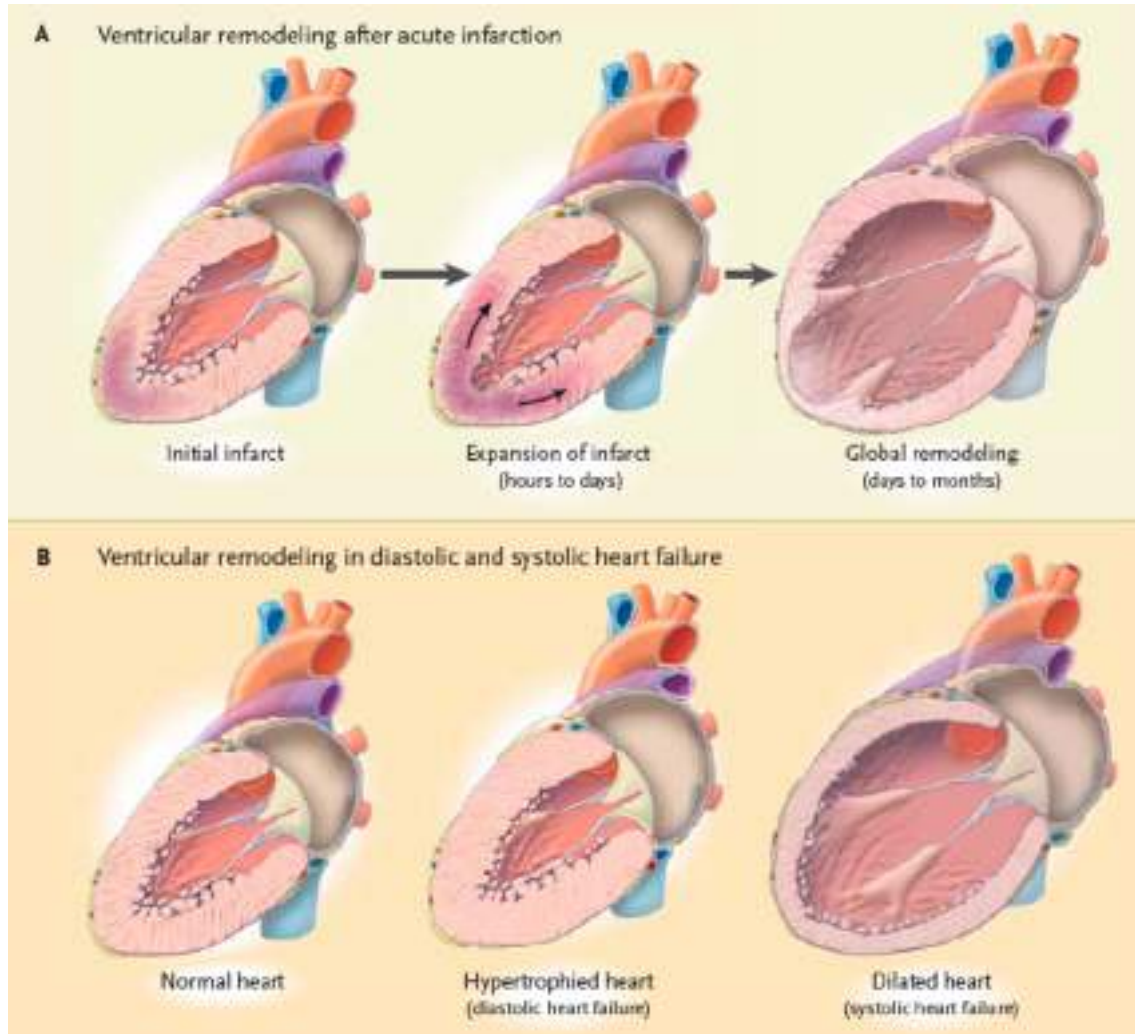


**Figure 4.3.** Figure A shows the ventricular remodelling process after an apical infarction. The initial infarct will not show clinically significant changes in the geometry. However, within days to month, the area affected becomes thinner and expands ending in global remodelling and dilatation. Figure B shows the remodelling process in classical diastolic and systolic heart failure. The myocardial wall thickens in diastolic heart failure while the dilatation occurs in systolic heart failure. A change in anatomical shape is clearly visible in any of these pathologies. Figure from Jessup et al. [140].

Mitral regurgitation can follow from the remodelling process. The result is an increased volume overload in the left ventricle reducing the cardiac output and thus putting more strain on the

work load on the heart. Thus, ventricular remodelling is a process which worsens the state of heart failure.

#### 4.2.5 Diastolic Heart Failure

The relaxation mechanism might be faulty in the cardiac tissue while the contraction still shows a normal ejection fraction. The filling volume of the ventricles is reduced due to slow relaxation and the cardiac output is limited especially when the heart frequency increases during exercise (see figure 4.3). This pathology leads to increased ventricular pressure and is called diastolic heart failure. Although the mechanism differs from the previously described, the symptoms of diastolic heart failure are very similar to those of a dilated, poorly contracting heart [140].

#### 4.2.6 Ventricular Dyssynchrony

Bundle branch blocks will delay contraction between the two ventricles (interventricular delay) but a diseased myocardium (dilated cardiomyopathy and scar from a myocardial infarction) with slowing conduction, will result in LV electromechanical dysfunction (intraventricular delay). Interventricular or intraventricular electrical delays are frequent in the HF population with the intraventricular delay being a greater predictor of mortality [80, 235]. The length of QRS complexes exceed 120 *ms* in a third of patients in heart failure [235]. But it has been shown that QRS duration and ventricular dyssynchrony do not necessarily correlate [185, 22]. QRS duration may not be an adequate indicator for dyssynchronous contraction. Over a third of patients with QRS complex length of over 120 *ms* do not show ventricular dyssynchrony while significant dyssynchrony can be found in about 30 % of patients with narrow QRS complex. Thus, left ventricular dyssynchrony can be rather defined by the electromechanical delay between septum and lateral wall (septal-to-lateral delay). In extensive dyssynchrony, this delay can be over 60 *ms* [22].

Asynchronous contraction as provoked by electromechanical delays results in a decreased ejection fraction and cardiac output. An increase in wall stress and delayed ventricular relaxation can also be observed reducing cardiac efficiency [309, 235].

#### 4.2.7 Clinical Classification of Congestive Heart Failure

The New York Heart Association (NYHA) classification of heart failure is a therapeutic classification for prescription of physical activity for patients suffering from CHF. The classification scheme includes four classes:

NYHA Class I: People with no limitation of activities; they suffer no symptoms from ordinary activities.

NYHA Class II: Patients with slight, mild limitation of activity; they are comfortable with rest or with mild exertion.

NYHA Class III: Patients with marked limitation of activity; they are comfortable only at rest.

NYHA Class IV: Patients who should be at complete rest, confined to bed or chair; any physical activity brings on discomfort and symptoms occur at rest.

Another classification scheme by the American College of Cardiology (ACC) and the American Heart Association (AHA) has been designed to rather describe the progression of heart failure itself and its evolution. It incorporates four stages of heart failure [140]:

Stage A: Patients with stage A are at high risk for the development of heart failure but have no apparent structural abnormality of the heart.

Stage B: Patients with stage B heart failure have a structural abnormality of the heart but have never had symptoms of heart failure.

Stage C: Patients with stage C heart failure have a structural abnormality of the heart and current or previous symptoms of heart failure.

Stage D: Patients with stage D heart failure have end-stage symptoms of heart failure that are refractory to standard treatment.

So far, the NYHA classification scheme has been used traditionally in clinical trials as one of the inclusion criteria of patients since the classification scheme by the ACC and AHA has only recently been published [140].

#### 4.2.8 Congestive Heart Failure Related to Atrial Fibrillation

Atrial fibrillation is common in patients with heart failure [92]. Due to reduced or rather no atrial contraction, the ventricular volume is decreased leading to a reduction in cardiac output. Thus, left ventricular function is compromised and CHF is worsened [255]. Ventricular contraction shows a poor rate control and an irregular response since the atrio-ventricular node (in conjunction with fast, chaotic excitation of the atria) cannot carry on physiologic excitation patterns. It can be stated that atrial fibrillation - or supraventricular arrhythmia in general - are often precipitating events that indicate and lead to the onset of either systolic or diastolic heart failure [140].

On the other hand, elevated ventricular end-diastolic pressure in a patient with hypertension or abnormal myocardial function leads to atrial stretch, which in turn incites the electrical instability [140, 210]. In fact, CHF is one of the most common clinical causes of atrial fibrillation [198]. Trials have been designed to evaluate the interrelationship between atrial fibrillation and congestive heart failure [26]. Their results have yet to be published.

## Therapy

*“Die Natur ist voll von unendlichen Ursachen, die noch niemals in Erfahrung getreten sind.”*

*Nature is full of infinite causes that have never came into experience yet.*

Leonardo da Vinci

Italian engineer, painter and sculptor (1452 - 1519)

The therapeutical strategies to relieve patients from congestive heart failure and from atrial fibrillation show a wide spectrum ranging from pharmacological options via interventional to surgical approaches. The choice of the correct strategy is still much discussed in both diseases. This chapter will only briefly touch pharmacological strategies since they are not subject to this work. But they always precede interventional and surgical options which will be described in detail in sections 5.1 and 5.2.

### 5.1 Therapeutical Options in Atrial Fibrillation

Since atrial fibrillation (AF) suppresses normal contraction of the atria and causes pathological excitation of the whole heart, the therapies against AF include rate or rhythm control, restoration and maintenance of sinus rhythm and prevention of thromboembolism [114], which reduces the risk of stroke and heart failure. Unfortunately, a cure for AF has not been identified yet. Thus, only symptomatic treatment relieves the patients of AF to date. The treatment options include pharmacological approaches, minimal-invasive interventional procedures as well as surgical procedures, atrial antitachycardial pacing, cardioversion and as ultima ratio often used in emergency treatment AV node ablation and pacemaker implantation (ablate and pace) [256].

There is an ongoing discussion whether the treatment should aim at controlling the heart's rate or whether a constant heart rhythm should be restored [24]. The strategies targeting rate control focus on keeping the ventricular rate, leaving the atria in AF, while rhythm control is supposed to

restore normal sinus rhythm, i. e. treating AF [34]. Ablating the AV node and pacing the ventricles will result in rate control, cardioversion and pharmacological treatment will restore sinus rhythm and rhythm control. Also, pharmacological treatment of rate control through e. g.  $\beta$ -blocker, verapamil, diltiazem, amiodarone in combination with chronic anticoagulation is not shown to be superior of rhythm control. The latter, however, can also be achieved through interventional or surgical treatment: through ablation strategies or special pacing maneuvers. Clinical trials have not proven either strategy to be superior to date [114]. No distinct advantage of rhythm control has been shown [304]. Still, different patient selection criteria and therapeutic interventions limit the general argument that both strategies achieve similar results [54]. However, rhythm control seems to be currently preferred since restoring the hearts function to close to physiological excitation is preferable to override the intrinsic hearts function. Rather undebated is the necessity of continuing antithrombotic treatment in any treatment option [54].

All clinical trials respective rate and rhythm control have had similar results; these studies have failed to demonstrate a clear advantage of one treatment strategy over the other [284]. Nevertheless, as new theories about AF appear, new treatment options emerge [141]. Since the variety of mechanisms of the initiation and maintenance of AF covers a large spectrum (see chapter 4.1.1), the choice of therapy must be adequately designed and focussed on the identified cause of AF. Whether the patient suffers from paroxysmal AF or persistent AF is vital for the choice and success of the therapeutical strategy [211, 47]. Surgical and interventional strategies are very promising in curing AF over a long period of time. Using new technology and procedures, even antithrombotic treatment can be reduced. Also, pharmacological antiarrhythmic treatment is only effective at the early stages of AF. Ongoing AF in patients will result in non-responders to drug treatment. Thus, interventional and surgical treatment remains the only option of treatment. However, no clinical trial has so far compared pharmacological treatment to interventional or surgical treatment yet since interventional and surgical treatment is so far only considered if pharmacological treatment has no effect in the respective patient. Hence, clinical trials on rate versus rhythm control (i. e. use of rate-controlling drugs, allowing atrial fibrillation to persist versus cardioversion and treatment with antiarrhythmic drugs to maintain sinus rhythm) primarily focussed on pharmacological strategies.

Pharmacological treatment targets specific ion channels to e. g. prolong the cells action potential. It is therefore not further discussed here since it is not subject to this work. One of the primary interests of this thesis is the optimisation of non-pharmacological strategies to cure supraventricular arrhythmia. Therefore, the following section further discusses the principal interventional and surgical treatment options, their respective strategy and their outcomes in published clinical trials.

### 5.1.1 Interventional and Surgical Therapies in Atrial Fibrillation

The advancement of surgical and interventional techniques allows for far less invasive operations than only a decade ago. This renders the possibility of AF treatment with more options. Endocardial as well as epicardial lesions can be set with new generation devices off pump, i. e. on the beating heart, leading to minimally invasive procedures [14, 166]. A multitude of ablation strategies has been developed and refined including interventional procedures, which were first reported in 1994 [176], as well as surgical approaches, whose beginnings go even further back to 1992 [72]. Since then, the ablation strategies aim at either curing persistent AF or targeting ectopic triggers responsible for paroxysmal AF [72]. Paroxysmal and persistent AF both describe different states of AF and thus, the ablation strategy has to be chosen accordingly. While paroxysmal AF may be treated by isolating the pulmonary veins only, the therapeutical option to cure persistent AF includes additional lesions leading to a more complex change of the substrate [72]. Thus, the ablation strategy has to be tailored according to the patients condition. However, the general aim of both ablation strategies is substrate modification so that AF cannot be sustained even when triggered [72]. Therefore, either transmural linear lesions can be set to isolate ectopic triggers or the area of conduction is reduced so that AF cannot be sustained. The first approach creates a conduction block which the excitation wavefront cannot pass. A smaller area of conduction works against the dispersion of re-entry wavefronts [72].

Although it has been stated that interventional strategies achieve higher success rates in curing AF (about 80 % success in interventional ablation vs. 30 - 50 % in antiarrhythmic medication [256, 68]), there are only few randomized clinical trials with small patient collectives comparing both approaches [292]. However, there is no debate that surgical ablation remains the most effective means to treat AF with the classic Cox Maze III procedure setting the golden standard with a success rate of over 90 % [94].

While interventional ablation strategies that isolate triggers are effective for treating paroxysmal AF, the surgical Maze procedure or its variations will prove more successful in curing persistent AF since continuous AF is not dependent on triggers any longer but is self-sustaining [47]. Thus, the following section describes both surgical and interventional ablation techniques. The differences in ablation lesion sets will be highlighted preceded by a discussion on the technologies used to create the lesions.

#### 5.1.1.1 Ablation strategies

Initially, the Cox Maze III procedure, which was evolved from five years experience, used the “cut-and-sew” technique to create transmural linear lesions. While the advantage of direct vision are the certainty of setting transmural linear lesions, these early approaches of ablation were conducted through median sternotomy which is a major trauma for the patient. While this surgical technique is highly effective [166, 205] even considered to be the most effective means of curing AF [94], the associated morbidity and mortality remains very high [72, 166]. In addition, the complexity of the

procedure leads to very few surgeons to perform such treatment [94]. The trauma of sternotomy, the cardiopulmonary bypass and the associated morbidity also lead to surgical ablation being only an adjunct therapy in mitral valve replacements [72, 176]. In an analysis of surgical ablation procedures, it was noted that 98.4 % of patients receiving surgical ablation using newer technologies to create the lesion sets were primarily undergoing other cardiac surgery, predominantly mitral valve surgery [148]. In fact, it is suggested that patients undergoing mitral valve surgery, who have at least a six month history of AF, should receive both mitral valve surgery and ablation of atrial fibrillation [93]. In its most general form, surgical procedures consist of isolation of all four pulmonary veins to prevent propagation of the ectopic foci and the re-entrant waves are blocked by multiple incisions on the right and left atria [205].

While the surgical procedure is based on creating a lesion epicardially, the use of interventional catheters to create lesions from the endocardial surface resulted in less complex and more importantly far less invasive ablation procedures. However, these interventional or so-called catheter-based procedures prove to be difficult, too. While catheter ablation is focussed on a mechanism-based curative treatment [265], the extension of ablation lesions to the left atrium proves more effective in treating AF but the production of complete linear lesions in the left atrium remains challenging [136]. The manipulation of the catheter may not allow the creation of complete linear lesions. Thus, continuous and transmural lesion sets cannot be guaranteed. Here, navigation systems were proposed to follow up the ablation sites. However, while the created lesions are easily localised, the discontinuities or leaks in the linear lesions remain difficult to find even with navigated ablation catheter [136]. The success rates of catheter ablation vary depending on the experience of the center in which the procedure is carried out. In centers which carried out about 200 procedures and more, the success rate is close to 90 % [33]. However, the success rate relative to the follow-up time does not perform as good with success rates ranging from 14.5 % to 76.5 % with a mean of 52 % in 8745 patients treated [33]. Thus, the success rates of catheter ablation only just reach the reported success rates in surgical procedures. The surgical approaches still show more impressive results than interventional, catheter ablation [40]. The drawback of surgical procedures is the invasive operation. The uncertainty of continuous, transmural lesions is a disadvantage in the interventional procedures. Further, creating lesions from the endocardial surface has a higher risk of damaging structures outside the heart like the esophagus [47]. This risk does not exist when creating lesions epicardially since the structures are visible and the atria are hollow and hence do not include structures to be damaged.

But newer technologies such as radio frequency (RF) ablation, cryo technology, microwave catheters, laser and ultrasound energy to create ablation lesions were then used in surgical procedures as well. Together with less invasive strategies, ablation under direct vision through keyhole surgery on the beating heart produced minimal invasive surgical procedures [94, 166, 47]. It has been reported that the completion of left atrial lesion sets requires nowadays only 10 - 20 minutes [96, 95, 97, 301, 86, 87, 38, 230, 48] under direct vision in minimal invasive procedures [94]. Gen-



eral guidelines in creating new strategies for ablation lesion sets were formulated by Cox [47] and Gillinov [94] which will be stated below:

1. Recognition of role of PVs and left atrium in the initiation and maintenance of AF.
2. Fast and safe creation of lesions sets to create conduction block under direct vision with alternate energy sources.
3. The procedure should be epicardial because of the greater safety of delivering the energy from epicardium to endocardium, instead of from the endocardium, where over-penetration may cause catastrophic complications.
4. The energy source should be capable of penetrating fat as well as atrial muscle to eliminate the need to dissect away the epicardial fat prior to its application.
5. The procedure should be capable of ablating intermittent AF, continuous AF and atrial flutter.
6. Cardiopulmonary bypass must be avoided.
7. The procedure should be endoscopic or minimally invasive, and be completed within  $< 60$  min.
8. In absence of complications, patients should be able to leave the hospital no later than on the first postoperative day.

Hence, the trauma of the surgical procedure is reduced to a minimum and the advantage of setting the lesions under direct vision is preserved, which is thought to be the main contributor of success in surgical ablation. This development enables treatment of patients without associated surgical indications [166]. Future perspectives of surgical ablation go even as far as using roboter assisted technology in closed chest procedures on the beating heart [72, 47].

#### **5.1.1.2 Ablation lesions sets**

While catheter-based interventions create the lesion sets endocardially, surgical procedures ablate the atria epicardially. The other differences in procedures are in the technology used and the lesion sets created. Since the aim is to create transmural lesions, regardless of the technology used and from which side of the atrium the incisions are made, the geometries of lesion sets will be briefly highlighted here.

##### ***From Cox-Maze III to the Minimaze procedure***

Cox et al. started to develop the Maze procedure as early as 1989 [50]. Using the cut-and-sew approach in the Cox-Maze III operation in the beginning, it remains the gold standard of curing AF by ablation strategies with 97 - 99 % success rates reported by Cox et al. [51, 49, 94, 95, 148]. This success rate was concerning the classical cut-and-sew approach as evaluated in a systematic review including all relevant clinical studies up to 2004 [148]. Comparing with alternative energy sources under consideration of the patient collectives of all clinical studies included, the cut-and-sew approach seems not to perform significantly better: an average of 84.9 % in more than 1500 patients for the cut-and-sew approach versus 78.3 % in almost 2300 patients in

studies using alternative sources of energy [148]. However, the Cox-Maze III procedure sets the standard.

Originally, the Cox-Maze III procedure included incisions on the left and right atrium. The lesions lead the excitation from sinus node to the atrio-ventricular node and interrupt the most common re-entrant circuits. Also, “blind alleys” are included to secure the excitation of the whole atrium. The pulmonary veins are encircled and isolated and the left atrial appendage is excised (see figure 5.1) [95]. The inclusion of many left and right ventricular lesions, however, leads to little atrial contraction. The aim therefore was to reduce the number of lesions to damage as little atrial tissue as possible to maintain atrial contraction. Thus, with new technology and an extensive clinical experience the surgical Cox-Maze-III procedure could be simplified to a so-called “Minimaze” approach (see figure 5.1) [47]. The rationale behind the reduction of lesion sets is that the traditional Maze procedure was designed to cure any form of AF due to any causes, thus including a multitude of lesions which may no longer be necessary since only a limited number of left atrial areas seem capable of sustaining multiple re-entrant circuits [111]. Further, since the local refractory period determines the minimum size of an atrial macro-reentrant circuit [50] and the right atrial refractive periods are longer than the left atrial refractive periods, it is assumed that the right atrial tissue is not able to sustain AF unless pathologically enlarged [47]. Cox summarizes based on [193] and his own findings in [48] concerning persistent conduction across the isthmus and coronary sinus lesions: “most patients with AF of either type could probably be cured by a ‘Mini-Maze Procedure’ which includes (1) an incision encircling the pulmonary veins, (2) a left atrial isthmus and companion coronary sinus lesions, and (3) a right atrial isthmus lesion” (see figure 5.1).

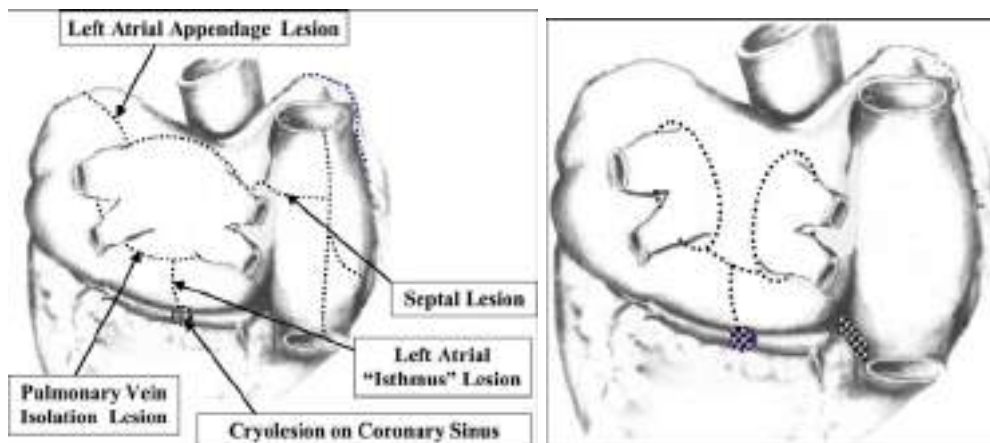


**Figure 5.1.** The diagram on the left shows the five left atrial lesions of the standard Cox-Maze-III surgical procedure of AF. With new technology it has been reduced to the Mini-Maze procedure where less incisions are made and two circumferential lesions around the left and the right pulmonary veins (PVs) are made instead of encircling all four PVs. Reproduced with permission of the author [47].

Ideally, the ablation procedure should be carried out with minimally invasive incisions either endoscopically or robotically, off pump and in less than one hour. Hence, the Minimaze procedure could treat 90 % of paroxysmal AF successfully just by encircling the pulmonary veins. The additional lesions sets in the left atrium contribute to cure even patients with chronic AF. Since the reduction of the Maze procedure to the Minimaze strategy reduces the number of additional lesions and since the procedure is becoming easier to carry out due to new technologies and surgical techniques, Cox argues that the additional lesions should be included in the treatment of paroxysmal AF as well [47]. However, statistically based clinical evidence is still due to be delivered.

#### ***Single circumferential ablation of all pulmonary veins***

Sueda et al. evaluated a simple left atrial procedure of ablating AF [274, 273, 126]. Their strategy was to encircle all four pulmonary veins at their orifices, connecting two lesions to the mitral valve annulus and excising the left atrial appendage (see figure 5.2). Pappone et al. [225] and Ernst et al. [76, 75] also carried out clinical studies by a single circumferential ablation of all four pulmonary veins. Their success rates yielded firstly 7 of 11 patients free of AF [274], then 86 % in 36 patients [273] and 4 of 21 patients [75]. The last result was due to the difficulty to set complete lesions.

#### ***Circumferential ablation of left and right pulmonary veins***

Melo et al. achieved electrical isolation of the pulmonary veins by two circumferential ablation lesions [180, 181]. Both left PVs were encircled and both right PVs were isolated with another ablation lesion (see figure 5.3). This ablation lesion set forms the basis of variants. Benussi et al. included a linear lesion connecting the superior PVs, the so called “roof” line, and a linear lesion from the left inferior PV to the mitral valve annulus (see figure 5.3) [16]. The success of these ablation strategies were 64 % in a clinical study including 43 patients [180] and up to 87 % in 41 patients including additional linear lesions [15]. Oral et al. achieved a success rate of 88 % using the approach in 2003 [213]. Ouyang et al. achieved even 95.1 % freedom from AF in 41 patients using circumferential ablation [215].

#### ***Circumferential ablation of each single pulmonary vein***

Pappone et al. tried a separate approach in 2000 by ablating each pulmonary vein by itself thus, leaving the atrial structure completely intact [228]. No additional lesions were carried out (see figures 5.4 - 5.5) although the ablation lesion could surround two PVs if they joined the same ostium. Thus, the strategy is only slightly different from circumferential ablation of the left and right PVs. Pappone et al. showed that the success rate were 85 % in patients with paroxysmal AF and 68 % in patients with permanent AF using this approach [226]. These results could be improved as shown in a later publication in 2003 [227]. In a 2004 published study, Pappone et al. could show improved results by including denervation in circumferential

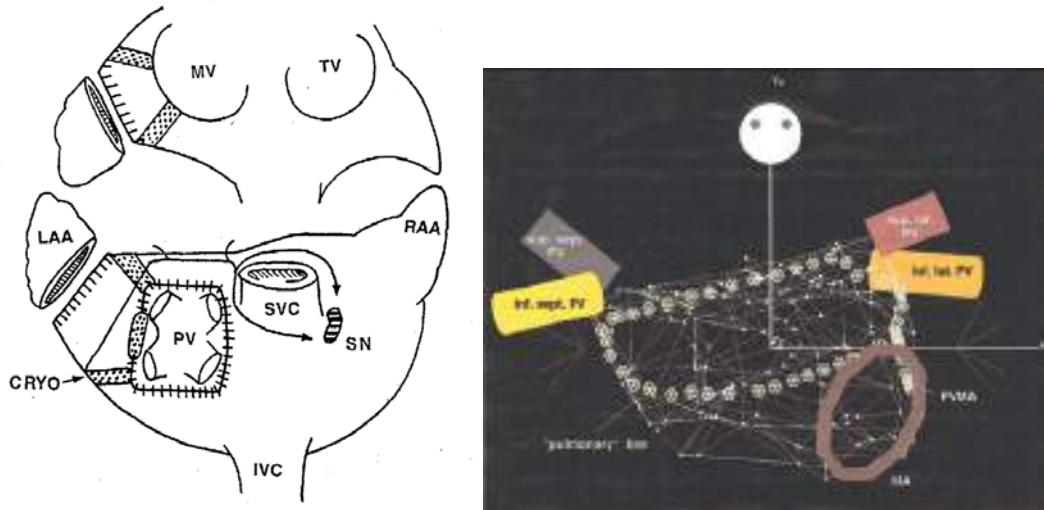


**Figure 5.2.** The figure on the left shows the left atrial ablation strategy by Sueda et al. [274]. The four pulmonary veins (PVs) were isolated and the left atrial appendage (LAA) was excised. Further lesions were set to the posterior wall of the left atrium, between the superior and posterior edges of the LAA (IVC = inferior vena cava; MV = mitral valve; RAA = right atrial appendage; SN = sinus node; SVC = superior vena cava; TV = tricuspid valve). Figure adapted from [274]. The figure on the right shows the anatomical reconstruction of the left atrium with intended ablation lines (pale dots) carried out by Ernst et al. [76]. All four PVs were isolated by one circumferential lesion and a linear lesion (PVMA) was added to connect the latter lesion to the mitral annulus (MA) indicated by the dark red ring. Inf indicates inferior; lat, lateral; PV, pulmonary vein; sup, superior, and sept, septal. Figure adapted from [76] and reproduced with permission from the authors.

ablation. 99 % of 100 patients in whom complete vagal denervation was achieved were free of AF [229]. Also, linear lesions are added: two roof lines and one to the mitral annulus (see figure 5.6). The overall success rate of the 297 patients included was 83.1 %. Adding linear lesions to the circumferential ablation set seems to be the state of the art currently. Newer publications all show circumferential ablation of each PV and additional linear lesions to suppress macro re-entrant circuits [176, 229, 223, 40, 213].

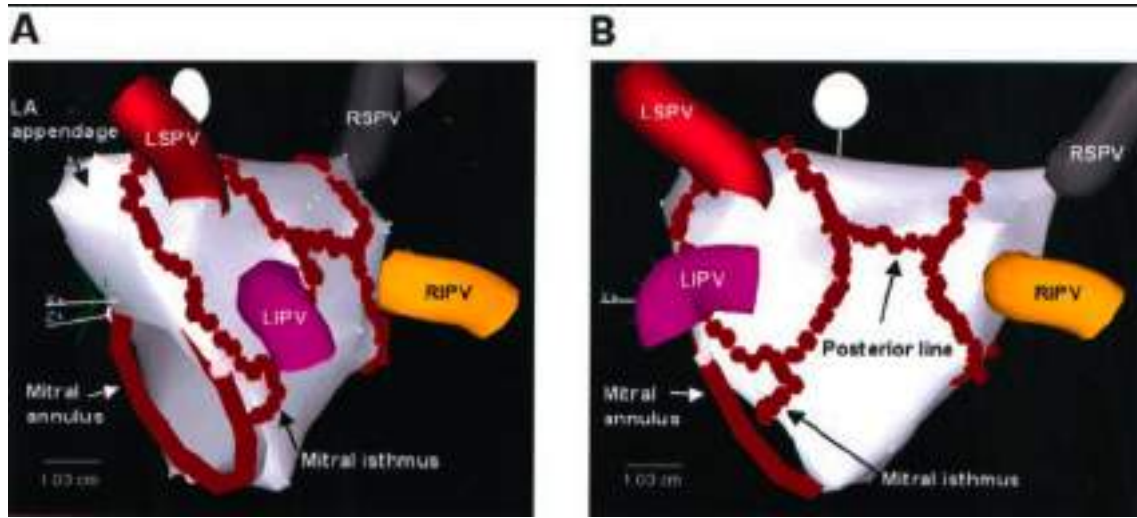


**Figure 5.3.** The ablation strategy pursued by Oral et al. [213] is shown here. The ablation lines (red marks) were created during left atrial radiofrequency ablation. A three-dimensional representation of left atrium and the pulmonary veins (PVs) was constructed with an electroanatomic mapping system. Left- and right-sided PVs are encircled. Also shown are ablation lines in mitral isthmus and posterior left atrium. A, Left posterior oblique projection; B, posteroanterior projection. LS indicates left superior; LI, left inferior; RS, right superior; RI, right inferior; and LA, left atrium. Figure adopted from [213]. The ablation strategy by Melo et al. [180, 181] which was also carried out by Ouyang et al. [215] includes the same circumferential lines but the linear lesions will not be included.

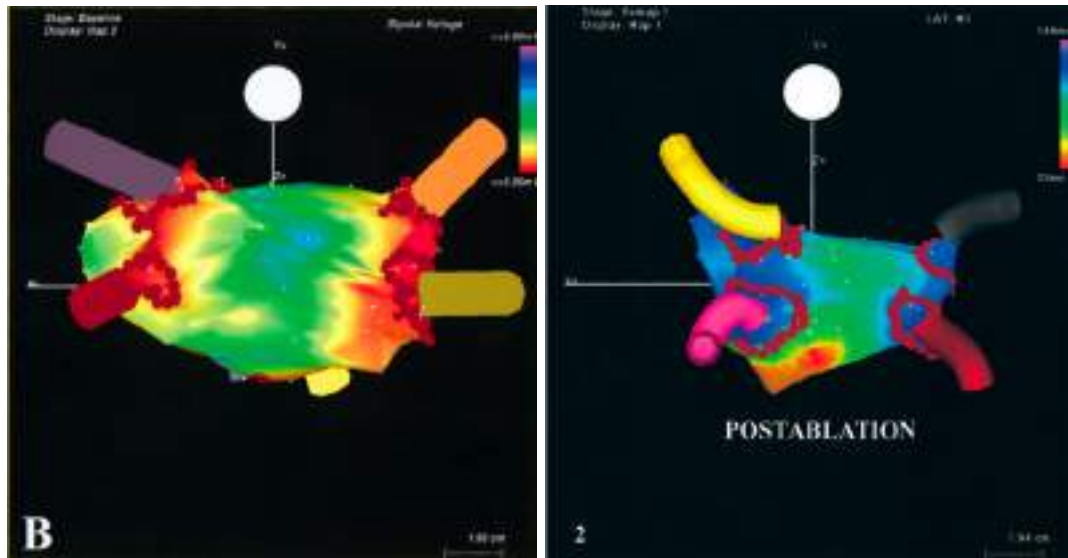


**Figure 5.4.** Shown is the posteroanterior view of a preablation (A) and postablation (B) voltage map of the left atrium depicting peak-to-peak bipolar electrogram amplitude. Red represents lowest voltage. The red dots indicate radiofrequency ablation lesions. Each pulmonary vein is isolated separately. Figure adopted from [228, 226].

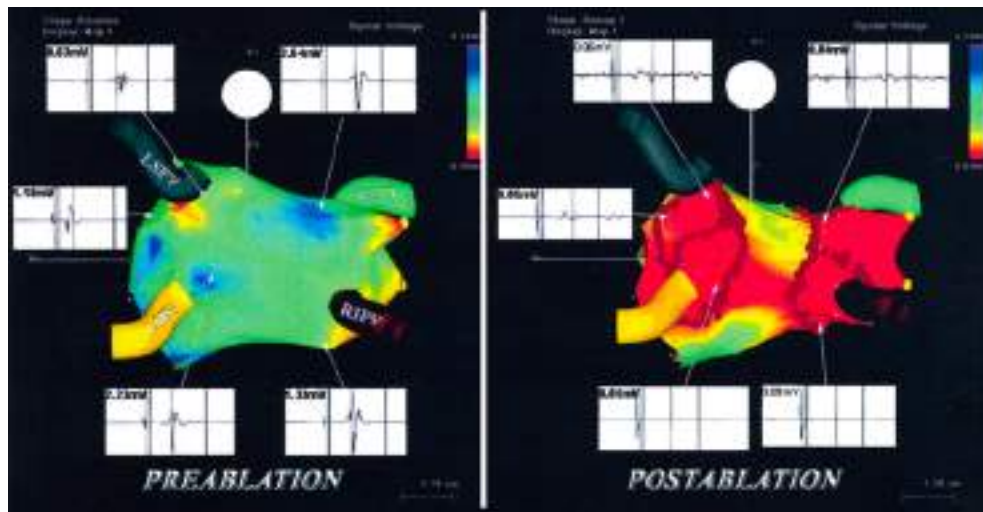


**Figure 5.5.** The circumferential ablation strategy of left atrial tissue surrounding the four pulmonary vein ostia. The electrical voltage inside the ablation line decreased significantly after ablation. Each pulmonary vein (PV) is isolated with two circumferential lesions around the left and right pulmonary veins and a linear lesion to separate the inferior and the superior PVs (Modified from J Am Coll Cardiol. 2003;42:185-197). Figure from [40].

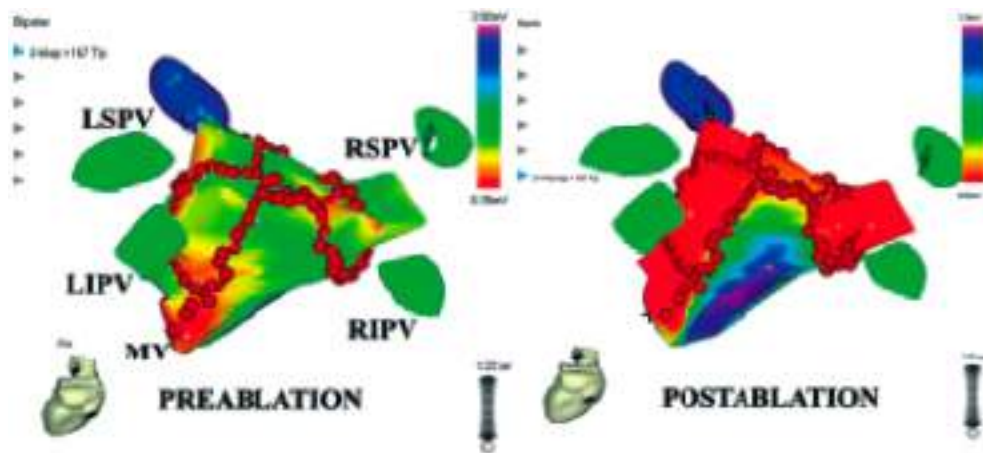


**Figure 5.6.** This figure shows the three-dimensional left atrial voltage maps (postero-anterior view: left, pre-ablation; right, post-ablation). The strategy applied by Pappone et al. includes circumferential lesions as well as linear lesions across the atrial roof and to the mitral valve (LIPV = left inferior pulmonary vein; LSPV = left superior pulmonary vein; MV = mitral valve; RIPV = right inferior pulmonary vein; RSPV = right superior pulmonary vein) [223].

***Left atrial linear ablation - “Seven ablation”***

Left atrial linear lesions were used in the ablation strategy by Gaïta et al. [84, 85], Kottkamp et al. [154] and Jaïs et al. who also included two right atrial lesions [135]. The ablation lesion either started at the mitral valve annulus leading past the left inferior PV to the left superior PV, straight across to the right superior PV and back to the mitral valve annulus in direct line pass the right inferior PV (see figure 5.7) [84, 135]. A variation is to stop at the right inferior PV, leaving the last segment to the mitral valve annulus untouched [85, 154]. This ablation strategy is also called “seven ablation” due to its characteristic form (see figure 5.7). The success rates yielded only 57 % long term maintenance of sinus rhythm patients [135]. Postoperative atrial flutter was observed due to incomplete lines of block resulting in further procedures to complete the lesions [176].

The low success rates resulted in surgeons abandoning this linear approach due to poor efficacy and a high complication rate involved [176].

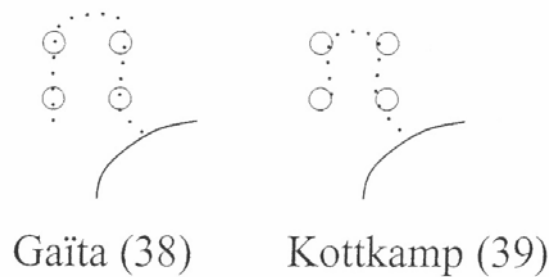


**Figure 5.7.** This schematic drawing shows the linear ablation approach by Gaïta (left) and Kottkamp (right). The lesion leads from the mitral annulus inside the pulmonary veins to the right inferior pulmonary vein. Figure from [136].

***Ablation of critical sites of re-entry***

Nademanee et al. published a completely new approach of ablating AF in 2004 [192]. In the intervention, they recorded an electro-anatomical map during spontaneous or induced AF in 127 patients. They observed areas of complex fractionated electrical potentials which were tagged. These areas were targeted in the ablation strategy based on the hypothesis that these sites are pivot points for re-entrant circuits. They yield a success rate of 91 %. The 12-month follow up showed 70 % still free of AF. It has to be noted that the ablation sites were not confined to the PVs which were therefore not targeted for isolation. This approach is regarded to be promising and has the potential to alter the understanding of the mechanisms of AF and therefore the ablation strategies [176]. However, it needs further clinical evaluation and reproduction in other clinical trials at different centers.

### ***Focal ablation***

Since most incidences of AF are due to firing foci in the PVs, the idea of focal ablation is to suppress AF by ablating the focus in question only. This strategy, however, did not pay off. It was very soon noticed, that more than one focus will occur and AF is not cured by focal ablation in a long term perspective [176]. Patients are rendered susceptible to recurrent AF due to multiple foci [120]. Hence, the focal ablation strategy is not carried out any longer.

### ***Segmental Ablation***

At the venoatrial junction, the extension of the left atrial myocardium into the pulmonary veins does not cover the entire ostial circumference [118]. Thus, electrophysiologically defined sites of preferential inputs to the pulmonary veins enable segmental ablation to electrically disconnect the PVs at the ostia without circumferential ablation in the majority of cases [109]. But the success rates of this procedure did not live up to the expectations with a recurrence rate of 30 % - 40 % [40]. Oral et al. showed explicitly that segmental ablation of the pulmonary veins yields lower success rates than circumferential ablation of the PVs (67 % vs. 88 %) [213].

#### **5.1.1.3 Technologies used to create ablation lesions**

Traditionally, transmural lesions were created under cardiac arrest with cardiopulmonary bypass by cutting atrial tissue and sewing it back together. Thus, scars were developed at these incisions leading to conduction block. Fortunately, this complex method is replaced mostly by using new technologies to create the lesion sets which results in faster operations times. Radiofrequency (RF) ablation is the most common used energy for ablation followed by cryotherapy. Microwave catheters, laser and ultrasound energy are less common but since they are the newest technologies, clinical data is hardly available [95]. The aim of all ablation strategies is to create transmural lesions. With 4 – 8 mm depth [72, 213, 223], these technologies achieve penetration of the atrial wall.

### ***Radiofrequency Systems***

Heating atrial tissue for about one minute at 60° C to 70° C will result in 3 – 8 mm deep lesions. Using either unipolar or bipolar radiofrequency (RF) devices, this is achieved by altering currents with a frequency between 350 kHz to 1 MHz. Usually, the lesion depth is sufficient to create transmural lesions. The heat is generated at the tip of the catheter where the temperature can reach 100° C locally. Consequently, surface charring and tissue vaporisation can occur when using in RF devices. Thus, there is an inevitable risk of thromboembolism. Also, esophageal injury has been reported. This disadvantage may be overcome by bipolar devices and catheters whose tip is cooled by a saline solution. Saline-cooled systems not only reduce surface charring but also allow deeper incisions. However, the advantages in RF systems are the applicability in endo- and epicardial procedures, flexibility concerning the probe, transmural access and the rapid creation of the lesions. RF ablation systems remain the most widely used systems for ablation. Many different systems (rigid probes, flexible probes, pencil tips, cooled



tips etc.) have been used in a multitude of ablation strategies. The creation of left-sided lesion sets usually takes 10 - 20 minutes with RF systems [95].

### ***Cryothermal Ablation***

Cryotherapy has been an important part of the Cox-Maze III procedure and has been used in many clinical trials [72, 148]. A nitrous oxide-based ( $N_2O$ ) cryoprobe cools atrial tissue to  $-60^\circ$  or more [56]. Applied for two minutes, it reliably creates transmural lesions. Since the tissue is frozen, the tissue architecture is preserved and thus, the surface of the atrium is kept smooth. A drawback of cryoprobes is their rigidity but securing transmural lesions is a major advantage of cryothermal ablation.

### ***Microwave Energy***

Microwave energy leads to lesions similar to lesions created with RF energy. High frequency electromagnetic energy heats the tissue by causing the water molecules to oscillate within the cells. This oscillation will heat the cells up and finally destroy them. Hence, conduction blocks are created. The advantage over RF systems are that the lesion depth and volume of the heated tissue is larger and this form of energy does not char the tissue. Thus, the certainty of transmural lesions is increased due to an increased lesion depth and the risk of thromboembolism is reduced due to no charring. Also, no esophageal injury has yet been reported with microwave energy in contrast to RF applications. Anyhow, microwave systems are not used much in clinical trials yet which does not allow direct comparison of results. However, the lesion sets used when ablating with microwave energy are similar to the ones created with other energy sources [95].

### ***Laser Systems***

Laser ablation of tachycardia is an alternative energy source to create lesions. The coherent light beam of the laser is penetrating the tissue where it is absorbed, split and scattered. Due to the following photothermal effect, the tissue is heated to the point where the cardiac cells are killed [56]. Thus, lesions are created in the tissue. Nd-YAG laser have been mostly used in clinical trials using laser ablation [157, 234, 291, 293, 82] but also argon laser [253]. While char formation was a problem in the early studies, the advancement of technology proved laser systems to create transmural linear lesions well. The use of a linear optical fibre diffuser reduces the ablation risks of pericarditis and the problems posed by epicardial fat even further. Using this approach, the pericardium can be left intact while destroying tissue at the subepicardial level [291, 82]. However, this technology has not yet been used in large clinical trials concerning atrial fibrillation [148]. Hence, its clinical outcome cannot yet be evaluated.

### ***Ultrasound Systems***

High-intensity focussed ultrasound (HIFU) is a new source of energy to create focussed transmural lesions. In contrast to all other energy sources, it is capable of preserving the integrity of coronary atrial walls [47]. Thus, epicardial ablations can be carried out across the coronary artery system to reach the left atrial wall near the posterior mitral annulus which has been a source of leakage in the lesion where the excitation could pass through. Microbubbles in the tissue expand and shrink cyclically causing damage to the tissue which destroys the cells. This process is called cavitation and is the major mechanism in HIFU ablation [56]. The flow of red blood cells and their respective distance from each other will maintain the body temperature and thus cooling the blood vessels around them. Hence, while the tissue is fixed and therefore will be destroyed, the vessels are capable of staying intact due to the cooling effect of blood and the integrity of the arterial wall is preserved. HIFU technology can be used in minimally invasive procedures without cardiopulmonary bypass and creates uniform, contiguous transmural lines of tissue ablation very rapidly. As laser therapy, ultrasound system - although promising in its application - have not been included yet in reviews comparing ablation strategies [148].

#### **5.1.1.4 Future perspectives of ablation strategies**

The challenges in AF surgery are the further development of routine off-pump, minimally invasive thoroscopic procedures and intraoperative electrophysiological assessment of the mechanisms of AF and the verification of the conduction block by the ablation line. Although the surgical maze and radial procedures already achieve a high success rates, it could be further increased by electrophysiologic guidance. The ablation procedure can only be optimised for each patient if additional information of the patho-physiology is gained. This can be either achieved through intraoperative mapping of AF [205] supported by information gained through computer simulations of the individual heart and its patho-physiology.

Interventional procedures lack the advantage of setting the lesions under direct sight which leads to incomplete lesions and increases the risk of injuries of e. g. the esophageal tract. Completing lesions using conventional RF technology is difficult to achieve but incomplete lesions lead to recurrences of AF or gap-related tachycardia [72, 75, 176, 95]. This left atrial atypical flutter due to conduction through gaps in the lesions is challenging the interventional procedures [39]. In fact, the occurrence of atrial flutter is between 3 % and 10 % depending on the ablation strategy [90, 224, 95]. Areas of fibrillating tissue has been seen in both, interventional and surgical approaches including linear or circumferential lesion sets [90, 224, 95, 206, 105, 61]. Including linear lesions to the circumferential approach has been shown to reduce the risk of atrial flutter since between 70 % and 80 % of these organized tachycardias seem to be macro reentrant [224].

Many ablation strategies exist to tackle the problems remaining in ablation therapy. They are

based on the current understanding of AF. The discussion of standardized treatment continues. That atrial size has an influence on AF maintenance is argued but also not confirmed [95]. Wide circumferential ablation has the benefit to reduce the risk of PV stenosis to a minimum but increases the incidence of macro re-entrant circuits to even 24 % [72]. And then, it has been reported that although 45 % of the PVs stayed electrically connected to the left atrial tissue, 80 % of these patients had freedom from AF. The mechanism behind this finding is still unknown [72, 226]. But to know the mechanism of AF in a specific patient is of vital importance for the choice of therapy [47]. Therefore, electro-anatomical imaging becomes the more important.

To widen the indication for AF ablation, improvements will have to be made in the navigation systems, in anatomical imaging of the ablation catheter with respect to known cardiac structure. The CARTO-merge system and Stereotaxis by Niobe target this issue by integrating cardiac image data into their navigation system (CARTO-merge) and by the development of a navigation system which allows the remote guidance of the catheter tip with the help of magnetic fields. This includes computer assisted manipulation for exactly control to place the ablation catheter. An image based evaluation of the lesions to verify their continuity and transmuralty of the line of conduction block is also still lacking [136]. The importance of procedural assistance by technology is the greater if viewed in the light of success rates: Only centres that carry out many ablation procedures will achieve a high success rate [148]. Small centres either do not offer the opportunity of ablation therapy or are not very efficient due to lack of experience. This is where medical technology can advance the procedures. However, it is widely accepted that catheter ablation of AF will become a routine and well-accepted treatment strategy for AF [68]. Surgical procedures will be improved and still set the golden standard for AF ablation.

A pre-operative therapy planning tool could guide the clinician in the choice of ablation strategy. This thesis suggest an approach with which to evaluate different ablation strategies on realistic anatomical data. The aim is to present a computer model with which different ablation strategies can be compared respective their lesions sets in a multitude of AF pattern due to different sites of initiation. The computer model will offer the opportunity to minimize the lesions sets reducing unnecessary incisions and thus leaving a greater part of the atrial structure intact.

### 5.1.2 Atrial Antitachycardial Pacing

The ability of newer generations of pacemakers and implantable cardioverter defibrillators (ICD) to carry out diagnostic tasks concerning atrial arrhythmia [98] is used to develop algorithms for atrial antitachycardial pacing with the aim of reducing AF burden and to deliver a therapy right at the onset of the tachycardia. The strategies for atrial antitachycardial pacing (AATP) can be distinguished into two groups: preventive measures and terminating measures. Since the physiological excitation is overdriven by the pacemaker, AATP is also called overdrive pacing. The ability of the pacemaker to sense pathological events is defined by a so-called physiological band which forms a zone around the physiological rate. For example, the Vitatron pacemaker by Dieren, the Netherlands, defines the lower pacing rate boundary to be at least 100 bpm. If the physiological rate, which is measured at set intervals, reaches above 100 bpm, the pacemaker rate will be set to 15 beats above the measured rate. Any event falling above that boundary is recognised to be atrial tachycardia. Current pacemakers follow a similar approach [187]. Based on this analysis, the therapeutical choice is between standard atrial pacing, multisite atrial pacing, pacing algorithms to increase the frequency of atrial pacing, pacing algorithms to maximise native ventricular conduction, novel atrial pacing sites like Bachmann's bundle or the coronary sinus ostium, a combination of prevention and termination algorithms or hybrid approaches which include medication during pacing [153]. These strategies and their implementation will be detailed below.

#### 5.1.2.1 Strategies of Atrial Antitachycardial Pacing

##### *Prevention of Atrial Fibrillation*

Pacing algorithms to prevent AF have become more sophisticated but atrial pacing is still at the early stages of development. The new generation pacemakers include signal analysis algorithms and have an increased memory capacity with which continuous monitoring can be realised [187]. These software-enabled pacemakers have been fitted with algorithms to prevent the onset of AF. The majority of paroxysmal AF episodes is due to bradycardia, premature atrial complexes (PACs) or immediate reinitiation of AF [123, 107, 305]. A increased intra-atrial conduction timing and an increased dispersion of atrial refractoriness leaves the atrium vulnerable to AF [153]. These different initiation mechanisms are taken care of by different pacing strategies. They are designed to increase the atrial baseline pacing rate through overpacing, to suppress PACs or to prevent pauses between beats due to e. g. interatrial conduction block [187, 243].

##### *Fixed rate pacing*

Fixed rate pacing is probably the simplest form of overdrive pacing. The device is set to pace at a constant frequency between 80 - 120 bpm [60, 77] or even up to 160 bpm [6]. This approach has been used in several studies to prevent AF [2, 101, 129].

Another approach mostly used in terminating AF episodes (see below) uses burst pacing. A

burst consists of a number of atrial pulses at a chosen percentage of the AF cycle length. An extension to this is the burst+ pacing mode that includes two premature atrial extastimuli following the initial burst [129, 101, 243]. A special form of burst pacing is to deliver 50Hz bursts [101, 220, 99, 243]. It has to be noted that the burst length is set to a limited time interval (0.5 s - 3 s) [2].

#### ***Incremental pacing***

Incremental or ramp therapy consists of a programmable number of atrial pulses delivered at decreasing intervals. The first pulse of each ramp sequence is delivered at a chosen percentage of the current atrial tachycardial cycle length. Subsequent pulses are delivered at progressively shorter intervals [129]. Similar to burst pacing, the pacing time interval is finite. Ramp pacing is used in terminating AF (see below).

#### ***Pace conditioning and rate soothing***

Dynamic sinus rhythm overdrive pacing [243] is used to condition the pacing frequency. The atrium is paced at least 95 % of the time during pace conditioning with a rate of about 15 bpm above the underlying intrinsic sinus rhythm [187]. If an intrinsic atrial sensed beat falls within the atrial paced period, the pacing frequency is increased. The overdrive pacing rate varies according to the implementation of the algorithm.

Rate soothing works in a similar manner. Only the increase in heart rate is small (e. g. 3 bpm). The rate is then reduced until a sinus beat is detected which causes another increase in the pacing frequency. Thus, the pacing rate floats just above the physiological heart rate (see figure 5.8) [187, 261, 161].

#### ***Post-PAC response***

The post-PAC response is aimed at reacting at short-long cycles in the atrium [243, 161]. The pacemaker response to a PAC (“post-PAC response” in the Vitatron Selection Pacemaker and similarly the “atrial rate stabilisation” algorithm by Medtronic) sets two beats following a PAC (see figure 5.8). Their timing is determined by the following rule. The average of the initial atrial sensed rhythm and the rate of the tachycardial beat sets the frequency of the first beat following the tachycardial beat. The second beat will occur at the initial atrial rate [187]. E. g. if the initial rate is 60 bpm (i. e. the period between two beats is 1 s) and a PAC occurs 0.5 s after an atrial beat (i. e. with 120 bpm), the pacemaker will stimulate the atrium at 0.75 s after the PAC (i. e. with 90 bpm) once and then return to the initial 60 bpm.

#### ***PAC suppression and post-AF response***

Premature atrial complexes occur often in clusters, i. e. one PAC is followed by several other PACs. On detection of the first PAC, the pacemaker rate is increased (e. g. by 15 bpm) so that the following premature complexes are suppressed. The increased rate is kept constant for a

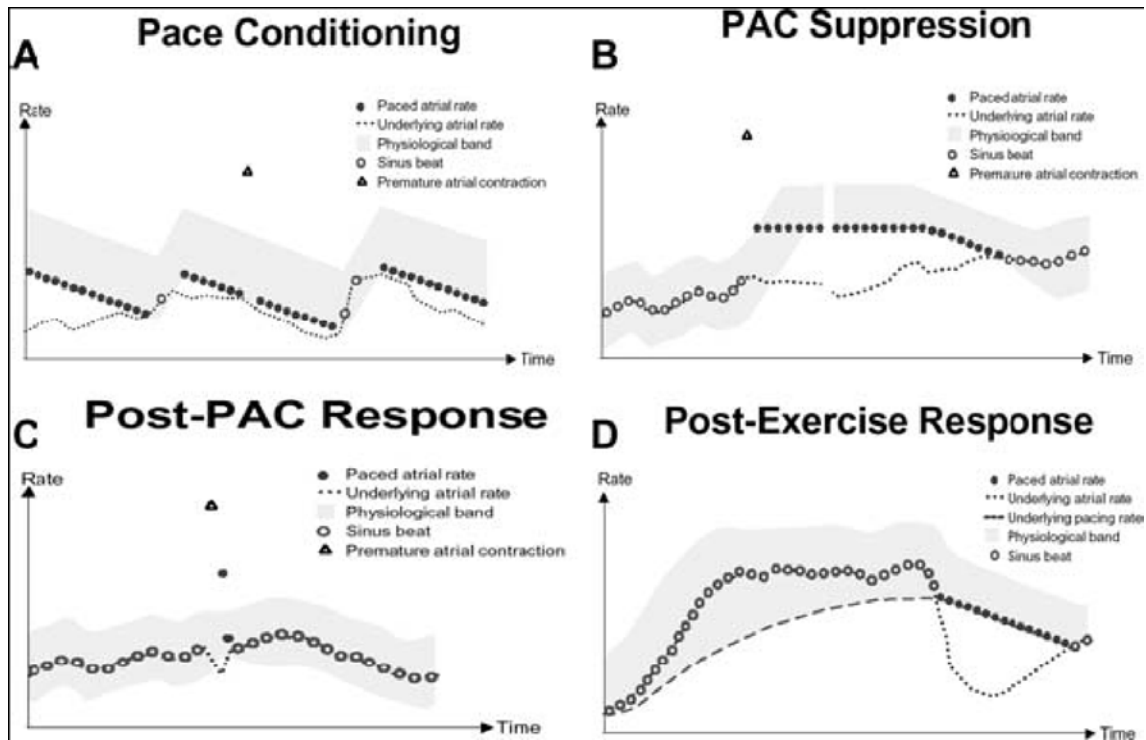


**Figure 5.8.** Four standard preventive atrial pacing algorithms applied are illustrated: (A) Pace Conditioning: On detection of a sinus beat the algorithm increases the pacing rate by 15 beats/min above the underlying heart rate; the atrium is paced for about 95 % of the time. Following an increase in rate there is a gradual decay. With this algorithm there is no increase in rate in response to a premature atrial beat (PAC). (B) PAC Suppression: On detection of a PAC, the atrial rate is increased by 15 beats/min above the physiological rate. Because multiple PACs often occur, this increase in rate is maintained for 600 beats after which it decreases gradually. Should an additional PAC occur during the 600-beat period, no additional rate increase occurs. (C) Post-PAC Response: This algorithm eliminates the compensatory pause that occurs after a PAC, by controlling the atrial rate for 2 beats. This corrects the interval and returns the heart to a normal sinus rhythm. (D) Post-Exercise Response: This aims to avoid the rapid fall in heart rate that normally occurs postexercise. The pacing algorithm intervenes and permits the rate to slow more gradually. Figure and text modified from [161].

period of time (e. g. 600 beats). If this period shows a stable rhythm without further PACs, the pacing rate is reduced, slowly decrementing to the previous rate. This algorithm can be found in the Vitatron Selection Pacemaker (see figure 5.8). The Guidant ProACT algorithm works similarly [187, 161]. After the end of the first occurrence of the arrhythmia, the pacemaker rate is set between 70 to 100 bpm for a constant period of time as in PAC suppression. Afterwards, the rate decays as described above. This way, the early recurrence of AF is stopped [243, 187].

#### *Post-exercise response*

Since the heart rate decreases drastically after exercise, the heart is vulnerable to AF in this

short period of post-exercise bradycardia. The pacemaker responds by keeping a heart rate of 90 % the exercise rate if the heart rate falls below that rate after the exercise. Thus, the drastic reduction in heart rate is counteracted. The pacemaker rate then decays slowly to the physiological rate and the pacemaker rate match. Afterwards, the pacing is stopped (see figure 5.8) [187, 243, 161].

### ***Termination of Atrial Fibrillation***

While all pacing strategies described above have been used in the treatment of AF to prevent the occurrence of arrhythmic episodes, only burst, burst+ and ramp pacing have been used to terminate AF [101]. The time interval of the pacing period varies. Some set the timing to less than one minute [129] others to less than 9 minutes or even to longer periods of time [101]. Also, the interval from detecting an episode of AF to the onset of the therapy varies between 1 - 5 minutes. Terminating AF by rapid pacing is given if the AF mechanism was such that pacing could interrupt the rhythm. Thus, re-entrant and triggered rhythms could be suppressed. The pacing must interrupt the rhythm of the driver of AF. If that is the case, AF terminates if the pacing is ended [153]. Unfortunately, the mechanisms behind AF termination through pacing is yet unknown.

Successful termination of AF can be defined if 5 consecutive sinus beats have been detected or if AF does not occur within 3 minutes [129]. Failure can be defined if AF recurred within one minute after terminating the pacing burst or if it failed to terminate AF completely [101].

### ***Pacing leads positioning***

Traditional pacing leads positioning mostly targeted the right atrial free wall or appendage [217, 113, 91, 59, 78, 106, 42, 23, 130]. Other pacing sites have been proposed: atrial septal pacing sites [113] like Bachmann's bundle [217, 146], coronary sinus ostium [217, 113], left atrial (coronary sinus, "roof" of the left atrium) [60, 78, 106, 57] and biatrial (e.g. right atrial appendage or high right atrium and the roof of the left atrium or the coronary sinus) [60, 91, 160, 59, 78, 106, 156, 184, 57]. The effect of septal pacing compared to right atrial appendage pacing is, that both atria are activated simultaneously, the non-uniform anisotropic conduction zone (triangle of Koch) is pre-excited and the P wave is shortened in the ECG. The PR interval<sup>1</sup> has been shown to be shortened when the pacing lead was placed in the atrial septum [113]. Biatrial pacing also stimulates both atria at the same time. Thus, the advantage of multisite or Bachmann's bundle pacing may correct atrial asynchrony or reduce abnormal activation due to conduction block between the atria [187].

### ***Clinical effectiveness of atrial antitachycardial pacing***

The mechanisms of success of pacing seem to be a combination of preventing bradycardia-induced AF, suppression of PACs, elimination of pauses after PACs and a reduction of dispersion of refractoryness [77]. The use of a single algorithm has hardly a positive effect on the AF burden [187].

---

<sup>1</sup> Time interval between the P wave and the R peak in the ECG

Only in including many of the algorithms mentioned above, AF burden can be reduced to over 50 % [165]. But not all combined algorithms lead to a reduction in AF burden although the time of pacing was increased from around 60 % to over 90 % [174, 130, 129, 158]. It has been demonstrated that rapid atrial pacing delivered for treating atrial tachycardia or atrial flutter may be effective in restoring sinus rhythm as high as 60 - 90 % [243, 233]. Greatest efficacy was observed if the atria were paced at a rate slightly higher than the arrhythmia rate in atrial flutter and atrial tachycardia. If extra stimuli were included in the pacing protocol, it proved even more effective [116]. Also, rapid pacing may lead atrial flutter to AF followed by a sinus rhythm restoration.

The termination of AF remains poor reaching only up to 30 %. No difference in efficacy in persistent and paroxysmal AF was observed. In contrast to these findings, atrial flutter and stable atrial tachycardia can be terminated with a success rate of over 50 %. All pacing therapies (ramp and burst/burst+) can be delivered to treat atrial flutter but some claim that only 50 Hz burst pacing can treat AF [101]. On the other hand, 50 Hz burst pacing has not shown great efficacy with respect to atrial cycle length and arrhythmia treatment [243, 101, 125]. In general, the efficacy of AATP to terminate AF was shown to increase the sooner the therapy took place, i. e. if the time of tachyarrhythmia detection to begin of therapy was short [243].

Post-operative atrial pacing has been shown to reduce the risk of new-onset AF [60]. Batrial overdrive pacing which is aimed at 100 % pacing at a rate slightly higher than sinus rhythm as well as biatrial and right atrial fixed high-rate pacing reduces AF burden by factor around 2.5 [60]. Batrial pacing has been shown to be more effective than both, left and right atrial pacing. In this study, the vulnerable window of opportunity of AF initiation was reduced through reducing non-uniform and asynchronous activation resulting from anatomic or functional block. It was also observed that the P wave dispersion, which indicates a heterogeneous distribution of conduction velocities, was best reduced in biatrial pacing rather than single site pacing [77]. It can be concluded that synchronous contraction of the atria either by septal or biatrial pacing renders the atria less vulnerable to re-entries and atrial premature beats.

Atrial lead positioning seems to play an important role in the success of AATP. Here, the septally placed pacing leads show a greater effect, reducing AF occurrence [217, 219, 218, 269, 113]. It is even suggested that atrial septal pacing should be considered as the primary pacing mode in patients with sinus bradycardia and paroxysmal AF [217]. So far, the problem remains to choose the site of stimulation and the most appropriate pacing device. The choice of atrial pacing site seems to be a determining factor for the success of the method with better results seemingly with the high or low septal lead positions [170]. These findings remain to be confirmed.

Overall, pacing prevention algorithms seem to work [35]. AATP is an effective tool to treat atrial tachyarrhythmia and it may stop 50 % of arrhythmia episodes [243, 129, 158]. Still, the global cardiac performance has not been influenced differently by biatrial, single left or single right atrial pacing in a recent study [57]. A multicenter randomised controlled trial of long-term biatrial pacing



previously failed to show benefit compared with single site or no atrial pacing [160]. These findings indicate the uncertainty about the mechanisms of successful atrial antitachycardial pacing. However, the electrical secondary prevention of atrial fibrillation is mainly based on variations of the atrial pacing site and sophisticated preventive pacing algorithms incorporated in the pacemaker software [306]. Also, since pacemaker and implantable cardiac defibrillator technology is rapidly evolving, it may play a significant role in future treatment and prevention of AF [3]. So far, the clinical benefit has only been shown for a minority of patients due to the lack of prospective predictability with respect to the electrophysiologic parameters of the individual patient [128]. There are clearly some patients who benefit from implantation of these devices but what remains unclear is how to identify this patient group [187]. Individualised selection of pacing algorithms based on individual diagnostic data of the patient may lead to a reduction in AF burden although there is little data identifying which patients might benefit most from which preventive pacing algorithms [161].

### **5.1.3 Other Therapeutical Options in Atrial Fibrillation**

Cardioversion through defibrillation is another option for AF treatment. It is mostly applied in pharmacological treatment of AF that targets rhythm control. The heart receives an electrical shock so that all cardiac cells will be set into the same state. Thus, any fibrillatory excitation is extinguished. It is regarded as being very effective [254, 179]. The electric shock is still very painful and uncomfortable for the patient since the energy needed to reset all cardiac cells is large. The development of this form of therapy is subject to other research and will not be further considered in this thesis.

### **5.1.4 Unresolved Issues in Atrial Antitachycardial Pacing**

While newer indications for permanent cardiac stimulations includes the prevention of paroxysmal AF as well [261], this issue whether to pace or not is much debated [19]. Clinical guidelines for AATP are not yet set into place although its utility as prophylactic measure especially after cardiac surgery has been investigated in clinical trials [171]. These trials however have shown inconsistent benefits on e.g. atrial fibrillation burden. This could be due to non-optimal atrial pacing site. AATP therapies are effective in treating spontaneous atrial tachyarrhythmias, mainly when delivered early after arrhythmia onset and/or on slower tachycardias. But as for the role of anti-tachycardia pacing, the technique remains to be validated. The problem is to choose the site of stimulation, the most appropriate pacing device and the most appropriate pacing algorithm in the light of current knowledge [170]. Especially an individualization is required. It has been shown that an individualized therapy reduces AF burden [161].

An individualized computer model of the atria and the simulation of AF will deliver the opportunity to evaluate systematically each pacing algorithm with respect to any pacing site chosen.

This also includes bi-atrial pacing strategies as well as dual site pacing. Further, the influence of AATP on the fibrillatory excitation as well as the mechanisms of the therapy with respect to the electrophysiological behaviour can be investigated. With the information obtained, new AATP strategies could be evaluated.

## 5.2 Therapeutical Options in Congestive Heart Failure

First choice of treatment in congestive heart failure (CHF) patients is medical therapy. Especially in heart failure patients in stage A to early stage C, medical treatment of hypertension, diabetes, ACE inhibitors and beta-blockers are appropriate [140, 235]. However, resistance to drugs especially over a long term treatment requires other therapeutical options. Furthermore, despite optimal pharmacological treatment, many patients suffer from refractory symptoms [185]. Severe left ventricular dysfunction and ventricular conduction delays increase the risk of sudden cardiac death. The resynchronization of the hearts contraction is called cardiac resynchronization therapy (CRT). It was shown that it improves haemodynamics and other symptoms of heart failure as well as survival [185]. Although CRT is an established therapy for CHF patients [25] today, a guideline for optimal treatment with biventricular pacing (BiVP) devices has not yet been established. This section describes the current state of BiVP treatment in CRT.

### 5.2.1 Cardiac Resynchronisation Therapy

Biventricular pacing was first introduced as a therapy in 1994. It was approved by the United States Food and Drug Administration and classified by many cardiological societies in 2001 and 2002, respectively [249]. Large QRS durations, loss of effective atrio-ventricular timing, mitral regurgitation and asynchronous contraction can be decreased by dual chamber pacing including a physiologic atrio-ventricular (AV) timing. It further improves left ventricular preload and decreases functional mitral regurgitation. CRT with implantable atrial-synchronized biventricular pacing devices reduces the conduction delay between the two ventricles and thus achieves an optimisation of the ejection fraction, too. Symptom improvement is achieved by left ventricular reverse remodelling [235]. Several multi-center trials [37, 1, 307, 115, 29, 44] have shown the benefits of CRT including improvement of NYHA functional class status, exercise capability and an improvement in quality of life [177, 249]. The mechanisms aimed at with BiVP are the restoration of interventricular septal and mechanical synchrony, the optimisation of diastolic function and the presystolic regurgitation [249].

#### 5.2.1.1 Indication for Cardiac Resynchronization Therapy

The indication for CRT and pacemaker implantation varies only slightly and can be summarized for CHF patients as follows [249, 8, 22, 145]:

- NYHA functional class III - IV
- optimal pharmacological treatment failed or did not improve cardiac function
- electromechanical dyssynchrony expressed in QRS durations of  $\geq 130 \text{ ms}$ <sup>2</sup>

---

<sup>2</sup> Some clinical studies include patients with QRS durations  $\geq 120 \text{ ms}$  [235, 8, 299]. However, a QRS durations of  $\geq 130 \text{ ms}$  has been set as standard indication by clinical societies [249].

- left or right bundle branch block and other intraventricular delays
- left ventricular end-diastolic diameter  $> 55 \text{ mm}$
- ejection fraction of  $\leq 35\%$
- no expected improvement from coronary revascularization/valve replacement

Patients with indication for CRT show delayed activation of the ventricular free wall segment and paradoxical interventricular septal motion. They have thus inter- and intraventricular conduction abnormalities, a reduced diastolic filling time and worsening of mitral regurgitation which alters global cardiac function [249].

#### 5.2.1.2 Implantation of a Biventricular Pacing Device

The implantation of a BiVP device includes the positioning of a right ventricular (RV) electrode and of a left ventricular (LV) electrode. The RV lead is placed endocardially i.e. inside the cavity. The RV apex has been the most extensively used site since it is accessible and reliable in a long-term perspective [43]. It was suggested, however, that this position is suboptimal and pacing sites at the septal wall or the right ventricular outflow tract seem to show better results in CRT [163, 245].

The implantation of the LV lead is rather more difficult. Since the left ventricle constitutes a major part in the cardiovascular high pressure system, an implantation of the LV lead on the endocardial surface is not performed. It is rather performed transvenously using a coronary sinus branch [235, 140] and is now a routine procedure [36]. This way, the LV lead is positioned at the lateral base, the posterolateral base or halfway between the base and the apex [249, 244]. However, the LV lead position is determined by the venous anatomy [244] and the procedure to fix the lead in an appropriate position is time consuming [8]. Alternatively, new lead systems allow a fixation of the left ventricular lead on the epicardial surface. This way, the pacing lead can be positioned anywhere on the left ventricle. However, the latter procedure requires thoracotomy or minimal invasive thoracotomy [8].

#### 5.2.1.3 Strategies and Optimisation of Cardiac Resynchronisation Therapy

Different pacing sites and the timing of the stimulation namely the setting of atrio-ventricular (AV) and interventricular (VV) delay give rise to the need for optimisation of CRT especially with respect to the individual patient [280, 299]. Concerning pacing sites it has been demonstrated by van Campen et al. [280] that an individual configuration of the pacing site for each patient improves the patients haemodynamics and the number of non-responders. While they showed that an optimisation of pacing sites does improve the success of the therapy, their optimisation therapy only consisted of Doppler flow measurements under consideration of overall nine different lead positions in

- two coronary sinus branches,

- the right atrial appendage,
- the right ventricular apex and
- the right ventricular outflow tract.

The AV delay was set to 100 *ms* and the VDD mode was chosen for pacing.

However, it was suggested that cardiac function and electrical stability may be improved by programming of optimal AV delay in dual chamber pacing. [271]. Several studies have pointed out that individualisation of AV delay and further VV delay in patients undergoing CRT leads to additional haemodynamic improvements [9, 281, 143, 191, 232, 27, 237, 268, 283]. Riedlbauchova et al. investigated optimal AV and VV delays with respect to cardiac output measured by Doppler echocardiography [244]. They investigated different AV delays ranging from 90 *ms* to 160 *ms* with increments of 10 *ms* in three pacing modes each for the atrial sensed and atrial paced case with

- biventricular stimulation with the left ventricular stimulus preceding the right ventricular stimulus by 4 *ms*,
- biventricular stimulation with the right ventricular stimulus preceding the left ventricular stimulus by 4 *ms*,
- single site left ventricular pacing

For the optimal AV delay, the VV delay was adjusted with left ventricular stimulation preceding right ventricular stimulation in a range of 4 *ms* to 20 *ms* with 4 *ms* increments and for the case when the right ventricular stimulation was carried out first in a range of 4 *ms* to 20 *ms* with 4 *ms* increments. The result in 19 patients was that the optimal AV delay was in all patients around 120 *ms* (atrial sensed mode) and 140 *ms* (atrial paced mode). However, the influence of the VV delay or rather the stimulation of the respective ventricle showed that left ventricular stimulation before right ventricular stimulation shows better results. However, the influence of VV delay on all AV delays tested was not investigated.

A recent study by Whinnett et al. showed in an analysis of shape, magnitude and relative importance of AV and VV delay that haemodynamic effects behave according to consistent patterns given changes in AV and VV delay [299]. They measured 35 different combinations of AV and VV delay measuring systolic blood pressure relative to a reference pacing configuration. The reference pacing was done at 110 beats per minute (bpm) with an AV delay of 120 *ms* and a VV delay of 0 *ms*. The AV delay was then set to 40, 80, 120, 140, 160 and 200 *ms*. The VV delay tested was 60, 50, 20, and 0 *ms* with a stimulation of the left ventricle first and 20 *ms* and 40 *ms* starting with right ventricular stimulation. They demonstrated in 15 patients that AV delay, whose response fitted closely to a parabola, has a greater effect on the haemodynamics than VV delay. Whinnett et al conclude that the curvilinear blood pressure response of changes in AV and VV delay may be used in developing a streamlined clinical protocol. Further, it was suggested that the VV delay

should also be optimised since it also adds to a haemodynamic benefit. The results of this study showed further that the blood pressure peak was individual to each patient respective both AV and VV delay [299].

#### 5.2.1.4 Unresolved Issues

A major issue concerning CRT is the high number of non-responders. Only two thirds of patients do respond [22, 309, 185, 310, 278, 8] since QRS duration might not be associated with mechanical dysfunction. Thus, QRS duration as indication criteria for CRT may not be appropriate. The magnitude of mechanical dyssynchrony at baseline is a better predictor of outcome [231, 308, 309, 104, 11]. It was demonstrated by Pitzalis et al. that a septum-to-posterior wall motion delay of  $\geq 130$  ms shows good accuracy to the reduction in left ventricular volumes in reversal remodelling during follow-up as well as a better clinical outcome [236].

However, van Campen et al. have shown that an optimal positioning of the pacing electrodes does reduce the number of non-responders [280]. Thus, the question of the optimal left ventricular pacing site, whether biventricular or left univentricular pacing is more beneficial and the issue of the relevance of the right-sided lead position [249, 92, 282] is an issue to be solved, yet. The optimal left ventricular pacing site is believed to be at the lateral or the posterolateral base close to the left ventricular base or halfway between the base and the apex. However, adjustments have to be considered with respect to the individual patient [280, 249]. Also, only 70 % of patients can be catheterized so that the intended lead position is achieved because of e. g. obstruction in the sinus coronarius. The only options that remain in these cases is either a suboptimal pacing position, minithoracotomy or thorascopy and the implantation of an epicardial fixation of the pacing lead or to abandon the procedure. Haemodynamically, the right ventricular pacing site is not required for an improvement and clinical benefits [270]. However, BiVP is the reference method for CRT and validated in randomized trials. Also, ICD systems require the right ventricular electrode to sense and release the high-voltage shock. Since the procedure of lead implantation is not made more complex by the right ventricular lead implantation, it is sensible to keep it. The relevance of the right ventricular lead position, however, is in question. While the right ventricular apex or the right atrial appendage are readily accessible and thus often chosen as pacing sites [43], alternative sites such as the septal wall, the right ventricular outflow tract or the midanterior wall provide additional support of left ventricular resynchronization [163, 245].

Recent studies have demonstrated the need for optimal adjustment of AV and VV delay for the individual patient [299, 244]. A systematic optimisation can only be achieved by sequentially pacing different AV delays and for each of these the VV delay needs adjustment so that the optimal setting can be chosen from a matrix of results. However, this procedure is time consuming in clinical practice and is therefore seldom carried out [277].

## The role of computer models in cardiac research

*“To find a fault is easy; to do better may be difficult.”*

Plutarch

Greek biographer and moralist (46 AD - 120 AD)

With respect to clinical trials, the investigation of therapeutical strategies has several drawbacks which are unfortunately unavoidable. For example, mortality is an endpoint for clinical trials in AF [18, 303, 204]. The most important problem remains the fact of application of a single configuration of lesions on the same patient. A direct comparison of alternative lesion patterns is impossible. The typical number of enrolled patients usually allows only analyses with limited statistical power. Thus, by developing a computer model of the atria and the arrhythmia, different ablation lesion patterns can repeatedly be tested on the same data set representing a single patient. So far, computer models have contributed to a better understanding of the mechanisms behind AF beginning with Moe et al. [188, 189] who presented first the multiple wavelet theory. Rotors and wavelets have been shown in computer simulations based on a detailed mathematical description of cardiac cells [286]. Nevertheless, a trade-off always has to be considered when carrying out cardiac modelling: the complex electrophysiology of a cardiac cell is modelled to a high degree of accuracy by many coupled partial differential equations and the anatomy is simplified [41]; the inclusion of anatomical details may be associated with a reduced accuracy in electrophysiological models. Therefore, most experiments were carried out using a two-dimensional (2D) patch representing atrial tissue but including detailed cardiac cell models [152, 151, 286, 289, 102]. However, some studies were carried out on a three-dimensional (3D) atrial model [112, 285, 287, 288, 58, 247, 138, 139]. But even in these investigations, a mono-layer model, i.e. a 2D surface folded in 3D space, is used [287, 20] and the anatomy mostly resembles spheres with holes to mimic the entries of veins. Other work concerning spiral waves is carried out on the surface of a simple sphere [247]. More recent studies try to include more realistic anatomical shapes of the atria [21, 138, 139, 285, 112]. These shapes are based on concentric shapes. Lately, the segmentation of the endocardial surface of the atria in three-dimensional magnetic resonance images delivers the shape of the cardiac model. In all of

these studies mentioned, simplifications on the model for the calculation of the electrophysiology have to be accepted to achieve a reasonable computational load [21, 41].

The research in computer models of cardiac electrophysiology is mostly concerned with basic research on mechanisms of cardiac function and cardiac pathologies ranging from simulation of atrial and ventricular fibrillation to the modelling of genetic defects in ion channel kinetics [294]. Based on this research, the understanding of pathologies is furthered which then might lead to the development of new treatment options and their safety assessment [28]. The simulation and optimisation of interventional, surgical or pacing therapies has not been carried out often. The research group around Kappenberger has carried out studies with respect to ablation therapy in atrial fibrillation [20, 58]. Concerning the investigation of curative treatment in a computer model, Dang et al. [58] evaluated the effect of ablation lesions in atrial flutter and sustained AF initiated by burst pacing at the sino-atrial node region. While the results yield conclusions for the termination of sustained AF, it does not reflect on the isolation of pulmonary veins where AF is thought to be mainly initiated. Also, the study by Dang et al. [58] modelled the underlying atrial electrophysiology by an adapted Luo-Rudy cell model for ventricular myocytes using only six different ionic currents to reduce computational load compared to twelve in the human atrial cell model by Courtemanche et al. [46]. The action potential duration, however, was adapted according to Virag et al. [288] to match atrial behaviour. While including electrophysiological detail, the atrial shape, although with curvature in 3D space, was a mono-layer model without tissue depth. Only atrial structures such as entries and exits of blood vessels were included. Another computational issue is given by the model of excitation propagation. Most detail is included by a bidomain approach yielding high computational cost. When evaluating interventional or surgical strategies, however, the excitation propagation model was simplified to the monodomain approach in [288, 58].

The lack of tools to model, simulate and investigate therapeutical strategies in supraventricular arrhythmias leads to the objective of this work to develop a biophysical model with which an ablation strategy can be planned on a realistic 3D anatomical model of the atria including wall thickness and detailed anatomical structures such as crista terminalis, pectinate muscles and Bachmann's bundle. Further, AF was initiated with respect to ectopic activity in the PVs. Some pacing algorithms as used in atrial antitachycardial pacing will be investigated by the model presented in this work.

The research in cardiac resynchronization therapy shows no study known to the author that tries to optimise the timing of pacemaker stimulation by modelling cardiac electrophysiology. Since the main interest in CRT is an optimal cardiac output, Rom et al. [248] try to adaptively optimise AV and VV delays by simulating cardiac electrical and haemodynamic behaviours and an adaptive CRT pacemaker. However, an underlying cardiac electrophysiological model and simulations based



on cardiac anatomy was not used in their work. Since optimisation of AV and VV delay is so far only carried out manually by the clinician, the second objective of this thesis is an automatic optimisation of the AV and VV delay as well as an evaluation of pacing lead position with respect to individual patient anatomy and different underlying pathologies.



**Modelling Cardiac Electrophysiology**



## Modelling the Anatomy of the Heart

*“All men by nature desire knowledge.”*

Aristotle

Greek critic, philosopher, physicist and zoologist (384 BC - 322 BC)

The modelling of linear cardiac function can be split into several parts which build on each other. First of all, an anatomical model has to be gained for which the electrophysiological properties have to be defined. The electrophysiology that is calculated based on the anatomical model is comprised of determining the action potential of a cell and of a conduction model that calculates the excitation propagation. Based on the electrophysiological computations, a tension development model could be applied followed by a deformation model to compute the deformation and cardiac output. These last two issues are subject to other research, however. Image acquisition and image processing to generate the anatomical model is also treated by others [252]. In this chapter, the anatomical models used in this work will be presented only briefly followed by a chapter on the methods to compute action potentials and excitation propagation.

### 7.1 Anatomical Image Data

The Visible Human Project started by the National Library of Medicine, Bethesda, USA, of the National Institute of Health aimed at creating a detailed anatomical model of a man and a woman at the end of the 1980's. A man and a woman sentenced to death agreed to be volunteers after their prosecution. The Visible Man data-set was then created by taking computed tomography (CT) and magnetic resonance imaging (MRI) scans before freezing the body and another CT scan of the frozen body. It was then cut into cryosections of 1 *mm* thickness that were photographed with a resolution of 2048 x 1216 picture elements (pixel). Since 2000 a higher resolution of 4096 x 2700 is available by digitized analogue pictures of the cryosections, the Visible Female data-set was produced in the same way only that the cryosections were of thickness 0.33 *mm*.



**Figure 7.1.** Digital cryosection image of the Visible Man, National Library of Medicine, Bethesda, USA, showing a transversal view through the heart.

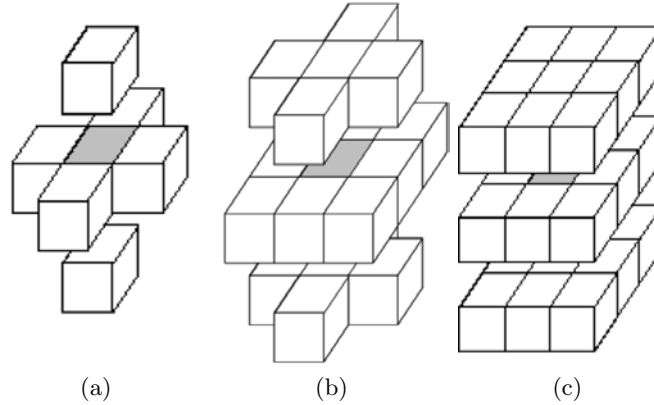
The digital images of the cryosections put together form a 3D data-set of very high resolution. The Visible Human Project aimed at delivering a high resolution data-set for scientific purposes. Clinical relevance does not exist, however, not even pathologically.

Image acquisition of patients hearts in clinical practice is carried out using CT, MRI or ultrasound imaging modalities. At the Institute of Biomedical Technology, six patient data-sets were taken for the identification of ischemic regions in the heart by measuring multi-channel electrocardiograms and by solving the inverse problem of electrocardiology. The three-dimensional MRI scans were carried out at the University of Würzburg. In this way, real patient data was gained for the simulation of cardiac resynchronization therapy described in chapter 9.3.1.

## 7.2 Digital Representation of the Image Data

The representation of the 3D image data in a three-dimensional array is most natural with respect to image acquisition since the 2D images or slices have an x and y resolution and the assemblance of slices gives the depth in z direction. While the pixel is one element in a digital picture, the voxel (volume picture element) is one element in a volume picture, i. e. a 3D image data-set. According to the resolution of the images acquired, the voxel side length can differ. Usually, the voxel side length is the same in x and y direction but differs in z direction. The voxel side length can be made equal by adding subsets of voxel, which are interpolated accordingly. The result is a data-set with isotropic cubic voxel. Each voxel has adjacent volume picture elements at its sides, edges and corners. Thus, different neighbourhoods can be defined for each voxel if only sides (6 - neighbourhood) or sides and

edges (18 - neighbourhood) or sides and edges and corners (26 - neighbourhood) are considered (see figure 7.2). To choose only the edge or only the corner voxel as neighbouring elements is not sensible in cardiac modelling since the cardiac tissue is not structured in that fashion. The accumulation of voxel forms a grid or a cubic mesh in a lattice structure.



**Figure 7.2.** This figure shows the different definitions of the neighbourhood of a cubic voxel: (a) 6er neighbourhood, (b) 18er neighbourhood and (c) 26er neighbourhood.

### 7.2.1 Image Segmentation and Classification

The cardiac structures can be extracted by using image processing and segmentation algorithms. Cardiac tissue of the same type shows in the images as having the same gray value. Unfortunately, cardiac structures are not simple structures. Standard segmentation algorithms cannot be easily applied due to artefacts in the image data or poor image quality. Moreover, automatic segmentation of cardiac structures is still subject to research. However, a region growing algorithm [296] can be applied to extract the endocardial cavities. A so called seed point is set by the user. Beginning from this point, the algorithm will search for neighbouring voxel that have the same value or that remain within a specified margin with respect to the value of the seed point.

A manual, interactive segmentation tool is given by deformable triangle meshes. A triangle mesh is placed within the 3D anatomical data-set. It can then be stretched and deformed interactively, giving the user the opportunity to adjust for complex structures accordingly [296]. The user selects a node of the triangle mesh and places it at another location. The nodes adjacent to it will also modify their location according to a given function, e.g. a Gaussian function. Although this method is time consuming, it is most effective in extracting complex cardiac structures. When finished deforming the triangle mesh, it is converted into the lattice format resulting in a boundary

of the cardiac structure. By including multiple triangle meshes and by filling the insides or outsides of these meshes with a certain tissue label, homogeneous structures can be created leading to an anatomical model of the heart.

Each extracted segment is associated with a certain numerical value given by the user. Thus, the voxels with a certain number belong to this specific segment that determines a certain anatomical cardiac structure. For each specified structure, electrophysiological properties can be defined that characterise the function of the cardiac cells at this place in the anatomy. The cardiac cells within the segmented structures form the type of tissue and determine a tissue class.



## Electrophysiological Model

*“The sciences do not try to explain, they hardly even try to interpret, they mainly make models. By a model is meant a mathematical construct which, with the addition of certain verbal interpretations, describes observed phenomena. The justification of such a mathematical construct is solely and precisely that it is expected to work.”*

Johann von Neumann

Computer scientist, mathematician (1903 - 1957)

The modelling of the electrophysiological behaviour of cardiac cells begins at the cellular level. In each cell, an action potential can be triggered under physiological conditions which will then be propagated to the neighbouring cells and thus across the whole heart since the cells are coupled (see section 3.2.1.1). Hence, to model the electrophysiological behaviour of the heart, a mathematical description of a cardiac cell is needed as well as a model for the excitation propagation.

### 8.1 Mathematical Description of Cellular Electrophysiology

Hodgkin and Huxley developed the first mathematical description for an action potential of a giant squid axon [122]. It was based on the assumption that the axons membrane behaves like a capacitor set in parallel with voltage sources and resistances describing ion movement through the membrane (see figure 8.1). With the use of experimental data, they developed a set of non-linear coupled differential equations. The change of transmembrane voltage in the squids axon was described including transmembrane currents, ion concentrations, intracellular components and gating variables. The extension and adaptation of the Hodgkin-Huxley Model lead to numerous electrophysiological descriptions of the cardiomyocyte (see table 8.1). Here, only the basic development of the cell models will be outlined according to the Hodgkin-Huxley model and the cell models used in this work will briefly be introduced.

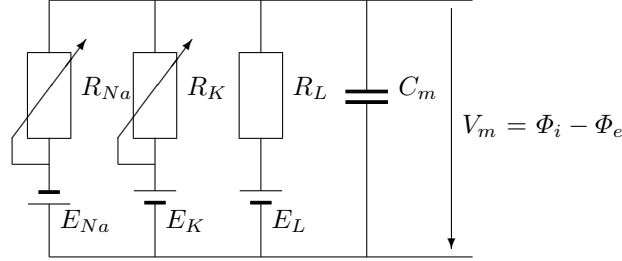


**Figure 8.1.** Electrical equivalent circuit of the cell membrane of the Hodgkin-Huxley model describing the electrophysiology of a giant squid axon. The resistors  $R_X$  describe the conductivity of the channels of type  $X$ . The voltage sources (Nernst voltages) are given by  $E_X$  (fig. from [263]).

### 8.1.1 Transmembrane Voltage $V_m$

The transmembrane voltage  $V_m$  is given by the electrical charge  $Q$  which is accumulated at the cells membrane which acts like a capacitor with capacitance  $C_m$ :

$$V_m = \frac{1}{C_m} Q \quad (8.1)$$

Thus, the change of transmembrane voltage which results in an action potential is given by the change of charge across the membrane. This is given due to the ion movement through the membrane. The time derivative of electrical charge which passes through the membrane is by definition the transmembrane current  $I_m$ . Including a stimulus current  $I_{stim}$  that invokes an action potential, equation 8.1 leads to

$$\frac{dV_m}{dt} = -\frac{1}{C_m} (I_m + I_{stim}) \quad (8.2)$$

### 8.1.2 Membrane Currents

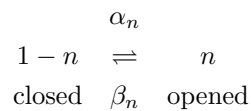
The transmembrane current  $I_m$  is determined by the sum of ion currents flowing through the membrane via ion channels, pumps and exchangers (see section 3.2.1.1). These ion pathways through the membrane can be open or closed at different times controlling the ion flux through the membrane. Thus, a description of the gating kinetics leads to the determination of membrane conductance which in turn leads to an equation to calculate the ion current.

An ion channel most basically can be in two states: open or closed. The sum of open or closed channels is described by a gating variable  $n$ . If the transition states are neglected, the fraction of

Year Author	Specimen	Species
1962 Noble [207]	Purkinje fiber	-
1975 McAllister, Noble, Tsien [178]	Purkinje fiber	-
1977 Beeler, Reuter [13]	Ventricular myocardium	Mammalian
1985 DiFrancesco, Noble [64]	Purkinje fiber	Mammalian
1987 Hilgemann, Noble [117]	Atrial working myocardium	Rabbit
1990 Earm, Noble [73]	Atrial working myocardium	Rabbit
1991 Luo, Rudy [167]	Ventricular myocardium	Mammalian
1994 Luo, Rudy [168] [169]	Ventricular myocardium	Guinea-pig
1994 Demir, Clark, Murphey, Giles [62]	Sinoatrial node	Mammalian
1996 Dokos, Celler, Lovell [67]	Sinoatrial node	Mammalian
1996 Demir, O'Rourke, Tomaselli, Marban, Winslow [63]	Ventricular myocardium	Dog
1998 Courtemanche, Ramirez, Nattel [46]	Atrial working myocardium	Human
1998 Jafri, Rice, Winslow [132]	Ventricular myocardium	Guinea-pig
1998 Noble, Varghese, Kohl, Noble [208]	Ventricular myocardium	Guinea-pig
1998 Nygren, Fiset, Firek, Clark, Lindblad [209]	Atrial working myocardium	Human
1998 Priebe, Beuckelmann [239]	Ventricular myocardium	Human
1999 Winslow, Rice, Jafri, Marban, O'Rourke [302] [214]	Ventricular myocardium	Dog
2000 Zhang, Holden, Kodama, Honjo, Lei, Varghese, Boyett [311]	Sinoatrial node	Rabbit
2001 Pandit, Clark, Giles, Demir [222]	Ventricular myocardium	Rat
2001 Puglisi, Bers [240]	Ventricular myocardium	Rabbit
2002 Bernus, Wilders, Zemlin, Verschelde, Panfilov [17]	Ventricular myocardium	Human
2004 Ten Tusscher, Noble, Noble, Panfilov [276]	Ventricular myocardium	Human
2004 Iyer, Mazhari, Winslow [131]	Ventricular myocardium	Human

**Table 8.1.** Electrophysiological models of cardiac cells.

channels in the open states are given by  $n$  and therefore the fraction of channels in closed states is given by  $1 - n$ :



where the transition from opened to closed state is described by the voltage dependent rate constants  $\alpha_n$ , whereas the opposite direction is described by  $\beta_n$ . This relationship yields a differential equation which describes the temporal change of the number of open gates:

$$\frac{dn}{dt} = \alpha_n(1 - n) - \beta_n n$$

Regarding the sodium ( $Na^+$ ) channel in the Hodgkin-Huxley model, two gating variables  $m$  and  $h$  are included for the activation and inactivation of the ion channel, respectively. Hence, four rate constants  $\alpha_m$ ,  $\beta_m$ ,  $\alpha_h$ , and  $\beta_h$  are defined that control the activation and inactivation process which is described by the time derivative of the gating variables:

$$\frac{dm}{dt} = \alpha_m(1 - m) - \beta_m m$$

and

$$\frac{dh}{dt} = \alpha_h(1 - h) - \beta_h h$$

The rate constants are dependent on the transmembrane voltage  $V_m$  (see figure 8.2). By solving the last two functions, the conductivity  $g_{Na}$  of the sodium channel can be computed, considering that the channel includes three independent but identical activation gates  $m$  and one inactivation gate  $h$ :

$$g_{Na} = m^3 h g_{Na,max} \quad (8.3)$$

with the maximal conductance for sodium ions  $g_{Na,max}$ . The sodium current  $I_{Na}$  results to:

$$I_{Na} = g_{Na}(V_m - E_{Na}) \quad (8.4)$$

with the transmembrane voltage  $V_m$  and the equilibrium voltage  $E_{Na}$  for  $Na^+$  ions given by the Nernst equation (see section 3.2.1.2).

Respectively, the channel kinetics of the potassium ( $K^+$ ) channel and the leakage current  $I_l$  can be determined.

## 8.2 Atrial and Ventricular Cell Models of the Human Cardiomyocyte

Regarding the electrophysiological behaviour of cardiomyocytes, a substantial amount of complexity was added to the cell models due to the mechanisms of ion transport through the membrane measured. Courtemanche et al. [46] developed a cell model for the human atrial myocyte (see figure 8.3). The membrane current is given by

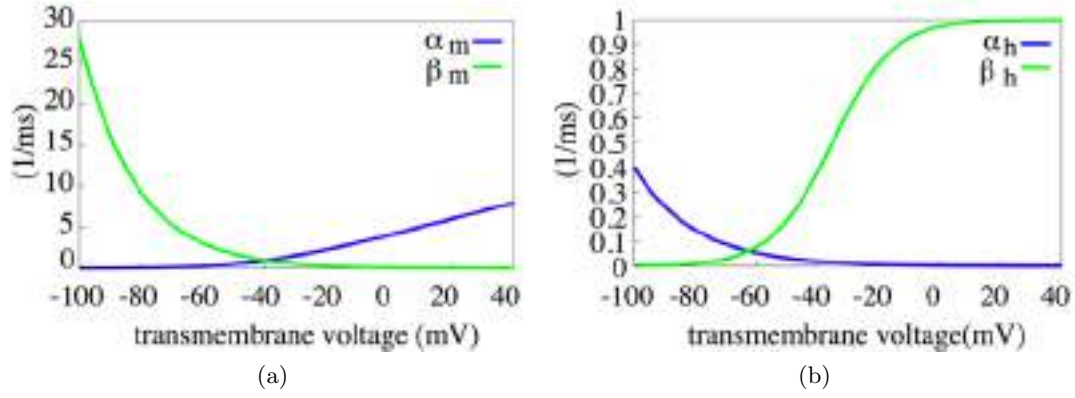


**Figure 8.2.** Voltage dependent rate constants in the Hodgkin-Huxley model for sodium channels. (a) The rate constant  $\alpha_m$  and  $\beta_m$  for the activation variable  $m$ . (b) The rate constant  $\alpha_h$  and  $\beta_h$  for the inactivation variable  $h$ .

$$I_m = I_{Na} + I_{K1} + I_{to} + I_{Kur} + I_{Kr} + I_{Ks} + I_{Ca,L} + I_{p,Ca} + I_{NaK} + I_{NaCa} + I_{b,Na} + I_{b,Ca}$$

Similarly, Priebe and Beuckelmann created a model for the ventricular myocyte [239] based on the measurement of ionic currents and concentrations (see figure 8.3). The membrane current is given by

$$I_m = I_{Na} + I_{K1} + I_{to} + I_{Kr} + I_{Ks} + I_{Ca} + I_{NaK} + I_{NaCa} + I_{b,Na} + I_{b,Ca}$$

with ionic currents included in either or both models:

- $I_{Na}$  - fast sodium current
- $I_{K1}$  - outward rectifier potassium current
- $I_{to}$  - transient outward potassium current
- $I_{Kur}$  - ultra rapid delayed potassium current
- $I_{Kr}$  - rapid delayed potassium current
- $I_{Ks}$  - slow delayed potassium current
- $I_{Ca,L}$  - L-type calcium current
- $I_{p,Ca}$  - pump outward calcium current
- $I_{NaK}$  -  $Na^+/K^+$  pump current
- $I_{NaCa}$  -  $Na^+/Ca^{2+}$  exchanger current
- $I_{b,Na}$  - background sodium current
- $I_{b,Ca}$  - background calcium current

Thus, further to ionic currents through the membrane, mechanisms concerning intracellular dynamics like calcium handling were included in both models, increasing the complexity of the calculation.

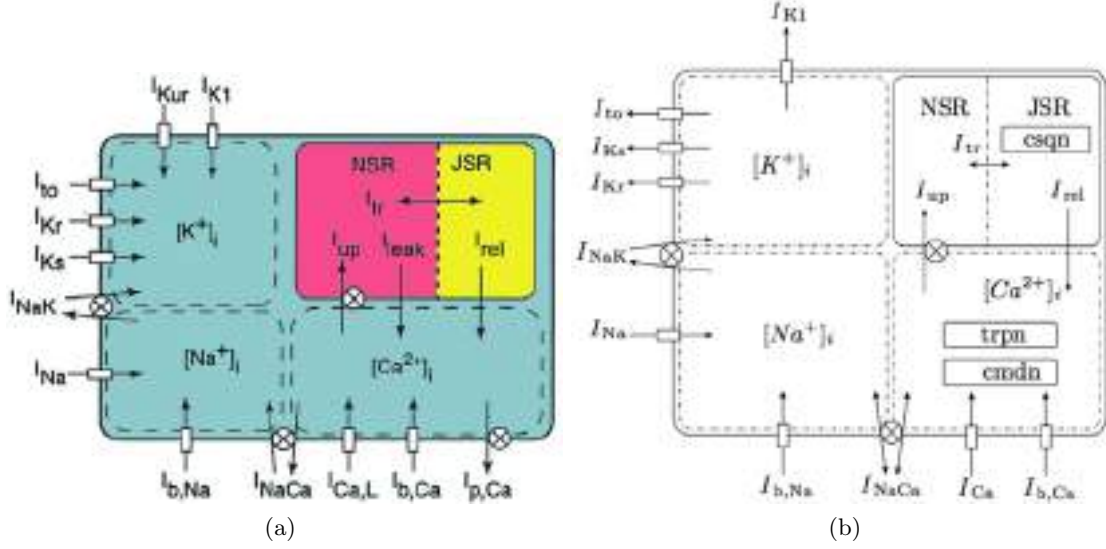


**Figure 8.3.** Schematic description of ionic model of Priebe Beuckelmann [239] of a human ventricular myocyte (left) and the Courtemance, Ramirez, Nattel [46] model of the human atrial myocyte (right), with ion currents, pumps, exchangers and other components. It contains detailed descriptions of ion currents, intracellular ion dynamics ( $[Ion]_i$ ), sarcoplasmic reticulum (SR) with network SR (NSR) and junctional SR (JSR), and calcium buffers like troponin (trpn), calmodulin (cmdn), and calsequestrin (csqn) (fig. from [263]).

These models further allow adaptation to more specific atrial or ventricular tissue like the sinoatrial node, the crista terminalis in the atria or the epicardial, midmyocardial or endocardial cells in the ventricle. They can also be adapted to tension development models that lead to a calculation of the force generation and contraction of the heart. A detailed description is given in their original work [239, 46] and the implementation is described in [263].

### 8.3 Excitation Propagation

The excitation propagation between cells in the heart can be modelled in several ways. On one hand, the ion flux in both the intra- and extracellular space can be taken into account by using Poisson's equation to determine the excitation conduction between two adjacent cells. On the other hand, simplified models that determine the excitation propagation according to a set of rules, which determine distinct states of cells, can be applied.

#### 8.3.1 Poisson's Equations to determine Excitation Propagation

The bidomain model based on Poisson's equation includes the ionic currents and concentrations in both intra- and extracellular space. A Poisson equation can be defined for both domains yielding

in a set of equations using the intracellular and extracellular conductivity tensor  $\sigma_i$  and  $\sigma_e$  to find the intracellular potential  $\Phi_i$  and the extracellular potential  $\Phi_e$ :

$$\nabla (\sigma_e \nabla \Phi_e) = -\beta I_m - I_{se} \quad (8.5)$$

$$\nabla (\sigma_i \nabla \Phi_i) = \beta I_m - I_{si} \quad (8.6)$$

with the membrane current  $I_m$  and the externally applied currents in the intracellular space  $I_{si}$  and in the extracellular space  $I_{se}$ .  $\beta$  represents the ratio of surface to volume of the cell. The conductivity tensors  $\sigma_i$  and  $\sigma_e$  are defined to consider the anisotropic electrical properties of cardiac tissue determined extracellularly by the fibre and sheet orientation and cylindrical shape of the cells and intracellularly mainly by the distribution density of gap junctions. The two bidomain equations are linked via the definition of the transmembrane potential  $V_m$ :

$$V_m = \Phi_i - \Phi_e \quad (8.7)$$

Given that no external stimulus current is applied, i. e.  $I_{si} = I_{se} = 0$ , and taking into account that the transmembrane current  $I_m$  is flowing from one domain into the other, a solution can be found that determines the influence of the spatial distribution of the transmembrane voltage  $V_m$  on the extracellular potential  $\Phi_e$ , which is the first part of the bidomain model:

$$\nabla ((\sigma_i + \sigma_e) \nabla \Phi_e) = -\nabla (\sigma_i \nabla V_m) \quad (8.8)$$

The second part of the bidomain model describes the intracellular stimulus current due to the influence of the intra- and extracellular currents as input to the electrophysiological models. It is given by

$$\nabla (\sigma_i \nabla V_m) + \nabla (\sigma_i \nabla \Phi_e) = \beta (C_m \frac{dV_m}{dt} + I_{stim}) - I_{si}. \quad (8.9)$$

considering equation 8.6 and equation 8.7 with the membrane capacitance  $C_m$  and the stimulus current  $I_{stim}$ .

Solving the bidomain equations requires a high degree of coupled partial differential equations. Computing the result is yet very time consuming. Even if the bidomain equations are reduced to the monodomain model under the assumption that the extracellular space has the same conductivity properties (namely the same anisotropy ratio) as the intracellular space, the computation time

needed to run a simulation of a single heart beat on realistic anatomical models is considered too large for the evaluation and optimization of therapeutical strategies as investigated in this work.

### 8.3.2 Cellular Automata

The use of a cellular automaton for the calculation of the excitation propagation gives an efficient method of computation. The anatomical model gives a finite, regular, discrete network of nodes whose interconnections are defined by their neighbourhoods. Each node, given by each voxel in the data-set, represents one macroscopic cell. On each cell, a finite automaton is running. The states of the automaton are updated at discrete time steps  $\Delta t$ . The states of a cell is given by the underlying electrophysiological parameters. The excitation propagation is then determined by a set of rules which take the anisotropic excitation propagation according to the fibre structure into account. Moreover, by defining different tissue types, i.e. . different electrophysiological parameters for a certain type of cardiac tissue, the heterogeneous nature of the hearts tissues can be satisfied. In this work, the adaptive cellular automaton developed by Werner, Sachse and Dössel [298, 297] was used. By taking into account not only the current state but also past states of the automata, the computation adapts to the different states in the simulation. Hence, given a certain geometry the automaton provides a spatial and temporal distribution of  $V_m$ .

#### 8.3.2.1 Electrophysiological Parameters of the Cellular Automaton

Depending upon the location of a voxel in the anatomical data-set, it is declared as cardiac tissue cell with respect to its electrophysiological function. The transmembrane voltage for each cell is not computed by detailed cell models during the simulation. Rather, action potentials are calculated by cardiac cell models before the simulation and are stored in memory which leads to an increase in simulation speed. Since the action potential differs for different stimuli frequencies and for stimulation of the cells in different refractive periods, the course of transmembrane voltage over time has to be calculated for a set of conditions. For atrial cells, the Courtemanche et al. [46] model is used to calculate an action potential for nine different stimuli frequencies (see figure 8.4). For each of these nine curves, a stimulation at four different times during an action potential, i.e. in different refractive periods, is determined. Thus, 36 action potentials are pre-calculated for each tissue type. While the Courtemanche et al. model was used for the computation of action potentials for atrial cells, the Priebe and Beukelmann model was used to determine the action potentials for the ventricular myocardium. For the cells of the excitation initiation and conduction system, automatic rhythmicity is included for the respective cell types. Cells of the sinus node, for example, will initiate an action potential with a set frequency of 72 beats per minute. During the simulation, the transmembrane voltage of a cell is determined depending on its past values. If a cell is stimulated while at rest, a certain curve of action potential is chosen, which determines the transmembrane voltage for the future time steps. The activation time will be stored in an isochrone file. If the



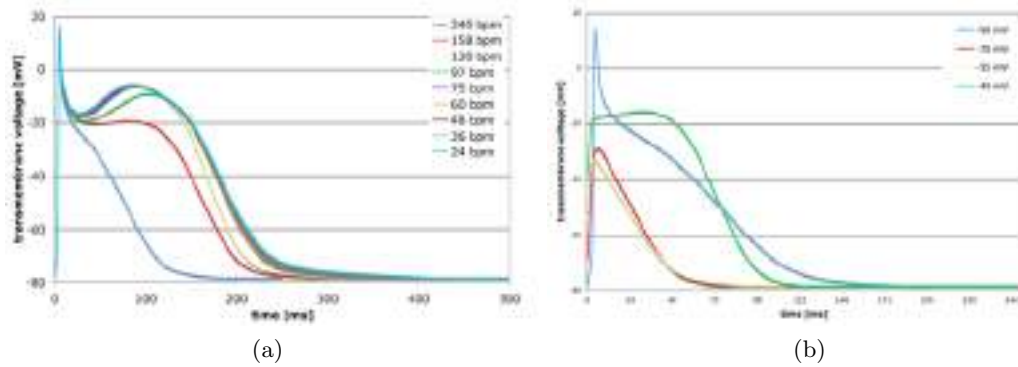


**Figure 8.4.** This figure shows nine different action potentials for nine different rates which are stored for the computation of the excitation propagation for the cellular automaton (a). The morphology also changes with respect to excitation at different levels in the action potential (b). Overall, for nine different frequencies a stimulation at four different times in the action potential cycle are computed with the cell model by Courtemanche et al. [46] for the simulation of the excitation propagation in the atria.

same cell is then stimulated again, the automaton will determine the stimulation frequency with the help of the stored isochrones as well as the refractive period the cell is in. Given the cell is not at rest but refractive, a different set of action potentials will be taken from memory. This approach yields a dynamic and adaptive method to compute the transmembrane voltage for a given cell at a given time.

### 8.3.2.2 Excitation Propagation

Once an action potential was triggered in a cell, the excitation will be carried forward to the neighbouring cells (see figure 8.5). The distance between cells and the conduction velocity of the tissue will determine the excitation propagation. The fibre orientation of cardiac tissue can be included which results in an anisotropic excitation conduction. Since the conduction along the cardiac fibres is faster than transversal, different excitation propagation times are defined to imitate the excitation propagation in the heart. Further, a distinction is made between tissue types. Since atrial working myocardium does not excite cells of the ventricular myocardium in the physiological case, the cellular automaton takes care of possible excitability from respective cells. Ventricular excitation includes the fast activation system of bundle of His, Tawara branches and Purkinje fibres. This conduction tree is projected onto the anatomical structures and can be manipulated separately.

### 8.3.2.3 Heterogeneous Cardiac Structures

Heterogeneous cardiac structures play an important role in the excitation of the heart. Especially concerning ventricular wall structures, the heterogeneous distribution of epicardial, midmyocardial

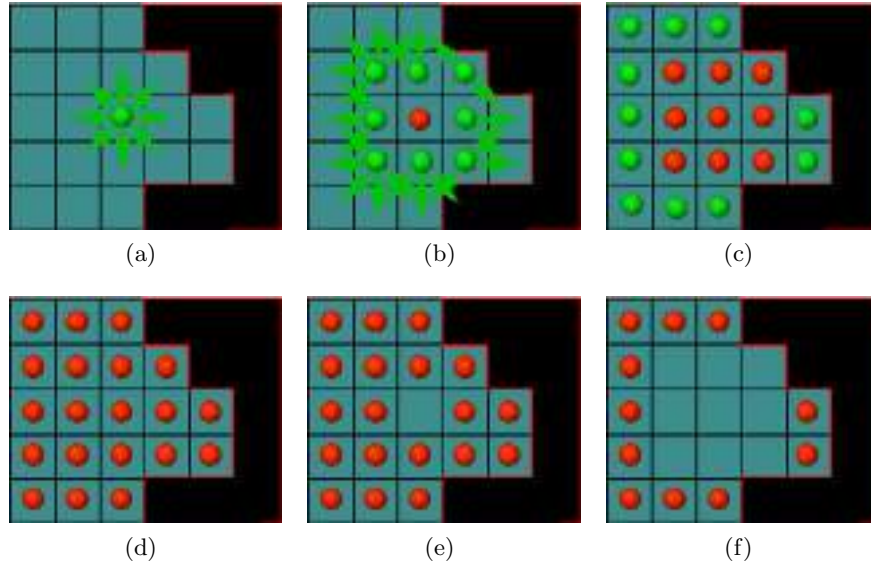


**Figure 8.5.** Neighbour propagation of a cellular automaton on a surface. Empty squares represent resting cells. Each excited cell (green), communicates the excitation to its eight neighbours (green arrow)(a,b). After an explicit time interval the cell switches to an unexcitable state (red)(c, d). Finally, the cell returns back to an excitable cell (e, f). This process proceeds along the given geometry. Figure from [263].

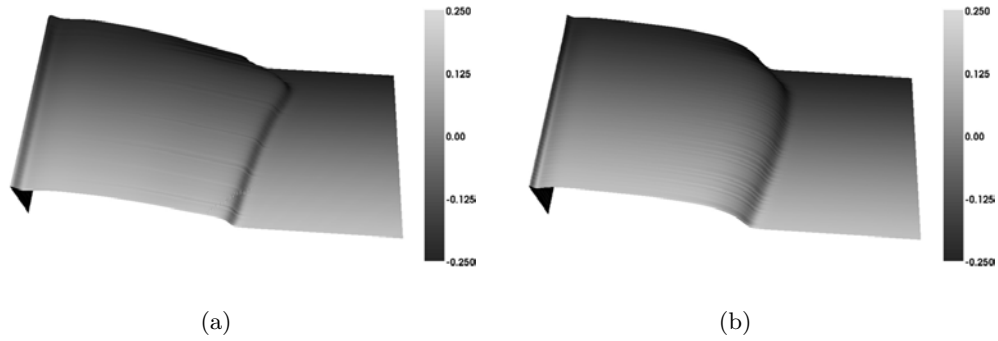


**Figure 8.6.** Modified morphologies included in the electrophysiological parameters of the cellular automaton to model the heterogeneous ventricular wall with endocardial, midmyocardial and epicardial cells. The action potentials for the midmyocardial cells show the longest action potential durations. (a) Priebe-Beukelmann model of human ventricular myocytes (B) tenTuscher model of human ventricular myocytes. Figure by D. Farina.

and endocardial cells is important to reflect physiological excitation of the heart [264]. The cellular automaton used in this work was adapted by Farina et al. [79] to include an adjustable distribution of action potential curves (see figure 8.6) for the ventricular wall.

**Modelling Cardiac Pathologies and Therapies**



## Modelling the Pathologies of the Heart

*“Man muss Chaos in sich tragen, um einen tanzenden Stern zu gebären.”*

*One must have chaos inside to give birth to a dancing star.*

Friedrich Nietzsche

German philosopher (1844 - 1900)

The simulation of pathological behaviour forms the underlying framework for the simulation of therapies. The pathologies have to resemble the cardiac diseases realistically. Only then, preventive and curative strategies can be evaluated in a computer model. Thus, the following chapter describes the simulation of heart disease in congestive heart failure as basis for the optimization strategies for cardiac resynchronisation therapy. It also describes the initiation of atrial fibrillation to evaluate ablation and antitachycardial pacing therapy.

### 9.1 Computer Model of Supraventricular Arrhythmia

Preliminary work has been carried out by Weiss in 2002 [294]. He compared the initiation of AF in two computer models. On one hand, AF was created by simulation of detailed cell models and the excitation propagation was calculated by the monodomain approach. On the other hand, the same protocol was carried out using a cellular automaton. The simulations were based on a two dimensional tissue patch of size 40 mm x 40 mm x 1 mm. Adjustments had to be made to adapt to realistic anatomy. These are described below.

Realistic anatomical models should be gained from 3D computed tomography or magnetic resonance imaging. The resolution and the segmentation of these datasets do not reach a high degree of accuracy, yet. Therefore, the Visible Female dataset of the National Library of Medicine, Bethesda, Maryland, USA, was chosen to investigate the influence of a detailed anatomical model on AF. The Visible Female dataset determines the underlying anatomical structures for the electrophysiological modelling in the computer simulations carried out in this section. Its model of the atria consists

of  $245 \times 278 \times 305$  cubic voxel with isotropic side length of 0.33 mm. 1,696,740 voxel of the dataset represent atrial tissue including sinus node, atrio-ventricular node and parts of the pulmonary veins. More complex anatomical structures like the crista terminalis, the pectinate muscles and the Bachmanns bundle have also been included [262]. The simulation of excitation propagation was carried out using the cellular automaton described in section 8.3.2.

The atria are made vulnerable to AF by setting short refractive periods and by reducing the conduction velocity at the same time. The conduction velocity is reduced to 40 % its original value to 400 *mm/s* similar to the work by Moe et al. [188, 189] where the conduction velocity was reduced to even 200 *mm/s*. For all simulations, the heart rate is set to the highest frequency which makes the cellular automaton select the short action potentials from memory when starting the simulation. Then, pulmonary vein firing is simulated by virtually exciting tissue at the veins ostia: Two stimuli cause a unidirectional block that leads to a rotor wave. The rotor wave is gained if the second stimulus is situated such that its excitation will meet cells in their absolute refractive phase and cells that are re-excitabile again (see figure 9.1). While the excitation in the area of absolute refractoriness will not cause an excitation wave front, the excitation in the neighbouring area will kick off an action potential. Due to the slower conduction velocity and the relaxation of the excited cells, the excitation wave front will travel into the area that was previously non-excitabile, creating a figure-of-eight re-entry that is quickly replaced by a rotor with its center at the position of the ectopic focus. This approach does not only model fast PV firing by two stimuli, it also represents the situation in which one single stimulus falls into an excitation wave front, e.g. the excitation wave front of a sinus rhythm. The difference between the latter and the simulation of two stimuli will only differ in the curvature of the wave front into which the second stimulus falls. The advantage of using two stimuli with spatial and temporal offset is that the timing of the occurrence of the ectopic beat can be better controlled. Also, the ectopic focus was modeled by a spherical stimulus which is advantageous in creating a rotor wave. It also approximates the measurements best. Using this approach, AF will be initiated by an arrhythmogenic excitation of a region in the pulmonary vein that falls in an excitation wave front and thus in areas of different refractive periods. A unidirectional block occurs resulting in a rotor wave.

The stimuli have a semi-spherical shape with radius around 6.5 *mm* situated on the epicardial surface. The first stimulus was set 200 *ms* after the onset of a sinus beat. The second stimulus had a position and time offset to the first stimulus of 6.27 *mm* and 34 *ms*, respectively. Thus, the timing of the ectopic beat is set according to the findings in [108, 194]. By placing the position of these stimuli in different regions of the atria, a multitude of excitation patterns can be generated. The ectopic foci were placed equidistant around each of the pulmonary veins using an interactive 3D visualization tool (see figure 9.2). At the left superior pulmonary vein (LSPV), a distinction was also made between placing the focus ostially or deeper inside the PV. Hence, 32 different locations of the ectopic focus were investigated. Further three set-ups were evaluated to observe the influence

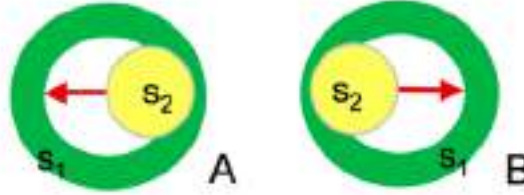


**Figure 9.1.** Schematic description of a unidirectional conduction block created by two stimuli  $s_1$  and  $s_2$ . Both stimuli are set apart spatially and temporally. The distance of the centers was the radius of the first stimulus. The temporal delay between stimulus  $s_1$  and  $s_2$  was 34 ms. While stimulus  $s_1$  will propagate concentrically, stimulus  $s_2$  falls partly in an area of absolute refractoriness and partly in an area where the cells are re-excitable. Thus, the excitation will not propagate to the right (A) or to the left (B), respectively. Since some areas of the second stimulus falls into a region or tissue that is re-excitable again, the excitation will be spread into the excitable area (indicated by the arrows). This way, a unidirectional block is created.

of the spatial offset of the second stimulus with respect to the spatial offset. In these simulations, the second stimulus was set either ostially or distally.

The time simulated was 2 s. However, one simulation was carried out for 17.5 s to investigate the excitation pattern over a longer period of time. The simulations carried out on a single processor Apple Macintosh 1.33 GHz PowerPC G4 with 1.25 GB SDRAM took about 20 minutes for 500 ms time simulated. On a dual processor Apple Macintosh 2 GHz PowerPC G5, the simulation time is reduced to 10 minutes for 1000 ms time simulated.

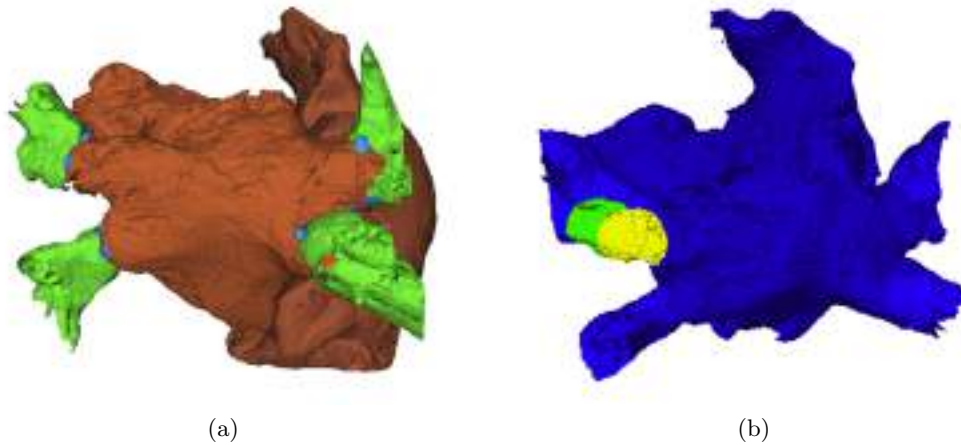


**Figure 9.2.** Location of stimuli to create AF. (a) The positions of the ectopic foci (blue) were placed equidistant around all four pulmonary veins (green) (only a selection is shown). (b) The two stimuli to create atrial fibrillation had a diameter of about 6.5 mm. The center of the second stimulus (yellow) had a spatial offset of about 6.5 mm to the center of the first stimulus (green).

## 9.2 Characterisation of Atrial Fibrillation

Excitation patterns of the atria in atrial fibrillation can be manyfold. The five predominant patterns are (see figure 9.3):

- Stable, consecutive wave fronts
- Streak like excitation (Snakes)
- Rotor waves
- Multiple wavelets
- Undeterminable excitation that seemingly looks random

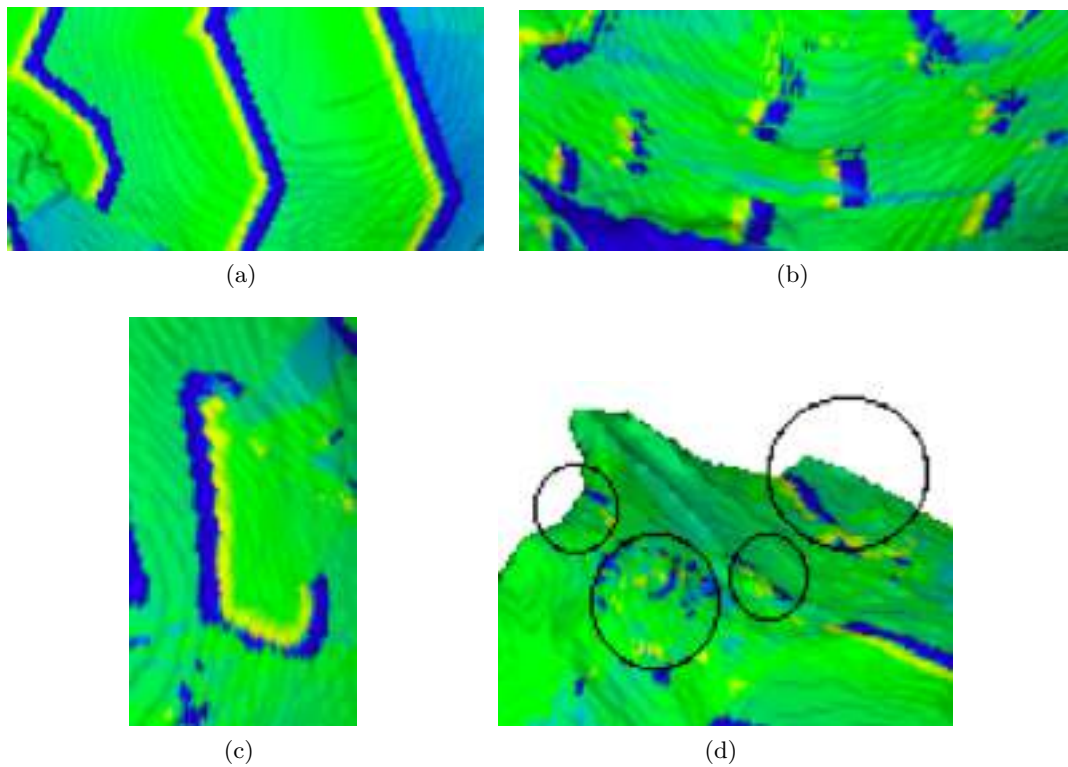


**Figure 9.3.** Four different excitation pattern which occur in AF: (a) broad wave fronts as in atrial flutter; (b) streak-like excitation called snakes; (c) rotor waves; (d) multiple wavelets.

Stable, consecutive wave fronts with broad wave fronts excite the atria. Each wave front stretches across the whole area in question and resembles a line (see figure 9.3.a). Snakes are small wave front segments that travel in the same direction but they do not form a continuous line across the area but rather excite the tissue in a disorderly fashion. They are limited to a local area and do not stretch across the whole atrium (see figure 9.3.b). Rotor waves have the form of a spiral wave



which turns around a focus. In general, the rotor is also a local phenomenon (see figure 9.3.c). Multiple wavelets are small circlets, i. e. the excitation of the atrial tissue is in a circular fashion (see figure 9.3.d). They occur in a local area of the atria. Complete chaotic excitation does not allow to recognise a certain excitation pattern. The excitation looks random and could be interpreted as a noise signal. The following section describes how these different classes of excitation pattern can be determined to characterize atrial fibrillation.

### 9.2.1 Segmentation and Classification of Excitation Patterns

The transmembrane voltage  $V_m$  at a given time during AF is saved as a floating point number in a lattice file made of cubic voxel. Thus, it can be represented as any other three-dimensional (3D) image and processed likewise. To extract the features of this 3D image data, the excitation pattern will be gained which can then be classified. The wave fronts determine the excitation pattern and will therefore be used to classify it. Classical segmentation methods would include the calculation of the gradient in x-, y- and z-direction of the coordinate system. However, the knowledge about an action potential allows for a different segmentation algorithm to extract the wave fronts of the excitation. The two different segmentation and classification methods will be described as follows. They are applied to two different patterns of atrial fibrillation shown in figure 9.4.

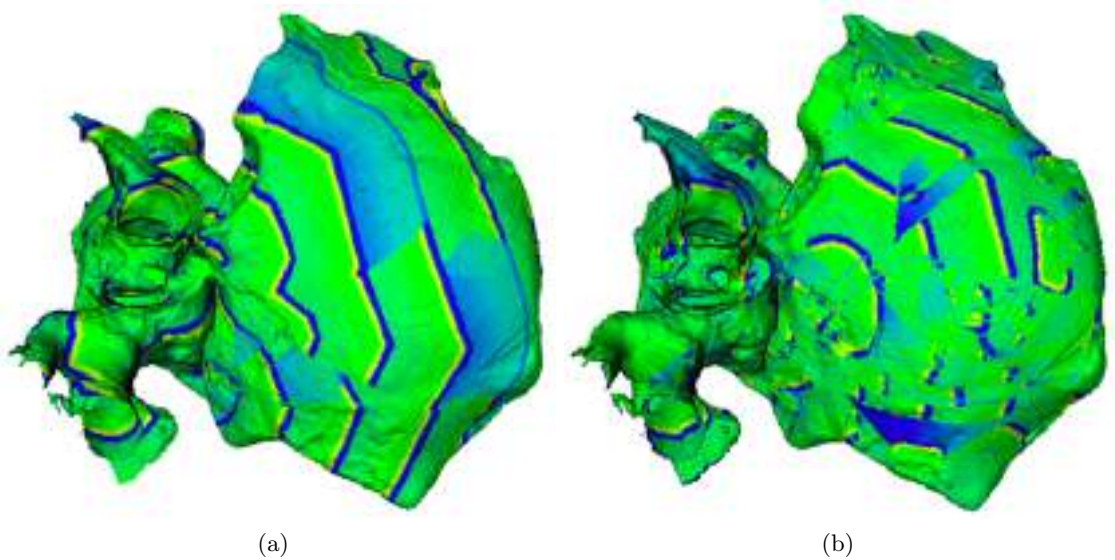


**Figure 9.4.** AF Patterns to test classification methods. (a) The regular pattern shows broad wave fronts only while (b) shows an excitation state of the atria which has broad wave fronts, rotors, snakes and wavelets.

### 9.2.1.1 Gradient Method

By calculating the gradient on a lattice that represents the transmembrane voltage  $V_m$  at a given time instant, the excitation wave fronts can be determined. This method makes use of the fast upstroke of the action potential. Since the gradient will be largest for the upstroke of the action potential, a threshold can be used to extract the edges of the excitation fronts. The transmembrane voltage at a given time instant is represented by a scalar field  $V_m$ . Thus, the gradient  $\mathbf{G}$  of  $V_m$  will represent the magnitude and direction of the rate of increase of  $V_m$ . The gradient of the transmembrane voltage is calculated by

$$\mathbf{G} = \text{grad } V_m = \nabla V_m = \frac{\partial V_m}{\partial x} \mathbf{a}_x + \frac{\partial V_m}{\partial y} \mathbf{a}_y + \frac{\partial V_m}{\partial z} \mathbf{a}_z \quad (9.1)$$

with the unit vectors  $\mathbf{a}_x$ ,  $\mathbf{a}_y$  and  $\mathbf{a}_z$  of the x, y and z direction in the Cartesian coordinate system. The magnitude of  $\mathbf{G}$  is then computed by

$$|\mathbf{G}| = \sqrt{\left(\frac{\partial V_m}{\partial x}\right)^2 + \left(\frac{\partial V_m}{\partial y}\right)^2 + \left(\frac{\partial V_m}{\partial z}\right)^2} \quad (9.2)$$

Since the gradient  $\mathbf{G}$  is a vector field, the computation of the divergence  $\text{div } \mathbf{G}$  and rotation or curl  $\text{rot } \mathbf{G}$  of the vector field can be easily computed by

$$\text{div } \mathbf{G} = \nabla \cdot \mathbf{G} = \frac{\partial G_x}{\partial x} + \frac{\partial G_y}{\partial y} + \frac{\partial G_z}{\partial z} \quad (9.3)$$

and

$$\text{rot } \mathbf{G} = \nabla \times \mathbf{G} = \left(\frac{\partial G_z}{\partial y} - \frac{\partial G_y}{\partial z}\right) \mathbf{a}_x + \left(\frac{\partial G_x}{\partial z} - \frac{\partial G_z}{\partial x}\right) \mathbf{a}_y + \left(\frac{\partial G_y}{\partial x} - \frac{\partial G_x}{\partial y}\right) \mathbf{a}_z \quad (9.4)$$

to gain additional information that characterizes the current excitation state of the atria.

The divergence  $\text{div } \mathbf{G}$  is a scalar field and gives a measure of how much the vector field diverges or emanates from a specific point. Positive divergence means the vector spreads out of that point. Negative divergence points out that the vector field converges at that point. Zero divergence is given if as many vectors are directed towards that point as vectors are directed away from that point.

The rotation  $\text{rot } \mathbf{G}$  yields a vector field and provides the maximum value of the circulation of the

vector field per unit area, i.e. the circulation density. At a specific point,  $\text{rot } \mathbf{G}$  may be regarded as the measure of the circulation, i.e. how much the vector field curls around that point. The magnitude of the rotation can be used as measure of the curl in a given area.

It is expected that the gradient itself is largest at the very beginning of the wave front. Thus, using thresholding, the front could be segmented. The divergence operator applied on the gradient of the wave front should indicate a rather straight wave front rather than wavelets or rotors. In contrast, the rotation operator will indicate areas with curvature, i.e. it should be large at the edges of rotors and wavelets.

### 9.2.1.2 Positive Transmembrane Voltage Method

The resting potential of the transmembrane voltage  $V_m$  is negative as it is for almost the whole duration of action potential. The beginning of an excitation wave front is characterised by cells where an action potential is triggered. The depolarization leads to a sign change in  $V_m$  that lasts for only a few milliseconds. Thus, by setting all negative values of the transmembrane potential  $V_m$  to '0' and all positive values to '1' the excitation wave front can be extracted for each given time for which the transmembrane potential is computed. The only limitation is that the action potentials triggered in cells that were still refractive do not have an overshoot that will depolarize the cells (see section 8.3.2). The excitation wave fronts created that way will not be detected by the algorithm described.

During sinus rhythm, the excitation spreads across the atria starting at the sinus node. Hence, a single wave front travels across the atria. Given this wave front reaches an anatomical boundary or obstacle, it is divided and a few separate wave fronts can be counted. In AF or atrial flutter, the number of wave fronts increases to a multitude of wave fronts across the atria. Its number will be much larger than the number of wave fronts during sinus rhythm. Therefore the number of wave fronts in a specific area has to be counted. Snakes can be distinguished from broad wave fronts by regarding the number of wave fronts with respect to the volume size: The excitation pattern of snakes will have a high number of wave fronts in a small space. Also, the volume of one wave front will be much smaller for snakes than for broad wave fronts. A little harder is the determination of rotors and wavelets. As with broad wave fronts, rotors are larger than wavelets. With respect to the volume around these patterns, it is expected that rotors take up more volume compared with wave fronts and wavelets occupy more volume than snakes.

Thus, the classification of excitation patterns is carried out according to the following criteria:

#### ***Criterion 1: AF vs. No AF***

The determination whether AF or no AF is present in either a wedge of the atria or the whole atria can be carried out simply by counting the number of wave fronts in the volume. The number will be low in the physiological case and high in the arrhythmia.

***Criterion 2: Wave fronts***

Wave fronts can be characterised as long lines spreading across large parts of the atria.

***Criterion 3: Snakes vs. wave fronts***

In contrast to wave fronts, snakes are short and there are many in a small volume.

***Criterion 4: Rotors vs. wave fronts***

Rotors have a distinct curvature at one end which is missing in wave fronts. Rotors spread across a large part of the atria similar to wave fronts. But it is expected that they occupy more volume in local space than wave fronts.

***Criterion 5: Wavelets***

Wavelets are small circles. Thus, they have a high degree of curvature. It is expected that they have a larger volume than snakes. But they are definitely smaller than rotors and wave fronts.

***Criterion 6: Undeterminable excitation***

If none of the latter four criteria are met, the excitation pattern is defined to be undeterminable.

To classify the excitation pattern according to these criteria, the following measures will be computed:

- number of wave fronts in a given volume,
- volume of each wave front/number of voxel per wave front,
- surface of each wave front.

## **9.3 Computer Model of Congestive Heart Failure**

Congestive Heart Failure (CHF) is generally characterised by a reduced cardiac output. Dilated or hypertrophic myocardium, dysfunction of the conduction system, e.g. atrio-ventricular block or bundle branch blocks and remodelling of the chambers are but a few patho-physiological mechanisms in heart failure [140]. This section describes the pathological characteristics included in this work.

### **9.3.1 Anatomical Model of Patients with Heart Failure**

The remodelling of the ventricular chambers leads to a change in the anatomical shape of the ventricles. This change is patient specific. An anatomical data-set of a patient was included in this study to account for differences in ventricular shape. A three-dimensional MRI data-set was captured at the Department of Radiology of the University of Würzburg. The patient was diagnosed

to have a left bundle branch block, a dilated heart and possibly a minor infarction. The latter, however, was not confirmed.

The MR data was adjusted to 192 x 163 x 180 voxel in the computer model with cubic side length of resolution 1 *mm*. While the ventricles could be segmented with good accuracy, the image quality did not allow for a detailed extraction of atrial structures.

The Visible Man (VM) data-set by the National Library of Medicine of the National Institute of Health, Bethesda, USA, was chosen as reference data set because of its anatomical detail. The VM heart includes both atria, ventricles and the cardiovascular system. It comprises over 360000 cubic voxel with 1 *mm* isotropic side length.

### 9.3.2 Modelling Blockages in the Cardiac Conduction System

Each data-set includes a conduction tree with atrio-ventricular (AV) node, bundle of His, left and right Tawara branches, the anterior and posterior left fascicle and the Purkinje fibres in both ventricles. A blockage in the conduction system can then be set at any of these structures. By setting the conduction properties of the AV node such that the His bundle is not excited, an AV block is created. Similarly, if the left or right Tawara branches are disabled to conduct, a left or right bundle branch block is created. The following pathologies of the conduction system are included in this work:

- AV block III - the AV node does not conduct atrial excitation to the ventricles with no compensatory rhythm present
- Left bundle branch block (LBBB) - the whole conduction tree following the left Tawara branches does not conduct the excitation

### 9.3.3 Modelling Ventricular Dyssynchrony

Ventricular dyssynchrony is due to a delayed mechanical activation of different parts of the ventricles. Inter- and intra ventricular conduction delay describes the excitation delay between the ventricles and within a ventricle, respectively. Based on the assumption that mechanical activation of a cardiac cell follows electrical excitation with a fixed time delay for all cardiac cells, the simulation of either activation or excitation will yield the same result when simulating the excitation propagation. Since the underlying model present in this work is an electrophysiological model and not a mechanical model, electrical excitation will be used to simulate cardiac activity. Hence, inter-ventricular delay can be modeled by reducing the electrical conduction velocity in both ventricles. Intraventricular delay is modeled by reducing the conduction velocity in one ventricle only. In this work, the conduction velocities were set to 100 %, 80 % and 60 % of the physiological values.

### 9.3.4 Summary of Pathologies in Heart Failure Simulated

For each patient data-set and the VM data-set, the different conduction abnormalities were simulated to yield reference values for the optimisation of AV and VV delay described in the next chapter. Table 9.1 summarizes the patho-physiological set-ups.

Blockage in the conduction system	Interventricular delay	
	vRV in %	vLV in %
AV block III	100	100
AV block III	80	80
AV block III	60	60
LBBB	100	100
LBBB	80	80
LBBB	60	60

**Table 9.1.** Patho-physiology included in this work for the simulation of cardiac resynchronization therapy. vRV - right ventricular conduction velocity; vLV - right ventricular conduction velocity; AV block III - atrio-ventricular block third degree; LBBB - left bundle branch block;

## Modelling Interventional and Surgical Therapies

*“Study without desire spoils the memory, and it retains nothing that it takes in.”*

Leonardo da Vinci

Italian engineer, painter and sculptor (1452 - 1519)

### 10.1 Computer Model of Ablation Therapy

Ablation lesions are either set endocardially or epicardially. The ablation catheter touches the surface and by application of the respective technology a lesion with 3 - 8 mm depth is created [72]. Since the atrial wall is thin and the risk of perforation is high, the technology is set to the lower value rather in the treatment of supraventricular arrhythmia.

Thus, the lesions sets investigated in this work were created using a 3D user interface and ray tracing techniques, which allow the user to draw a line on the epicardial surface. The epicardial surface was chosen due to better visibility when performing the procedure. The lesion depth was set to 3 mm. Thus, the operational technique was mimicked in which the surgeon creates lesions only seeing the cardiac surface without detailed knowledge of the tissue depth at the point of the catheter.

Ten different left atrial ablation lesion sets were created according to clinical studies carried out in recent years (see figure 10.1 and 10.2). A linear ablation lesion set as described by Kottkamp et al. [154] was defined by a line starting at the inside of the right inferior pulmonary vein (RIPV) leading to the right superior pulmonary vein (RSPV) across to the left superior pulmonary vein (LSPV). The lesion then follows down to the left inferior pulmonary vein (LIPV) and to the mitral annulus (MA). The circumferential approach taken by Pappone et al. in 1999 [225] was implemented by encircling each pulmonary vein on its own. This approach lead to a further lesion set as described in a review article by Chen et al. [40]: if the lesions are set further proximal, the circles around the left PVs and the right, respectively, will intersect. Thus, the lesion set comprises two circumferential lesions around the left and the right PVs, respectively, and two linear lesions separating

the inferior and the superior PVs each. Melo et al. [180] carried out circumferential ablation of the left and right PVs only giving the fourth ablation set investigated in this work. Based on the circumferential ablation lesions based on the Melo et al. strategy, two linear lesions were added to link the mitral annulus to the lesion around the left PVs and the other linking both circumferential lesions at the left atrial roof. Benussi et al. first investigated this approach clinically [16]. Adding a couple of additional linear lesions to the latter approach, ie. lesions separating the inferior and the superior PVs and further adding another roof lesion, two more ablation strategies are described as tested by Pappone et al. in 2004 [224] and 2005 [223].

The final three ablation strategies implemented were based on the left atrial lesion set of the Cox-Maze III procedure [47]: all four PV were encircled by a single circumferential lesion and linear lesions were added (a) to the mitral annulus and the left orifice, (b) a single linear lesion to the mitral annulus only and (c) two linear lesions to the mitral annulus. The latter two strategies were investigated by Ernst et al. [76] and Sueda et al. [273]. While recent studies tend to include only circumferential lesions around left and right PVs and adding linear lesions as described by Benussi et al., the ablation strategies included in this study mostly cover the whole spectrum of ablation lesion sets investigated so far clinically.

The simulations were carried out in the following manner: Each AF triggering focus investigated in chapter 9.1 was subject to each ablation strategy. The ectopic beat occurred after the lesion set was completed, ie. the tissue of the ablation lesion was set to have non-conducting properties before the start of the simulation. The initial ablation lesions, where the lesion depth was set to 3 mm only, is called the first procedure. A second procedure was carried out for each ablation strategy guaranteeing complete transmuralty of the lesion, i. e. the lesion depth was increased after the first set of simulation to cut through the tissue wall completely. Success of the ablation strategy was defined if the atria showed normal sinus rhythm after 2 s time simulated. Hence, the results were obtained from 460 simulations for ten different ablation strategies.

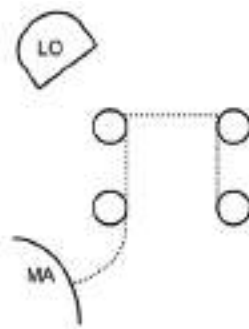


**Figure 10.1.** Schematic diagram of the ablation lesion set carried out by Kottkamp et al. [154]. The epicardial view shows the left orifice (LO) at the top behind the left superior pulmonary vein. At the bottom left, the mitral annulus (MA) is shown. The pulmonary veins (PVs) are indicated by the circles with the right PVs on the right side. The dotted lines indicate the ablation lesion.



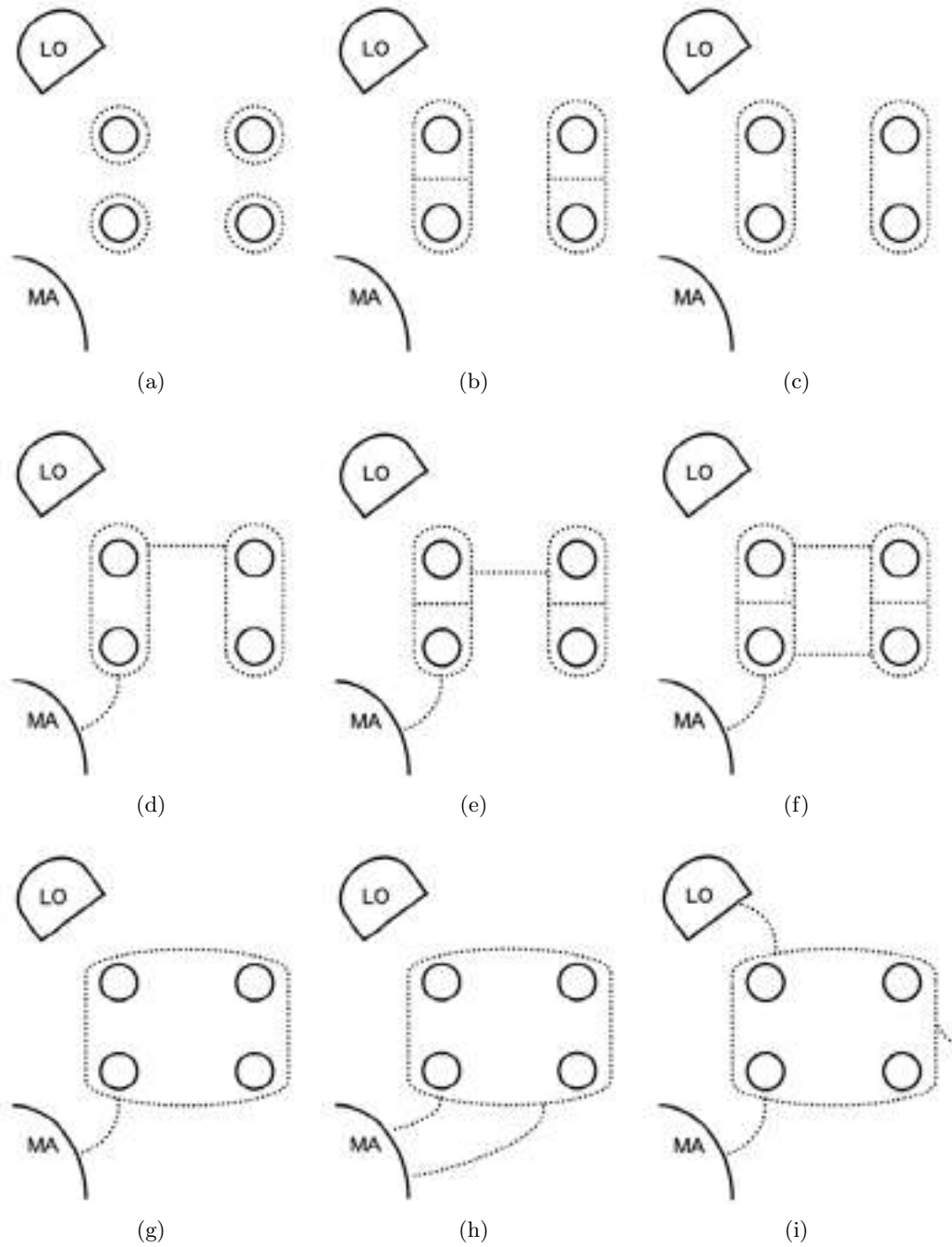


**Figure 10.2.** Schematic diagramm of the ablation lesion set described by (a) Pappone et al. 1999 [225], (b) Chen et al. 2005 [40], (c) Melo et al. 1999 [180], (d) Benussi et al. 2000 [16], (e) Pappone et al. 2005 [223], (f) Pappone et al. 2004 [224], (g) Ernst et al. 1999 [76], (h) Sueda et al. 1997 [273] and (i) Cox 2004 [47]. The epicardial view shows the left orifice (LO) at the top behind the left superior pulmonary vein. At the bottom left, the mitral annulus (MA) is shown. The pulmonary veins (PVs) are indicated by the circles with the right PVs on the right side. The dotted lines indicate the ablation lesion.

## 10.2 Computer Model of Atrial Antitachycardial Pacing

To evaluate the effect of electrode position in preventive AATP, 72 virtual electrodes were placed interactively on the right atrium (see figure 10.3). Atrial pacing was carried out using one electrode at a time only.

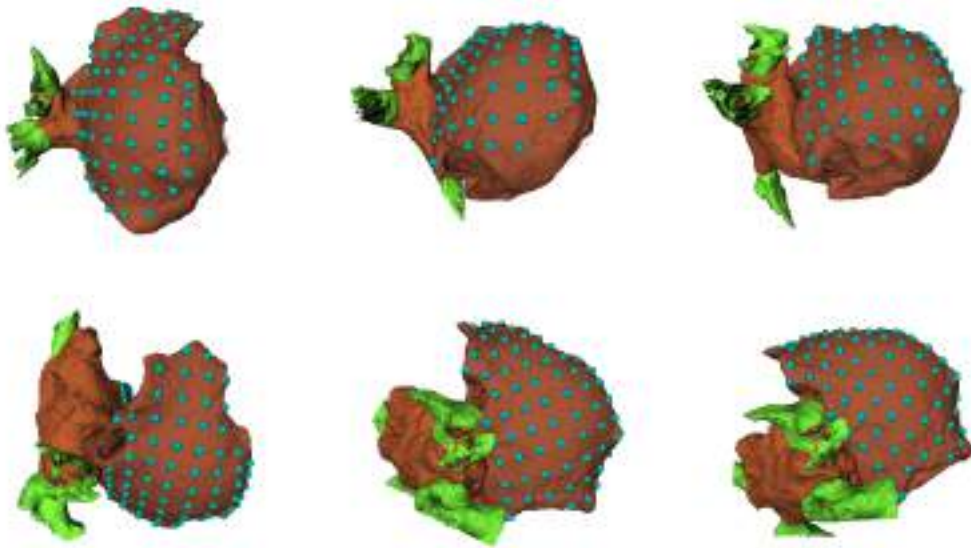


**Figure 10.3.** This figure shows the 72 equally spaced electrodes on the right atrium to investigate the influence of the electrode position on the outcome of atrial antitachycardial pacing. The blue dots indicate the electrodes position, atrial tissue is brown and the pulmonary veins are indicated by the yellow structures.

Preventive pacing algorithms simulated were premature atrial complex (PAC) suppression and Post-PAC response. Pace conditioning and Post-Exercise response was not investigated since heart rate changes are not included in the physiological model. Burst pacing was modeled to evaluate pacing algorithms for the termination of AF. The premature atrial activity was initiated at  $t = 0, ms$ . At this time, the sinus node was set to depolarize and an initial beat in the pulmonary veins at the location of the ectopic focus was triggered. This caused the atria to depolarize prematurely which would be recognized as a PAC. The ectopic beat or second PAC leading to AF was set at  $200 ms$ . To differentiate between the two PACs, the first will be called PAC and the second will be called ectopic beat since it triggers AF without any intervention.

### *Post-PAC Response*

Post-PAC response is characterized by controlling the atrial rate for two beats [161]. The pacing rates reported in literature vary between 60 bpm to 130 bpm. Since the time between

the PAC and the ectopic beat is only 200 ms, only one pacing stimulus occurs even with the highest pacing rate of 130 bpm. The preventive pacing was stopped after the ectopic beat occurred at 200 ms. To further investigate the onset of AF with respect to the pacing stimuli, the timing of the pacing stimulus was set to 50 ms, 100 ms, 150 ms and 200 ms before the ectopic beat (see figure 10.4). Success was defined if the atria were at rest after 500 ms.

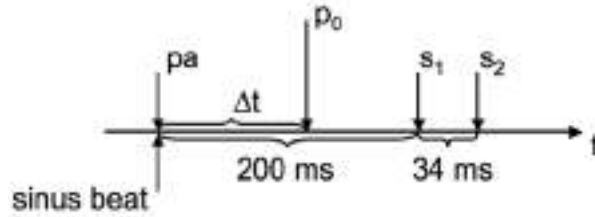


**Figure 10.4.** This schematic diagram illustrates the timing of the pacing stimulus with respect to the sinus beat and the premature atrial activation (pa) for the post-PAC (premature atrial complex) response algorithm simulated. The premature atrial activation is achieved by triggering action potentials simultaneously at the sinus node and the location of the ectopic beat. The pacing stimulus  $p_0$  is set between the premature beat and the stimuli  $s_1$  and  $s_2$  with a time offset of  $\Delta t$ . The stimuli  $s_1$  and  $s_2$  are supposed to be suppressed by the pacing stimulus. If they are not suppressed, they lead to atrial fibrillation.

### *PAC Suppression*

To model PAC suppression, the pacing rate was set to frequencies of 400 bpm to 1200 bpm with increments of 100 bpm. The pacing started right after the PAC and was maintained for 500 ms (see figure 10.5). Success was defined if the atria were at rest after 750 ms.

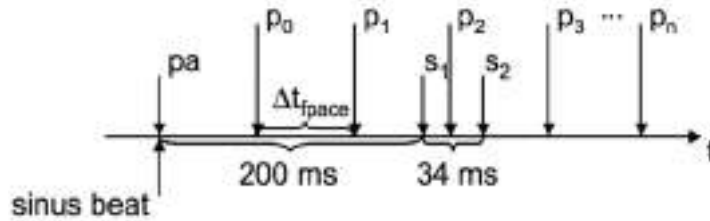


**Figure 10.5.** This schematic diagram illustrates the timing of the pacing stimuli with respect to the sinus beat and the premature atrial activation (pa) for the PAC (premature atrial complex) suppression algorithm simulated. The premature atrial activation is achieved by triggering action potentials simultaneously at the sinus node and the location of the ectopic beat. The pacing stimuli follow the premature beat (pa) with a set frequency. The timing between two successive pacing stimuli is set to  $\Delta t_{pace}$ . The stimuli  $s_1$  and  $s_2$  are supposed to be suppressed by the pacing stimuli.

### *Burst Pacing*

Burst pacing to terminate AF was carried out as follows: 1800 ms after the first stimulus of

the ectopic beat, the pacing was initiated with frequencies ranging between 400 bpm to 1200 bpm with increments of 100 bpm (see figure 10.6). The pacing was stopped after 6800 *ms*. Success was defined if normal sinus rhythm was established after 7500 *ms*. Due to the high computational demand of these simulations, only every second electrode was used to pace the atrium.

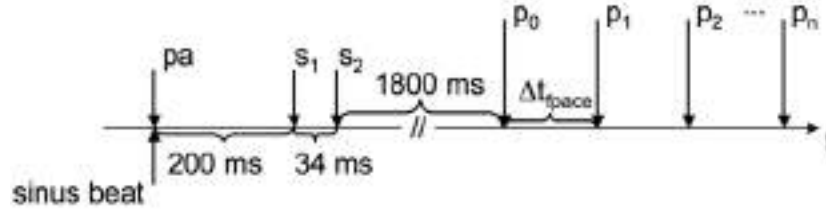


**Figure 10.6.** This schematic diagram illustrates the timing of the burst pacing strategy with respect to the sinus beat and the premature atrial activation (pa). The premature atrial activation is achieved by triggering action potentials simultaneously at the sinus node and the location of the ectopic beat. The stimuli  $s_1$  and  $s_2$  lead to atrial fibrillation. The first pacing stimulus  $p_0$  is set 1800 *ms* after the stimulus  $s_2$ . The consecutive pacing stimuli follow with a set frequency of  $1/\Delta t_{pace}$ .

The pacing protocol was generated automatically as well as the simulations. They were carried out on a single 2 GHz Apple Macintosh PowerPC G5 processor. Simulating 1 s real time took 10 minutes computation time.

### 10.3 Computer Model of Cardiac Resynchronisation Therapy

A biventricular pacing (BiVP) device comprises three electrodes: a sensing electrode in the right atrium and two pacing leads, one each in the left and right ventricle. When the electrode in the atrium measures an excitation, either the left or the right ventricle is stimulated after a programmed delay, called atrio-ventricular (AV) delay. Since the left ventricle is commonly stimulated before the right ventricle, a positive AV delay refers to left before right ventricular stimulation. A negative AV delay refers to a right before left ventricular stimulation in this work. The sensing electrode can be placed anywhere in the right atrium. Thus, it will record an atrial activation at different times with respect to its position. The AV delay has to be adjusted accordingly. However, while the AV delay varies with respect to each patient, the relative timing of the interventricular (VV) delay remains constant. Since the atrial electrode is used for sensing only, an investigation of different electrode positions in the ventricles is carried out since an individualization and optimal lead localization is required to achieve an optimal therapeutical outcome [280].

### 10.3.1 Electrode Positions in Cardiac Resynchronization Therapy

Any time of atrial activation could be used to reflect different positions of the sensing electrode. However, since atrial activation remains constant in all simulation, the results remain constant except for a timing delay that reflects the difference between sinus node activation and the position of the electrode. Thus, one reference value has to be chosen. The activation of the atrio-ventricular node is chosen as reference time for the AV delay in the patient data-sets since the atria are not present in these data-sets. To demonstrate that any other point in the atria could be chosen to set the AV delay with respect to an individual anatomy, the activation of the sinus node is taken as reference time for the AV delay for the Visible Man data set which includes the atria. Thus, in all simulations, the reference time for the AV delay is 0 *ms*.

The right ventricular apex has been chosen as the location of the right ventricular pacing lead (see figures 10.7 - 10.8). The left ventricular electrodes are placed in the anterior and posterior branches of the coronary sinus as well as the left ventricular free wall (see figure 10.7 - 10.8). The positions were chosen interactively trying to achieve equally spaced positions covering the whole surface of the left ventricular epicardial wall. Overall, 12 different electrode positions were placed on the left ventricle. Pacing was performed for each pair of right and left ventricular pacing position yielding 12 electrode set-ups for each pathology to investigate the influence of electrode position in CRT.

### 10.3.2 Optimisation Strategy

#### 10.3.2.1 Discrete Simulation in the Complete Parameter Space

For each electrode pair, the AV and VV delay was optimised. The optimization is carried out similar to the study by Whinnett et al. [299] where an optimization parameter was measured with respect to different timing of the AV and VV delay:

- AV delay ranging from 60 *ms* to 220 *ms* (Visible Man)/260 *ms* (patient) with increments of 20 *ms*
- VV delay ranging from -30 *ms* to 50 *ms* (Visible Man)/70 *ms* (patient) with increments of 10 *ms*

The parameter space was enlarged for the patient data set since it represented a dilated heart where increased activation timing can be expected. For each parameter set-up, the cardiac output in form of blood pressure peaks was measured by Whinnett et al. In this work, a different parameter was chosen to optimise the pacemaker timing:

The optimisation strategy used is based on the assumption that the optimal cardiac output is given during sinus rhythm if no pathological changes in the electrophysiology are present. Thus, the aim of the pacing therapy has to be to achieve a cardiac activation that is as close to the sinus rhythm

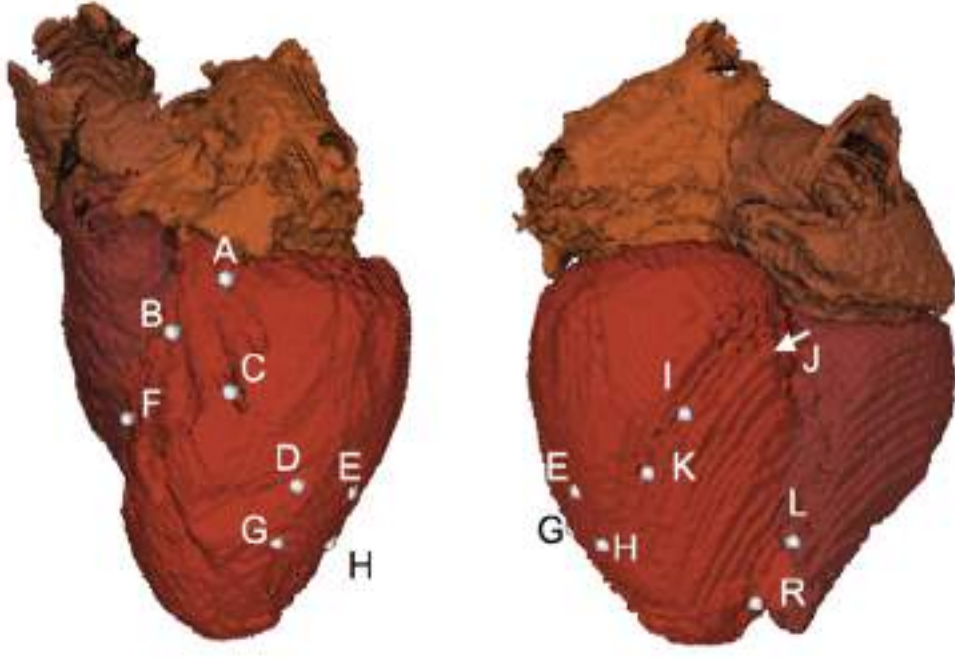


**Figure 10.7.** This figure shows the electrode positions of the pacing leads for the evaluation of electrode position in cardiac resynchronization therapy in the Visible Man data set in anterior view (left) and posterior view (right).

as possible. For this purpose, the isochrones, i. e. the time of activation for each cardiac cell which is represented by a voxel in the anatomical data-set, are computed for the heart for one cardiac cycle. The activation time, or isochrone, is defined as the time of action potential initiation. The isochrones for the physiological excitation during sinus rhythm are used as reference parameter. Then, the isochrones for the respective pathological excitation is computed. The root mean square error  $E_{RMS}$  between the two simulations can be computed as measure of difference between the physiological and pathological activation:

$$E_{RMS} = \sqrt{\frac{1}{N} \sum_{i=1}^N (x_i - e_i)^2} \quad (10.1)$$

Thus, the  $E_{RMS}$  delivers the deviation of the activation time of the pathology from sinus rhythm for the whole number of voxel elements  $N$  with the activation time  $x_i$  of voxel  $i$  for the sinus rhythm and the activation time  $e_i$  of voxel  $i$  for the pathology.

By placing stimuli at the ventricles, the activation of the myocardium is forced to be closer to

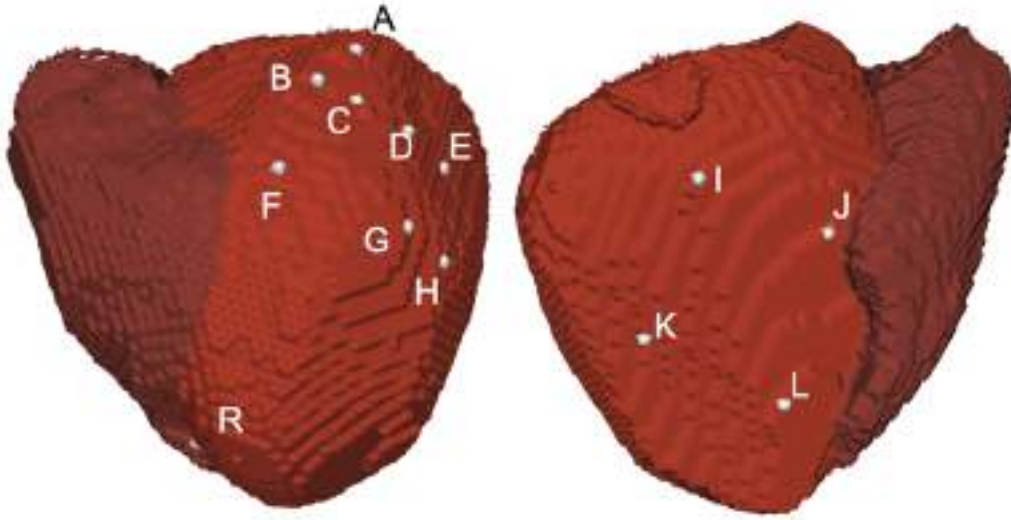


**Figure 10.8.** This figure shows the electrode positions of the pacing leads for the evaluation of electrode position in cardiac resynchronization therapy in the patient data set in anterior view (left) and posterior view (right).

the physiological activation time. Thus, an optimisation can be achieved by minimising the root mean square error  $E_{RMS}$  through adjustment of the AV and VV delay. The algorithm can be described as follows:

1. Compute the isochrones for the physiological case.
2. Compute the isochrones for the pathological case.
3. Compute the isochrones for each electrode pair and each AV and VV delay
4. Calculate the root mean square error  $E_{RMS}$  for the pathology and all pacing set-ups taking the isochrones for the physiological case as reference.
5. The smallest error will give the optimal electrode set-up with optimised AV and VV delay.

For each electrode pair, a two-by-two matrix of  $E_{RMS}$  is gained with respect to AV and VV delay. The smallest error yields the pacemaker timing that achieved highest resemblance to the sinus rhythm with respect to cardiac activation. Hence, the optimisation strategy used in this work is a minimisation of the root mean square error. It is independent on QRS duration but rather represents a measure of activation of the cells.

### 10.3.2.2 Downhill Simplex Algorithm

So far, the above strategy is carried out when optimising AV and VV delay resulting in around 100 different set-ups for the pacemaker timing. Although the presented computer model computes one simulation in less than 5 minutes on an Apple Macintosh PowerPC G5 for the Visible Man data-set,

the completion of 100 simulations for 12 different electrode set-ups takes about three days and six hours. To decrease the overall number of simulations per electrode, the downhill simplex algorithm by Nelder and Mead [201] was implemented. It was adjusted to a two-dimensional search algorithm with the AV delay giving one dimension and the VV delay being the other. The algorithm was taken from “Numerical Recipes in C. The Art of Scientific Computing” by Press et al. [238] and adjusted to the presented application. It was chosen since this algorithm only requires function evaluation and not derivatives. The computer simulations produce the  $E_{RMS}$  value as output. A derivative cannot be directly calculated from the simulations but requires five simulations per derivative. The calculation of only five derivatives would require 25 simulations. The downhill simplex algorithm is expected to perform better.

The simplex in two dimensions (2D) is given by a triangle with three points or vertices. It can be initialised anywhere within the boundaries of the 2D parameter space. The initial simplex is a guess. The following algorithm is then supposed to search the rest of the parameter space for - at least a local - minimum. The results of the simulations described in the previous section suggested, however, that local minima are not critical if even existing. Thus, the initial three vertices give the parameter set-up for the first three simulations. The resulting three values of the  $E_{RMS}$  are then sorted and labeled with the lowest, middle and highest value. The vertex with the highest value will be reflected in the first iteration and the new  $E_{RMS}$  value is computed (see figure 10.9.b). If it is smaller than the previous highest value, the reflection is extended by factor 2 to find the next vertex for which the  $E_{RMS}$  is computed (see figure 10.9.c). If it is larger than the initial highest value, the triangle is compressed along the dimension of the reflection by factor 2 (see figure 10.9.d) which is also called contraction of the triangle along one dimension. Given the new value is still higher than the initial highest value, the simplex contracts further but in multiple dimensions (see figure 10.9.e). Afterwards, the algorithm starts again with an iteration step.

A termination criterion  $c$  has to be defined to stop the iteration of the algorithm. It is set to

$$\frac{E_{RMSmax} - E_{RMSmin}}{E_{RMSmax} + E_{RMSmin}} < c_{termination} \quad (10.2)$$

with  $c_{termination} = 0.0005$ ,  $E_{RMSmin}$  being the lowest value of the three simplex vertices and  $E_{RMSmax}$  being the highest value of the simplex vertices after an iteration step.

The termination criterion defines the accuracy of the result. A trade off has to be considered for iteration steps versus accuracy of the result. The smaller the difference between the lowest  $E_{RMS}$  the more iteration steps are required. In this work, the iteration should lead to less than 20 simulations, ie. a decrease of computational load of about 80 %.



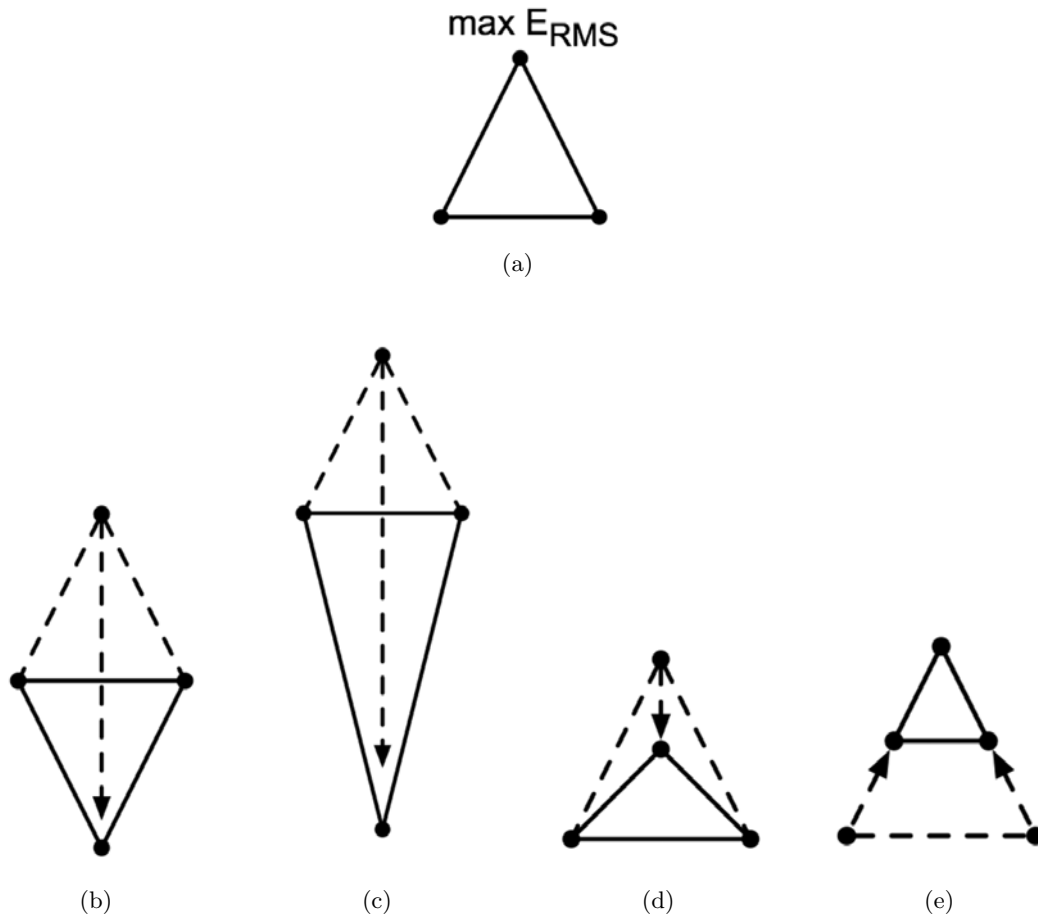


**Figure 10.9.** Possible outcomes for an iteration step of the Downhill Simplex Algorithm [238]: (a) The initial simplex defines a triangle in two dimensions. The vertices define the parameters, i. e. the AV and VV delay for the three initial simulations. The resulting  $E_{RMS}$  are sorted from lowest to highest value. The vertex of the highest value  $\max E_{RMS}$  will be reflected to find a new parameter set for the next simulation (b). If the new value is below the the previous  $\max E_{RMS}$ , the reflection is extended by factor two (c). If it is higher, the simplex will be compressed in one dimension (d). The last step in the iteration is a contraction in multiple dimension (e) before the algorithm starts the next iteration step. The points indicate the vertices, the lines the sides of the simplex. The dashed lines indicate the position of the previous simplex and the dashed arrows show the direction in which the vertices move.



## **Results and Conclusions**



## Results: Pathology

*“For the things we have to learn before we can do them, we learn by doing them.”*

Aristotle

Greek critic, philosopher, physicist and zoologist (384 BC - 322 BC)

### 11.1 Simulation of Supraventricular Arrhythmia

It was possible to create AF by setting the ectopic focus at all pulmonary veins. Out of 35 different locations of the ectopic focus, 23 (63.8 %) lead to AF that lasted for the time period simulated. Only 13 (36.1 %) did not show AF after 1 s. It was possible to create AF by setting ectopic foci into all pulmonary veins (see table 11.1).

Location	Simulations	AF	No AF
LSPV (proximal)	9	6	3
LSPV (distal)	10	4	6
RSPV	8	5	3
LIPV	5	4	1
RIPV	4	4	0
Overall	36	23	13

**Table 11.1.** This table shows the distribution of ectopic foci simulated. Atrial fibrillation could be initiated at all pulmonary veins. LSPV - left superior pulmonary vein; RSPV - right superior pulmonary vein; LIPV - left inferior pulmonary vein; RIPV - right inferior pulmonary vein; AF - atrial fibrillation

The ectopic beat simulated creates rotor waves due to a unidirectional block. The center of these rotors is the respective location of the ectopic focus. The initial re-entries will be self-terminating. Either the excitation of the atria then returns to the sinus rhythm or the fibrillatory excitation continues due to macro re-entrant circuits that sustain the fibrillation. Driving rotors can be recognized as well as a break up of the stable rotor wave fronts. While stable excitation wave fronts

can be classified as fast atrial flutter, the break up of the wave fronts causes an excitation which can be named deterministic chaos that represents atrial fibrillation.

#### 11.1.1 Macro Re-entries

Every initiating rotor will eventually be replaced by a different excitation pattern due to the complex anatomical structures. The wave fronts of the ectopic beat occur with a very high frequency and the excitation of the atria is dominated by the rotor around the ectopic focus. Thus, when the last wave front that is caused by the initial rotor occurs, the excitation will travel across the atria. In the cases of sustained AF, the excitation wave front will follow a re-entrant pathway (see figure 11.1). Another driving rotor will be established that causes the atria to fibrillate. In the timespan simulated, these rotors persisted or the wave fronts were broken up to create chaotic AF.

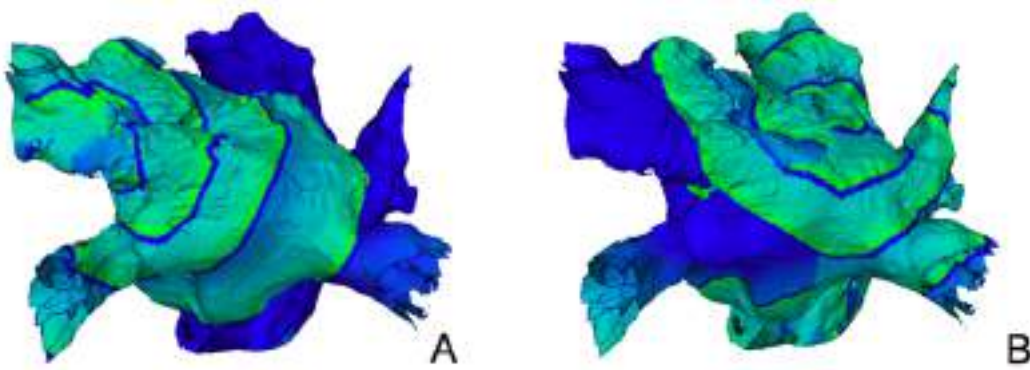


**Figure 11.1.** Latero-dorsal view on the left atrium at 138 ms (A) after the initiating trigger. The rotor wave is situated at the left superior pulmonary vein (A) with its center around the initial ectopic focus. The stable excitation pattern is characteristic for atrial flutter. The initial rotor is self-terminating and flutter is maintained due to a second macro re-entrant circuit after 660 ms (B). The transmembrane voltage is shown. The dark lines on the atrial surface indicate the excitation wave fronts.

#### 11.1.2 Driving Rotor

Figure 11.2 shows the results of a simulation where the ectopic beat was set at the left inferior PV. The re-entrant excitation will result in a rotor with focus between the hearts valves in this case (figure 11.2 (B)). This pattern can be observed in other simulations as well. The stable excitation pattern will be broken up eventually and after a few seconds, the atria will show complete chaotic excitation (see figure 11.7).

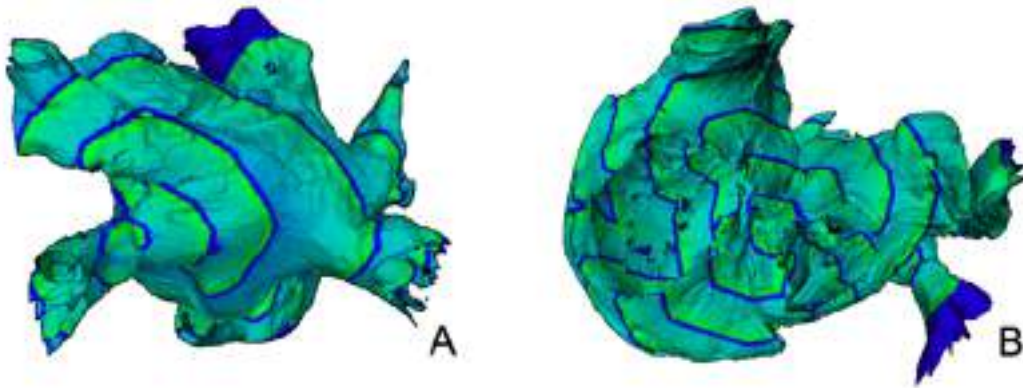


**Figure 11.2.** (A): Latero-dorsal view on the left atrium at 184 ms after the initiating trigger. The rotor wave is situated at the left inferior pulmonary vein with the center around the initial trigger. The stable excitation pattern is characteristic for atrial flutter. (B): View on the valve plane (the ventricles are hidden for visualization) at 716 ms after the initial trigger. A new dominant rotor wave with center between the mitral and tricuspidal valve has replaced the rotor wave around the initial trigger at the left inferior pulmonary vein. The transmembrane voltage is shown. The dark lines on the atrial surface indicate the excitation wave fronts.

### 11.1.3 Break-up of Stable Excitation Wave Fronts

Figure 11.3 is an example of wave front break-up that leads to chaotic atrial fibrillation. The break up of the stable re-entrant circuits occurred if the wave fronts travel across tissue with different refractive properties which is mostly where the atrial wall has not a smooth curvature on the atrial surface. While parts of the excitation wave front will be determined by e.g. an action potential that is triggered out of the resting phase of the cell, the other part falls into an area of tissue that is in its phase of relative refractoriness or even absolute refractoriness. The result is that the atrium is left in a state of regional heterogeneities concerning the excitation state of the cells. The points where the wave fronts break-up can be marked by areas of complex anatomical structures (see figure ??). At either a notch in the wall thickness or the orifices of blood vessels or similar anatomical structures, the break-up of the wave front occurs. Once the break-up of the wave front happens, further AF mechanisms can be observed due to local refractoriness.

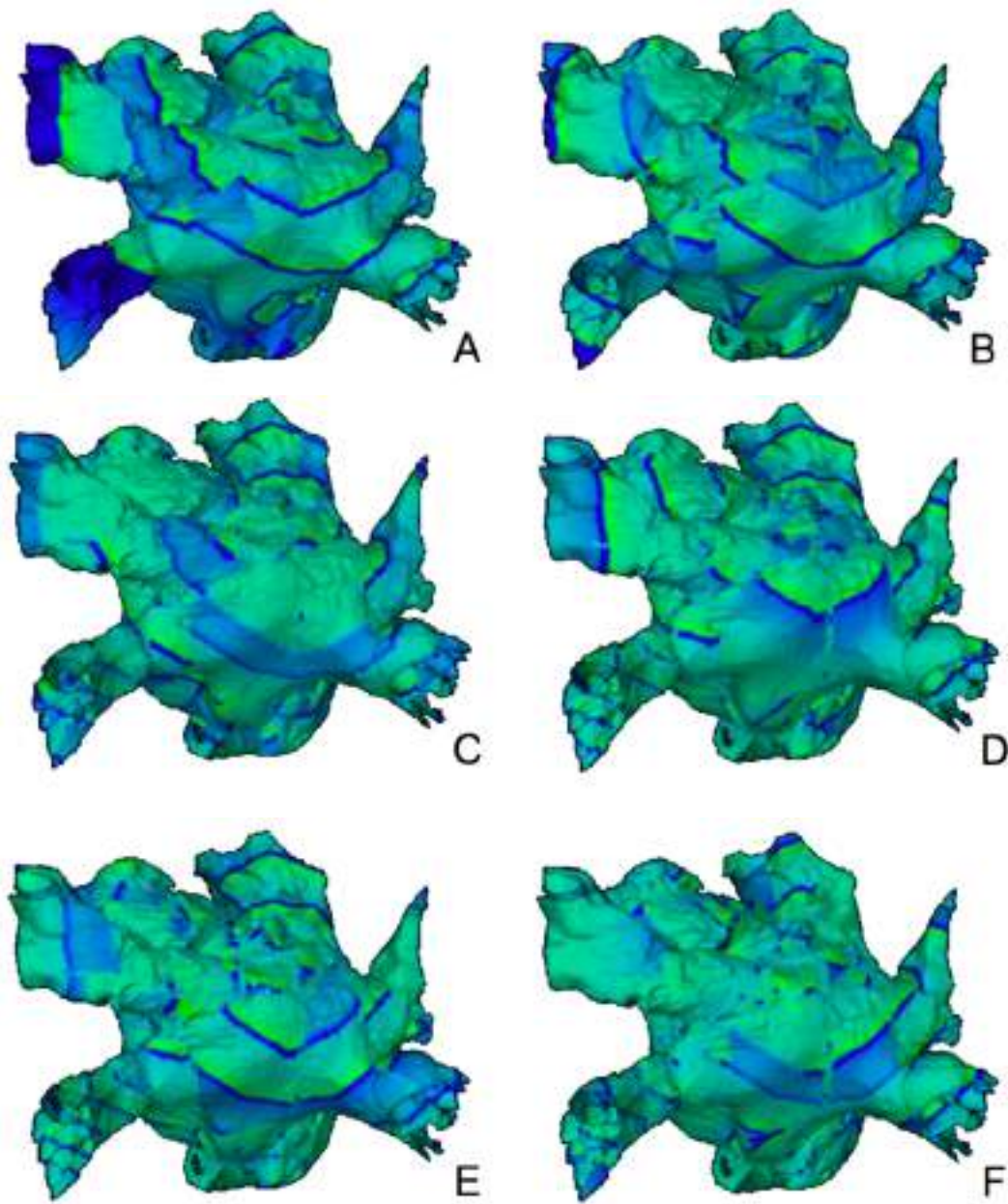


**Figure 11.3.** Latero-dorsal view of the left atrium. Figures (A) - (F) depict the time instances at 898 *ms*, 958 *ms*, 1000 *ms*, 1096 *ms*, 1192 *ms*, 1288 *ms*, respectively, of a simulation where the ectopic focus was set at the proximal left superior PV. The break-up of wave fronts can be clearly seen on the left atrial roof. Different cycle length and excitation pattern in different areas of the atria result from this break up. The transmembrane voltage is shown. The dark lines on the atrial surface indicate the excitation wave fronts.



#### 11.1.4 Local Excitation Pattern

The macroscopic view onto the left atrium shows that the excitation of large parts of the atria is still determined by stable excitation wave fronts. The wavelength of the excitation differs (see figure 11.4). The excitation of the PVs shows a high frequency while time delay between successive wave fronts remains larger in the right atrium with respect to the PVs. At a later time instance, however, this situation can be reversed: while the atrial roof is excited by quasi-chaotic excitation pattern, the areas at the edges of the atria including the pulmonary veins show a stable excitation pattern. In the latter case, the excitation of the PVs has a greater wavelength (see figure 11.5). Overall, several excitation patterns and cycle lengths occur in different regions of the atria and the PVs at the same time instance (see figures 11.4 - 11.6). Rotors, wavelets as well as snakes can be seen in different parts of the atria (see figure 11.6). At the break up of the wave fronts, a streak-like excitation pattern can be observed. The excitation in that area is determined by the local refractoriness. The small wave fronts follow a distinct pathway in one direction. At the edges of both left and right atrial roof, small rotor waves appear. Often, these rotors will turn into small wavelets, exciting the area around its center by circulatory movements. Consequently, other small wavelets appear in the same area.

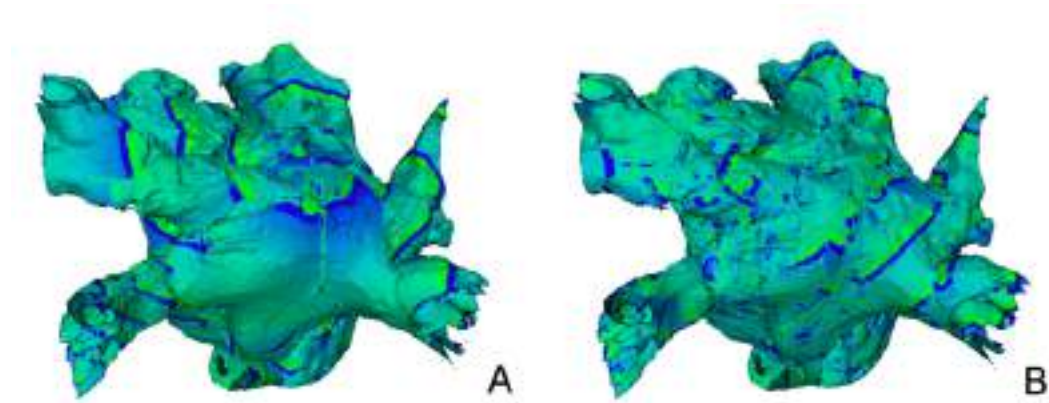


**Figure 11.4.** Latero-dorsal view of the left atrium showing the excitation pattern at 884 ms (A) and 1670 ms (B) after the initial trigger. The ectopic focus was set in the left superior pulmonary vein. The excitation pattern differs in separate regions of the atria. The break-up of wave fronts is clearly visible between the left and right superior pulmonary vein (A). Also, a shorter cycle length can be recognized in the left inferior pulmonary vein than in the right atrium. At a later instance (B), the excitation pattern has changed. Now, the atrial roof is dominated by wavelets, i.e. short cycle length can be observed. A stable pattern can be seen at the right pulmonary veins with longer cycle length. The transmembrane voltage is shown. The dark lines on the atrial surface indicate the excitation wave fronts.

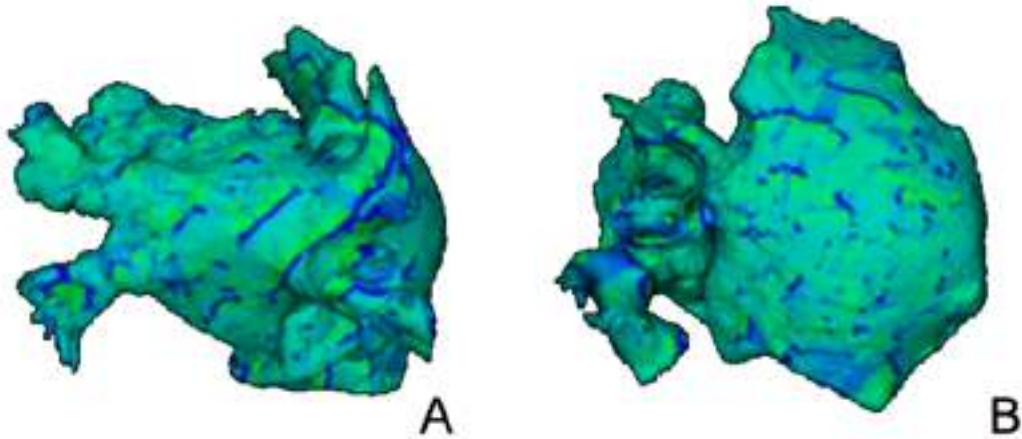


**Figure 11.5.** Excitation of the atria at 1658 ms after the initial trigger. The ectopic focus was set in the left superior pulmonary vein. The excitation pattern differs in separate regions of the atria. While the excitation is dominated by multiple wavelets at the roof of the right atrium (right), stable wave fronts can be observed at the right pulmonary veins (left). The transmembrane voltage is shown. The dark lines on the atrial surface indicate the excitation wave fronts.

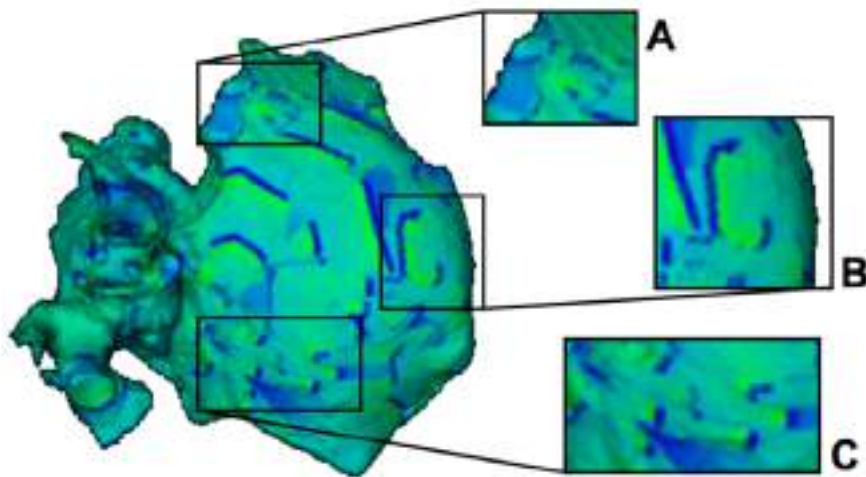


**Figure 11.6.** View onto the right atrium at 1326 ms after the initial trigger at the left superior pulmonary vein. Multiple wavelets (A) and rotor waves (B) can be observed at smooth areas of the atrial roof. Streak-like excitation pattern similar to snakes occur at the same time (C). The snakes are caused by the break-up of the stable excitation wave fronts in areas of the atria where the anatomical structures are not smooth. The transmembrane voltage is shown. The dark lines on the atrial surface indicate the excitation wave fronts.

### 11.1.5 Chaotic Excitation of the Atria

While the excitation in the area of the atrial roof is dominated by small wavelets, the regions further out show an excitation by broad wave fronts. The further the simulation time advances the more multiple wavelets can be counted that spread over the whole atrium until complete chaotic excitation can be observed.

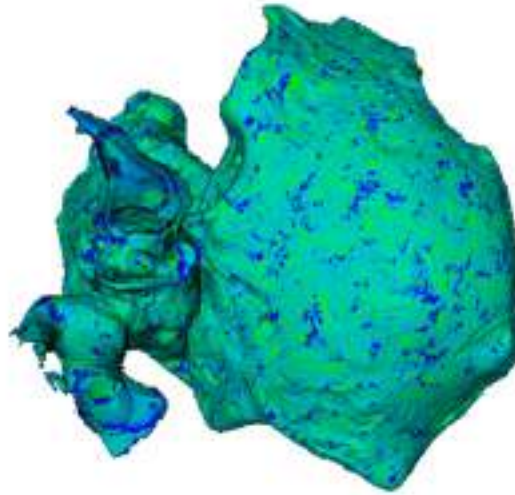


**Figure 11.7.** View onto the right atrium at 17266 ms after the initial trigger at the left inferior pulmonary vein (see figure 11.2). The chaotic excitation pattern can be classified as atrial fibrillation. The transmembrane voltage is shown. The dark lines on the atrial surface indicate the excitation wave fronts.

### 11.1.6 Location of the Ectopic Focus

Comparing the results from placing the focus proximal vs. distal at the left superior pulmonary vein, AF occurred more often if the focus was located proximal (table 11.1). The simulations to investigate spatial dependence of the two AF initiating stimuli, however, showed that either both set-ups created AF or both did not lead to a fibrillatory excitation of the atria (see figures 11.8 - 11.11), i. e. whether the second stimulus was set ostially or deeper into the PV had only an effect on the excitation pattern but not on the initiation of AF.

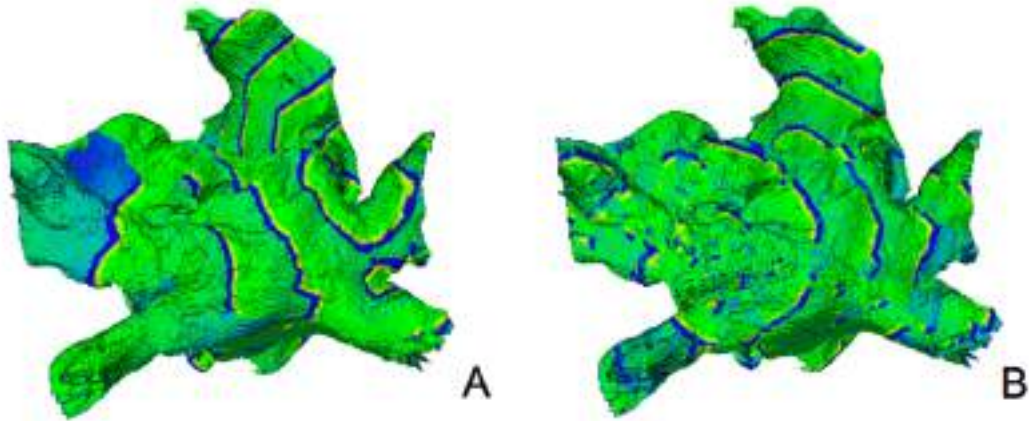


**Figure 11.8.** The ectopic focus was set at the left superior pulmonary vein near the left atrial appendage and the atrial septum. The unidirectional conduction block was set either deeper into the left superior-pulmonary vein (A) or distal, close to the ostia (B). Both set-ups produce atrial fibrillation although a different excitation pattern can be recognized at 700 *ms* after the first stimulus of the ectopic beat. The excitation pattern between the two respective set-ups, however, differs. The transmembrane voltage is shown (latero-dorsal view). The dark lines on the atrial surface indicate the excitation wave fronts.

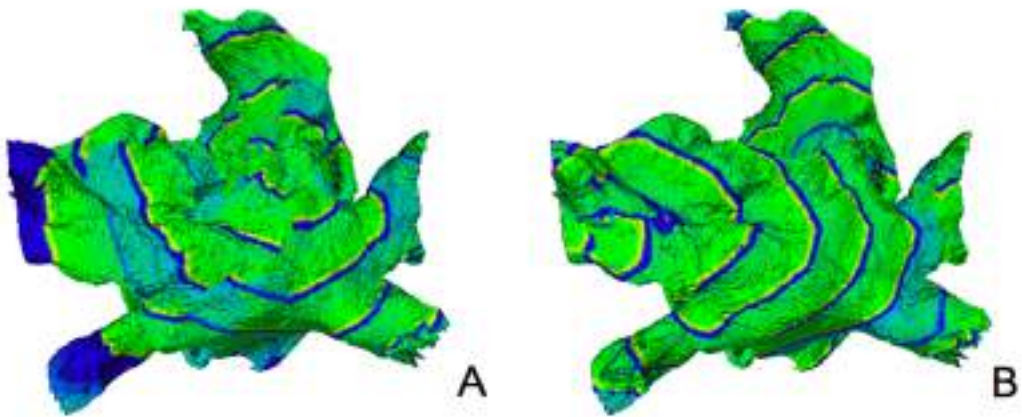


**Figure 11.9.** The ectopic focus was set at the left superior pulmonary vein near the atrial roof. The unidirectional conduction block was set either deeper into the left superior-pulmonary vein (A) or distal, close to the ostia (B). Both set-ups produce atrial fibrillation although a different excitation pattern can be recognized at 700 *ms* after the first stimulus of the ectopic beat. The excitation pattern between the two respective set-ups, however, differs. The transmembrane voltage is shown (latero-dorsal view). The dark lines on the atrial surface indicate the excitation wave fronts.

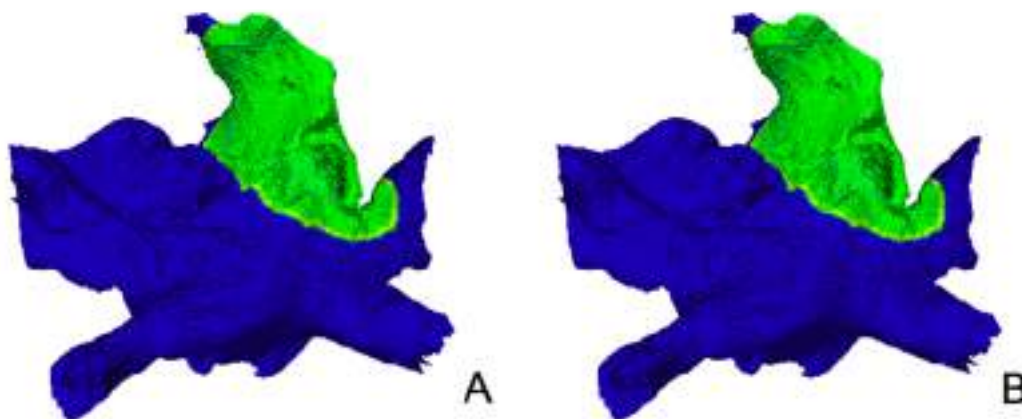


**Figure 11.10.** The ectopic focus was set at the left superior pulmonary vein on the far side of the vein opposite the atrial roof. The unidirectional conduction block was set either deeper into the left superior-pulmonary vein (A) or distal, close to the ostia (B). Both set-ups did not produce atrial fibrillation. The excitation pattern therefore does not differ at 700 *ms* after the first stimulus of the ectopic beat. The transmembrane voltage is shown (latero-dorsal view). The dark lines on the atrial surface indicate the excitation wave fronts.

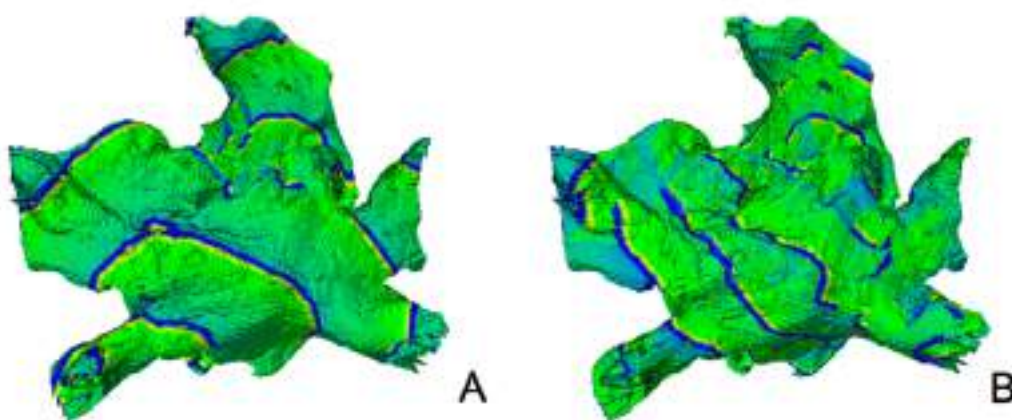


**Figure 11.11.** The ectopic focus was set at the left inferior pulmonary vein between both left pulmonary veins. The unidirectional conduction block was set either deeper into the left superior-pulmonary vein (A) or distal, close to the ostia (B). Both set-ups produce atrial fibrillation although a different excitation pattern can be recognized at 700 *ms* after the first stimulus of the ectopic beat. The excitation pattern between the two respective set-ups, however, differs. The transmembrane voltage is shown (latero-dorsal view). The dark lines on the atrial surface indicate the excitation wave fronts.



### 11.1.7 Results of Excitation Pattern Classification

The following section describes the results of excitation pattern classification. Adjustments of the presented method will be described and the arguments will be presented here. A general discussion of both methods is presented in section 13.2.

The classification methods were applied on two different excitation pattern in the atria. The first includes mostly straight excitation wave fronts and is called hereafter excitation pattern A (see figure 9.4.a). The second includes all classes of excitation pattern, i.e. wave fronts, rotors, snakes and wavelets, and is called excitation pattern B (see figure 9.4.b).

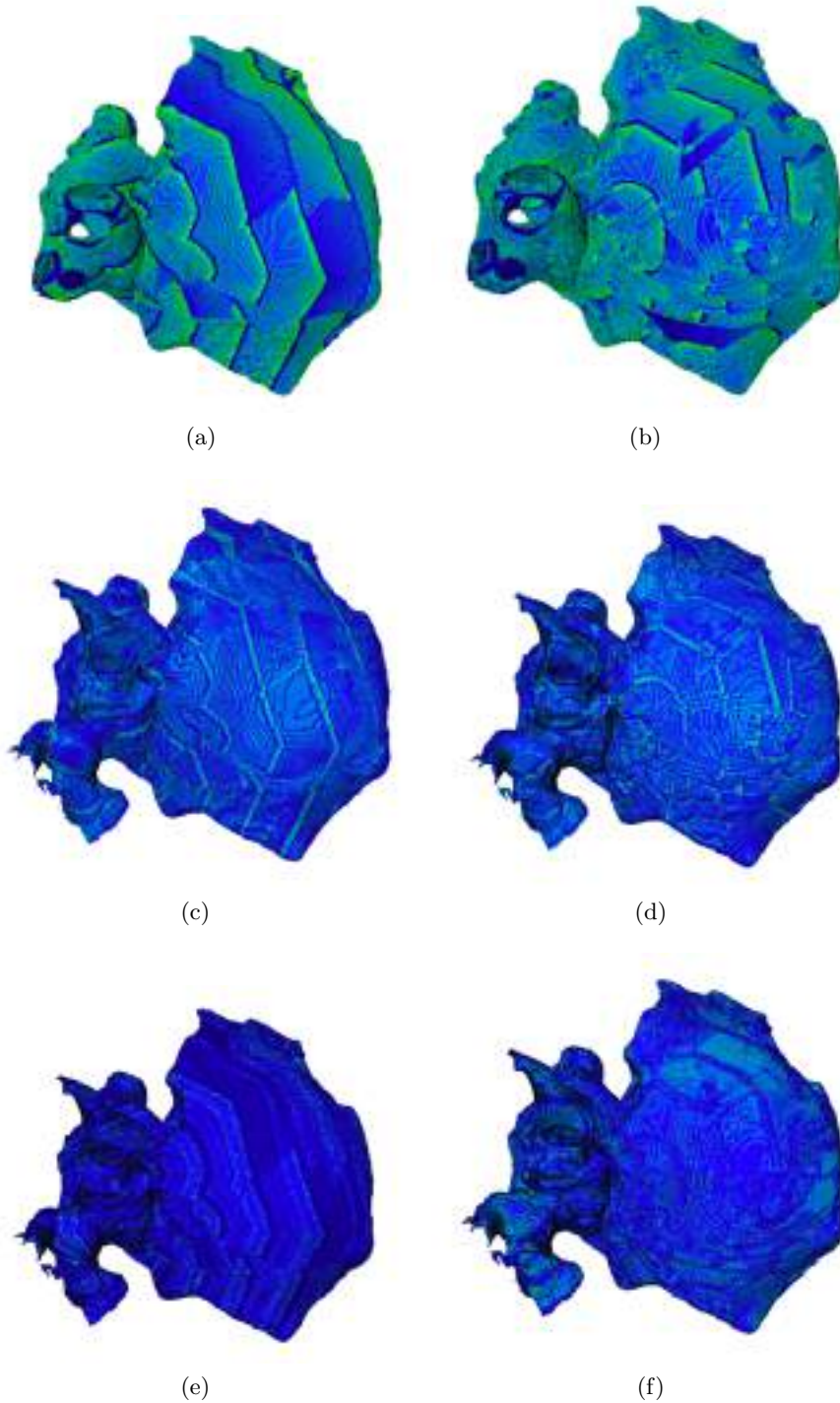
#### 11.1.7.1 Classification by Gradient Method

Figure 11.12 shows the magnitude of the gradient of the two different excitation pattern. The gradient is computed for every voxel in the data set. The resulting vector field is used to compute the divergence (fig. 11.12.c-d) and the magnitude of the curl (fig. 11.12.e-f). The wave fronts are clearly visible in the gradient lattices (fig. 11.12.a-b). Broad wave fronts can be observed in the resulting divergence and curl lattices. However, small structures like snakes or wavelets cannot be distinguished.

The magnitudes of the gradient, the divergence and the rotation is large on the surface of the tissue. This is caused by the computation of the gradient because it can be large if the tissue on the surface has for example the transmembrane voltage of  $-80\text{ mV}$ . Since the surrounding voxel have the value of  $0\text{ mV}$ , the gradient will be large. This error is carried forward when computing the divergence and rotation (see figure 11.12).

To eliminate this border problem, the segmentation of the wave fronts by the Positive Potential Method is applied: Only the gradients within the segmented wave fronts will be set, the other voxel are reset to zero (see figure 11.13). This way, the voxel at the surface are mostly eliminated. Only a wave front which touches the surface of the atria is included. However, since the gradient at the wave front points from negative to positive potential, too, the error at the tissue surface is acceptable.

The gradients still contain values with several orders of magnitude. Also, the segmented wave front has a width of several voxel which is undesirable since the gradient at the back of the wave front points in the opposite direction of the gradient right at the front. Thus, a further segmentation step is included by thresholding based on the magnitude of the gradient. Threshold values were chosen to be 50000, 70000, 100000, 150000 and 200000. The results of the thresholding for excitation pattern A is displayed in figure 11.14 which shows a cross-section through the atrial wall. It can be noticed that the higher the threshold, the smaller the width of the wave front. It can be also noticed that the wave fronts will show breaks the higher the threshold. Above a threshold of 100000, no clear wave fronts can be determined. Therefore, the divergence and the rot operator is only applied to the gradients with threshold up to 100000.



**Figure 11.12.** The figures on the left show the magnitude of the gradient (a), the divergence (c) and the magnitude of the rotation operator (e) for excitation pattern A. On the right is displayed the respective figures for the magnitude of the gradient (b), the divergence (d) and the magnitude of the rotation operator (f) for excitation pattern B. The view is onto the right epicardial surface with the left atrium on the left. The blue colors indicate small values, the bright colors indicate large values.

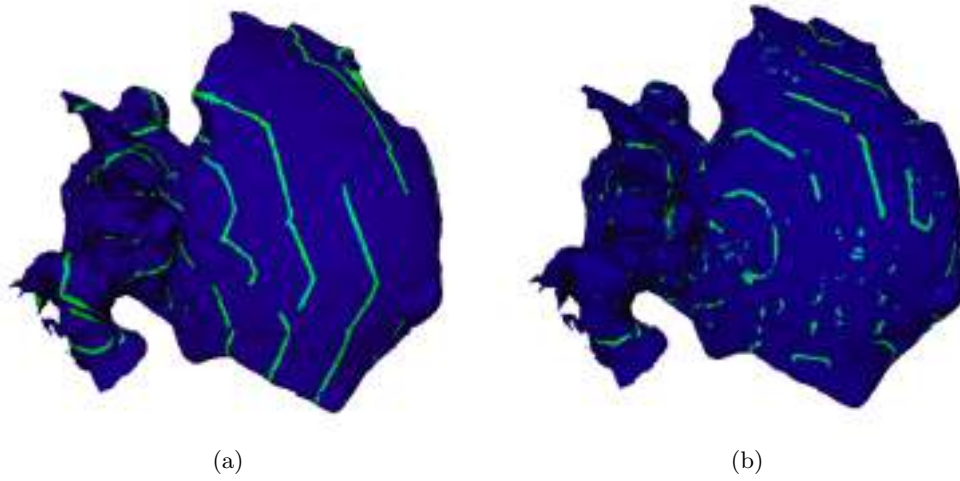


**Figure 11.13.** This figure shows the magnitude of the gradient of all voxels which had a positive transmembrane voltage of excitation pattern A (a) and B (b).

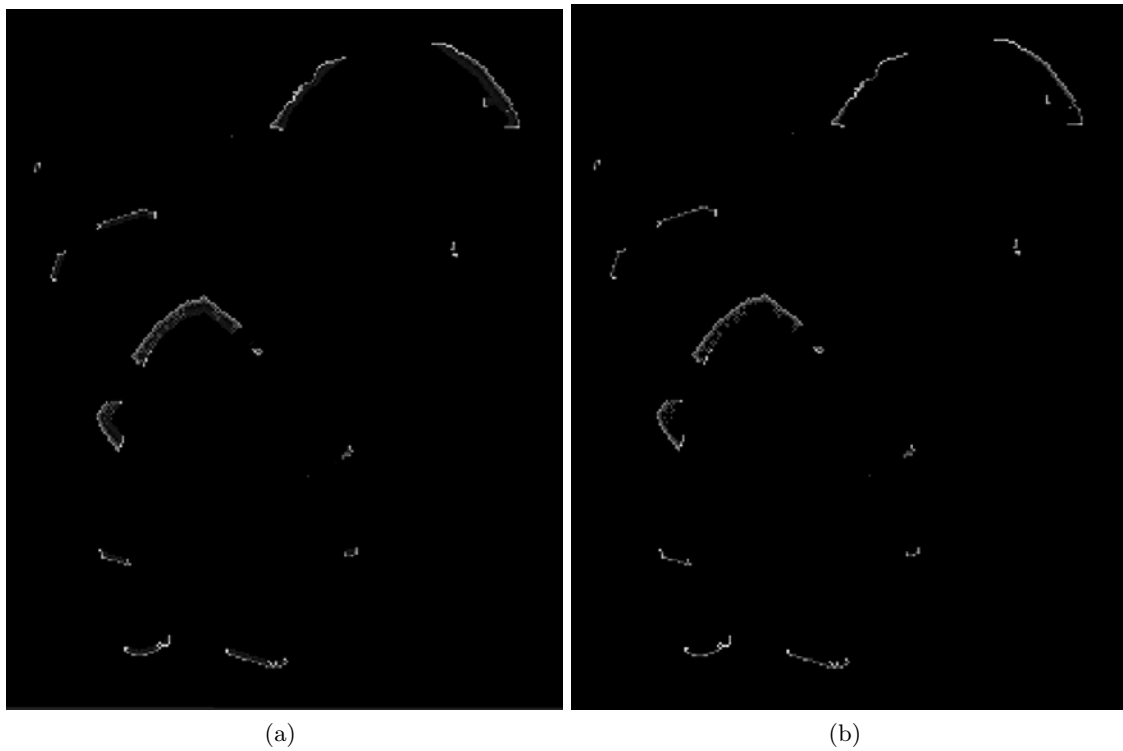


**Figure 11.14.** A cross-section through the atria is shown. Figure (a) displays the gradient for the voxel with positive transmembrane voltage. Figure (b) shows the same cross-section for the excitation pattern with gradients of a magnitude larger than 50 000.



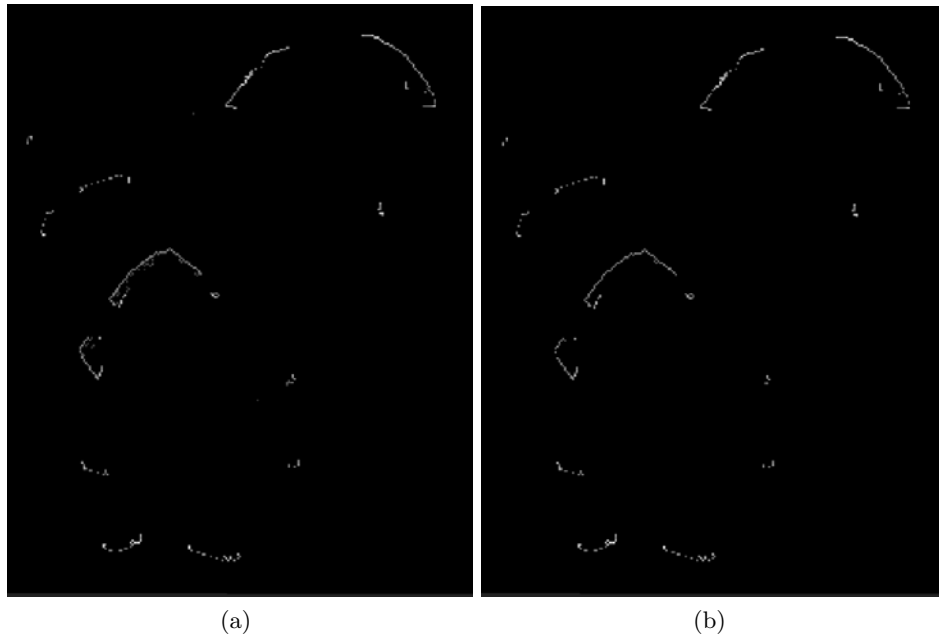


**Figure 11.15.** A cross-section through the atria is shown. This figure shows the same cross-section for the excitation pattern as in figure 11.14 with gradients of a magnitude larger than 70 000 (a) and 100 000 (b)

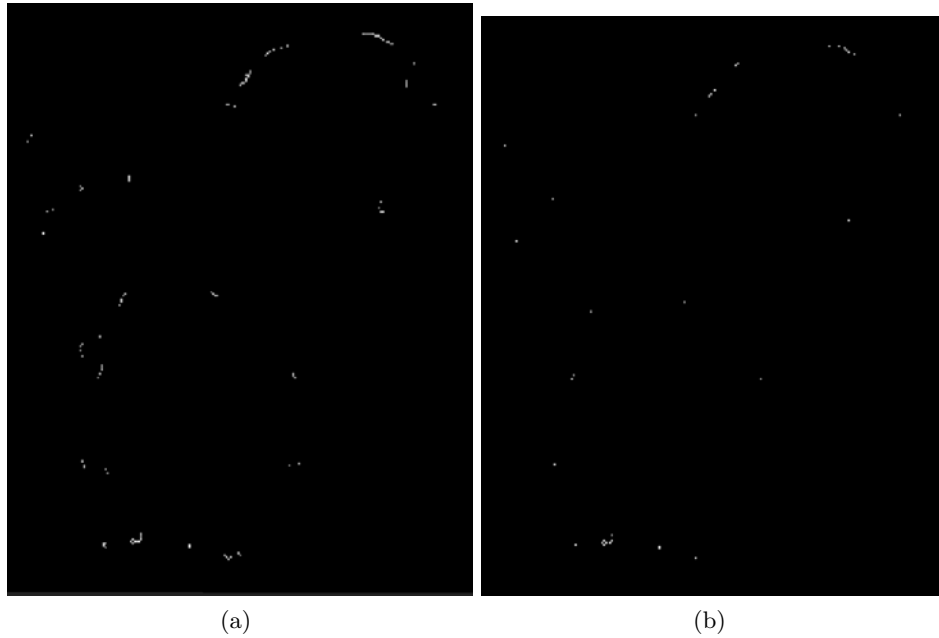


**Figure 11.16.** A cross-section through the atria is shown. This figure shows the same cross-section for the excitation pattern as in figure 11.14 with gradients of a magnitude larger than 150 000 (a) and 200 000 (b)

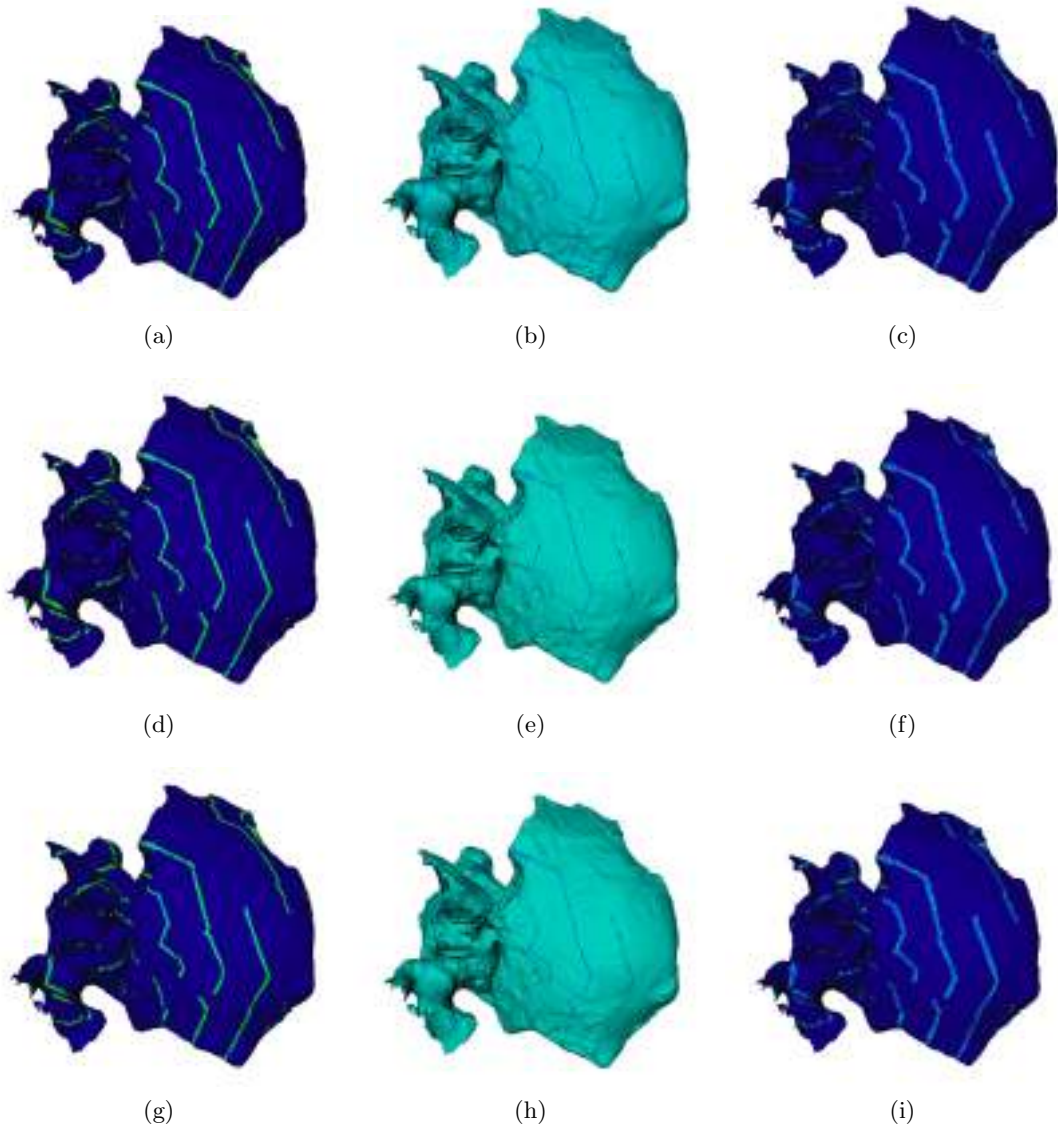


**Figure 11.17.** Based on the preprocessed gradient results of excitation pattern A, the divergence (middle column) and rotation (right column) operator were computed for thresholded gradients (left column) with thresholds 50 000 (top), 70 000 (middle) and 100 000 (bottom).

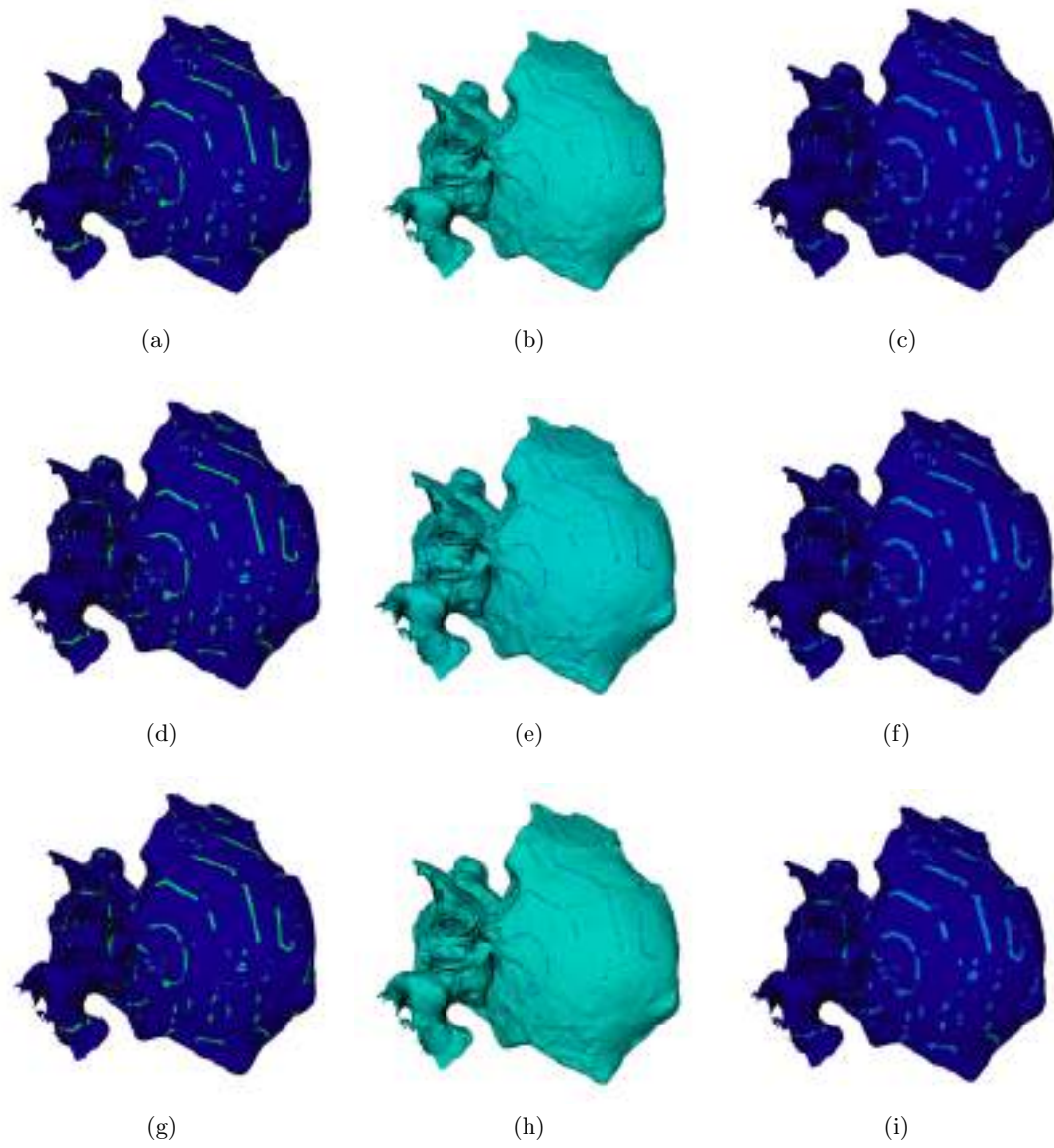


**Figure 11.18.** Based on the preprocessed gradient results of excitation pattern B, the divergence (middle column) and rotation (right column) operator were computed for thresholded gradients (left column) with thresholds 50 000 (top), 70 000 (middle) and 100 000 (bottom).

### 11.1.7.2 Classification by Positive Potential Method

Setting all positive transmembrane potentials to ‘1’ and all other potentials to ‘0’ captures the wave fronts as displayed in figure 11.19. The excitation fronts can be clearly distinguished. 1588 wave fronts were counted in the lattice of excitation pattern A and 4016 wave fronts in the lattice of excitation pattern B. Figure 11.20 shows the surface over the wave front volume. A linear relationship can be recognized for all wave fronts. While the points of excitation pattern A cluster around a single linear line, excitation pattern B shows a wider dispersion that indicates two cluster. However, a classification for wave fronts with a volume below 200 voxel does not show distinguishable cluster.

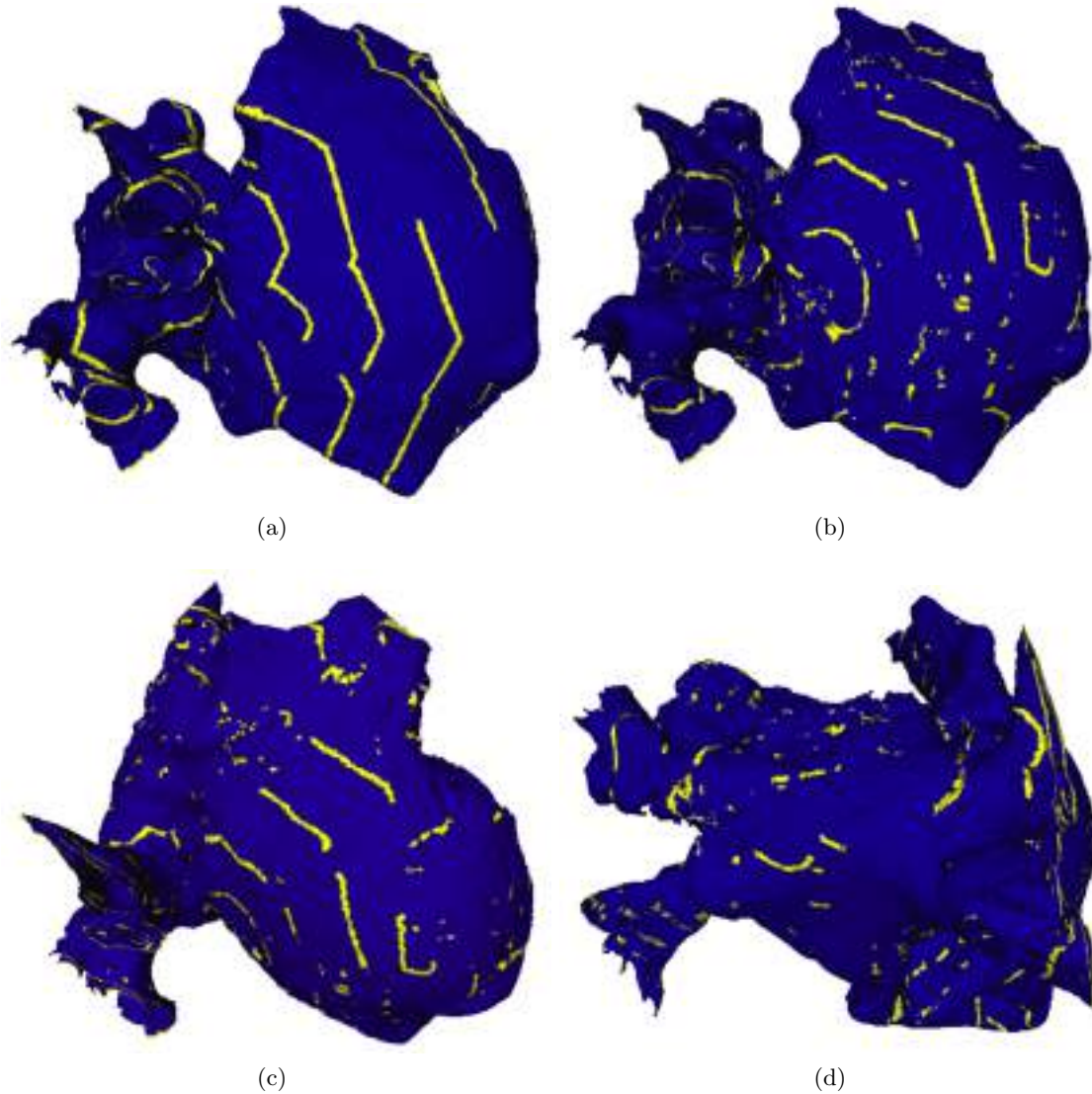
Looking at the right atrium only, excitation pattern A had 817 wave fronts; excitation pattern B 1646. Distinct clusters cannot be recognized, however, considering wave front volume and wave front surface. Therefore, local excitation patterns are investigated. Figure 11.21 shows wedge preparations including mainly broad wave fronts (wedge 1 - see fig. 11.21.a), a rotor and a wave front (wedge 2 - fig. 11.21.b), snakes (wedge 3 - fig. 11.21.c) and wavelets (wedge 4 - fig. 11.21.d). The virtual wedge preparations show that in each is a dominant excitation pattern class. However, in wedge 1, small wave fronts are present, in wedge 2, a rotor and a broad wave front and small fronts are visible, in wedge 3, the predominant excitation pattern class show snakes who are surrounded by larger wave fronts and in wedge 4 wavelets and larger wave fronts are present.

Table 11.2 summarizes the computed wave front count, volume, surface and front volume per tissue volume for each tissue wedge. 168 wave fronts were counted in wedge 1 which - normalized to the tissue volume - yields a value of 0.016. This value is higher in wedge 2 with 0.019. 223 wave fronts were counted in wedge 3 which yields a normalized value of 0.024. For wedge 4, the normalized wave front count is 0.017.

Wedge	Wave front count	Tissue Volume [ $mm^2$ ]	Wave Fronts/Volume
1 - Fronts	168	10403.22	0.016
2 - Rotor	158	8170.44	0.019
3 - Snakes	223	9433.46	0.024
4 - Wavelets	68	3974.52	0.017

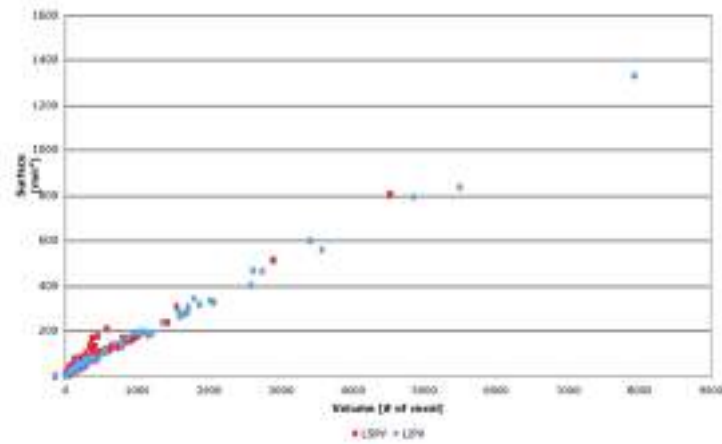
**Table 11.2.** This table shows the results of the detection of wave fronts in the virtual wedge preparations.

Looking at the individual wave front size normalized to the volume of the virtual wedge preparation yields the results displayed in figure 11.22. In wedge preparation 1, six wave fronts are above the threshold of 0.02, five wave fronts are above 0.01 and the rest is below 0.01. The largest wave front has a volume of 0.0870. Wedge 2 has only three wave fronts above 0.02 with a predominant wave front of normalized volume of 0.17. The other two only have a value of 0.08 and 0.06. In wedge 3, which is has predominantly snakes, six wave fronts reach a normalized volume of over 0.02. Three

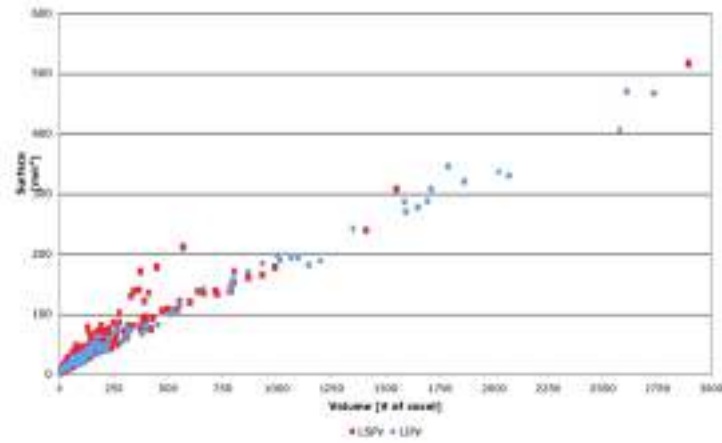


**Figure 11.19.** This figure shows the segmented wave fronts by means of the Positive Potential Method. (a) shows the result for excitation pattern A in right atrial epicardial view, (b) shows the results for excitation pattern B in the same view. (c) and (d) also display the results for excitation pattern B with a view onto the right atrial appendage (c) and the left atrium in a latero-dorsal view (d).

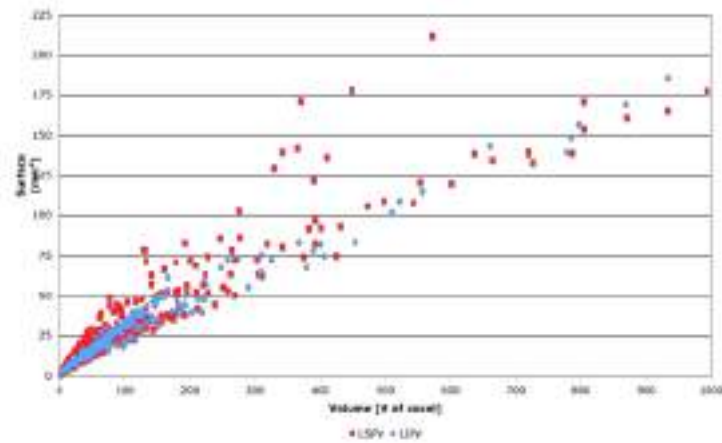
reach a value above 0.01. The other 214 wave fronts are below this value. Wedge preparation 4 has one wave front with a normalized volume of 0.07. Three have a value of 0.013, 0.016 and 0.011. The other 64 detected waves fall below 0.01.



(a)



(b)



(c)

**Figure 11.20.** Figure (a) - (c) display the same results with a different resolution. In blue are shown the wave fronts detected in excitation pattern A with respect to their surface over their volume. In red are shown the wave fronts detected in excitation pattern B with respect to their surface over their volume.

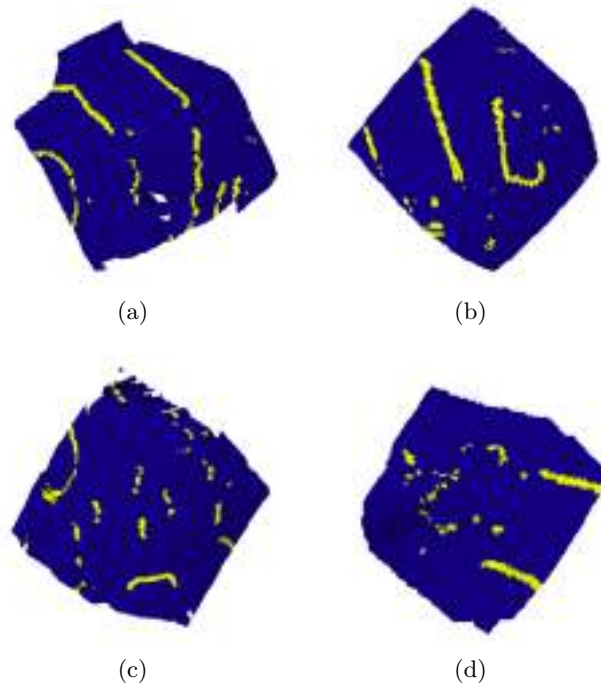


**Figure 11.21.** This figure shows the virtual wedge preparations from excitation pattern B to analyse (a) broad wave fronts (b) rotors (c) snakes and (d) wavelets.

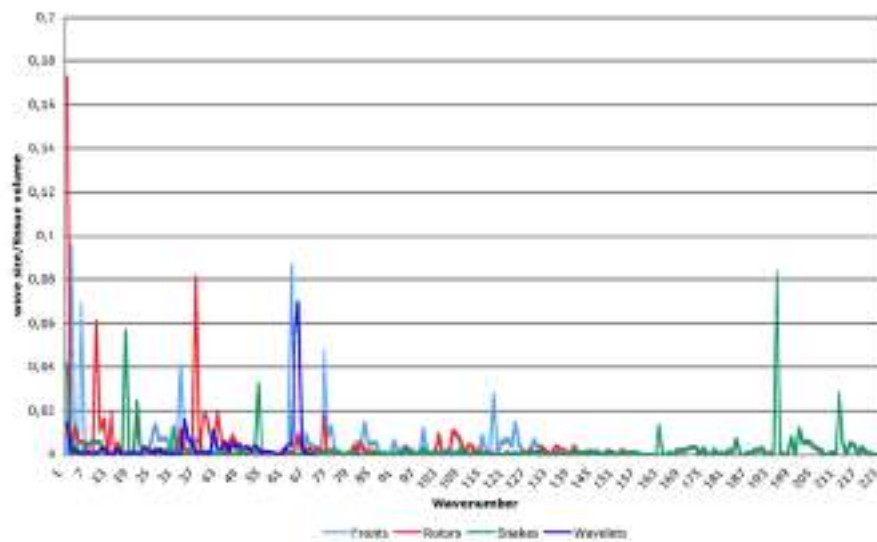


**Figure 11.22.** This graph displays the results of the relative volume of a detected wave front to the volume of the wedge preparation.



## 11.2 Simulation of Congestive Heart Failure

### 11.2.1 Simulation of Blockages in the Cardiac Conduction System

In both anatomical data-sets used in this work, the atrio-ventricular (AV) block III lead to a non-excitation of the ventricles. In the time simulated, no secondary or tertiary rhythm was triggered. Comparing the isochrones of the simulation of the sinus rhythm with the simulation of the AV block, the root mean square error  $E_{RMS}$  was 51.6 *ms* for the Visible Man data-set and 107.31 *ms* for the patient data-set. The  $E_{RMS}$  for the simulation of the left bundle branch block (LBBB) is almost a magnitude lower with 7.56 *ms* for the Visible Man data-set and 37.17 *ms* for the patient data-set. In both simulations, the right ventricle was excited physiologically and the left ventricle was then excited by the excitation wave front spreading from the right to the left ventricle.

### 11.2.2 Simulation of Ventricular Dyssynchrony

By reducing the interventricular conduction velocity, the  $E_{RMS}$  will not change for the simulation of the AV block III. However, for the LBBB simulations, the  $E_{RMS}$  increased to 11.27 *ms* and 17.7 *ms* for 80 % and 60 % of the physiologic conduction velocity, respectively, for the Visible Man data-set and to 51.89 *ms* and 66.01 *ms* in the patient data-set.



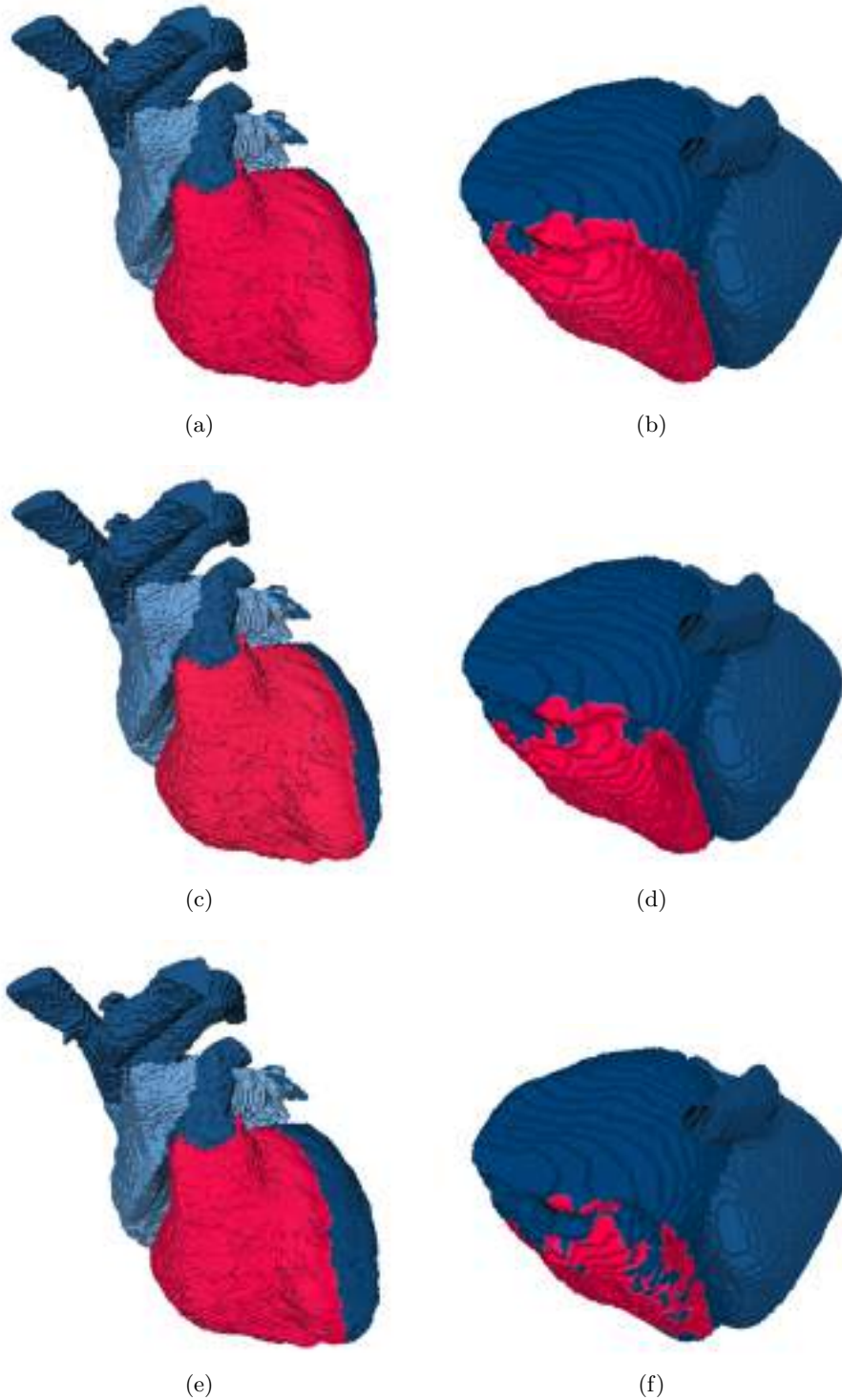


**Figure 11.23.** This figure shows the effect of reducing ventricular conduction velocity in a left bundle branch block: Visible Man data set at 250 *ms* (a) and patient data set at 350 *ms* (b) with 100 % conduction velocity, Visible Man data set at 250 *ms* (c) and patient data set at 350 *ms* (d) with 80 % conduction velocity, Visible Man data set at 250 *ms* (e) and patient data set at 350 *ms* (f) with 60 % conduction velocity. The red color indicates excited tissue. The anterior view is shown.



## Results: Therapy

*“Advice is judged by results, not by intentions.”*

Cicero

Roman author, orator and politician (106 BC - 43 BC)

### 12.1 Simulation of Ablation Therapy

Ten different ablation lesions were tested on 23 different ectopic foci that create AF if no therapy is applied:

- Kottkamp et al. 1999 [154] - “Seven ablation” - Linear ablation lesions, only (section 12.1.2).
- Pappone et al. 1999 [225] - Circumferential ablation lesions around each pulmonary vein (section 12.1.3).
- Melo et al. 1999 [180] - Circumferential ablation lesions around both left and right pulmonary veins (section 12.1.4).
- Benussi et al. 2000 [16] - Circumferential ablation with two additional linear lesions (section 12.1.5).
- Chen et al. 2005 [40] - Circumferential ablation of left and right pulmonary veins including separation of inferior and superior pulmonary vein (section 12.1.6).
- Pappone et al. 2005 [223] - Isolation of each pulmonary vein including two additional linear lesions (section 12.1.7).
- Pappone et al. 2004 [229] - Isolation of each pulmonary vein including three additional linear lesions (section 12.1.8).
- Ernst et al. 1999 [76] - Circumferential ablation lesion around all pulmonary veins including one additional linear lesion (section 12.1.9).
- Sueda et al. 1997 [273] - Circumferential ablation lesion around all pulmonary veins including two additional linear lesion (section 12.1.10).

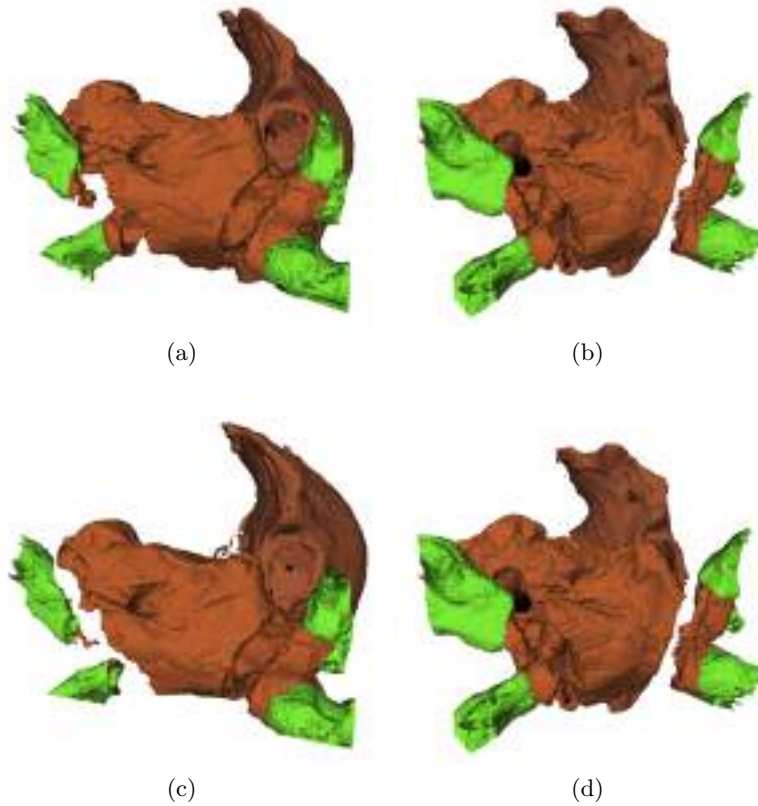


**Figure 12.1.** Different views on the left atrium show whether the lesions created around the pulmonary veins were not transmural (a) after the first procedure or whether they were transmural (b). A second procedure was carried out for all ablation strategies with transmural lesions (c - d).

- Cox et al. 2004 [47] - Circumferential ablation lesion of all pulmonary veins with additional lesions to the left orifice and the mitral annulus (section 12.1.11).

Transmurality of the lesions was not achieved for all lesions if the lines were drawn on the epicardial surface. Transmurality was achieved, however, by ablating the connecting tissue again (see figure 12.1). Thus, the ablation strategies were simulated twice on all 23 ectopic foci: Once with non-transmural lesions (hereafter referred to as the first 1<sup>st</sup> procedure) and once with complete transmural lesions (hereafter referred to as the second 2<sup>nd</sup> procedure) (see chapter 10.1).

The results of the overall 460 simulations is presented in table 12.1. The ablation strategy which encircles left and right PV each with two additional linear lesions to the mitral annulus and linking the PVs across the atrial roof (Benussi et al. 2000) shows the best result with 78.3 % success rate in the first procedure. The same circumferential lesions only (Melo et al. 1999), ie. without linear lesions, produce a smaller success rate with 73.9 %. If transmural lesions are ensured, however, these two approaches both yield a 100 % success rate.

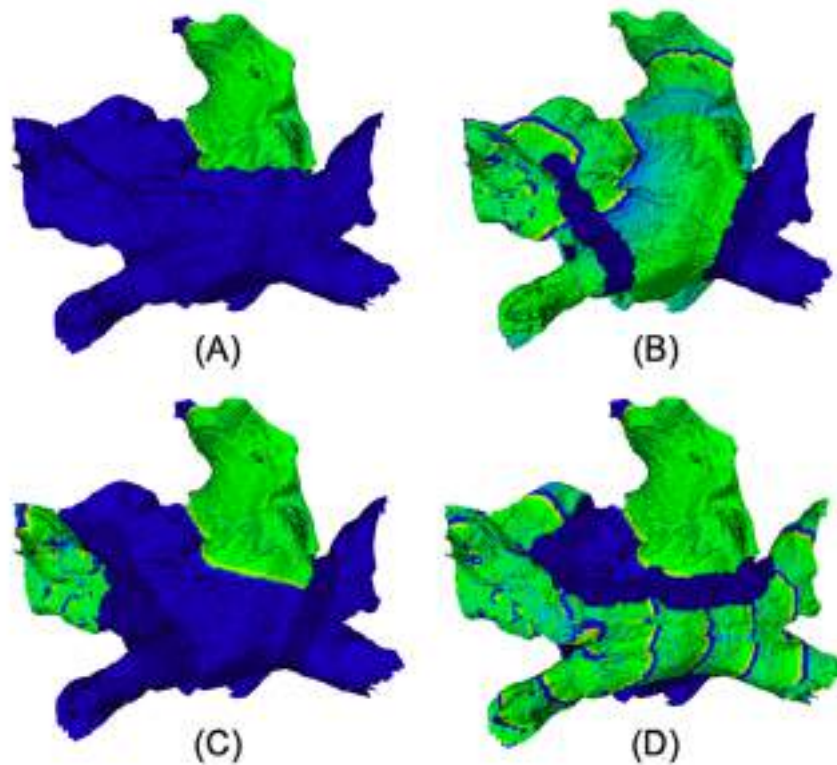


**Figure 12.2.** Summary of simulation of ablation strategies: Results of ablation strategies at 900 ms. The initial trigger was set at the left superior pulmonary vein. (A) The ablation strategy by Benussi et al. yielded the highest success rate in the first procedure with non-transmural lesions. The same ectopic trigger still caused fibrillatory conduction if the linear lesions were left out (B). If transmurality was achieved, the success rate was increased (C). However, fibrillation was observed in the isolated regions (C - D). The transmembrane voltage is shown. The dark lines on the atrial surface indicate the excitation wave fronts.

This can also be observed for the ablation strategies based on single PV isolation. While the first approach (Pappone et al. 1999) during the first procedure had a low success rate of 52.1 % only, the second approach (Chen et al. 2005) proved a higher success rate of 65.2 %. Moreover, if two additional linear lesions are included, one connecting the LIPV to the mitral annulus and one connecting both superior PVs (Pappone et al. 2005), the success rate is increased to 69.5 %. A further linear lesion on the atrial roof between the inferior PVs also yields a success rate of 73.9 %. The last three strategies all show a 100 % success rate when complete transmural lesions were achieved in a second procedure. A second procedure was not applicable to the single PVs approach since the lesions were completely transmural in the first place. An improvement of the strategy leads to the ablation lesions described in [40].

The ablation strategies based on one circumferential lesion show the lowest success rates for strategies where the PVs are isolated. If one (Ernst et al. 1999) or two (Sueda et al. 1997) linear lesions

Strategy	1st procedure Success rate in %	2nd procedure Success rate in %	Literatur Success rate in %
Kottkamp et al. 1999	17.4	n/a	67
Pappone et al. 1999	52.1	n/a	83
Melo et al. 1999	73.9	100	61
Benussi et al. 2000	78.3	100	49
Chen et al. 2005	65.2	100	80
Pappone et al. 2005	69.5	100	98.5
Pappone et al. 2004	73.9	100	96
Ernst et al. 1999	34.8	52.2	4
Sueda et al. 1997	34.8	47.8	34
Cox et al. 2004	56.5	100	97
Overall	50.86	87.5	66.95

**Table 12.1.** Results of ablation strategies. The first procedure indicates lesions set epicardially with a set tissue depth leading to non-transmural lesions at some positions. Transmurality was ensured in the second procedure.

are present linking the circumferential lesion to the mitral annulus at the left PVs, a success rate below 50 % is gained. The left atrial lesion set of the Cox procedure (Cox et al. 2004), where a lesion is included to the left orifice, yields a success rate of 56.5 %. Complete transmural only improves the success of the strategy in the latter case significantly. 100 % success rate is gained then for the latter case compared to 47.8 % (Sueda et al. 1997) and 52.2 % (Ernst et al. 1999) of the other two strategies. However, it was noticed that while the sinus rhythm was regained after the therapy, the areas within the circumferential lesions were fibrillating often. While the fibrillatory excitation only occurred in the respective PVs if each PV is isolated separately or if left and right PVs are isolated separately, the whole of the left atrium seems to be fibrillating if only one circumferential lesion around all PVs is included in the ablation strategy.

The least successful result is shown for the case where linear lesions only make up the ablation lesion set (Kottkamp et al. 1999). With only 17.4 % in the first procedure, a second procedure with transmural lesions was not thought to improve the results significantly if at all.

### 12.1.1 Simulation Results vs. Clinical Studies

Some of the success rates reported in clinical studies show different results than the computer simulations. While Kottkamp et al. report a success rate of close to 70 % for the strategy with linear lesions only, the computer simulations do not even exceed 20 %. Pappone et al. report in their respective studies success rates that are around 30 % higher than the first procedure in the computer simulations. However, if complete transmural is included in the computer simulations, they prove highest success rates not achieved clinically. The strategies based on the Cox-Maze III procedure have a far smaller success rate compared with the computer simulations apart from the

studies carried out by the Cox group itself.

The following sections illustrate the results of each ablation strategy in detail.

### 12.1.2 Simulation of Linear Ablation Lesions

The success rate of preventing AF using the ablation strategy presented by Kottkamp et al [154], which is based on linear lesions only (see figure 12.3), showed the lowest success. The lesions did not isolate the ectopic foci which then were able to excite the whole atrium. Thus, rotor waves were generated, which lead to AF. The typical break-up of wave fronts, chaotic excitation and different excitation pattern were recognised (see figure 12.4). However, in four of the 23 ectopic foci set-ups, the therapy lead to a re-establishment of the sinus rhythm. This was caused by the ablation lesion running right through the ectopic focus (see figure 12.4). Thus, the rotor wave could not be fully established and the ectopic activity did not lead to AF. In the four successful cases, the ectopic focus was situated almost on the left atrial wall rather than in the pulmonary veins. The successful therapy was gained in three of four cases at the left inferior pulmonary vein, where the lesion extended further the pulmonary vein to the mitral annulus. Only one ectopic focus at the right inferior pulmonary vein could be prevented to induce AF. All ectopic foci situated at the superior PVs induced AF (see table 12.2). The success of the ablation using linear lesions only is not based on the assumption that AF is prevented by isolating the triggering focus. There is ongoing research of the influence of the autonomic nervous system and the ganglia [257]. The hypothesis is that an ablation of the regions around the ganglionated plexi will also lead to a high success rate in preventing AF. So far, the clinical reports show that the success rate for RF ablation of paroxysmal AF can be above 90 % [257]. The linear lesion strategy presented here would lead across the ganglia. Since the behaviour and the influence of the latter on AF is not included in this model, a second procedure with transmural lesions was not carried out.

Location of the ectopic focus	Sustained AF	Success
LSPV proximal	6	0
LSPV distal	4	0
RSPV	5	0
LIPV	1	3
RIPV	3	1
overall	19	4

**Table 12.2.** Sustained atrial fibrillation and successful therapy after the first procedure of the linear ablation lesion strategy only reported by Kottkamp et al. [154]. A second procedure was not carried out.

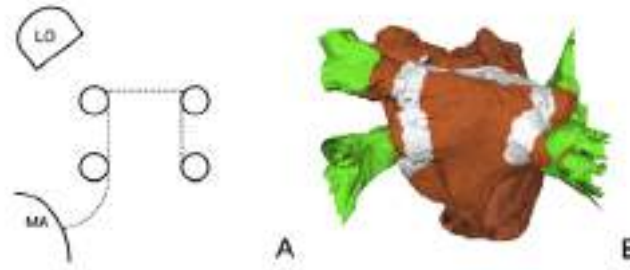


**Figure 12.3.** This figure illustrates the transfer of the schematic description of the linear ablation strategy (A) onto the anatomical model (B). A: The epicardial view shows the left orifice (LO) at the top behind the left superior pulmonary vein. At the bottom left, the mitral annulus (MA) is shown. The pulmonary veins (PVs) are indicated by the circles with the right PVs on the right side. The dotted lines indicate the ablation lesion. B: The latero-dorsal view of the left atrium shows the pulmonary veins in yellow, the cardiac tissue in brown and the created lesion in white.

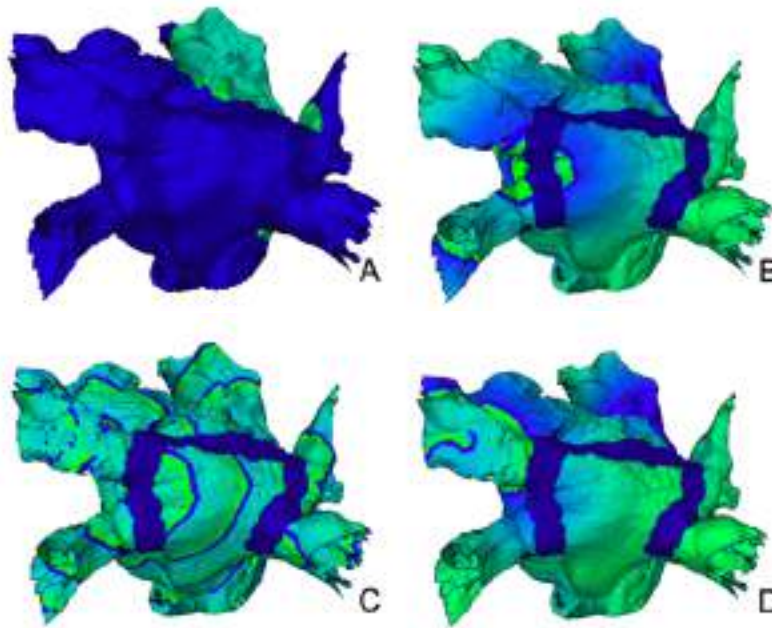


**Figure 12.4.** The ablation strategy described by Kottkamp et al. [154] showed successful mostly at the left inferior pulmonary vein. However, only in four out of 23 simulations, atrial fibrillation was prevented (A). The success was achieved when the ablation lesion was set onto the ectopic focus (B). Otherwise (D) the atria were fibrillating after 900 *ms* if the ectopic focus was not infringed by the lesion (C). The transmembrane voltage at (A) 900 *ms*, (B) 240 *ms*, (C) 900 *ms* and (D) 240 *ms* is shown. The narrow dark lines on the atrial surface indicate the excitation wave fronts. The broad dark lines indicate no electrical activity, i. e. the location of the ablation lesions.



### 12.1.3 Simulation of Circumferential Ablation Lesions around each Pulmonary Vein

The circumferential ablation strategy carried out by Pappone et al. in 1999 [225] produced a success rate of 52.1 %, i. e. AF was prevented in 12 out of 22 simulations after the first procedure (see table 12.3). The main mechanism behind the success was that the ablation lesion was set on top of the ectopic focus. The ablation lesions were placed in the pulmonary veins, hardly touching myocardial tissue, thus, changing the course of excitation propagation for the most part of the ectopic foci whose excitation of the atria did not lead to re-entrant waves and AF. No re-entrant waves or fibrillatory excitation was observed in the isolated PVs. It can be noted that the circumferential lesion at the LSPV was least successful in isolating the ectopic foci (see table 12.3) while the lesion around the RSPV prevented four of five ectopic foci to induce AF. The lesions of this approach were transmural in the beginning so that no second procedure had to be carried out. An improvement on this approach would be only gained if the lesions were set closer to the ostia which then leads to the procedure described by Chen et al. as described below (see section 12.12).

Location of the ectopic focus	Sustained AF	Success
LSPV proximal	5	1
LSPV distal	2	2
RSPV	1	4
LIPV	2	2
RIPV	1	3
overall	11	12

**Table 12.3.** Sustained atrial fibrillation and successful therapy after the first procedure of the circumferential ablation of each pulmonary vein strategy reported by Pappone et al. 1999 [225]. The lesions were all transmural in the first procedure and therefore, a second procedure was not carried out.

### 12.1.4 Simulation of Circumferential Ablation Lesions around both Left and Right Pulmonary Veins

The lesions encircling each side of the pulmonary veins, i. e. one lesion around both left PVs and one isolating the right PVs, were set at the PV ostium (see figure 12.7). The success rate of suppressing AF initiation by isolating the ectopic focus was with 17 out of 23 the second best result compared with the other ablation strategies. The right pulmonary veins were completely isolated in the first procedure and no ectopic focus caused AF. The lesions at the left pulmonary veins were not completely transmural after the first procedure. Thus, the ectopic foci could trigger an excitation that spread across the atria which caused AF in six of twelve cases (see figure 12.8). Especially the triggers deeper inside the pulmonary veins created a chaotic excitation pattern (see table 12.4).

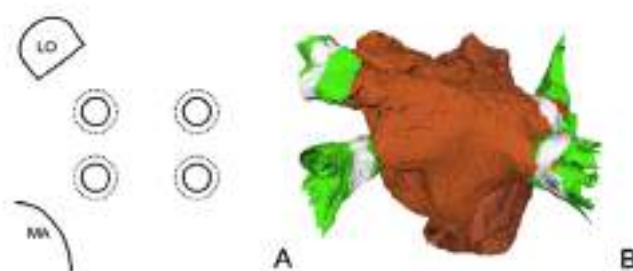


**Figure 12.5.** This figure illustrates the transfer of the schematic description of the ablation strategy with four single circumferential lesions (A) onto the anatomical model (B). A: The epicardial view shows the left orifice (LO) at the top behind the left superior pulmonary vein. At the bottom left, the mitral annulus (MA) is shown. The pulmonary veins (PVs) are indicated by the circles with the right PVs on the right side. The dotted lines indicate the ablation lesion. B: The latero-dorsal view of the left atrium shows the pulmonary veins in yellow, the cardiac tissue in brown and the created lesion in white.

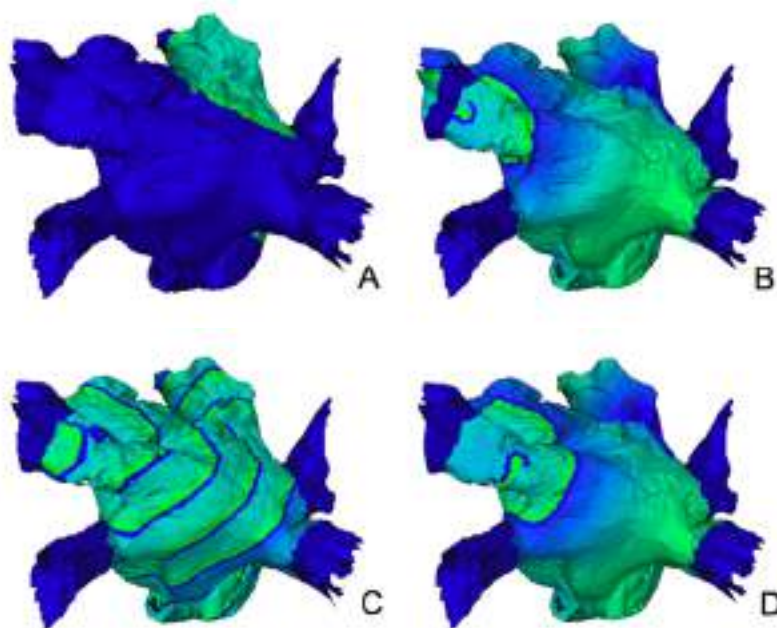


**Figure 12.6.** Exemplary results of the circumferential ablation strategy described by Pappone et al. 1999 [225]: (A) demonstrates the successful prevention of atrial fibrillation provoked by an ectopic beat at the left superior pulmonary vein. The ablation lesions, however, were also leading across the position of the ectopic beat (here at the distal part of the left superior pulmonary vein) which suppressed the generation of the initial rotor (B). But atrial fibrillation occurred in almost 50 % of cases (C) because the ectopic focus was situated closer, i. e. proximal, to the atrial roof (D) and thus was not isolated by the lesions. The transmembrane voltage at (A) 900 ms, (B) 240 ms, (C) 900 ms and (D) 240 ms is shown. The narrow dark lines on the atrial surface indicate the excitation wave fronts. The broad dark lines indicate no electrical activity, i. e. the location of the ablation lesions.

Checking for transmuralty and carrying out a second procedure to ensure disconnection of the pulmonary veins, lead to a 100 % success rate at preventing AF. Fibrillation in the isolated pulmonary veins could be observed (see figure 12.8). In these cases, stable re-entrant wave fronts as well as chaotic excitation occurred in the PVs.

Location of the ectopic focus	Sustained AF	Success
LSPV proximal	1	5
LSPV distal	3	1
RSPV	0	5
LIPV	2	2
RIPV	0	4
overall	6	17

**Table 12.4.** Sustained atrial fibrillation and successful therapy after the first procedure of the circumferential ablation strategy reported by Melo et al. [180]. The second procedure with complete transmural lesions lead to a prevention of atrial fibrillation in all simulations.

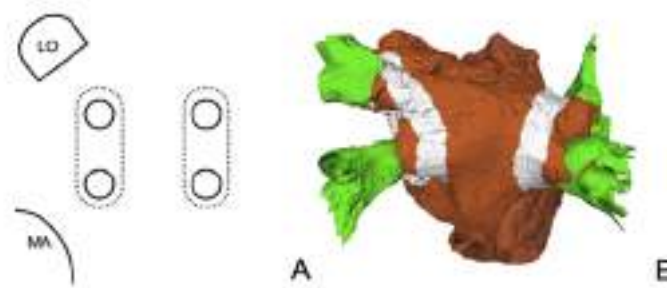


**Figure 12.7.** This figure illustrates the transfer of the schematic description of the ablation strategy with two single circumferential lesions (A) onto the anatomical model (B). A: The epicardial view shows the left orifice (LO) at the top behind the left superior pulmonary vein. At the bottom left, the mitral annulus (MA) is shown. The pulmonary veins (PVs) are indicated by the circles with the right PVs on the right side. The dotted lines indicate the ablation lesion. B: The latero-dorsal view of the left atrium shows the pulmonary veins in yellow, the cardiac tissue in brown and the created lesion in white.

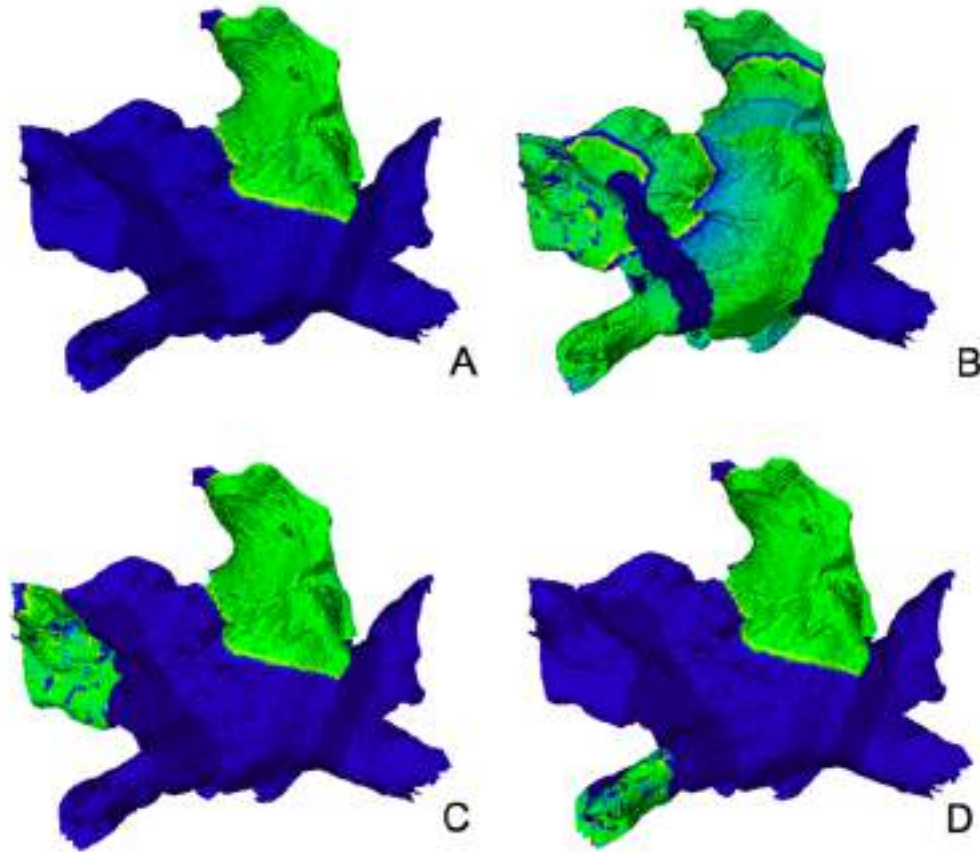


**Figure 12.8.** Exemplary results of the circumferential ablation strategy described by Melo et al. 1999 [180]: (A) demonstrates the successful prevention of atrial fibrillation provoked by an ectopic beat at the distal part of the left superior pulmonary vein. Fibrillation in the pulmonary veins caused atrial fibrillation in the atria if the ablation lesion was not transmural (B) Here, the stimulus was set at the left superior pulmonary vein close to the atrial roof. The same ectopic beat was prevented to cause atrial fibrillation, if the ablation lines were transmural (C). Fibrillation in the pulmonary veins was observed in some simulations while sinus rhythm was achieved in others (C - D). The transmembrane voltage at 900 *ms* is shown. The narrow dark lines on the atrial surface indicate the excitation wave fronts. The broad dark lines indicate no electrical activity, i. e. the location of the ablation lesions.

#### 12.1.5 Simulation of Circumferential Ablation with Two Additional Linear Lesions

Including two extra linear lesions to the circumferential ablation of both left and right pulmonary veins as carried out by Benussi et al. in 2000 [16] showed the highest success rate in the simulations with respect to the first procedure. The posterior line on the left atrial roof and the line to the mitral annulus (see figure 12.9) prevented that the chaotic excitation propagation triggered from deep inside the left superior pulmonary vein was maintained in two of four set-ups for the ectopic focus (see table 12.5). Otherwise, the results were similar to the results of the circumferential

ablation of each side of the PVs (see section 12.1.4). The right pulmonary veins were isolated completely and fibrillatory excitation could be observed in the isolated parts (see figure 12.10). Also, after complete transmuralty of the lesions was achieved in the second procedure, the success rate of the ablation strategy yielded 100 %.

Location of the ectopic focus	Sustained AF	Success
LSPV proximal	1	5
LSPV distal	2	2
RSPV	0	5
LIPV	2	2
RIPV	0	4
overall	5	18

**Table 12.5.** Sustained atrial fibrillation and successful therapy after the first procedure of the circumferential ablation with two additional linear lesions reported by Benussi et al. [16]. The second procedure with complete transmural lesions lead to a prevention of atrial fibrillation in all simulations.

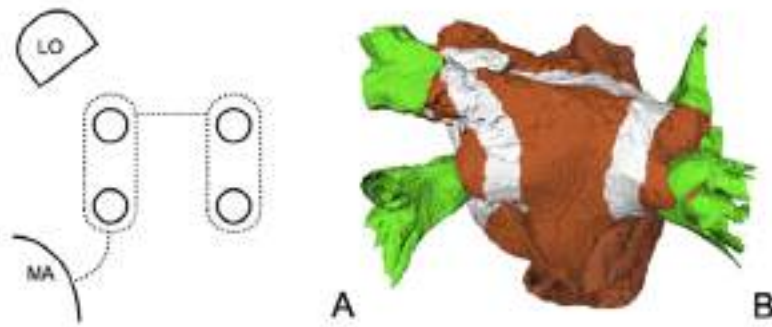


**Figure 12.9.** This figure illustrates the transfer of the schematic description of the ablation strategy with two circumferential lesions and two linear lesions at the atrial roof and to the mitral annulus (A) onto the anatomical model (B). A: The epicardial view shows the left orifice (LO) at the top behind the left superior pulmonary vein. At the bottom left, the mitral annulus (MA) is shown. The pulmonary veins (PVs) are indicated by the circles with the right PVs on the right side. The dotted lines indicate the ablation lesion. B: The latero-dorsal view of the left atrium shows the pulmonary veins in yellow, the cardiac tissue in brown and the created lesion in white.

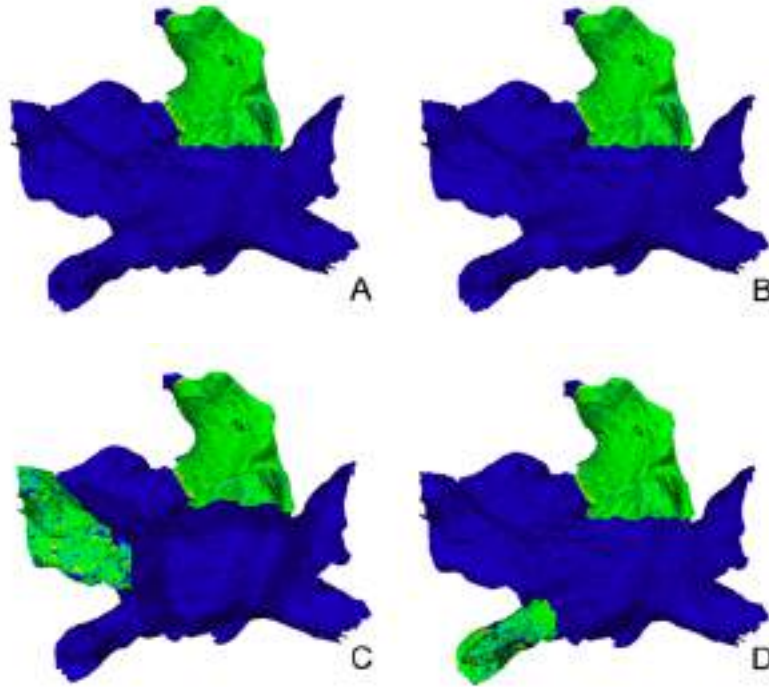


**Figure 12.10.** Exemplary results of the circumferential ablation strategy described by Benussi et al. [16]: (A) demonstrates the successful prevention of atrial fibrillation provoked by an ectopic beat at the distal part of the left superior pulmonary vein. The additional linear lesion lead to a higher success rate than the circumferential ablation strategy. Figure B shows the same simulation set-up as in figure 12.8 B. Here, however, sinus rhythm was established and atrial fibrillation was prevented. With transmural lesions, the result of both ablation strategies is similar (C - D): Fibrillation in the isolated pulmonary veins was observed. The transmembrane voltage at 900 ms is shown. The narrow dark lines on the atrial surface indicate the excitation wave fronts. The broad dark lines indicate no electrical activity, i. e. the location of the ablation lesions.

#### 12.1.6 Simulation of Circumferential Ablation of Left and Right Pulmonary Veins Including Separation of Inferior and Superior Pulmonary Veins

By setting the lesions closer to the left atrial myocardium in the single PV ablation procedure (see section 12.1.3) automatically leads to an overlap of lesions set around the superior and inferior PVs. Thus, this procedure can be carried out by simply encircling both pulmonary veins as shown in section 12.1.4 and adding one linear lesion each between the pulmonary vein spitting the circumferential lesion in two parts (see figure 12.11). The success of this strategy was marked with 15 out of 23 simulations (65.2 %). The second procedure yielded 100 % success. However, a non-transmural lesion at the left pulmonary veins still caused AF in eight of 14 cases (see table 12.6), which is higher than the circumferential ablation strategy without additional lesions separating the superior and inferior PVs. The simulations where the ablation strategy failed to suppress AF show

different excitation patterns: While stable wave fronts dominated the excitation of the atria due to re-entries in some cases, chaotic fibrillation could be observed in the supposedly isolated parts. Hence, the atria were still excited by the ectopic activity. The chaotic excitation pattern in the pulmonary veins did not spread across the lesions though, but caused stable wave fronts in the atria (see figure 12.12). The successful isolation due to complete transmural lesions lead to the re-installment of the sinus rhythm with occasional fibrillation in the isolated parts (see figure 12.12).

Location of the ectopic focus	Sustained AF	Success
LSPV proximal	2	4
LSPV distal	3	1
RSPV	0	5
LIPV	3	1
RIPV	0	4
overall	8	15

**Table 12.6.** Sustained atrial fibrillation and successful therapy after the first procedure of the circumferential ablation strategy described by Chen et al. [40]. The second procedure with complete transmural lesions lead to a prevention of atrial fibrillation in all simulations.

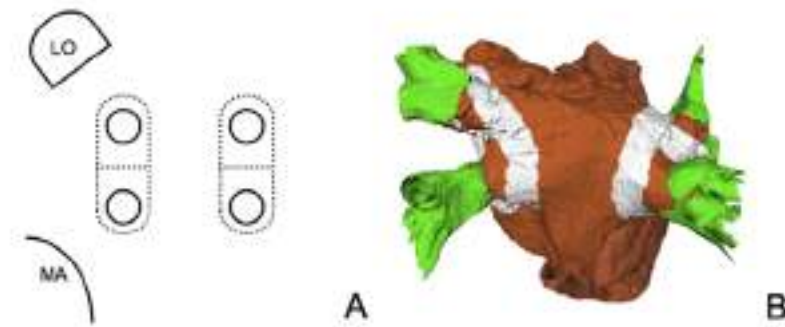


**Figure 12.11.** This figure illustrates the transfer of the schematic description of the ablation strategy with two circumferential lesions and a separate isolation of the inferior and superior pulmonary veins (A) onto the anatomical model (B). A: The epicardial view shows the left orifice (LO) at the top behind the left superior pulmonary vein. At the bottom left, the mitral annulus (MA) is shown. The pulmonary veins (PVs) are indicated by the circles with the right PVs on the right side. The dotted lines indicate the ablation lesion. B: The latero-dorsal view of the left atrium shows the pulmonary veins in yellow, the cardiac tissue in brown and the created lesion in white.



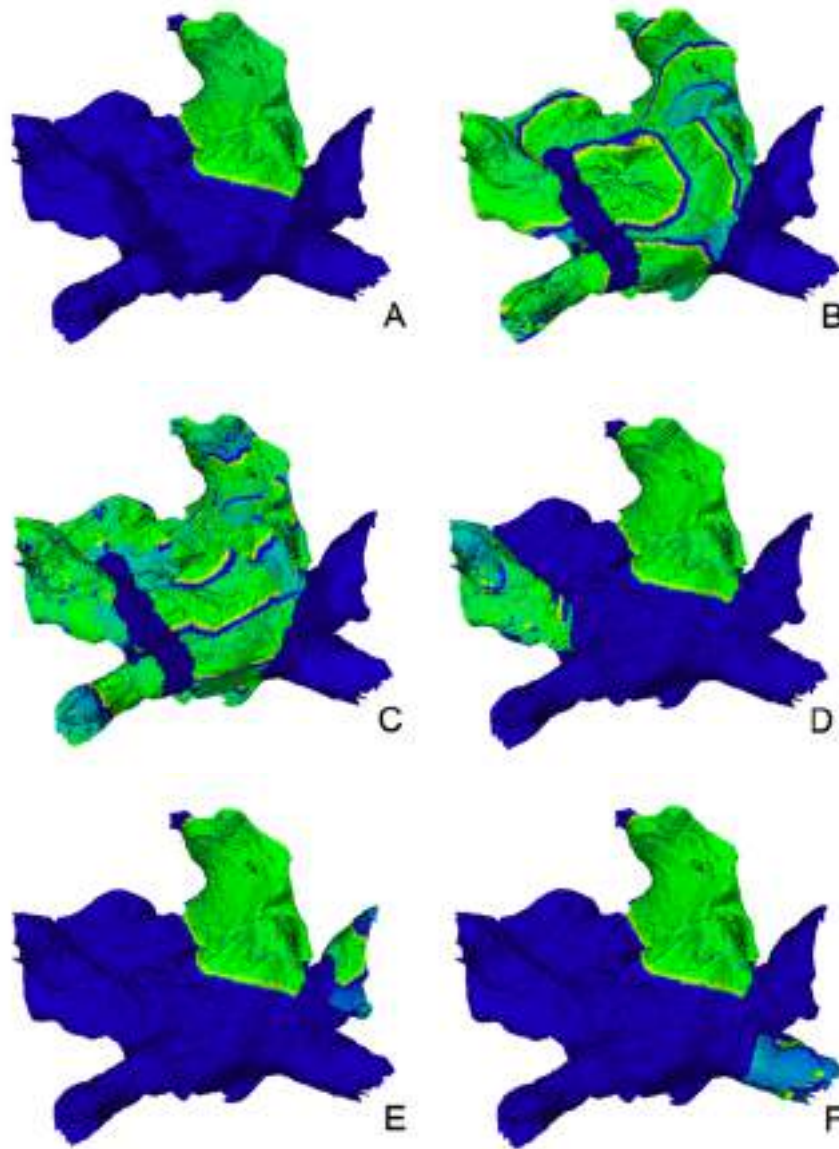


**Figure 12.12.** Exemplary results of the circumferential ablation strategy described by Chen et al. [40]: (A) demonstrates the successful prevention of atrial fibrillation provoked by an ectopic beat at the left inferior pulmonary vein. In this case, the second stimulus of the ectopic beat was situated ostially. The same position of this ectopic focus caused fibrillation if the second stimulus was placed closer to the pulmonary vein (B). The additional isolation of the inferior and superior pulmonary vein did not lead to an improvement in the success rate compared to the simpler circumferential ablation strategy (C). However, transmural lesions also lead to a 100 % success rate in all simulations (D). Fibrillation in the isolated pulmonary veins was observed as in other ablation strategies (E - F). The transmembrane voltage at 900 *ms* is shown. The narrow dark lines on the atrial surface indicate the excitation wave fronts. The broad dark lines indicate no electrical activity, i. e. the location of the ablation lesions.



### 12.1.7 Simulation of Isolation of Each Pulmonary Vein Including Two Additional Linear Lesions

The procedure carried out by Pappone et al. in 2005 [223] included circumferential and linear lesions as well as PV separating lesions (see figure 12.13). With the additional linear lesions, a higher success rate was achieved compared with the same lesion set excluding the atrial roof and mitral annulus lesion. The incomplete lesion at the left pulmonary veins, however, did not isolate them completely, leading to AF. As described before in sections 12.1.4 - 12.1.5, the ectopic foci situated at the distal part of the left superior pulmonary vein were able to create rotor waves that sustain, which in turn causes fibrillatory excitation of the atria. Transmural lesions isolated the ectopic foci in 100 % of simulations. Here, chaotic excitation in the isolated parts was observed as well (see figure 12.14).

Location of the ectopic focus	Sustained AF	Success
LSPV proximal	2	4
LSPV distal	3	1
RSPV	0	5
LIPV	2	2
RIPV	0	4
overall	7	16

**Table 12.7.** Sustained atrial fibrillation and successful therapy after the first procedure of the linear ablation lesion strategy only reported by Pappone et al. 2005 [223]. The second procedure with complete transmural lesions lead to a prevention of atrial fibrillation in all simulations.

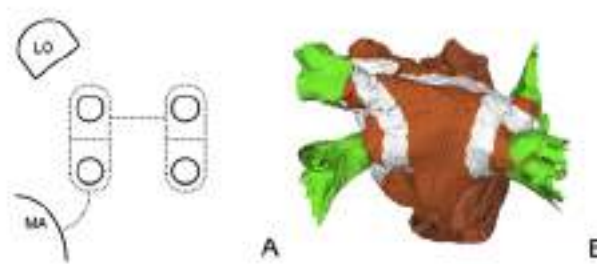


**Figure 12.13.** This figure illustrates the transfer of the schematic description of the ablation strategy of isolating each pulmonary vein with additional atrial roof lesion and a lesion to the mitral annulus (A) onto the anatomical model (B). A: The epicardial view shows the left orifice (LO) at the top behind the left superior pulmonary vein. At the bottom left, the mitral annulus (MA) is shown. The pulmonary veins (PVs) are indicated by the circles with the right PVs on the right side. The dotted lines indicate the ablation lesion. B: The latero-dorsal view of the left atrium shows the pulmonary veins in yellow, the cardiac tissue in brown and the created lesion in white.

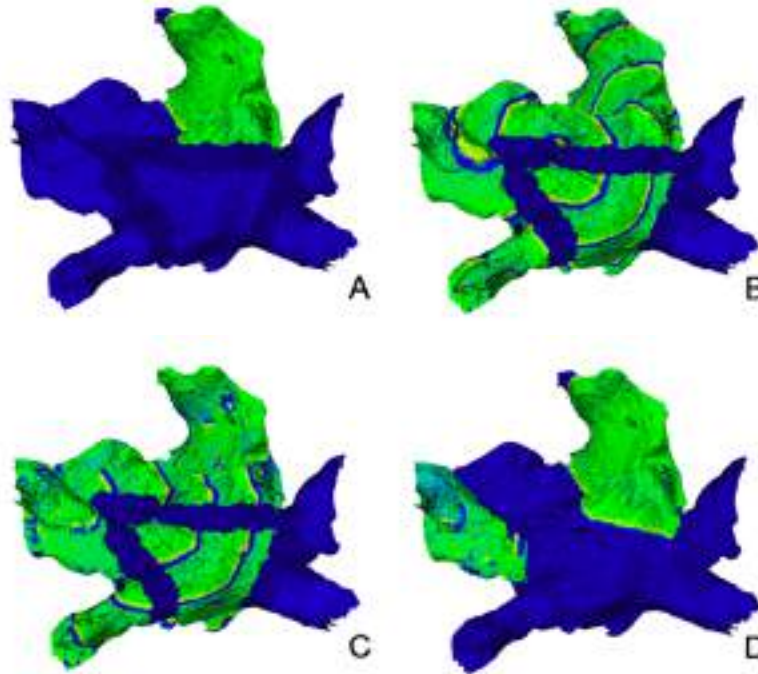


**Figure 12.14.** Exemplary results of the circumferential ablation strategy described by Pappone et al. 2005 [223]: (A) demonstrates the successful prevention of atrial fibrillation provoked by an ectopic beat at the the right superior pulmonary vein. Figures B and C demonstrate that the additional isolation of the inferior and superior pulmonary vein did not lead to an improvement in the success rate compared to the simpler circumferential ablation strategy (compare figure 12.10). Fibrillation in the isolated pulmonary veins was observed as in other ablation strategies (D). The transmembrane voltage at 900 *ms* is shown. The narrow dark lines on the atrial surface indicate the excitation wave fronts. The broad dark lines indicate no electrical activity, i. e. the location of the ablation lesions.

### 12.1.8 Simulation of Isolation of Each Pulmonary Vein Including Three Additional Linear Lesions

If three linear lesions are placed to connect the left inferior PVs, the superior PVs and the left inferior PV to the mitral annulus (see figure 12.15), the success rate can be augmented. AF triggered in the left superior pulmonary vein is prevented in six of ten different set-ups (see table 12.8). Otherwise, the results are similar to the previously described ablation strategies (see section 12.1.7).

Location of the ectopic focus	Sustained AF	Success
LSPV proximal	2	4
LSPV distal	2	2
RSPV	0	5
LIPV	2	2
RIPV	0	4
overall	6	17

**Table 12.8.** Sustained atrial fibrillation and successful therapy after the first procedure of the linear ablation lesion strategy only reported by Pappone et al. 2004 [224]. The second procedure with complete transmural lesions lead to a prevention of atrial fibrillation in all simulations.

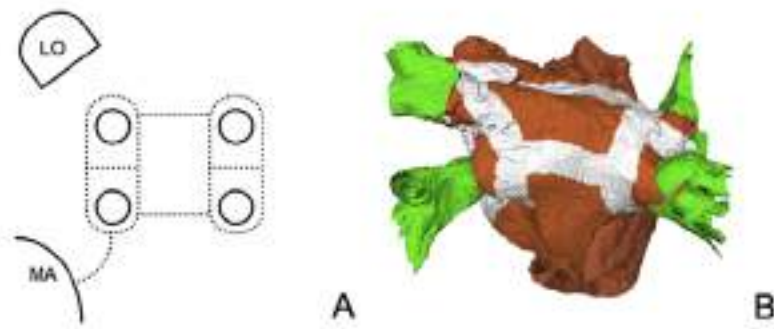


**Figure 12.15.** This figure illustrates the transfer of the schematic description of the ablation strategy of isolating each pulmonary vein with two additional atrial roof lesion and a lesion to the mitral annulus (A) onto the anatomical model (B). A: The epicardial view shows the left orifice (LO) at the top behind the left superior pulmonary vein. At the bottom left, the mitral annulus (MA) is shown. The pulmonary veins (PVs) are indicated by the circles with the right PVs on the right side. The dotted lines indicate the ablation lesion. B: The latero-dorsal view of the left atrium shows the pulmonary veins in yellow, the cardiac tissue in brown and the created lesion in white.

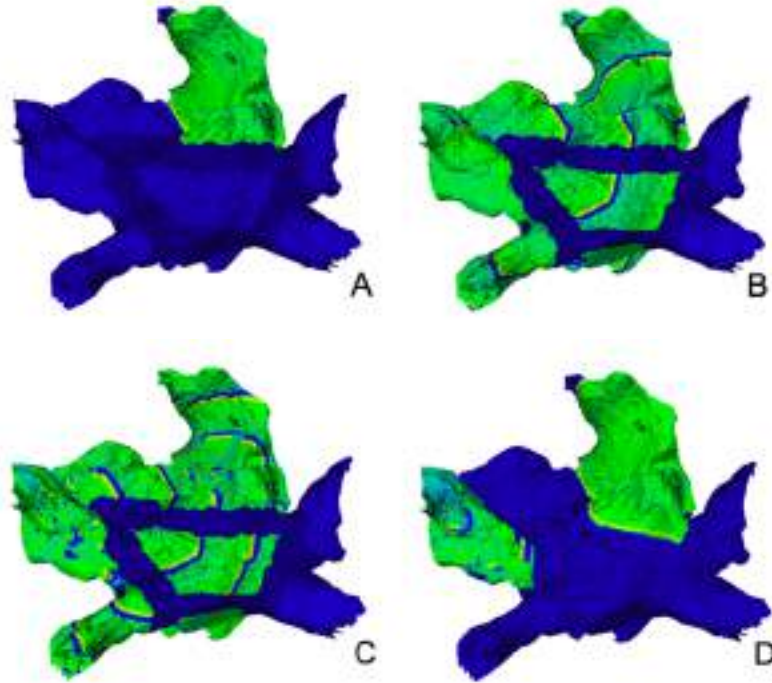


**Figure 12.16.** Exemplary results of the circumferential ablation strategy described by Pappone et al. 2004 [224]: (A) demonstrates the successful prevention of atrial fibrillation provoked by an ectopic beat at the right superior pulmonary vein. Figures B and C demonstrate that the additional isolation of the inferior and superior pulmonary vein did not lead to an improvement in the success rate compared to the simpler circumferential ablation strategy (compare figure 12.10). The additional third linear lesion did only improve the success rate by one simulation compared to the same procedure with only one lesion on the atrial roof. Fibrillation in the isolated pulmonary veins was observed as in other ablation strategies (D). The transmembrane voltage at 900 *ms* is shown. The narrow dark lines on the atrial surface indicate the excitation wave fronts. The broad dark lines indicate no electrical activity, i. e. the location of the ablation lesions.

### 12.1.9 Simulation of Circumferential Ablation Lesion around All Pulmonary Veins Including One Additional Linear Lesion

The success rates of the ablation strategy, which includes one single circumferential lesion (see figure 12.17), is lower than the other strategies that use two or four circumferential lesions (see table 12.1). Especially the ectopic foci at the right pulmonary veins are not isolated as well as if two circumferential lesions around the left and right PVs, respectively, were used (see table 12.17). Sinus rhythm was established in eleven of 23 different simulation set-ups in the first procedure. Ensuring transmuralty in the second procedure, the success rate was increased by one further successful simulation at the right inferior PV. On the left atrial roof, excitation patterns like rotors, multiple wavelets and the break-up of wave fronts leading to the streak-like excitation of the atria is observed (see figure 12.18). The transmuralty of lesions does not guarantee 100 % success in this lesion set up.

The excitation pattern is changed however, often showing an increased wavelength in the excitation propagation. The excitation is sustained by macro re-entrant circuits (see figure 12.18). It can be observed that the initiation of the chaotic excitation is located in the area of the left pulmonary veins even if the ectopic focus was situated at the right pulmonary veins (see figure 12.18 (C) - (D)). Also, the macro re-entrant waves will have foci different from the initiating rotor (see figure 12.18 (E)).

Location of the ectopic focus	1st procedure		2nd procedure	
	Sustained AF	Success	Sustained AF	Success
LSPV proximal	3	3	3	3
LSPV distal	2	2	2	2
RSPV	4	1	4	1
LIPV	1	3	1	3
RIPV	2	2	1	3
overall	12	11	11	12

**Table 12.9.** Sustained atrial fibrillation and successful therapy after the first and second procedure of the linear ablation lesion strategy only reported by Ernst et al. [76].

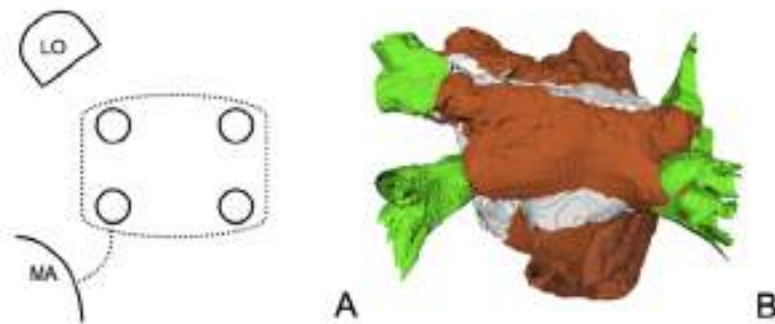


**Figure 12.17.** This figure illustrates the transfer of the schematic description of the ablation strategy a single circumferential lesion and a lesion to the mitral annulus (A) onto the anatomical model (B). A: The epicardial view shows the left orifice (LO) at the top behind the left superior pulmonary vein. At the bottom left, the mitral annulus (MA) is shown. The pulmonary veins (PVs) are indicated by the circles with the right PVs on the right side. The dotted lines indicate the ablation lesion. B: The latero-dorsal view of the left atrium shows the pulmonary veins in yellow, the cardiac tissue in brown and the created lesion in white.

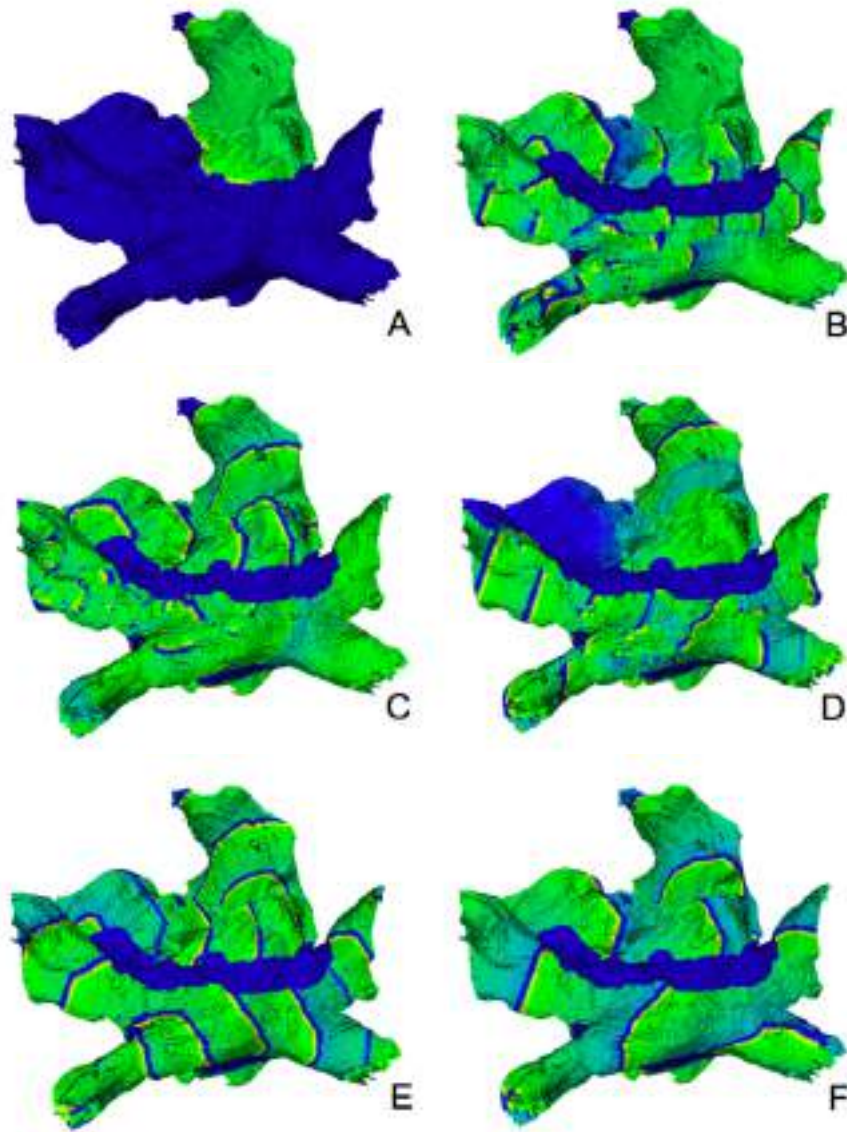


**Figure 12.18.** Exemplary results of the circumferential ablation strategy described by Ernst et al. [76]: (A) demonstrates the successful prevention of atrial fibrillation provoked by an ectopic beat at the left superior pulmonary vein. Transmural lesions did not improve the overall success rate of the ablation strategy (B - F). Fibrillation and a break-up of wave fronts was observed in either both (B) or the left atrium (C). The left atrium remained fibrillating in some simulations while the right atrium regained sinus rhythm (D). Also, macro re-entrant circuits were observed (E) with wave fronts travelling in seemingly opposite directions in the atria (F). The transmembrane voltage at 900 *ms* is shown. The narrow dark lines on the atrial surface indicate the excitation wave fronts. The broad dark lines indicate no electrical activity, i.e. the location of the ablation lesions.



### 12.1.10 Simulation of Circumferential Ablation Lesion around All Pulmonary Veins Including Two Additional Linear Lesion

The second linear lesion is also drawn to the mitral annulus (see figure 12.19). The success rate is not augmented. Neither transmural lesions will improve the result of this particular strategy (see table 12.10). The results show exactly the same excitation pattern as the circumferential lesion approach described in section 12.1.9. The only difference is one ectopic focus at the left inferior pulmonary vein that is isolated by completely transmural lesions. While the strategy with one lesion to the mitral annulus is showing no AF, the strategy including two lesions to the mitral annulus is unsuccessful.

Location of the ectopic focus	1st procedure		2nd procedure	
	Sustained AF	Success	Sustained AF	Success
LSPV proximal	3	3	3	3
LSPV distal	2	2	2	2
RSPV	4	1	4	1
LIPV	1	3	2	2
RIPV	2	2	1	3
overall	12	11	12	11

**Table 12.10.** Sustained atrial fibrillation and successful therapy after the first procedure of the linear ablation lesion strategy only reported by Sueda et al. [273].

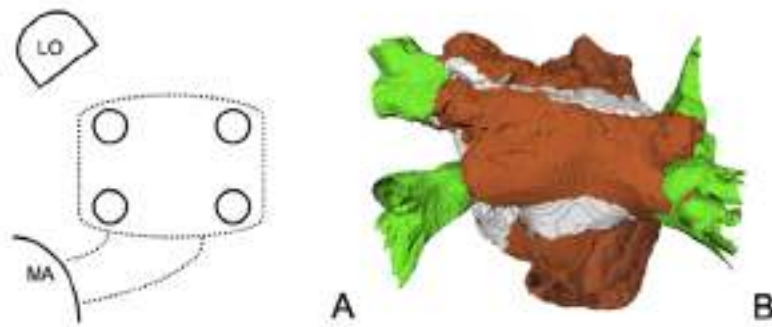


**Figure 12.19.** This figure illustrates the transfer of the schematic description of the ablation strategy a single circumferential lesion and two lesion to the mitral annulus (A) onto the anatomical model (B). A: The epicardial view shows the left orifice (LO) at the top behind the left superior pulmonary vein. At the bottom left, the mitral annulus (MA) is shown. The pulmonary veins (PVs) are indicated by the circles with the right PVs on the right side. The dotted lines indicate the ablation lesion. B: The latero-dorsal view of the left atrium shows the pulmonary veins in yellow, the cardiac tissue in brown and the created lesion in white.

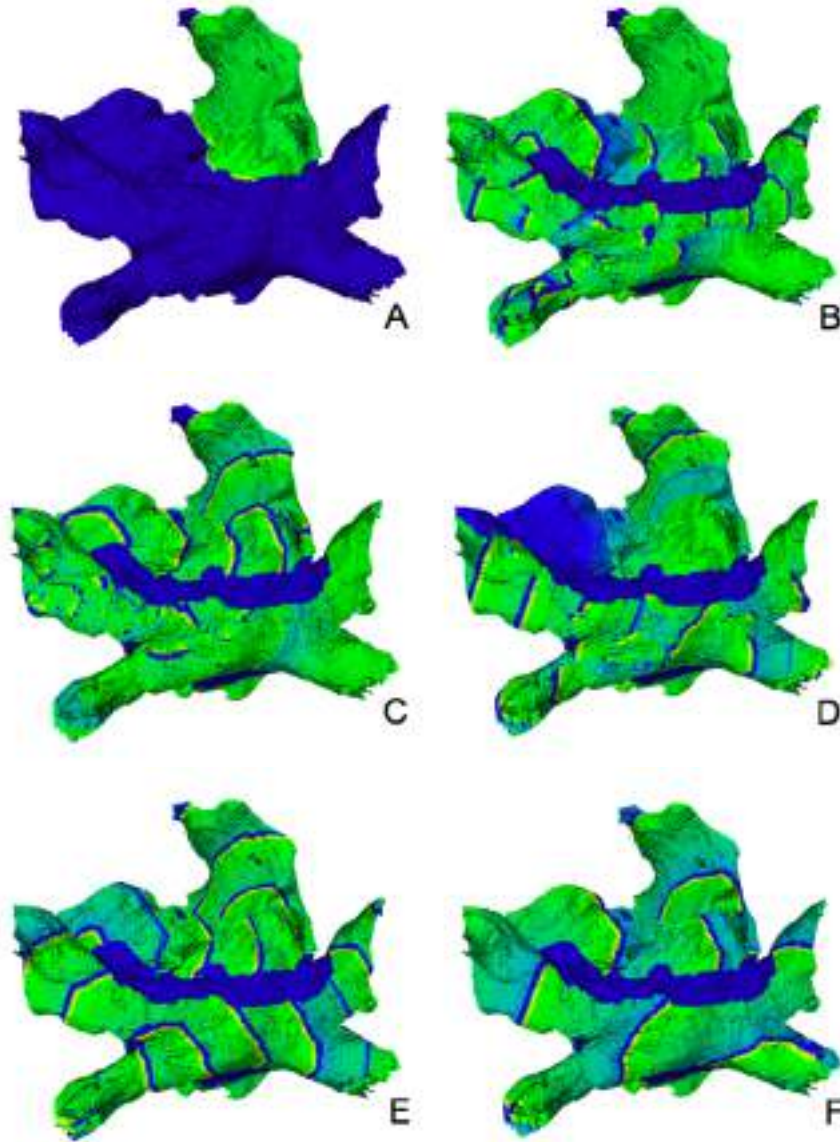


**Figure 12.20.** Exemplary results of the circumferential ablation strategy described by Sueda et al. [273] which are similar to those described in the last section (compare with figure 12.18): (A) demonstrates the successful prevention of atrial fibrillation provoked by an ectopic beat at the left superior pulmonary vein. Transmural lesions did not improve the overall success rate of the ablation strategy (B - F). Fibrillation and a break-up of wave fronts was observed in either both (B) or the left atrium (C). The left atrium remained fibrillating in some simulations while the right atrium regained sinus rhythm (D). Also, macro re-entrant circuits were observed (E) with wave fronts travelling in seemingly opposite directions in the atria (F). The transmembrane voltage at 900 ms is shown. The narrow dark lines on the atrial surface indicate the excitation wave fronts. The broad dark lines indicate no electrical activity, i. e. the location of the ablation lesions.



### 12.1.11 Simulation of Circumferential Ablation Lesion of All Pulmonary Veins with Additional Lesions to the Left Atrial Appendage and the Mitral Annulus

The ablation strategy that included one linear lesion to the mitral annulus as well as to the left atrial orifice has a success rate above 50 % with 13 out of 23 simulations in the first procedure (see table 12.11). The transmuralities of the lesions created in a second procedure yielded even a success rate of 100 %. The left atrium was observed to be fibrillating in some cases while the right atrium was excited physiologically (see figure 12.22). Within the fibrillating left atrium, the initiating trigger is replaced by other re-entrant mechanisms that sustain AF in the isolated parts. Chaotic excitation can be observed at the same time with stable excitation wave fronts.

Location of the ectopic focus	Sustained AF	Success
LSPV proximal	2	4
LSPV distal	2	2
RSPV	4	1
LIPV	0	4
RIPV	2	2
overall	10	13

**Table 12.11.** Sustained atrial fibrillation and successful therapy after the first procedure of the linear ablation lesion strategy only described by Cox [47]. The second procedure with complete transmural lesions lead to a prevention of atrial fibrillation in all simulations.

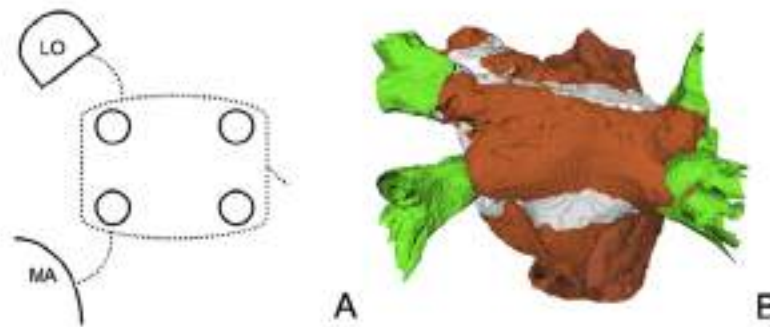


**Figure 12.21.** This figure illustrates the transfer of the schematic description of the ablation strategy a single circumferential lesion and a lesion to the mitral annulus and to the left atrial orifice (A) onto the anatomical model (B). A: The epicardial view shows the left orifice (LO) at the top behind the left superior pulmonary vein. At the bottom left, the mitral annulus (MA) is shown. The pulmonary veins (PVs) are indicated by the circles with the right PVs on the right side. The dotted lines indicate the ablation lesion. B: The latero-dorsal view of the left atrium shows the pulmonary veins in yellow, the cardiac tissue in brown and the created lesion in white.

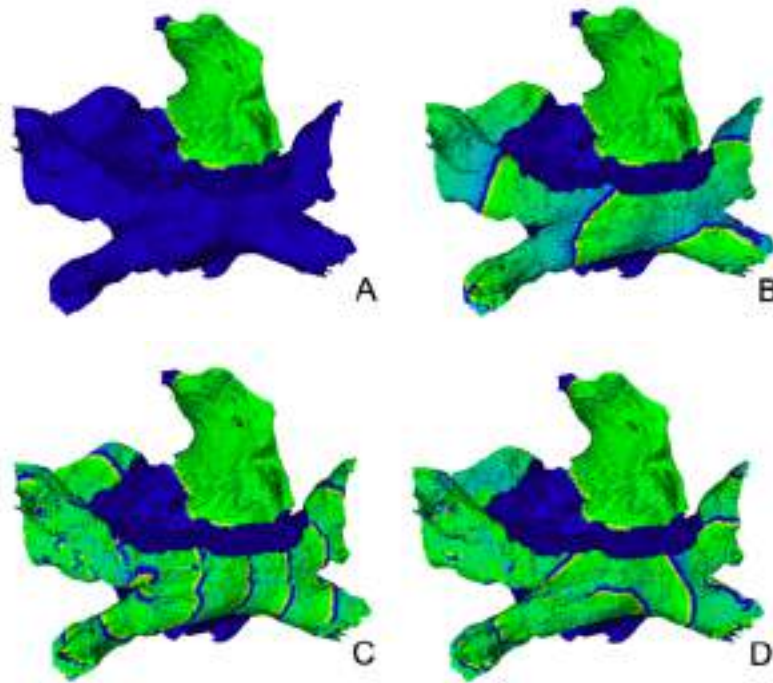


**Figure 12.22.** Exemplary results of the circumferential ablation strategy described by Cox [47]: (A) demonstrates the successful prevention of atrial fibrillation provoked by an ectopic beat at the left superior pulmonary vein. Transmural lesions did improve the overall success rate of the ablation strategy to 100 % (B - D). However, macro re-entrant circuits (B) and left atrial fibrillation (C - D) with break-ups of wave fronts were observed. The transmembrane voltage at 900 *ms* is shown. The narrow dark lines on the atrial surface indicate the excitation wave fronts. The broad dark lines indicate no electrical activity, i.e. the location of the ablation lesions.

## 12.2 Results: Atrial Antitachycardial Pacing

Atrial antitachycardial pacing (AATP) has only been briefly investigated by implementing standard preventive pacing algorithms as well as burst pacing for the termination of atrial fibrillation (AF). Therefore, this section highlights the observations of the results only. The development of new pacing algorithms is subject to other studies. However, the results described in this section lead to important conclusions which are discussed in chapter 13.4.

### 12.2.1 Simulation of Atrial Antitachycardial Pacing to Prevent Atrial Fibrillation

288 simulations were carried out to evaluate post-PAC response as preventive AATP. None of these simulations were successful in suppressing the ectopic beat and atrial fibrillation (AF) was observed in all simulations. Either the pacing stimulus did not have an effect due to the premature stimulus at the location of the ectopic beat (for all stimulation at  $50\text{ ms}$  -  $100\text{ ms}$ ) or the excitation wave front due to pacing stimulus did not reach the ectopic centre in time to prevent it (mostly for pacing stimulation at  $200\text{ ms}$ ). However, the pacing stimulus had an influence on the excitation propagation and the excitation pattern because it caused the area around the pacing site to be in different refractive periods of different states of stimulation (see figure 12.23).

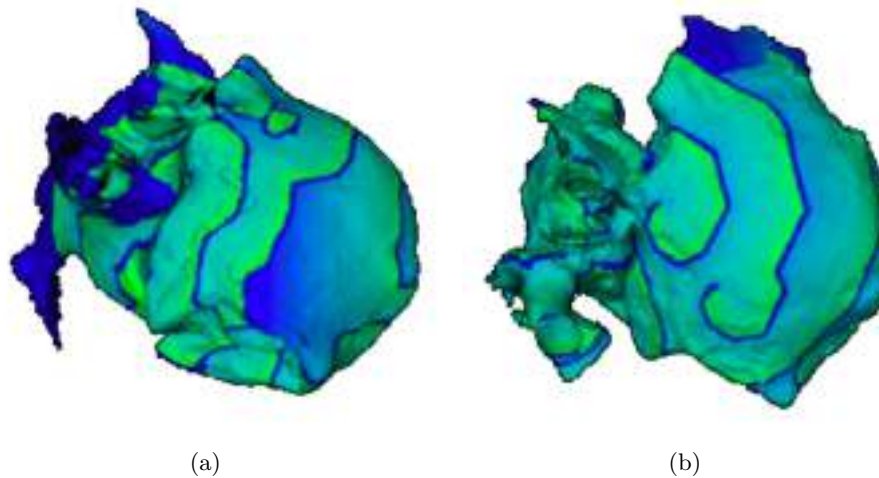


**Figure 12.23.** The post-PAC response algorithm was not able to suppress the ectopic beat in the pulmonary veins in all simulations. The excitation pattern was changed however: Figure (a) shows the excitation pattern without pacing stimulus. Figure (b) shows the same pathological set-up but with a pacing stimulus at  $200\text{ ms}$  before the ectopic beat right in the middle of the right atrial roof. Two rotor waves can be clearly distinguished to drive the excitation together with another focus in the left atrium. The transmembrane voltage at  $900\text{ ms}$  is shown in both figures. The narrow dark lines on the atrial surface indicate the excitation wave fronts.

846 simulations were carried out to investigate the PAC suppression algorithm with respect to pacing frequency and electrode position. The pacing simulated did not lead to the suppression of the ectopic beat that caused AF. If the pacing frequency was low, i.e. 600 beats per minute (bpm), the pathological excitation did override the pacing stimuli (see figure 12.24.a). However, a break-up of wavefronts was achieved in some simulations with a pacing frequency of 800 bpm (see figure 12.24.b). An increase in pacing frequency above 1000 bpm leads to controlling the excitation propagation on the right atrial roof (see figure 12.24.c-d).

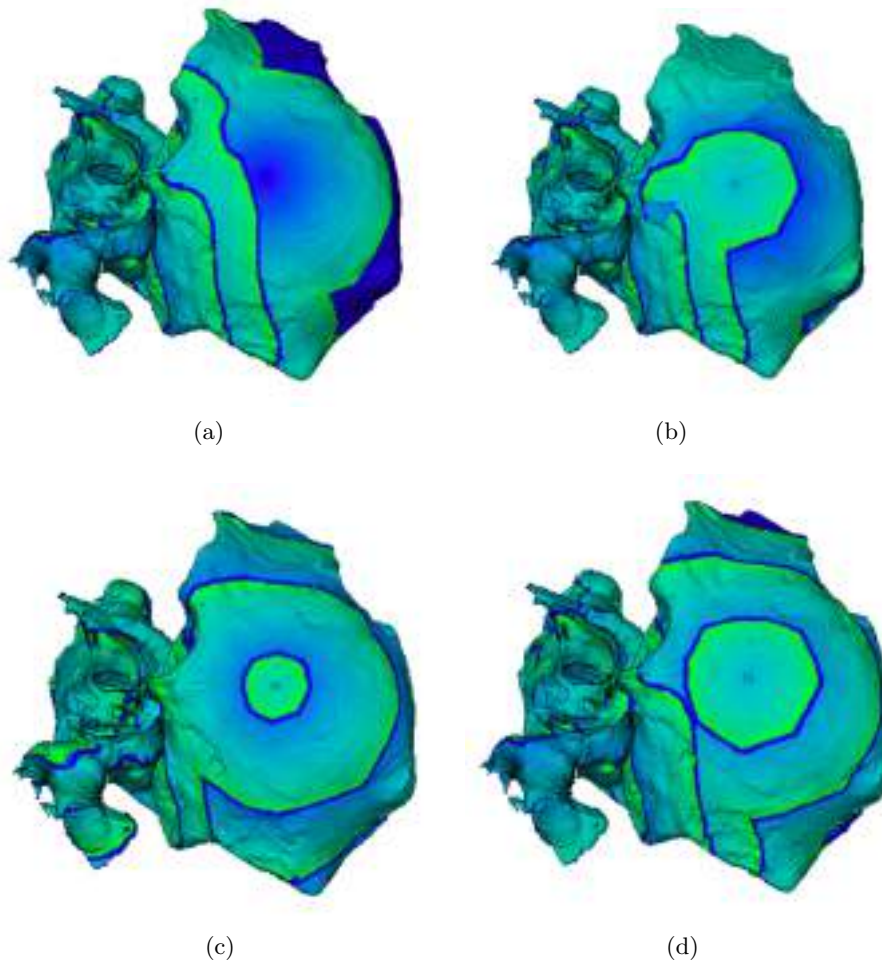


**Figure 12.24.** The PAC suppression algorithm also did not yield a successful suppression of the ectopic beats. Figure (a) shows the stimulation of the right atrial roof at 600 beats per minute (bpm). The pacing frequency is too slow to dominate any of the atrial area. It is overridden by the fast excitation wave fronts of the driving circuit. An increase in pacing frequency to 800 bpm leads to a break-up of wave fronts (b). A further increase to 1000 bpm (c) and 1200 bpm (d) shows that the right atrial excitation is dominated by the pacing stimuli but does not spread over the whole atrium. The transmembrane voltage is shown. The narrow dark lines on the atrial surface indicate the excitation wave fronts.

**12.2.2 Simulation of Atrial Antitachycardial Pacing to Terminate Atrial Fibrillation**

Normal sinus rhythm was not restored in any of the 423 simulation carried out to investigate AATP to terminate AF although the time simulated was 7500 *ms*. At 7500 *ms*, the excitation pattern in all simulations did not show any regular structures, i. e. it was quasi-chaotic similar to the results described in section 11.1.5.

### 12.3 Results: Cardiac Resynchronisation Therapy

Figure 12.25 demonstrates the result of the optimisation algorithm. The root mean square error  $E_{RMS}$  between the isochrone lattices of the physiological (fig. 12.25.a) and the pathological (fig. 12.25.b) simulation for the atrio-ventricular (AV) block III (100 % conduction velocity) shows no error in the atria since they are excited in the same way in both simulations. The ventricular excitation differs greatly though, and therefore, the error is large (fig. 12.25.c). The optimized therapy shows only a small error around the electrode positions (fig. 12.25.f) since the excitation of the ventricles in the simulation of the therapy (fig. 12.25.e) is as close as possible to the physiological simulation (fig. 12.25.d).

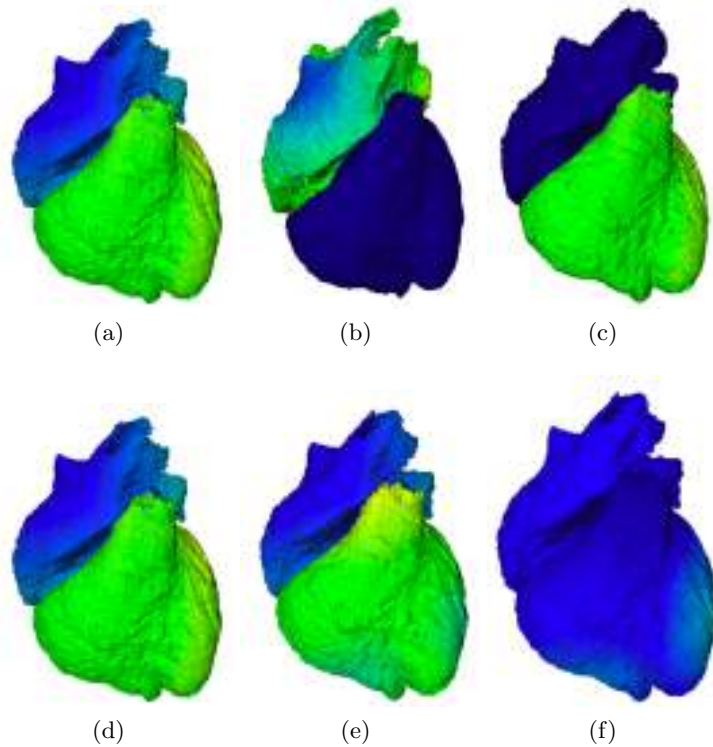


**Figure 12.25.** Figure (a) and (d) shows the isochrones of the simulation of the sinus rhythm in the Visible Man data set. The blue colour shows early activation and the bright yellow shows late activation. Figure (b) shows the isochrones for the simulation of the AV block III. Figure (e) shows the isochrones of the same pathology, only paced by two stimuli at the ventricles. Figure (c) and (f) show the square error between the isochrones of the sinus rhythm and the pathology or therapy, respectively. In both cases, the error is zero in the atria (blue) since they are activated physiologically. The error is large for the pathological simulation (yellow) since the ventricles are not excited at all (c). For the simulation of the therapy, the error is small and can only be recognized around the location of the pacing electrodes (f).

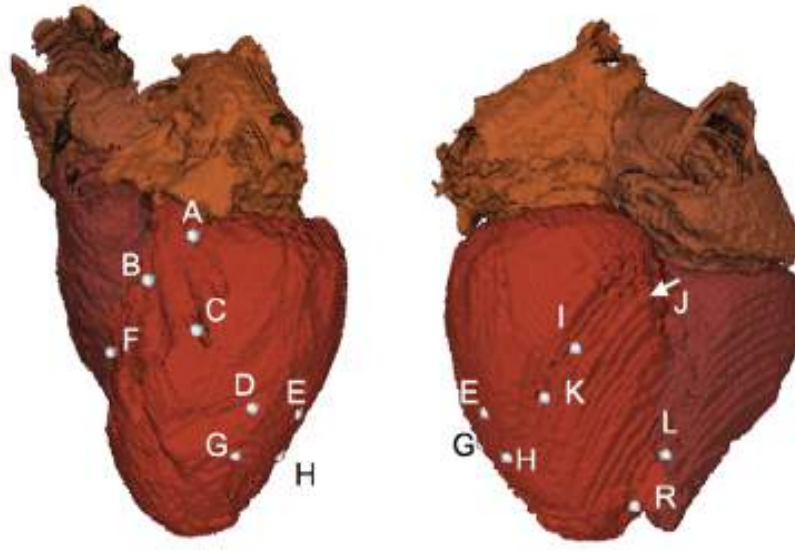


**Figure 12.26.** This figure shows the electrode positions of the pacing leads for the evaluation of electrode position in cardiac resynchronization therapy in the Visible Man data set in anterior view (left) and posterior view (right).

Pathology	Pacing Lead	AV-delay	VV-delay	$E_{RMS}$	Simulations	Algorithm
AV block (0 %)	RA	100	20	3.99	972	sequential
AV block (0 %)	RI	234	117	3.18	301	DSA
AV block (20 %)	RL	100	10	4.59	972	sequential
AV block (20 %)	RI	217	117	4.23	280	DSA
AV block (40 %)	RA	60	40	5.91	972	sequential
AV block (40 %)	RG	343	-134	5.19	256	DSA
LBBB (0 %)	RB	120	-10	5.28	972	sequential
LBBB (0 %)	RH	220	138	5.23	226	DSA
LBBB (20 %)	RB	100	0	6.84	972	sequential
LBBB (20 %)	RE	206	13	6.77	225	DSA
LBBB (40 %)	RK	60	30	9.50	972	sequential
LBBB (40 %)	RK	188	34	9.49	219	DSA

**Table 12.12.** Summary of CRT optimisation on the Visible Man data set.

For a better overview, figures 10.7 - 10.7 are displayed in figures 12.26 - 12.27 again. Tables 12.12 - 12.13 summarize the results of the optimisation with respect to optimal electrode position, timing and pathology<sup>1</sup>.

<sup>1</sup> The results presented in this section have been produced in cooperation with Mrs Raz Miri who carried out the simulations of the presented methods supervised by Matthias Reumann. Parts of these results were presented at the IASTED Biomed conference in Innsbruck, Austria, 2007 [182].



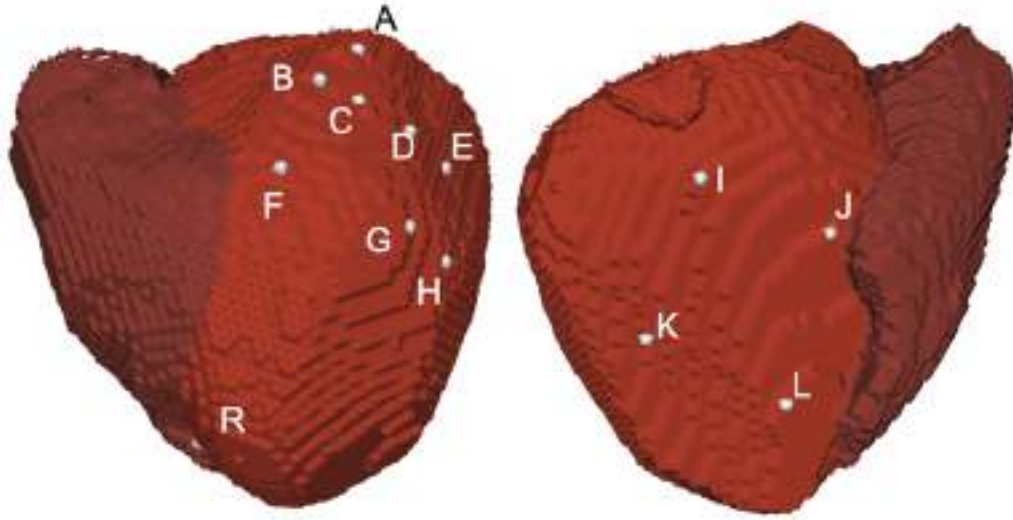


**Figure 12.27.** This figure shows the electrode positions of the pacing leads for the evaluation of electrode position in cardiac resynchronization therapy in the patient data set in anterior view (left) and posterior view (right).

Pathology	Pacing Lead	AV-delay	VV-delay	$E_{RMS}$	Simulations	Algorithm
AV block (0 %)	RJ	260	0	3.21	1452	sequential
AV block (0 %)	RL	249	111	3.90	282	DSA
AV block (20 %)	RL	260	-20	3.28	1452	sequential
AV block (20 %)	RL	234	127	4.27	330	DSA
AV block (40 %)	RL	240	-30	4.63	1452	sequential
AV block (40 %)	RL	211	109	5.38	387	DSA
LBBB (0 %)	RK	160	70	10.12	1452	sequential
LBBB (0 %)	RK	228	11	9.89	265	DSA
LBBB (20 %)	RK	160	40	13.50	1452	sequential
LBBB (20 %)	RK	188	34	12.59	284	DSA
LBBB (40 %)	RK	120	20	19.66	1452	sequential
LBBB (40 %)	RK	109	84	18.92	212	DSA

**Table 12.13.** Summary of CRT optimisation on the patient data set.

The optimal electrode position varied according to the underlying pathology in the VM data set. Both optimization methods did not produce the same optimal electrode positions apart from the LBBB simulation with 40 % reduction in interventricular conduction delay where both methods determined the electrode pair RK in one of the posterior-lateral branches of the coronary sinus as the ideal electrode position. The sequential optimization method mostly found the optimal electrode position in the anterior branches of the coronary sinus close to the base (electrode pairs



RA and RB). Only the simulations of the AV block with 20 % reduction in conduction delay and the LBBB simulations with 40 % reduction had an optimum ERMS with a left ventricular electrode in the posterior left ventricular wall. The DSA optimization method found the optimal electrode positions to be in the posterior region of the left ventricle. They were either situated in the posterior-lateral branches of the coronary sinus (electrode pairs RI and RK) or in the lateral free wall close to the apical region (electrode pairs RG, RH and RE).

The simulations on the patient data set yield different results for the optimal electrode set up. Both optimization algorithms find the same electrode pairs to be optimal with respect to pathology simulated except for the AV block without reduced interventricular conduction velocity (electrode pair RJ vs. RL). In the latter case, however, the left ventricular electrodes were both situated in the posterior branch of the coronary sinus. For all simulations of the AV block, the optimal left ventricular electrode was situated at position L, which is at the posterior ventricular wall closest to the apex. For all simulations of the LBBB and both optimization methods, the optimal electrode pair was found to be RK where the left ventricular electrode is placed in a posterior-lateral branch of the coronary sinus between base and apex.

The optimal timing delays varied according to the underlying pathology and optimal electrode position. In general it can be noticed that the reduction in interventricular conduction velocity lead to a reduction in AV delay in both optimization methods. This cannot be said for the VV delay. However, the VV delay was mostly positive, ie. left before right ventricular stimulation produced the best results in all but four cases: For the AV block with 40 % reduction in conduction velocity in the VM data set the DSA optimization method produced the lowest ERMS with right before left ventricular stimulation. Here, the AV delay was 209 ms and the VV delay was set to 134 ms. For the AV block in the patient data set with reduced conduction velocity, the sequential optimization method showed the best result for an AV delay of 250 ms and 220 ms and a VV delay of 10 ms and 20 ms with right ventricular stimulation first. The only case where right before ventricular stimulation had the best result in the simulations of the LBBB was with the VM data set without reduction in conduction velocity where the sequential optimization method found an AV delay of 110 ms and a VV delay of 10 ms to be most optimal. The VV delay in the simulations using the sequential optimization method did not exceed 40 ms for the optimal set up although a maximal VV delay of 50 ms was set. However, using the DSA method, the VV delay was set to values greater than 100 ms in seven cases, mostly in the simulations of the AV block in both anatomical data sets.

With respect to computational load, the DSA optimization method reduces the number of simulations significantly from e.g. 972 simulations to as little as 219 simulations (VM data set with 40 % reduced conduction velocity and a LBBB). The relative reduction in the number of simulations to find the optimal electrode position and timing delays is even greater for the simulations with the patient data set. Here, it is reduced from 1452 simulations to 212 - 387 simulations. However, it can

be noted, that the downhill simplex algorithm finds smaller  $E_{RMS}$  values for each pathology and anatomy. The simulation number varies accordingly but always stays below 30 % of the simulations needed for the sequential search.

The following section describes the results of the optimisation strategy presented in this work with respect to the Visible Man data-set and the patient data-set in detail.

### 12.3.1 Optimization of CRT on the Visible Man Data-Set

For each electrode combination, an optimal set-up of atrio-ventricular (AV) and interventricular (VV) delay has been found for all pathologies simulated (see tables 12.14 - 12.16). The results show that for each electrode position there is only one combination of AV- and VV-delay which produces the smallest root mean square error  $E_{RMS}$  (see appendix on attached CD). The  $E_{RMS}$  differs between electrode pairs in all pathologies.

Lead Position	A-V block III			LBBB		
	min $E_{RMS}$	AV-delay	VV-delay	Min $E_{RMS}$	AV-delay	VV-delay
No pacing	51.6	n/a	n/a	7.47	n/a	n/a
RA	3.99	100	20	5.60	120	-10
RB	4.18	140	-30	5.28	120	-10
RC	4.16	140	-30	5.38	120	-10
RD	4.14	140	-30	5.71	120	-10
RE	4.08	140	-30	5.50	120	-10
RF	4.07	140	-30	6.00	120	-10
RG	4.28	140	-30	6.42	140	-30
RH	4.21	140	-30	6.03	140	-30
RI	4.31	140	-30	5.71	140	-30
RJ	4.07	140	-30	6.33	120	-10
RK	4.14	140	-30	5.56	120	-10
RL	4.07	140	-30	6.29	120	-10

**Table 12.14.** The minimal  $E_{RMS}$  in  $[ms]$  in different electrode positioning for the conduction velocity set to 100% of the physiological values is shown for the Visible Man data set. The corresponding AV and VV-delays are shown, also, together with the respective electrode set-up. The optimisation was carried out by the sequential search algorithm.

#### 12.3.1.1 Atrio-Ventricular Block in the Visible Man Anatomy

For the AV block III with 100 % conduction velocity in the Visible Man data-set, the minimum error was between 3.99  $ms$  and 4.31  $ms$  with a mean of 4.14  $ms$  for all electrodes (see figure 12.28). The electrode pair RA produced the best result and the pair RG the highest minimum error. The standard deviation of the error from the mean was only 0.09.

Lead Position	A-V block III			LBBB		
	min $E_{RMS}$	AV-delay	VV-delay	Min $E_{RMS}$	AV-delay	VV-delay
No pacing	51.6	n/a	n/a	11.16	n/a	n/a
RA	4.67	80	50	7.36	80	20
RB	5.32	80	30	6.84	100	0
RC	5.31	120	-20	6.89	100	0
RD	5.23	120	-20	7.28	100	0
RE	5.13	120	-20	6.98	100	0
RF	5.30	120	-20	8.03	100	0
RG	5.42	120	-20	8.47	120	-30
RH	5.31	120	-20	7.76	100	0
RI	5.38	120	-20	7.18	100	0
RJ	5.29	120	-20	8.39	100	-10
RK	5.21	120	-20	6.96	100	0
RL	4.59	100	10	8.33	80	40

**Table 12.15.** The minimal  $E_{RMS}$  in  $[ms]$  in different electrode positioning for the conduction velocity set to 80% of the physiological values is shown for the Visible Man data set. The corresponding AV and VV-delays are shown, also, together with the respective electrode set-up. The optimisation was carried out by the sequential search algorithm.

Lead Position	A-V block III			LBBB		
	min $E_{RMS}$	AV-delay	VV-delay	Min $E_{RMS}$	AV-delay	VV-delay
No pacing	51.6	n/a	n/a	17.63	n/a	n/a
RA	5.91	60	40	10.52	60	20
RB	6.81	60	40	9.81	60	20
RC	7.40	100	-20	9.62	60	30
RD	7.09	60	40	10.23	60	30
RE	7.01	60	40	9.73	60	30
RF	7.47	100	-20	11.91	80	0
RG	7.38	100	-20	12.02	100	-30
RH	7.28	100	-20	10.80	60	20
RI	7.28	100	-20	9.95	60	30
RJ	7.46	100	-20	12.21	60	-10
RK	6.94	60	40	9.50	60	30
RL	7.01	80	50	11.93	60	50

**Table 12.16.** The minimal  $E_{RMS}$  in  $[ms]$  in different electrode positioning for the conduction velocity set to 60% of the physiological values is shown for the Visible Man data. The corresponding AV and VV-delays are shown, also, together with the respective electrode set-up. The optimisation was carried out by the sequential search algorithm.

In the simulations with reduced conduction velocity, a similar behaviour can be observed: For 80 % conduction velocity, the mean  $E_{RMS}$  for all electrode pairs was 5.18 with the electrode pair RL producing the best result with 4.59  $ms$  followed closely by electrode set-up RA with 4.67  $ms$ .

Electrode pair RG had the highest minimum error with 5.42 *ms*. For 60 % conduction velocity, the mean  $E_{RMS}$  was highest with 7.09 *ms*. In this pathology, the electrode pair RA had the lowest  $E_{RMS}$  value with 5.91 *ms*. The highest minimum  $E_{RMS}$  was given by the electrode pair RF. The standard deviation from the mean was 0.27 *ms* and 0.43 *ms* in the simulations with 80 % and 60 % conduction velocity, respectively.

The  $E_{RMS}$  for the pathological case (51.6 *ms*) was reduced by an order of magnitude. It can be noted however, that the mean  $E_{RMS}$  increased with a reduction in conduction velocity (see figure 12.28). But the best  $E_{RMS}$  was always below 15 % of the  $E_{RMS}$  of the pathology. The error range of the minimum  $E_{RMS}$  was also largest for the simulation with the lowest conduction velocity with a range of 1.6 *ms*. In the other two pathological conditions, the range between lowest and highest minimum  $E_{RMS}$  was 1.21 *ms* (100 % conduction velocity) and 1.24 *ms* (80 % conduction velocity).

The optimal AV-delay in the simulations with 100 % conduction velocity was 140 *ms* for all electrode set-ups with the exception of electrode pair RA where the optimal AV-delay was 100 *ms* (see table 12.14). The optimal VV-delay was mostly -30 *ms*. It was 20 *ms* for electrodes RA. The optimal timing changes with a reduced conduction velocity. The optimal AV-delay is mostly 120 *ms* with a VV-delay ranging between -20 *ms* to 50 *ms* but being -20 *ms* in nine of twelve electrode set-ups for the AV block with 80 % interventricular conduction velocity (see table 12.15). The optimal AV-delay is even smaller with 60 % conduction velocity. It is 100 *ms* in electrode set-up RC and RF - RJ. Electrode pairs RA, RB, RD, RE and RK had a minimal  $E_{RMS}$  at 60 *ms* AV-delay. For electrodes RL, the optimal AV-delay was 80 *ms*. The optimal VV-delay was 40 *ms* for electrodes with 60 *ms* AV-delay and -20 *ms* for those with 100 *ms* AV-delay. Electrode pair RL had a VV-delay of 50 *ms* for the lowest  $E_{RMS}$  (see table 12.16).

Figure 12.29 shows the simulation results for the optimal electrode positions for the AV block in the Visible Man anatomy.

### 12.3.1.2 Left Bundle Branch Block in the Visible Man Anatomy

The optimisation for the left bundle branch block (LBBB) generally yields higher  $E_{RMS}$  values than for the AV block. However, the same tendency in the mean error value can be recognised for the reduction in conduction velocity: the smaller the interventricular conduction velocity, the larger the minimum  $E_{RMS}$ . But also the larger the gain in the optimization. For 100 % conduction velocity, the mean  $E_{RMS}$  is very close to the  $E_{RMS}$  of the simulation of the pathology (5.82 *ms* vs. 4.47 *ms*) (see figure 12.30). The best electrode set-up RB produced a  $E_{RMS}$  of 5.28 *ms* which is 70.68 % of the  $E_{RMS}$  of the pathology. A greater improvement was recognized for the simulations with 80 % and 60 % conduction velocity where the optimal parameters delivered a  $E_{RMS}$  of 61.29 % and 53.89 % with respect to the pathological isochrones. The optimal electrode set-up was given by electrodes RB with 6.84 *ms* (80 % conduction velocity) and RK with 9.50 *ms* (60 % conduction

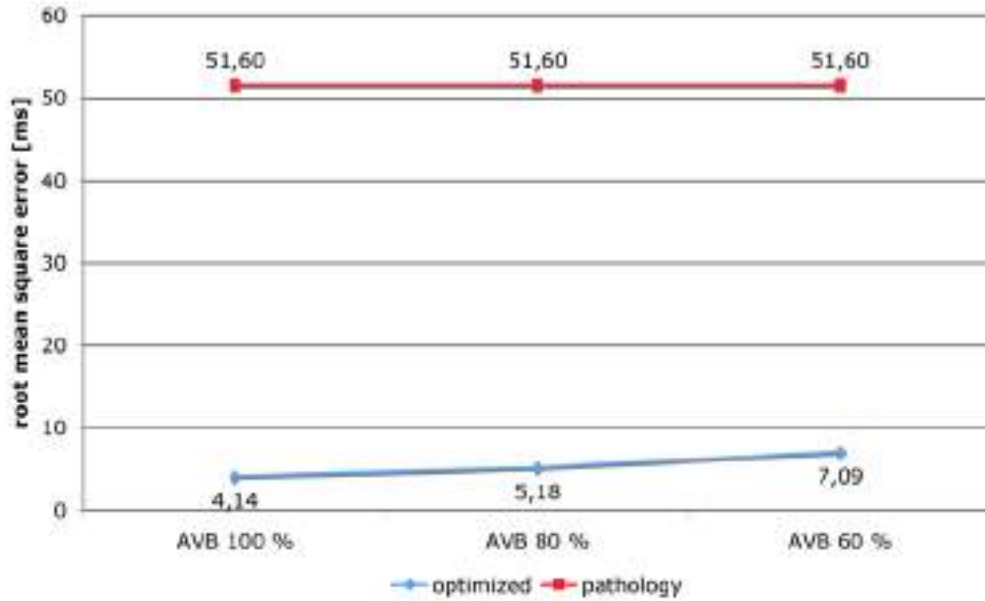


**Figure 12.28.** This figure shows the mean root mean square error with respect to the simulated pathology of an AV block III (AVB) and reduced conduction velocity in the Visible Man data set using a sequential search of the minimum values. The connecting lines are for visualization only.

velocity). The worst electrode set-ups were given by electrode pair RG (100 - 80 % conduction velocity) and RJ (60 % conduction velocity). The standard deviation was  $0.39\text{ ms}$  (100 % conduction velocity),  $0.62\text{ ms}$  (80 % conduction velocity) and  $1.05\text{ ms}$  (60 % conduction velocity) .

Similar to the simulations of the AV block III, the AV-delay generally decreased with decreasing conduction velocity. For 100 % conduction velocity, it was mostly  $120\text{ ms}$ . Only electrode pairs RG to RI showed an optimal AV-delay of  $140\text{ ms}$ . The VV-delay differed according to electrode set-up with  $-10\text{ ms}$  and  $-30\text{ ms}$  for an AV-delay of  $120\text{ ms}$  and  $140\text{ ms}$ , respectively (see table 12.14). With 80 % conduction velocity, the VV-delay was mostly optimal with  $0\text{ ms}$ . Only electrodes RA ( $20\text{ ms}$ ), RG ( $-30\text{ ms}$ ), Rj ( $-10\text{ ms}$ ) and RL ( $40\text{ ms}$ ) had a non-zero VV-delay. The optimal AV-delay was  $100\text{ ms}$  in all electrode set-ups except in electrodes RA, RG and RL where it was  $80\text{ ms}$ ,  $120\text{ ms}$  and  $80\text{ ms}$ , respectively (see table 12.15). The AV-delay of  $60\text{ ms}$  gave the best  $E_{RMS}$  values in all simulations of the LBBB with 60 % interventricular conduction delay apart from electrode set-up RF ( $80\text{ ms}$ ) and RG ( $100\text{ ms}$ ). The VV-delay, however, ranged between  $-30\text{ ms}$  and  $50\text{ ms}$  (see table 12.16).

Figure 12.31 shows the simulation results for the optimal electrode positions for the left bundle branch block in the Visible Man anatomy.

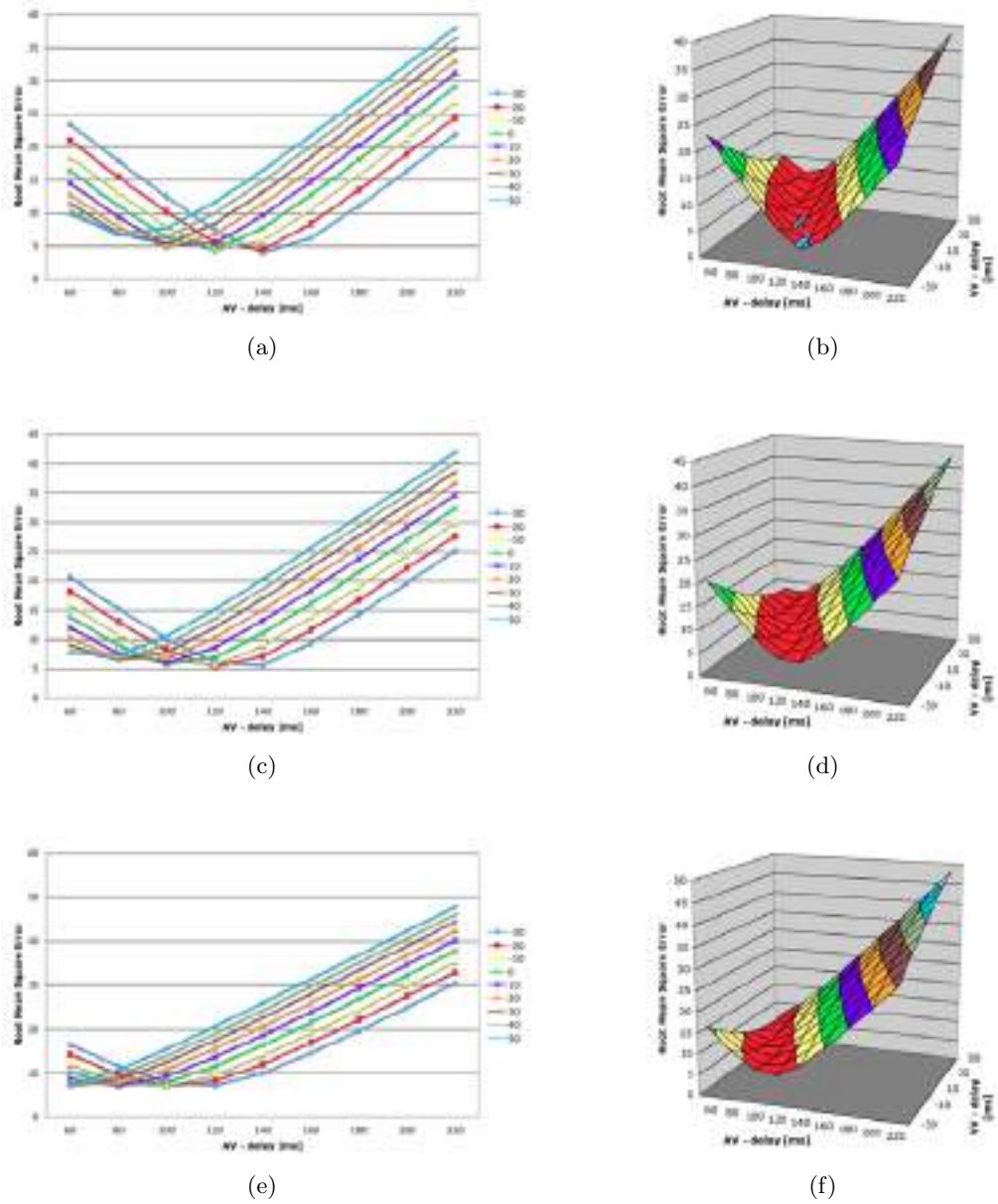


**Figure 12.29.** The root mean square error is shown in  $[ms]$  with respect to AV- and VV-delay for the best electrode position in the simulations of the AV block on the Visible Man data set using the sequential search algorithm.

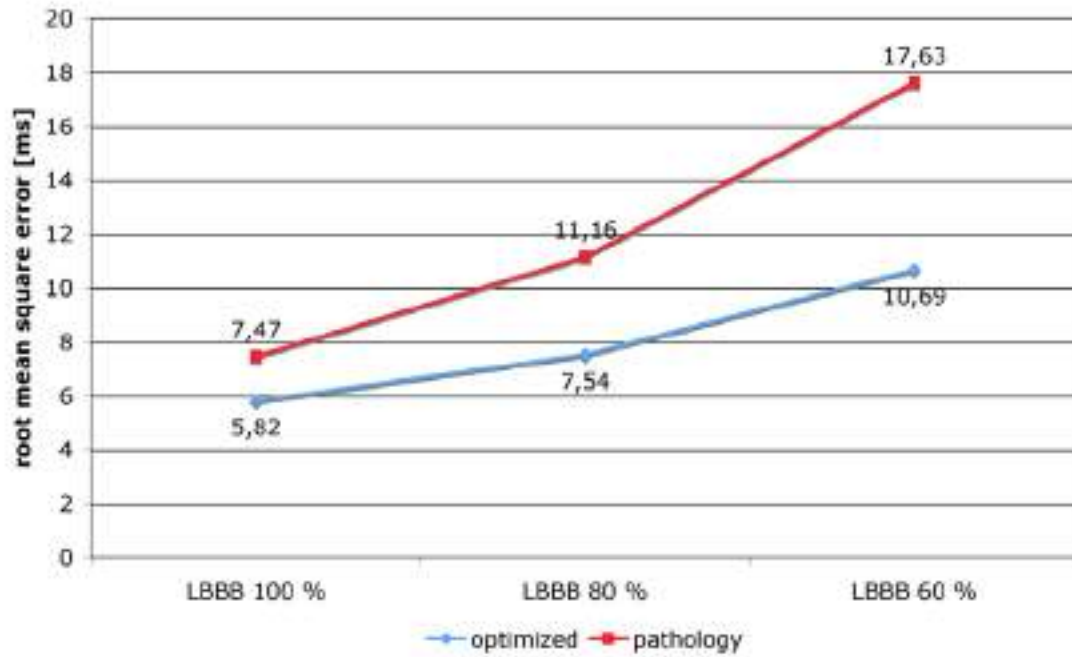


**Figure 12.30.** This figure shows the mean root mean square error with respect to the simulated pathology of a left bundle branch block (LBBB) and reduced conduction velocity in the Visible Man data set using a sequential search of the minimum values. The connecting lines are for visualization only.

### 12.3.2 Optimization of CRT on the Patient Data-set

The simulations with the patient anatomy yields results that are more distinct than those of the Visible Man data-set. However, as in the simulations with the Visible Man anatomy, an optimal electrode set-up was found for each pathology (see tab. 12.17 - 12.19).

#### 12.3.2.1 AV Block III in the Patient Anatomy

The  $E_{RMS}$  is reduced below 5 % of the  $E_{RMS}$  in the simulation of the pathology AV block III for all electrode set-ups. For the simulations with 100 % conduction velocity, electrode set-up RJ had the lowest  $E_{RMS}$  with 3.21 ms. For reduced conduction velocities, electrode pair RL had the lowest  $E_{RMS}$  with 3.28 ms (80 % conduction velocity) and 4.63 ms (60 % conduction velocity). The standard deviation of the minimal error was 0.56 ms, 0.31 ms and 0.23 ms, respectively, with a mean error for all minimum values of 3.88 ms, 3.86 ms and 5.07 ms (see figure 12.33). Thus, even the largest optimal  $E_{RMS}$  was only 5.34 ms (100 % conduction velocity, electrode pair RH), 4.19 ms (80 % conduction velocity, electrode pair RE) and 5.30 ms (60 % conduction velocity, electrode pair RA).

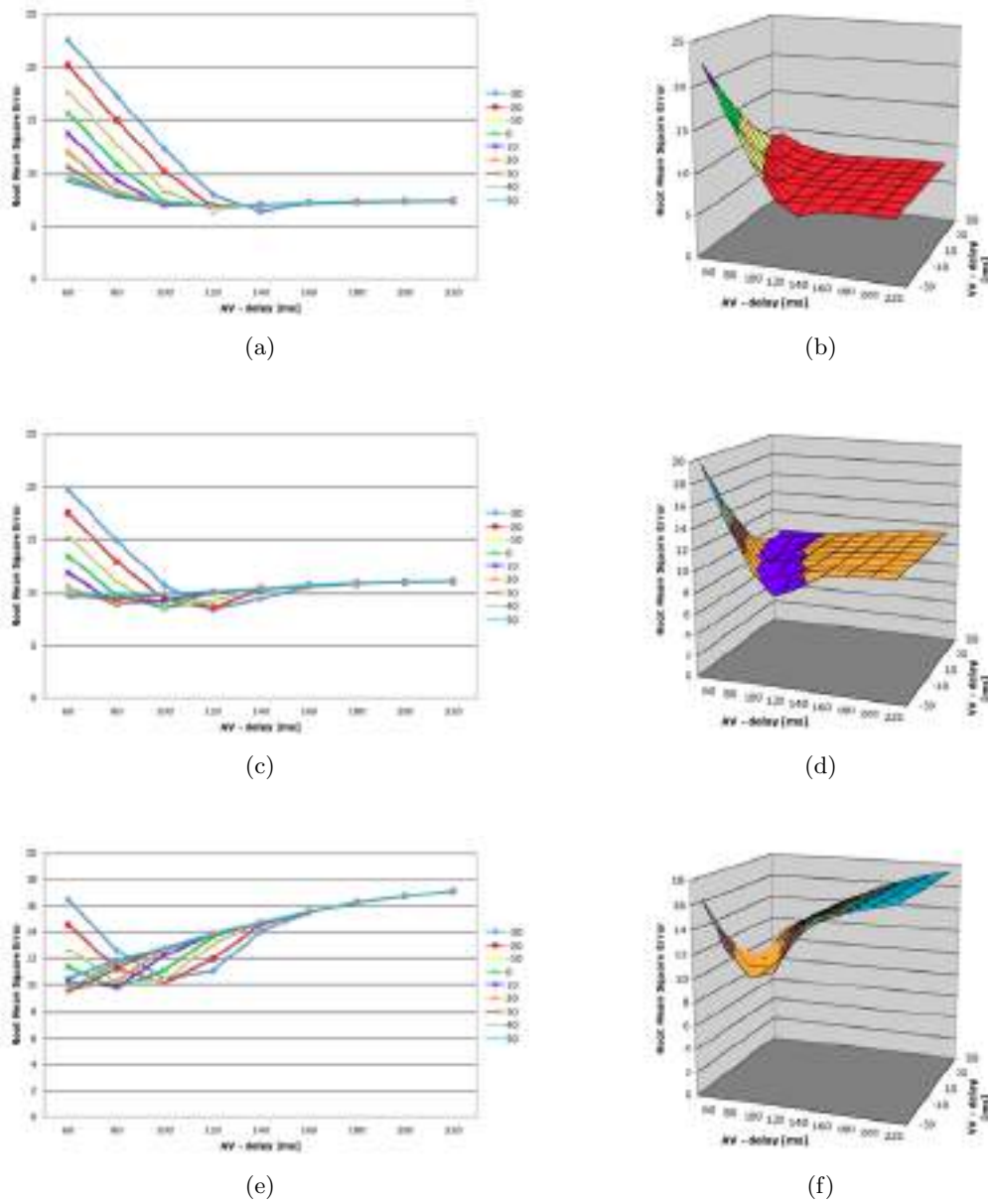


**Figure 12.31.** The root mean square error is shown in  $[ms]$  with respect to AV- and VV-delay for the best electrode position in the simulations of the left bundle branch block on the Visible Man data set using the sequential search algorithm.

The optimal AV-delay was 260  $ms$  for all electrode set-ups with conduction velocities of 100 % and 80 %. With a reduced conduction velocity of 60 % the optimal AV-delay was 240  $ms$  for all



Lead Position	A-V block III			LBBB		
	min $E_{RMS}$	AV-delay	VV-delay	Min $E_{RMS}$	AV-delay	VV-delay
No pacing	107.31	n/a	n/a	37.17	n/a	n/a
RA	4.34	260	-10	13.40	220	0
RB	4.15	260	-10	13.61	220	0
RC	4.41	260	-10	13.11	220	0
RD	4.43	260	-10	12.68	240	-20
RE	4.77	260	-10	11.83	240	-20
RF	3.85	260	-10	13.47	220	0
RG	4.25	260	-10	12.29	220	0
RH	4.34	260	-10	11.81	240	0
RI	3.62	260	-10	11.53	220	0
RJ	3.21	260	0	13.78	260	-20
RK	4.16	260	-10	10.12	220	0
RL	5.61	260	-10	13.08	160	70

**Table 12.17.** The minimal  $E_{RMS}$  in [ms] in different electrode positioning for the conduction velocity set to 100% of the physiological values is shown for the patient data. The corresponding AV and VV-delays are shown, also, together with the respective electrode set-up. The optimisation was carried out by the sequential search algorithm.

Lead Position	A-V block III			LBBB		
	min $E_{RMS}$	AV-delay	VV-delay	Min $E_{RMS}$	AV-delay	VV-delay
No pacing	107.31	n/a	n/a	51.89	n/a	n/a
RA	4.15	260	-20	17.27	180	0
RB	3.95	260	-20	17.52	160	40
RC	4.11	260	-20	17.11	160	40
RD	4.09	260	-20	16.18	180	10
RE	4.19	260	-20	14.98	200	0
RF	3.75	260	-20	18.35	160	20
RG	4.06	260	-20	16.02	180	10
RH	4.08	260	-20	15.19	180	20
RI	3.56	260	-20	14.97	180	10
RJ	3.43	260	-20	19.88	180	-20
RK	3.70	260	-20	13.50	160	40
RL	3.28	260	-20	16.29	140	70

**Table 12.18.** The minimal  $E_{RMS}$  in [ms] in different electrode positioning for the conduction velocity set to 80% of the physiological values is shown for the patient data. The corresponding AV and VV-delays are shown, also, together with the respective electrode set-up. The optimisation was carried out by the sequential search algorithm.

electrode pairs. The VV-delay changed, however, with respect to conduction velocity. For 100 % conduction velocity, it was  $-10$  ms for all electrodes but RJ (0 ms). A 20 % reduction in the con-

Lead Position	A-V block III			LBBB		
	min $E_{RMS}$	AV-delay	VV-delay	Min $E_{RMS}$	AV-delay	VV-delay
No pacing	107.31	n/a	n/a	66.01	n/a	n/a
RA	5.30	240	-30	25.96	80	50
RB	5.13	240	-30	27.16	60	70
RC	5.27	240	-30	26.11	80	40
RD	5.22	240	-30	24.57	100	40
RE	5.28	240	-30	22.32	100	60
RF	5.01	240	-30	29.88	80	70
RG	5.25	240	-30	25.04	120	20
RH	5.25	240	-30	22.96	120	30
RI	4.85	240	-30	22.95	100	30
RJ	4.81	240	-30	32.61	100	0
RK	4.86	240	-30	19.66	120	20
RL	4.63	240	-30	26.75	60	70

**Table 12.19.** The minimal  $E_{RMS}$  in  $[ms]$  in different electrode positioning for the conduction velocity set to 60% of the physiological values is shown for the patient data. The corresponding AV and VV-delays are shown, also, together with the respective electrode set-up. The optimisation was carried out by the sequential search algorithm.

duction velocity caused the optimal VV-delay to decrease to  $-20\ ms$  and a further reduction to 60 % of the physiological conduction velocity showed optimal  $E_{RMS}$  with  $-30\ ms$  for all electrodes. Figure 12.32 shows the simulation results for the optimal electrode positions for the AV block in the patients anatomy.

### 12.3.2.2 Left Bundle Branch Block in the Patient Anatomy

The simulations of CRT on the patients anatomy with a left bundle branch block showed similar results to the Visible Man anatomy with respect to the reduction in conduction velocity. The lower the conduction velocity, the higher the optimal  $E_{RMS}$ . While the  $E_{RMS}$  could be reduced from  $37.17\ ms$  to  $10.12\ ms$  given 100 % conduction velocity in the best case, it was only reduced to about 30 % of the  $E_{RMS}$  in the simulation of the pathology with 60 % conduction velocity (see figure 12.34). The optimal electrode pairs were RK for all conduction velocities with an  $E_{RMS} = 10.12\ ms$ ,  $E_{RMS} = 13.5\ ms$  and  $E_{RMS} = 19.66\ ms$  for conduction velocities 100 %, 80 % and 60 %, respectively. The highest optimal  $E_{RMS}$  were at electrode pair RJ with  $E_{RMS} = 13.78\ ms$ ,  $E_{RMS} = 19.88\ ms$  and  $E_{RMS} = 32.61\ ms$ . The mean optimal  $E_{RMS}$  for all electrodes increased by 4 - 5 % with a respective reduction of 20 % conduction velocity. The standard deviation of the optimal errors was  $1.08\ ms$  (100 % conduction velocity),  $1.72\ ms$  (80 % conduction velocity) and  $3.48\ ms$  (60 % conduction velocity).

The AV-delay ranged from  $160\ ms$  (electrode pair RL) to  $260\ ms$  (electrode pair RJ) and the

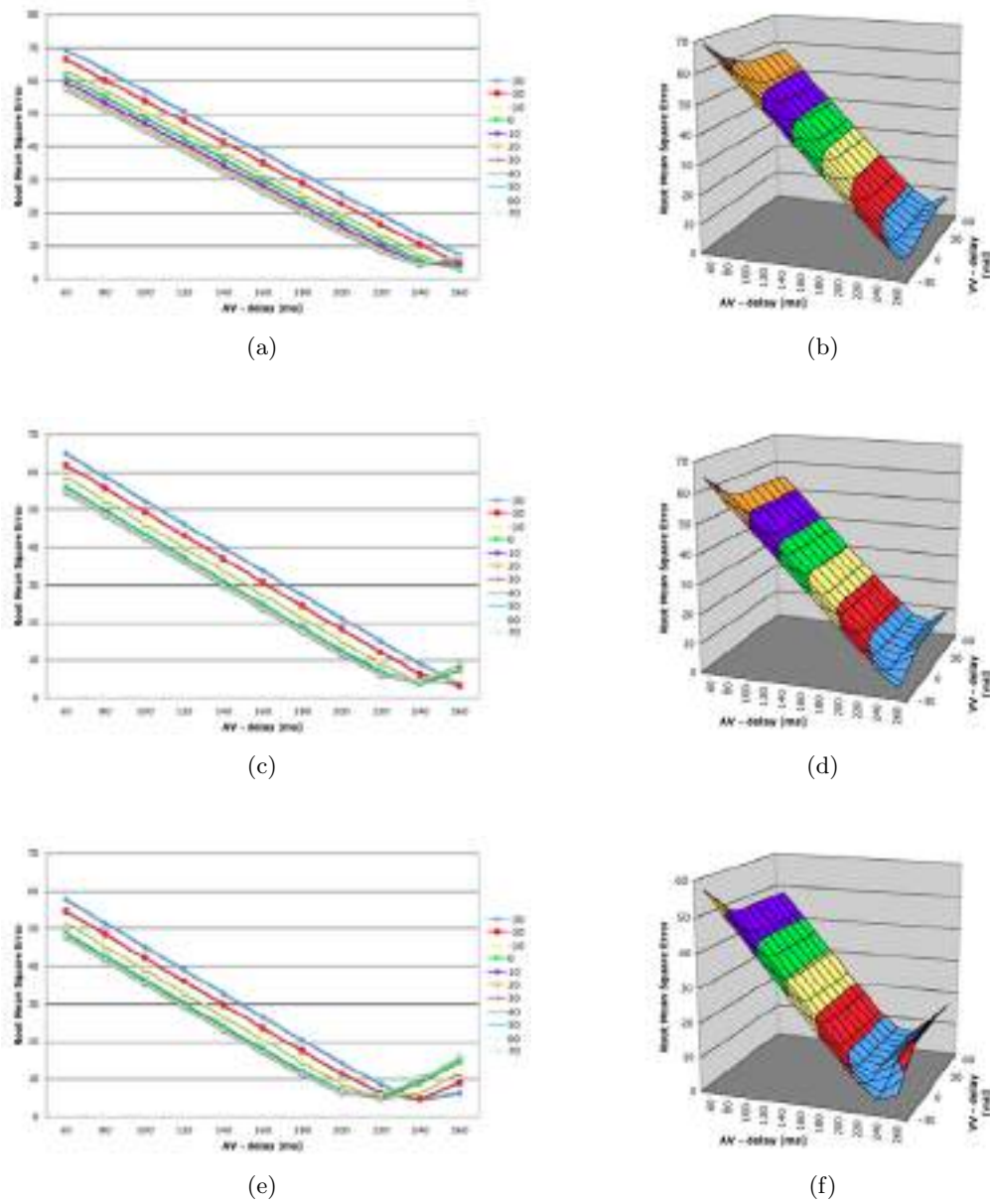


**Figure 12.32.** The root mean square error is shown in  $[ms]$  with respect to AV- and VV-delay for the best electrode position in the simulations of the AV block on the patient data set using the sequential search algorithm.

VV-delay was between  $-20\ ms$  and  $70\ ms$  for the simulations with 100 % conduction velocity. However, it was mostly  $220\ ms$  and  $0\ ms$  for the AV- and VV-delay (see table 12.18). A reduction

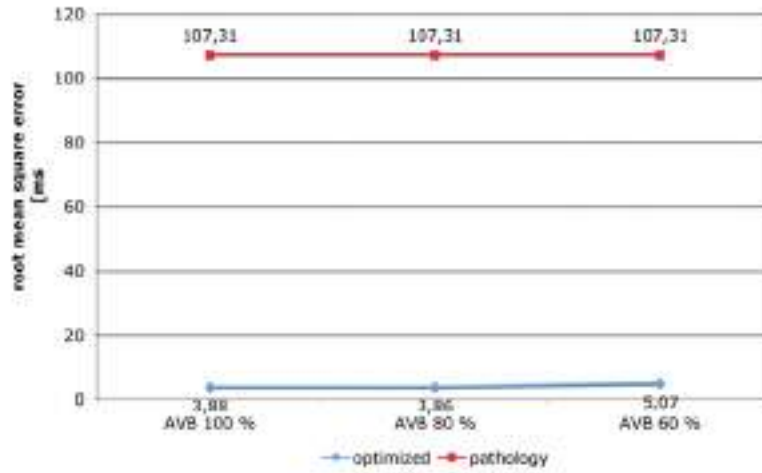


**Figure 12.33.** This figure shows the mean root mean square error with respect to the simulated pathology of an AV block III (AVB) and reduced conduction velocity in the patient data set using a sequential search of the minimum values. The connecting lines are for visualization only.

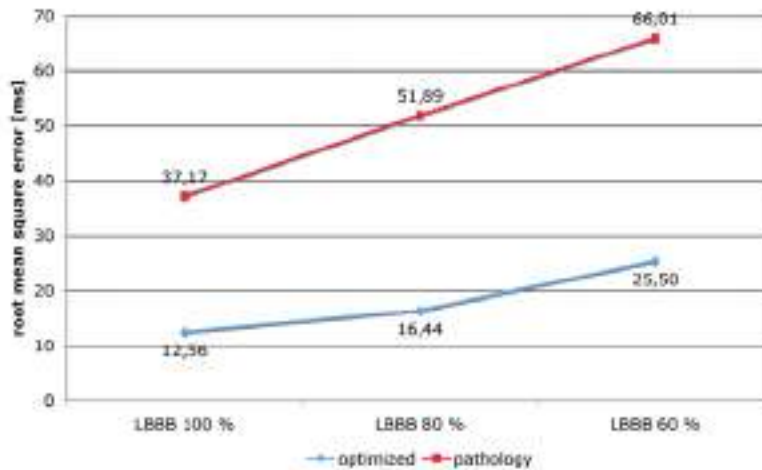


**Figure 12.34.** This figure shows the mean root mean square error with respect to the simulated pathology of an left bundle branch block (LBBB) and reduced conduction velocity in the patient data set using a sequential search of the minimum values. The connecting lines are for visualization only.

in AV-delay can be observed for the simulations with reduced conduction velocity. This behaviour is in conjunction with an increase in VV-delay. For 80 % conduction velocity, an AV-delay of 160 ms/180 ms with a VV-delay of 20 ms/10 ms produced the lowest  $E_{RMS}$  (see table 12.18). With 60 % conduction velocity, it was mostly  $100 \pm 20$  ms for the AV-delay. The VV-delay, however, ranged between 0 ms and 70 ms (see table 12.19).

Figure 12.35 shows the simulation results for the optimal electrode positions for the left bundle branch block in the patients anatomy.

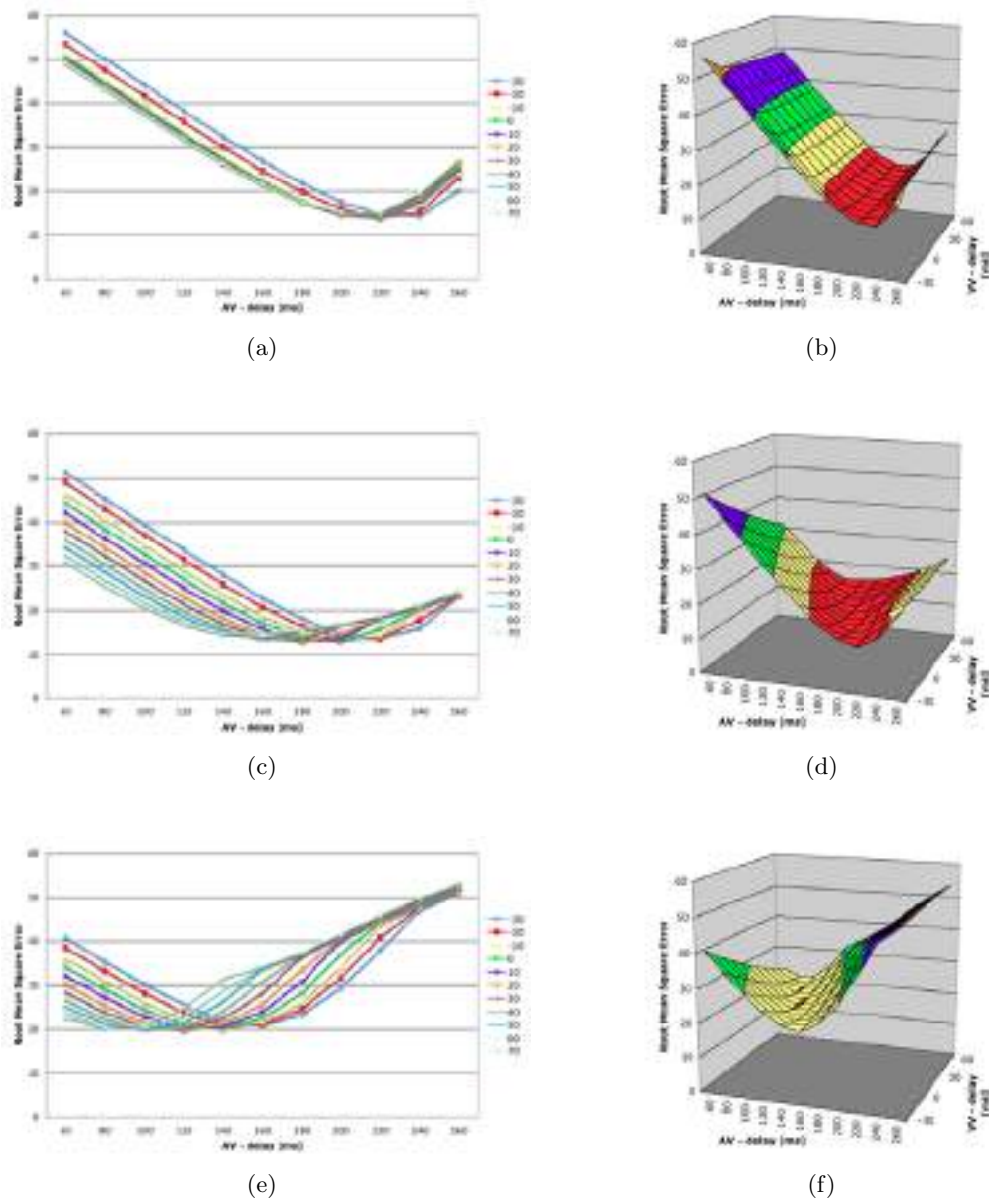


**Figure 12.35.** The root mean square error is shown in  $[ms]$  with respect to AV- and VV-delay for the best electrode position in the simulations of the left bundle branch block on the patient data set using the sequential search algorithm.

### 12.3.3 Optimization of CRT using the Downhill Simplex Algorithm

The intention of using the downhill simplex algorithm to find optimal AV- and VV-delay was to reduce the computation time significantly. While the simulation of all electrode and timing set-ups of one pathology took 972 simulations in the Visible Man and 1452 simulations in the patient data set, the mean simulation count for one pathology using the downhill simplex algorithm was around 250 for the Visible Man data set and 293 for the patient data set. While the simulation of all electrode and timing set-ups took 4-5 days on six processors in daily routine, the results for using the downhill simplex algorithm was gained overnight in roughly 18 hours on the same six processors. The following section describes the results of using this search algorithms with respect to the previous sections.

#### 12.3.3.1 Minimum Search in the Visible Man Data Set with AV block III

Tables 12.20 - 12.22 summarize the results of the simulations with the Visible Man data-set and an AV block III with 100 %, 80 % and 60 % of the physiological ventricular conduction velocity, respectively. The minimal root mean square errors found do not differ greatly between the downhill simplex algorithm and the ordinary computation of the  $E_{RMS}$  values on the grid. It also shows the same behaviour with respect to the reduction in conduction velocity: 4.00 *ms*, 5.14 *ms* and 6.98 *ms* as the mean  $E_{RMS}$  for all electrodes (see figure 12.36). It can be noted that these values are below those obtained previously, i. e. achieve better results. The standard deviation is also in the same range below 0.5 *ms*. The electrode positions with which the best pacing set-up was gained differs. Electrode pair RI yields the best results with 3.18 *ms* and 4.23 *ms* for 100 % and 80 % conduction velocity. The lowest  $E_{RMS}$  for the 60 % conduction velocity simulations was obtained by pacing leads RG with 5.91 *ms*.

Concerning AV- and VV-delay for the optimal timing in all electrodes, the AV-delay ranged from 104.80 *ms* to 196.19 *ms* and the VV-delay from -85.78 *ms* to 44.71 *ms* (100 % conduction velocity) (see table 12.20). Only four of the twelve electrode pairs had a positive VV-delay. For electrodes RI, an AV-delay of 107.33 *ms* and a VV-delay of 44.71 *ms* produced the smallest  $E_{RMS}$  (see table 12.20).

Only six of twelve electrode set-ups had a negative VV-delay as optimal timing when reducing the conduction velocity by 20 %. These values were smaller in magnitude, also, with a range between -55.89 *ms* and 43.44 *ms* with the only exception of 84.59 *ms* for electrodes RG. The optimal AV-delay was smaller for all electrodes. For most electrode pairs, the AV-delay was below 100 *ms* and ranged from 80.78 *ms* to 167.46 *ms* (see table 12.21).

The optimal AV-delays decreased even further to a range of 48.85 *ms* to 134.48 *ms*. The trend of increasing VV-delay with decreasing conduction velocity is also visible with only four of twelve VV-delays being negative. The VV-delay ranged around  $56 \pm 15$  *ms* for the positive VV-delays. For electrode pair RG, which produced the lowest  $E_{RMS}$  value, it was 42.07. This value was obtained in 17 simulations for this electrode pair instead of 81 simulations previously (see table 12.22).

The number of simulations for each electrode ranged between 12 to 35. As shown in figure 12.36, the number of simulations per pathology decreased with decreasing conduction velocity: 301 (100 % conduction velocity), 280 (% conduction velocity) and even 256 for the simulations with 60 % conduction velocity. Thus, the results are obtained in 25 - 30 % of the time compared to the sequential search algorithm.

Lead Position	A-V block III			
	min $E_{RMS}$	AV-delay	VV-delay	Simulations
No pacing	51.6	n/a	n/a	n/a
RA	3.97	154.91	-44.08	27
RB	4.07	188.73	-78.57	29
RC	3.97	161.91	-50.10	28
RD	4.05	176.42	-67.02	26
RE	4.07	178.85	-68.88	27
RF	4.39	114.91	26.53	19
RG	3.89	104.80	14.19	30
RH	4.07	196.19	-85.78	27
RI	3.18	107.33	44.71	20
RJ	4.25	111.09	21.97	16
RK	4.02	157.41	-48.00	27
RL	4.04	177.16	-66.76	25

**Table 12.20.** The minimal  $E_{RMS}$  in different electrode positioning for the conduction velocity set to 100% of the physiological value in the Visible Man data set. The corresponding AV and VV-delays are shown, also, together with the respective electrode set-up. The results were computed by the downhill simplex search algorithm

### 12.3.3.2 Minimum Search in the Visible Man Data Set with Left Bundle Branch Block

The simulations of the LBBB in the Visible Man data set produced almost exactly the same results with respect to the mean error and the lowest error values (see tables 12.23 - 12.25): 5.82 *ms* vs. 5.94 *ms* (100 % conduction velocity), 7.54 *ms* vs. 7.82 *ms* (80 % conduction velocity) and 10.69 *ms* vs. 10.67 *ms* (60 % conduction velocity). The error range, however, is greater for the simulations with the downhill simplex algorithm (compare figures 12.30 and 12.37). However, the results were obtained even faster than in the simulations of the AV block. Only 219, 225, 226 simulations were needed to find an optimal AV- and VV-delay for all electrodes in the simulations with 60 %, 80 % and 100 % conduction velocity, respectively. Again, while there is a decrease in conduction velocity, there is a decrease in the number of simulations needed.

Lead Position	A-V block III			
	min $E_{RMS}$	AV-delay	VV-delay	Simulations
No pacing	51.6	n/a	n/a	n/a
RA	5.35	98.95	9.43	23
RB	5.22	167.46	-67.75	29
RC	5.47	92.60	15.66	19
RD	5.17	151.95	-53.12	28
RE	5.23	154.33	-55.89	35
RF	5.47	102.5	43.44	14
RG	4.66	80.78	84.59	15
RH	5.12	87.56	22.49	23
RI	4.23	94.17	19.50	19
RJ	5.30	104.80	-6.77	25
RK	5.31	106.76	-1.95	23
RL	5.15	156.17	-55.62	27

**Table 12.21.** The minimal  $E_{RMS}$  in different electrode positioning for the conduction velocity set to 80% of the physiological value in the Visible Man data set. The corresponding AV and VV-delays are shown, also, together with the respective electrode set-up. The results were computed by the downhill simplex search algorithm

Lead Position	A-V block III			
	min $E_{RMS}$	AV-delay	VV-delay	Simulations
No pacing	51.6	n/a	n/a	n/a
RA	6.89	50.55	50.31	25
RB	7.24	134.48	-53.39	23
RC	7.00	48.85	52.14	21
RD	7.19	122.03	-36.82	23
RE	7.36	102.15	-16.75	30
RF	7.42	88.90	43.03	16
RG	5.91	57.19	42.07	17
RH	6.76	56.22	42.25	23
RI	6.48	71.17	67.16	18
RJ	7.51	80	50	15
RK	6.93	56.36	43.43	21
RL	7.11	122.03	-36.82	24

**Table 12.22.** The minimal  $E_{RMS}$  in different electrode positioning for the conduction velocity set to 60% of the physiological value in the Visible Man data set. The corresponding AV and VV-delays are shown, also, together with the respective electrode set-up. The results were computed by the downhill simplex search algorithm

With respect to pacemaker timing, it can be noted that the VV-delay in all simulations of the LBBB is generally positive. Only for the simulations with 100 % conduction velocity, five of twelve VV-delays were below zero but not greatly. For all conduction velocities, the VV-delay was 50 ms



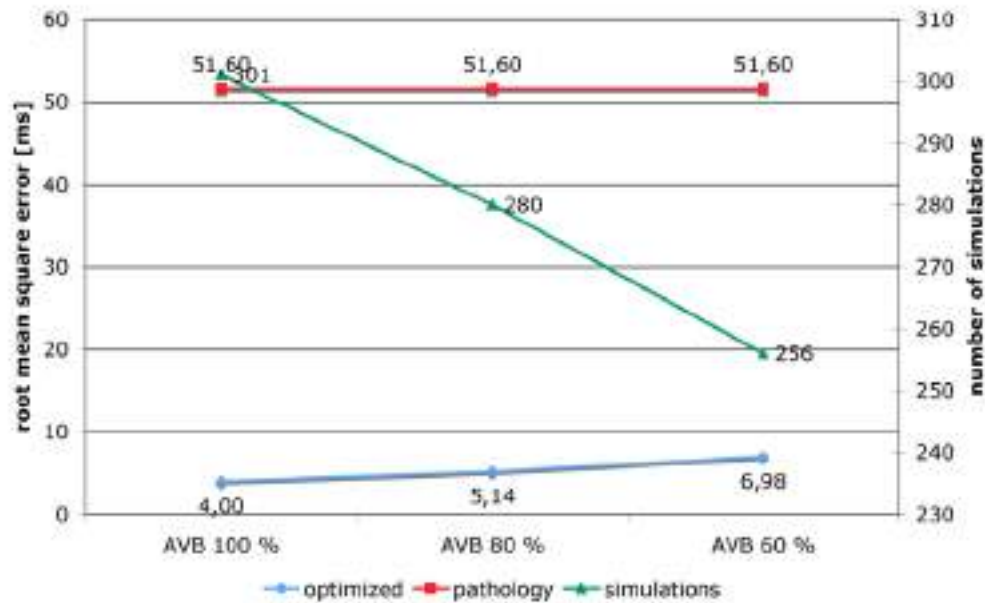


**Figure 12.36.** This figure shows the mean root mean square error with respect to the simulated pathology of an AV block III (AVB) and reduced conduction velocity in the Visible Man data set using the downhill simplex algorithm. Also shown is the number of simulations which were carried out to achieve the results. The connecting lines are for visualization only.

Lead Position	LBBB			
	min $E_{RMS}$	AV-delay	VV-delay	Simulations
No pacing	7.47	n/a	n/a	n/a
RA	5.80	120	15	14
RB	7.07	120	15	13
RC	6.04	120	15	14
RD	6.38	110	50	14
RE	5.30	113.98	-1.47	23
RF	6.01	111.25	29.22	20
RG	5.58	112.74	-0.27	28
RH	5.23	116.32	-3.70	31
RI	6.33	98.87	31.54	21
RJ	6.25	108.75	18.28	19
RK	5.57	115.41	-3.07	25
RL	5.68	128.94	-15.79	4

**Table 12.23.** The minimal  $E_{RMS}$  in different electrode positioning for the conduction velocity set to 100% of the physiological value in the Visible Man data set. The corresponding AV and VV-delays are shown, also, together with the respective electrode set-up. The results were computed by the downhill simplex search algorithm

Lead Position	LBBB			
	min $E_{RMS}$	AV-delay	VV-delay	Simulations
No pacing	11.16	n/a	n/a	n/a
RA	6.99	98.06	2.13	23
RB	9.92	94.69	38.79	12
RC	7.29	98.06	2.13	23
RD	8.63	80	50	12
RE	6.77	91.36	13.77	27
RF	8.13	102.36	35.25	15
RG	7.36	92.48	11.29	19
RH	6.87	100.31	4.34	21
RI	8.28	84.14	32.02	17
RJ	8.33	93.04	25.05	16
RK	6.93	97.66	6.84	28
RL	8.31	99.06	51.37	13

**Table 12.24.** The minimal  $E_{RMS}$  in different electrode positioning for the conduction velocity set to 80% of the physiological value in the Visible Man data set. The corresponding AV and VV-delays are shown, also, together with the respective electrode set-up. The results were computed by the downhill simplex search algorithm

Lead Position	LBBB			
	min $E_{RMS}$	AV-delay	VV-delay	Simulations
No pacing	17.63	n/a	n/a	n/a
RA	9.72	63.79	21.32	19
RB	12.01	93.13	-17.27	20
RC	10.20	56.14	32.50	20
RD	10.90	55.31	24.02	16
RE	9.53	50.16	35.92	22
RF	11.96	80	50	14
RG	10.51	55.74	27.13	18
RH	9.76	60.68	25.20	20
RI	11.95	56.56	13.09	15
RJ	12.16	70	6.25	15
RK	9.49	48.55	42.45	19
RL	9.89	71.41	10.76	21

**Table 12.25.** The minimal  $E_{RMS}$  in different electrode positioning for the conduction velocity set to 60% of the physiological value in the Visible Man data set. The corresponding AV and VV-delays are shown, also, together with the respective electrode set-up. The results were computed by the downhill simplex search algorithm

at the most but ranged around  $20 \pm 15$  ms. The AV-delay timing, however, changed with respect to conduction velocity: the lower the conduction velocity the lower the AV-delay.

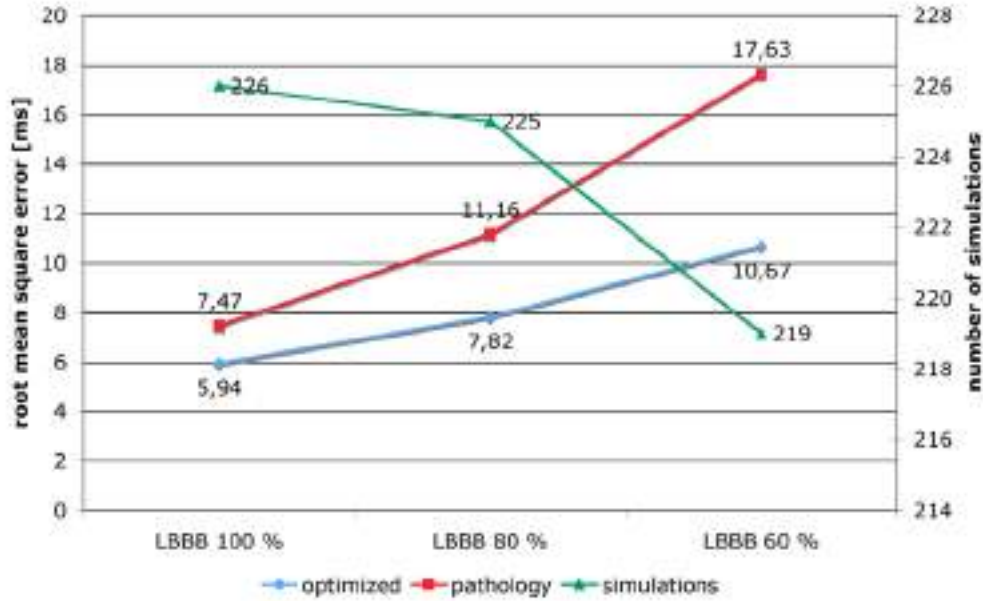


**Figure 12.37.** This figure shows the mean root mean square error with respect to the simulated pathology of an left bundle branch block (LBBB) and reduced conduction velocity in the Visible Man data set using the downhill simplex algorithm. Also shown is the number of simulations which were carried out to achieve the results. The connecting lines are for visualization only.

The electrode position to produce the smallest  $E_{RMS}$  differed. For the simulations with 100 % conduction velocity, electrode pair RH yielded the best result with an  $E_{RMS} = 5.32 \text{ ms}$ . Electrodes RE with  $E_{RMS} = 6.77 \text{ ms}$  and RK with  $E_{RMS} = 9.49 \text{ ms}$  had the best results for the simulations with 80 % and 60 % conduction velocity, respectively.

### 12.3.3.3 Minimum Search in the Patient Data Set with AV Block III

A different picture is given by the simulations with the patient data set (see figure 12.38 and tables 12.26 - 12.27). The downhill simplex algorithm does not achieve a mean  $E_{RMS}$  value as low as before given an AV block III as pathology. However, the best electrode positions with an optimal timing delay yield  $E_{RMS}$  values that are closer to the previously acquired optimal positions. Electrode pair RL produces the lowest error (3.9 ms) with an AV-delay of 248.87 ms and a VV-delay of 111.22 ms for the simulations with 100 % conduction velocity. It is the same electrode pair with an AV-delay of 234.4 ms and a VV-delay of 126.73 ms that yields the lowest  $E_{RMS}$  with 4.27 ms in the simulations with 20 % reduced conduction velocity. For 40 % reduction in the conduction velocity, the optimal electrode did not change. The AV-delay is smaller with 211.4 ms but the VV-delay is in the vicinity of the previous values with 108.52 ms.

It can be noted that the range, in which the optimal timing lies, is not as wide compared with the Visible Man data set. The range of the AV-delay is only about 43 *ms* and 24 *ms* for the VV-delay in the simulations with 100 % conduction velocity (see table 12.27). With reduced conduction velocities it seems not to be so. But only large AV-delays yield negative VV-delays. Considering an AV-delay of  $215 \pm 20$  *ms* only, the VV-delay will lie a range of 109 *ms* to 227 *ms* (see table 12.27). For the simulations with 60 % conduction velocity, the magnitude of both AV- and VV-delay is smaller and more diverse (see table 12.28).

With respect to speed-up of the simulations, the results were obtained within 22 % - 29 % of the previous simulation time.

Lead Position	A-V block III			
	min $E_{RMS}$	AV-delay	VV-delay	Simulations
No pacing	107.31	n/a	n/a	n/a
RA	10.02	205.59	114.12	21
RB	9.06	215.55	130.12	20
RC	9.42	213.75	106.88	18
RD	9.74	213.75	106.88	18
RE	9.38	227.73	128.68	22
RF	7.07	228.91	130.53	21
RG	9.87	215.55	130.12	19
RH	9.72	220	137.5	20
RI	6.35	234.34	116.55	22
RJ	4.41	243.81	137.69	25
RK	6.69	241.80	123.32	26
RL	3.90	248.87	111.22	28

**Table 12.26.** The minimal  $E_{RMS}$  in different electrode positioning for the conduction velocity set to 100% of the physiological value in the patient data set. The corresponding AV and VV-delays are shown, also, together with the respective electrode set-up. The results were computed by the downhill simplex search algorithm

#### 12.3.3.4 Minimum Search in the Patient Data Set with Left Bundle Branch Block

The results of the simulations with the left bundle branch block in the patient data were gained faster compared with the simulations of the AV block III in the same data set with an average of 254 simulations. The simulations with 60 % conduction velocity were even carried out in 16 % of the previous simulation time.

Lead Position	A-V block III			
	min $E_{RMS}$	AV-delay	VV-delay	Simulations
No pacing	107.31	n/a	n/a	n/a
RA	5.01	354.57	-119.73	32
RB	5.01	340.61	-105.53	61
RC	9.64	197.62	108.79	21
RD	9.95	195.82	122.46	22
RE	9.55	211.09	122.73	19
RF	7.25	211.09	122.73	19
RG	5.01	533.13	-298.04	46
RH	10.10	194.38	115.63	19
RI	6.57	216.91	117.13	23
RJ	5.04	226.37	117.78	23
RK	6.83	228.59	116.04	21
RL	4.27	234.41	126.73	24

**Table 12.27.** The minimal  $E_{RMS}$  in different electrode positioning for the conduction velocity set to 80% of the physiological value in the patient data set. The corresponding AV and VV-delays are shown, also, together with the respective electrode set-up. The results were computed by the downhill simplex search algorithm

Lead Position	A-V block III			
	min $E_{RMS}$	AV-delay	VV-delay	Simulations
No pacing	107.31	n/a	n/a	n/a
RA	9.79	152.86	81.84	20
RB	8.58	169.75	59.76	23
RC	6.52	309.44	-98.40	45
RD	6.52	309.44	-98.40	45
RE	6.53	344.92	-135.46	35
RF	7.89	178.01	81.34	23
RG	6.54	343.29	-134.47	49
RH	6.52	323.63	-112.78	37
RI	6.01	200.93	30.85	40
RJ	6.36	198.01	118.09	24
RK	7.49	205.74	93.89	25
RL	5.38	211.40	108.52	21

**Table 12.28.** The minimal  $E_{RMS}$  in different electrode positioning for the conduction velocity set to 60% of the physiological value in the patient data set. The corresponding AV and VV-delays are shown, also, together with the respective electrode set-up. The results were computed by the downhill simplex search algorithm

The results of the root mean square error, however, are similar to the previously obtained results with a mean of 15.74 *ms* (100 % conduction velocity), 16.65 *ms* (80 % conduction velocity) and 25.59 *ms* (60 % conduction velocity) (see figure 12.39). Only the simulations with 100 %

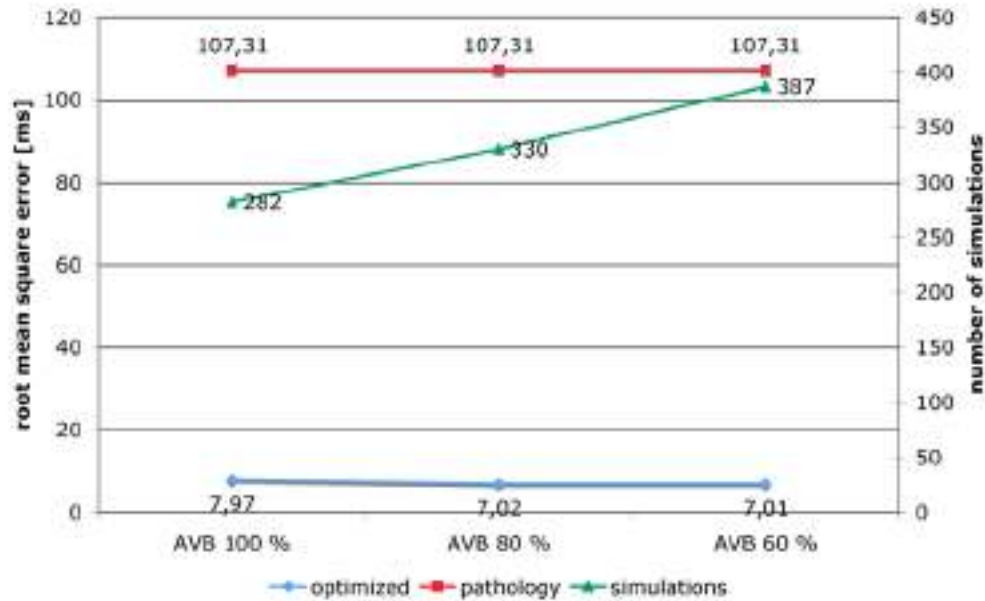


**Figure 12.38.** This figure shows the mean root mean square error with respect to the simulated pathology of an AV block III (AVB) and reduced conduction velocity in the patient data set using the downhill simplex algorithm. Also shown is the number of simulations which were carried out to achieve the results. The connecting lines are for visualization only.

conduction velocity yield a mean  $E_{RMS}$  which is higher compared with the results which were computed without the downhill simplex algorithm. With regard to the lowest overall  $E_{RMS}$ , the downhill simplex algorithm found a pacemaker timing which yield better results with 9.89 ms (100 % conduction velocity), 12.59 ms (80 % conduction velocity) and 18.92 ms (60 % conduction velocity). These results are obtained in the simulations with electrode pair RK which therefore seems the optimal electrode set up compared with the other electrode positions (see tables 12.29 - 12.31).

The optimal timing of the AV- and VV-delay has only positive values. For 100 % conduction velocity, the range of the VV-delay is large with values between 3.24 ms and 137.5 ms. For electrode set up RK, the VV-delay was 10.51 ms. The AV-delay did not vary as much with values between 175.94 ms and 228.32 ms. The latter value was the AV-delay at electrodes RK, which had the best  $E_{RMS}$  12.29).

The AV-delay was generally lower in the simulations with 80 % conduction velocity ranging from 146.93 ms to 205.76 ms (see table 12.30). Also, the VV-delay was lower with values from 9.87 ms to 106.05 ms. The best results were gained with an AV-delay of 187.66 ms and a VV-delay of 33.73 ms at pacing leads RK.

This trend of reduced AV-delay with reduced conduction velocity is continues for the simulations with 60 % conduction velocity. The VV-delay varies, however, and does not show the same behaviour. The AV- and VV-delay ranged between 48.87 *ms* - 111.44 *ms* and 9.53 *ms* - 112.72 *ms*, respectively. For electrode pair RK, the AV- and VV-delay was 108.75 *ms* and 83.91 *ms* for the best result.

The average number of simulations per electrode set up was higher than for the Visible Man data set. The fastest searches required 12 - 20 simulations to reach the minimal  $E_{RMS}$ . However, some electrode set ups required over 40 simulations (pathology: LBBB) up to even 61 simulations (pathology: AV block III).

Lead Position	LBBB			
	min $E_{RMS}$	AV-delay	VV-delay	Simulations
No pacing	37.17	n/a	n/a	n/a
RA	16.05	175.94	52.19	23
RB	15.82	180.91	52.77	33
RC	15.74	215	102.5	14
RD	15.01	211.41	108.52	16
RE	14.28	220	137.5	14
RF	14.57	194.38	115.63	19
RG	13.97	220	137.5	14
RH	13.33	220	137.5	17
RI	11.29	229.06	3.24	27
RJ	14.80	211.09	122.73	20
RK	9.89	228.32	10.51	46
RL	10.94	186.56	53.55	22

**Table 12.29.** The minimal  $E_{RMS}$  in different electrode positioning for the conduction velocity set to 100% of the physiological value in the patient data set. The corresponding AV and VV-delays are shown, also, together with the respective electrode set-up. The results were computed by the downhill simplex search algorithm

Lead Position	LBBB			
	min $E_{RMS}$	AV-delay	VV-delay	Simulations
No pacing	51.89	n/a	n/a	n/a
RA	18.34	173.85	31.56	23
RB	18.86	162.85	53.69	18
RC	18.04	180.95	34.32	31
RD	17.36	189.88	27.07	24
RE	16.27	205.76	13.07	25
RF	18.77	154.92	106.05	21
RG	16.83	171.48	40.088	20
RH	16.10	180.65	32.22	23
RI	14.61	189.88	27.07	24
RJ	17.32	190.08	9.87	30
RK	12.59	187.66	33.73	24
RL	14.69	146.93	69.67	21

**Table 12.30.** The minimal  $E_{RMS}$  in different electrode positioning for the conduction velocity set to 80% of the physiological value in the patient data set. The corresponding AV and VV-delays are shown, also, together with the respective electrode set-up. The results were computed by the downhill simplex search algorithm

Lead Position	LBBB			
	min $E_{RMS}$	AV-delay	VV-delay	Simulations
No pacing	66.01	n/a	n/a	n/a
RA	27.98	69.34	84.97	21
RB	28.89	48.87	112.72	23
RC	27.13	62.42	98.60	18
RD	25.64	83.01	80.80	22
RE	23.39	111.44	64.53	17
RF	29.92	75	80.63	16
RG	24.78	79.92	98.88	18
RH	23.58	106.48	70.71	17
RI	22.13	110.88	51.38	16
RJ	29.79	103.75	9.53	13
RK	18.92	108.75	83.91	12
RL	24.95	60.80	90.49	19

**Table 12.31.** The minimal  $E_{RMS}$  in different electrode positioning for the conduction velocity set to 60% of the physiological value in the patient data set. The corresponding AV and VV-delays are shown, also, together with the respective electrode set-up. The results were computed by the downhill simplex search algorithm



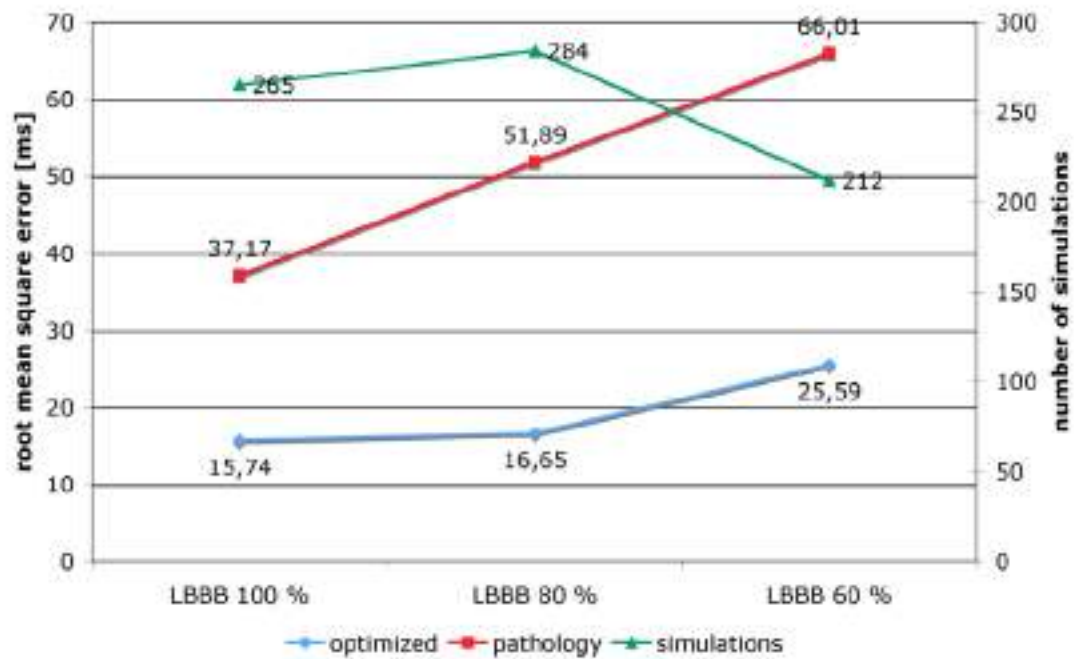


**Figure 12.39.** This figure shows the mean root mean square error with respect to the simulated pathology of an AV block III (AVB) and reduced conduction velocity in the patient data set using the downhill simplex algorithm. Also shown is the number of simulations which were carried out to achieve the results. The connecting lines are for visualization only.



## Discussion

*“In all things of nature there is something of the marvelous.”*

Aristotle

Greek critic, philosopher, physicist, and zoologist (384 BC - 322 BC)

### 13.1 Computer Model of Atrial Fibrillation

The model of AF initiation by ectopic activity reflects the findings in literature with respect to occurrence in relation to sinus beat and frequency of focal discharges [108, 290]. The arrangement of the stimuli  $s_1$  and  $s_2$  does not seem to influence the generation of AF. It can be hypothesized that either an area is vulnerable for AF initiation, then the positioning of stimulus  $s_2$  with respect to  $s_1$  can be neglected, or AF will not appear in any arrangement of  $s_1$  and  $s_2$ . The simulations show further that the initiating rotor will be self-terminating and is not the driving rotor. Re-entrant circuits created by rotor waves at another location will re-excite the atria. These re-entries will be sustained. Thus, if a focus of a driving rotor were ablated, the therapy would probably cure the current instance of AF. The recurrence rate might be still high in that case since the area of abnormal activation would not have been treated due to misleading excitation pattern beforehand. The break up of the wave fronts occurs at structurally heterogeneous areas of the atria. The excitation pattern will look similar to the findings in [4]. While snakes first characterize the break up of the pattern, small rotors and multiple wavelets appear at anatomically smooth areas. Thus, the maintenance of atrial fibrillation in the atria is due to both rotors and snakes in the computer simulations. However, the further the longer AF persisted in the simulation, the more dominant the multiple wavelets became confirming Moe's wavelet theory [189]. In the end, the maintenance of AF seems to depend on the local refractoriness and excitability in all computer simulations at a later stage of the simulation when the stable rotor wave breaks up and wavelets appear. Since wavelets have a small radius, their pathways are not so much influenced by macroscopic anatomical structures. This behavior has been observed in [153]. However, this result may be due to the anatomical model used. Although the model presented in this work shows a realistic 3D

anatomy including wall thickness, crista terminalis, Bachmann's bundle and the pectinate muscles, even further detail is required to reflect the fibrous structures observed in [4].

The issue of measuring different cycle lengths at different times and areas of the atria has also been observed in the computer models. The results reflect both findings in [212, 200], which seem to be contradictory at a first glance. The computer simulations show the dependence of excitation pattern on the initiating stimulus and the genesis of AF. The cycle length is generally shorter in the pulmonary veins than in the atria at the onset of AF. The longer the fibrillation persists the more chaotic the excitation pattern becomes in the atria. At a later time instance, the regions further from the roof of the atria, e.g. the pulmonary veins, often show stable re-entrant circuits and hence a longer cycle length compared with the atria. Hence, the results of [212, 200] do not contradict each other but reflect the importance of evaluating the arrhythmia on an individual patient basis including its pathogenetic history.

Since the conduction velocity of the tissue was homogeneously reduced in all computer simulations, fragmented conduction was not included. Still, a high percentage of pulmonary vein triggers lead to a chaotic excitation pattern. The minimum radius of the focus to initiate a rotor wave depends on the conduction velocity. The smaller the conduction velocity the smaller can be the radius to create a rotor wave. Nevertheless, the results indicate that foci situated ostially more often create AF. Also, AF was generated due to ectopic foci situated at all pulmonary veins in one anatomical model. Thus, the computer model presented allows simulating different set-ups of AF initiation.

Chaotic behaviour given by mother rotors and multiple wavelets has been observed in 2D patches using a complex mathematical description of the electrophysiology [286, 264, 139]. The anatomical structures a to mono-layer model with curvature in 3D space in conjunction with simplified cell models yield the result of re-entrant waves and multiple wavelets [139]. The results of this work show that the use of realistic 3D anatomical models is even more important. Although only a rule-based approach was used to determine the excitation propagation in the atria, many mechanisms thought to initiate and maintain AF have been observed like rotors, re-entrant circuits, multiple wavelets and snakes. A further advantage is that the approach taken in this work is fast. The simulation using complex anatomic structures presented by other authors takes weeks although higher computation power was used [262]. Thus, the presented work is more suitable for therapy planning and optimization. The realistic 3D anatomical model can be used interactively to evaluate transmural lesions in the therapeutical planning of AF prevention. The operative procedure can therefore be modeled accurately. 2D or mono-layer models are not suitable in this context since they neither reflect the complex anatomical structures nor various lesion depths can be simulated.

### 13.2 Classification Methods of Excitation Patterns in AF

The characterization of excitation pattern by gradient methods did not yield results with which to classify excitation patterns into broad wave fronts, rotors, wavelets and snakes in the excitation pattern investigated in this work. The gradient need to be pre-processed for the computation of the divergence and rotation operator due to undesirable effects at the epi- and endocardium. Due to the curvature of the atrial anatomy, these methods do not yield distinguishable results. Thresholding the gradient to extract the wave front only is also not trivial. The higher the threshold the less distinct is the wave front. If the threshold is too low, the wave front has a width which distorts the following computations. Since the gradient, divergence and rotation operation is applied to one voxel only, the whole wave front which includes several voxels, cannot be classified using this approach. However, a more sophisticated approach based on the gradients of the transmembrane voltage might lead to interesting results.

The Positive Potential Method shows results which can be interpreted as follows: First of all, the initial segmentation of the wavefronts is fast and straight forward. Then, the initial wave front count gives a measure to determine whether AF is present or not. In both test patterns, over 1500 wave fronts were counted. Also, the higher the degree of quasi-chaotic excitation, the higher the wave count. Although an automatic determination whether AF is present or not can be directly applied, a classification of specific excitation pattern into broad wave fronts, rotors, snakes and wavelets cannot be attempted looking at the atrial tissue as a whole. Tendencies are seen, however, since a large volume of a wave front is not characteristic for wavelets and snakes. The absolute volume of rotors and wave fronts is larger than for snakes and wavelets.

But considering wave fronts in the pulmonary veins (PVs) and wave fronts in the right atrium, a wave front will be smaller in the PVs than on the atrial roof. This result indicates that the classification of excitation pattern has to be considered in a smaller volume or rather, that different excitation pattern could be described as local phenomenon. Looking at different virtual wedge preparations, one recognized that the wave front count per volume does not differ greatly between fronts, rotors and wavelets. Only in the wedge preparation where snakes were predominant, the counted wave fronts had a larger number. A reason is that the segmentation based on the positive potential yields wave fronts which might be separated by one voxel or a single voxel in the vicinity of the wave front has still positive potential. If an erosion followed by dilation were applied to the segmented wave fronts, it can be expected that the criterion ‘wave front count per tissue volume’ characterises the different excitation pattern better.

However, looking at the size of a wave front with respect to the volume in question, different thresholds could be applied to classify different excitation pattern. While this work has only demonstrated the possibility of automatic classification of excitation pattern, future work will have to focus on evaluating and adjusting in detail the criteria suggested here. However, based on the presented

results, an alternative classification of atrial fibrillation or rather excitation pattern in atrial fibrillation could be worked out. So far, this work has presented an automatic method to determine AF or no AF in the atria.

### 13.3 Evaluation of Ablation Strategies

The initiation of AF by an  $s_1/s_2$  stimulation strategy yields a manifold of different excitation pattern ranging from atrial flutter to complete non-deterministic, chaotic AF. The results show the importance of atrial structures which cause the stable wavefronts created by the initial trigger to break up. This break-up of wavefronts in turn leads to the streak-like excitation pattern that has been observed by the Allessie group in a goat model [4]. However, rotor waves and smaller wavelets are also visible indicating that not only one single mechanism is responsible to maintain AF but different mechanisms can occur at the same time. In complete chaotic AF, the excitation of the atria is due to multiple wavelets mostly. Only at the edges of the atria (ie. right atrial appendage or PVs) stable wavefronts were investigated in our results. Thus, the discussion on which mechanism is solely responsible for the maintenance of AF has to be redirected to a more individual investigation of the patients anatomy and patho-physiology. Since not only one mechanism was present in our computer simulations, the mechanisms responsible in maintaining AF in a specific patient will most likely be manifold, too.

Also, the simulations show different cycle lengths in different areas of the atria: while the cycle length may be shorter in the PVs at an earlier time with respect to the cycle length at the atrial roof, this relation can be reversed with a shorter cycle length at the atrial roof rather than in the PVs. Both cases have been observed in clinical studies before, where it was discussed as contradictory [83]. Our results resolve the contradiction by suggesting that the measurement of cycle length highly depend on the location of the measurement in the heart and on the time measured after AF onset.

Since AF was successfully triggered by over 65 % of the ectopic foci in the pulmonary veins included in this study, and since the ectopic activity reflects the findings in literature with respect to occurrence in relation to sinus beat and frequency of focal discharges [108], the presented approach is suitable to investigate preventive ablation strategies further.

#### 13.3.1 Comparison of Ablation Strategies

The results show that a combination of circumferential ablation and linear ablation lesions yields the best results with respect to non-transmural lesions. It has to be noted however, that the hypothesis that the success rate is higher the more linear lesions are included does not necessarily hold. Regarding the circumferential lesion of each left and right PVs (Melo et al. 1999) versus the strategy where superior and inferior PVs are additionally isolated (Chen et al. 2005), the circumferential lesions without separating superior and inferior pulmonary veins (Melo et al. 1999)

show a 8.7 % higher success rate. Only if the linear lesions at the atrial roof and the lesion to the mitral annulus is included, the success rates are the same. However, including only two additional linear lesions to the strategy first presented by Melo et al. the success rate is highest in the first procedure.

All three ablation strategies where all PVs are surrounded by one circumferential lesions show lower success rates in the first procedure. This can be explained by the location of the lesion with respect to the ectopic foci: If a lesion is situated on top of the ectopic focus or is partially covering the area of the focus, then the focus can be suppressed and AF will not occur. The lesions encircling each PV or left and right PVs cover more area around the PVs than the single lesion around all PVs. Thus, the latter ablation strategy will not target as many positions of the ectopic foci. If the lesions are not transmural, the rotor waves will propagate across the whole atrium and AF is sustained since the rotor waves initiated by the ectopic focus can be developed due to the unablated area of the left atrium.

However, additional linear lesions increase the success rate in the single circumferential lesion strategy, also. The results suggest that instead of two lesions connecting to the mitral annulus, a lesion to the left orifice increases the success rate. Transmurality of the lesion set does not lead to 100 % success rates automatically if only the lesion to the mitral annulus is included. Only a slight increase in success rates is observed. Again, the importance of the lesion to the left orifice is seen since the simulation with transmural lesions in the latter case yield 100 % success of the strategy. This success rate is also shown in all other simulations that include transmural lesions indicating the importance of electrical isolation of the PVs. Only the ablation strategy that does not include circumferential lesions is not successful because the ectopic foci were not isolated. This strategy was only successful in suppressing the ectopic beats in the cases where the ablation lesion lead across the position of the ectopic beat.

The role of transmural lesions on the success of the ablation therapy has been shown to be very important. Only transmural lesions resulted in an isolation of the ectopic foci in the computer simulations which indicates the importance of complete isolation of the PVs.

### 13.3.2 Comparison with Clinical Studies

Regarding the mechanisms and excitation pattern in the simulations, the results reflect the findings in literature well. In ablation studies, fibrillation in the isolated parts has been observed, also [83]. However, a direct comparison between the results presented here and the corresponding clinical studies can only be carried out to a certain extend. While clinical studies include more than one patient, the simulations were computed on one single anatomical data set. However, the underlying pathology varies for each patient. The simulations covered 23 different ectopic beats and thus as many different pathological behaviour. In clinical studies, only one ablation strategy can be tested on one patient but an arbitrary number of different lesion sets (in the presented work ten different strategies) can be evaluated on the model. A further distinction has to be made. The success rates

reported in clinical studies are often based not on the first procedure but on several follow-up procedures that had to be carried out to complete the lesion sets. Regarding the second procedure in the computer model, the success rates exceed the one reported clinically. However, pulmonary vein firing is not the only cause for AF. Ectopic activity has been measured on the atrial roof, the crista terminalis and other locations. These were not included in this study since the objective was to investigate left atrial lesions with respect to their PV isolating property in paroxysmal AF triggered by ectopic beats in the PVs.

### 13.3.3 Limitations

The comparison with clinical studies shows both drawback and advantage of the biophysical model presented in this work. Only one detailed anatomical data set with such high resolution and detail was present in this study. Bringing the model to a clinical application must include the generation of a patient specific anatomical data set. With the current imaging modalities, the resolution will be too low. However, the detail of atrial structures could be included in the model according to the knowledge of atrial structures. Further, electrophysiological measurements would improve the cardiac model. Given catheter measurements as carried out with the Carto system by Biosense or the EnSite System by St. Jude, the model presented in this work could be parameterized to become a patient specific model. Carto-merge by Biosense even integrates CT image data to map the electrophysiological measurements onto anatomical information.

With regard to other computer models of the heart, the speed of the simulations is a major advantage of the presented method. However, it is rule-based and thus approximates cardiac electrophysiology rather than calculating cellular electric activity. Nevertheless, only reduced complexity of the anatomy allows the use of cardiac cell models to date. With multi-processor technology, however, the simulations will be carried out in future on complex whole heart anatomical models including electrophysiological cell models. This also will cover other disadvantages of the current system. The methodology, however, of initiating atrial fibrillation by ectopic beats at the PVs is likely to stay. So far, most other studies achieved AF with pacing maneuvers only. Thus, the presented method seems to be closer to clinical measurement with regard of initiating AF. Further, the mechanisms of AF presented in our model show a high degree of variety, which allows the evaluation of different ablation strategies appropriately. Also, since the anatomical model is a multi-layer model, ie. wall thickness is included, the issue of transmuralitY can be investigated in a simulation environment that is close to possible clinical planning tools in the future. However, although the anatomical model shows many details, more complex structures, especially at the pulmonary ostia and the left atrium needs to be included.



### 13.4 Investigation of Atrial Antitachycardial Pacing

The poor results of the simulations do not correlate with the clinical findings in the investigation of atrial antitachycardial pacing (AATP). Preventive AATP algorithms do achieve reasonable success rates in suppressing episodes of paroxysmal AF. If a combination of post-PAC (premature atrial complex) response, PAC suppression, exercise response and pace conditioning is applied, the successful suppression of AF reaches 100 % in clinical studies [153]. This poses the question whether the simulations have to be improved or whether the clinical studies cannot be generalized. Two possibilities to improve the simulations can be given:

1. The premature atrial complex is not modelled correctly. The occurrence of a PAC is defined by electrocardiogram. No information is given whether it is due to an early activation of the sinus node or whether it is due to abnormal activation in another part of the atrium. Thus, the model of the PAC has to be improved in future work.
2. The general model of homogeneous conduction in the atria needs to be improved. The faster conduction properties of crista terminalis and the Bachmanns bundle will contribute to an improved excitation propagation of the pacing stimulus. The atrial model on which the simulations were based needs to be reparameterized including heterogeneous conduction.

While the preventive AATP was unsuccessful in the simulations, the burst pacing to terminate AF cannot be easily be named unsuccessful although no sinus rhythm was established. Clinically, a stable rhythm in AF is required for burst pacing. If this stable rhythm is present, the pacing manoeuvre tries to target the cells in refractive phases to break-up the stable rhythm. Thus, fast atrial flutter will become atrial fibrillation due to burst pacing. It has been observed that the AF caused by pacing is self-terminating in up to 50 % of patients [153]. In all simulations to terminate AF, the pacing burst was set at a time when the atria showed stable excitation wave fronts. At 7500 ms, the atria were fibrillating. Thus, the success of burst pacing to terminate AF in the computer simulations needs to be either defined as successful break up of stable excitation pattern, or the self-termination of AF needs to be modeled accordingly. In the first case, the burst pacing was successful 100 % since the atria were fibrillating in all simulation set-ups. The second case was not subject to this thesis. It is suggested, however to further investigate spontaneous termination of AF in future work.

### 13.5 Optimisation of Cardiac Resynchronisation Therapy

The simulation on both, Visible Man and patient data, showed that the optimisation strategy to minimize the root mean square error between physiological and pathological or paced excitation is feasible. A minimal error was found for each electrode set-up. This means that the optimization could be carried out pre-operatively - to determine optimal pacing lead position with the respective

AV- and VV-delays - and it can also be run post-operatively to find the optimal timing delays for a given electrode position. The method of optimisation is independent on anatomical shape as well as patho-physiology so far. Not included in this work was the influence of infarction scars which is subject to other research. However, the presented method to optimise electrode position and timing delays can be used to investigate the parameter space, i.e. for different positions and delays, at any point similarly to what is done in clinical studies. Since 1320 simulations were carried out for one pathology on the patient anatomical data set and the time for one simulation was about four minutes, the overall time for all 1320 simulations was 88 hours. Although this can be decreased by reducing the limits of the parameter space e.g. evaluate six left ventricular electrodes only, a greater reduction is achieved by the implementation of the downhill simplex algorithm. It reduces the number of simulations for one pathology and one anatomical data set to about 16 hours. A further reduction in simulation time could be achieved by running parallel simulations on large computers.

### 13.5.1 Sequential Search versus Downhill Simplex Search Algorithm

The major advantage of the downhill simplex algorithm (DSA) is its speed. It produced the results with only 16 - 30 % of simulations needed for the sequential search. Also, while the sequential search has to be limited for the values of AV- and VV-delay, the downhill simplex algorithm uses the whole parameter space. It is therefore not fixed on predetermined fixed values of AV- and VV-delay and can therefore achieve results with a higher resolution. The results computed with the DSA sometimes exceed the limits set to the sequential search which indicates that the limits should be extended. By doing so, the number of simulations would increase for the sequential search and the relative speed up of the DSA is even greater.

The issue about optimal electrode positions and timing delays remains. While the optimal electrode positions were mostly the same using either search method for the patient data, it differed greatly for the Visible Man data set. Therefore, also the timing delays differed greatly in the simulations with Visible Man data. This indicates, however, that an individual adjustment of AV- and VV-delay is important with respect to electrode position. The validity of either method can only be investigated by experimental or clinical studies.

### 13.5.2 Comparison with Clinical Studies

Only few studies investigated specifically electrode position and AV- and VV-timing [244, 280, 299]. The timing delays were investigated by incrementally setting the respective delays similar to the simulations without the simplex algorithm which returns information of all timing set-ups at all discrete points in the parameter space. The optimal parameter were found by the maximal cardiac output which corresponds to minimizing the root mean square error in the simulations. However,

these studies do not suggest an optimization strategy, i.e. how the optimal parameter could be determined in a fast and automatic way. To evaluate different electrode positions with different timing delays takes too much time in clinical practice. The presented computer algorithms can be run in the background automatically and delivers the required information. The optimal timing delays found in this work compare with the clinical standards.

### 13.5.3 Limitations

There are three points which need to be further investigated:

1. The optimisation procedure is based on the electrical isochrones, i.e. the electrical activation of a cell. How well does this correspond to the mechanical activation?
2. The simulation of the pathological set-up needs further investigation and improvement especially with respect to ischemia in congestive heart failure.
3. Is the root mean square error an appropriate predictor of the optimal parameter set-up?

With respect to the issue of electrical versus mechanical activation the following should be taken into account: The simulations computed the electrical activation. If mechanical activation follows electrical activation with a fixed delay, the simulations in this work are valid since the timing offset will be added to all cardiac cells. Since the computer simulations take into account the activation of a cell, the issue can be solved by adjusting electrical activation to the mechanical delay. In the presented method, the activation delay could be set according to patient specific input data. Mechanical activation follows electrical activation and thus, by specifying different activation delays, the issue can be focussed on the activation only and becomes void.

The pathologies have been simulated based on current knowledge of the pathologies. The methodology of optimizing electrode position and timing delays is set on top of this input. Hence, it can be regarded as independent on the underlying pathological simulations. If new insights are gained to model the electrophysiology and the pathologies more appropriately, they can be easily incorporated and the optimization strategy can be set on top of the new model without much change. Thus, the automatic optimization of AV- and VV-delay remains valid. However, the model of the pathology needs further refinement. An adjustment of the activation delay with respect to clinical measurements especially including the American Heart Association classification of ventricular segments needs to be included. Also, current results on modelling cardiac infarction needs to be included to investigate the validity of the presented model for accurate pathologies.

The only issue which needs validation is the hypothesis of the optimization strategy. In this work it was assumed that ideal cardiac function is achieved if the excitation of the ventricles is as close to the physiological rhythm as possible. Based on this assumption, the root mean square error of the activation times was computed. Clinical or experimental studies will have to be carried out whether the root mean square error correlates with the best cardiac function. However, ideally, the computer model is extended to include mechanical contraction with which the cardiac output

can be calculated. This extended model could then be used to compare an optimization parameter which is used in clinical practice or rather which the clinician is interested in when carrying out cardiac resynchronization therapy.

## Conclusion

*“Wagner: Ach Gott! die Kunst ist lang! Und kurz ist unser Leben! (Faust)”*

*Wagner: Oh God! the art is long! And short is our life! (Faust)*

Johann Wolfgang von Goethe

German dramatist, novelist, poet and scientist (1749 - 1832)

### 14.1 General Conclusion

The results of this work demonstrate the potential of computer models in cardiology. With respect to basic research, the computer model can be used to investigate the influence of different parameters. It has been demonstrated that the rule-based computer model can be used to simulate chaotic excitation patterns that resemble atrial fibrillation. The importance to include complex atrial structures has been shown. While the detailed description of the electrophysiology by cell models still requires long simulation times, the presented model can be used to investigate atrial activity within the tissue during atrial fibrillation. This enables future basic research since measurements are carried out on either the epicardial or endocardial surface of the atria. Also, the limitation of measurement systems does not allow to look at the heart with a global view. Only a certain area - sometimes as small as the catheter tip - in a certain time window can be regarded. The computer model enables the researcher to look at the whole atria at the same time which allows the analysis on a different level. Since the simulation results are in accordance with clinical findings so far, it is well suitable to further investigate AF mechanisms and therapeutical strategies.

This thesis has also shown how the computer model can be used to investigate interventional strategies to cure AF. The major advantage compared with clinical studies is that different ablation strategies can be tested for a given anatomy and patho-physiological set-up. Again, the results reflect the findings in literature. However, the integration of patient data and clinical validation is needed. The simulations have shown that a thorough isolation of the pulmonary veins must be stressed for successful ablation. Non-transmural lesions might lead to post-ablation fibrillation

and flutter. With respect to non-transmural lesions, it was shown that additional linear lesions will increase the success rate. At the same time, to include a multitude of linear lesions will not increase the success rate significantly. Especially the simulations of circumferential ablation of each pulmonary vein with linear lesions compared with left and right pulmonary vein lesions shows the need for patient specific therapy planing. Sometimes less lesions produce superior results.

The results of the simulations suggest that the ablation strategy described by Benussi et al. [16], i. e. circumferential ablation of the left and right pulmonary vein with two additional lesions at the left atrial roof and to the mitral annulus is the most promising strategy. However, since it is desirous to set as little lesions as possible to keep the trauma as low as possible, the computer model offers the possibility of preoperatively plan an intervention.

Atrial antitachycardial pacing could not compare with clinical findings in every aspect. The reason was the homogeneous atrial tissue with isotropic conduction properties. Also, the pacing algorithms did not include a-priori knowledge which could improve the results greatly. Intelligent algorithms that e. g. react immediately on sensed signals and an improved atrial model will bring more insight into this form of therapy.

Regarding other work in the field of computer models for the evaluation of therapeutical strategies in AF this thesis presents the only three-dimensional AF model including tissue depth. Therefore, it is more suitable to be used to plan and investigate non-pharmacological therapies in AF.

With respect to an optimisation of cardiac resynchronization therapy, it can be concluded that this thesis offers a fully automatic optimisation strategy which is completely novel. The algorithm finds the optimal atrio-ventricular and interventricular delay timing for a given electrode set-up. This has been shown not only on the reference data-set of the Visible Man heart but also on a patient data-set where the effects of optimal biventricular pacing was even more visible due to the pathological deformation of the ventricles. The results compare well with clinical studies which suggest that the presented model could be suitable for clinical routine. Again, clinical evaluation and validation and more detailed patient specific data will be required to make the computer model fit for clinical application. However, the computer simulations support the hypothesis that electrode positioning and timing of the stimuli plays an important role to achieve optimal results. They have to be adjusted to each patient. The presented model offers the opportunity to pre-operatively plan an ideal positioning of the electrodes but also to adjust the pacemaker timing post-operatively for a given electrode set-up.

## 14.2 Concluding Remark

Finally, the objective of this thesis was

*to produce a computer model with which non-pharmacological therapies can be evaluated and optimised with respect to realistic anatomical structures leading to an individual patient therapy planning in the future.*

This thesis has shown that the presented computer model of the heart has the potential of an individual patient therapy planning to date. Non-pharmacological therapies were evaluated and have been optimised in the computer model. The results of this thesis show the importance of an individualisation of a therapy to improve the clinical outcome. Thus, the next step will be to integrate the computer model into clinical practice and to integrate patient specific data into the computer model.





## Perspective

*“We must always change, renew, rejuvenate ourselves; otherwise we harden.”*

Johann Wolfgang von Goethe

German dramatist, novelist, poet and scientist (1749 - 1832)

### 15.1 Future Research Issues

The research in modelling atrial fibrillation will continue based on this thesis. The results of this work prove promising to be adapted in clinical studies where a direct comparison between planned procedure and conducted procedure will validate both, computer models and ablation strategies. The objective would be

***to create a computer model of atrial fibrillation of the individual patient to support the cardiologist during diagnosis and therapy planning.***

For this purpose, future work will be carried out with regard on increasing anatomical detail, including patient specific anatomical and electrophysiological data. The following points describe milestones to further advance the computer model for an integration in clinical practice:

- Based on high quality imaging modalities (CT and/or MRT and/or ultrasound), a virtual anatomical model of a patient will be created individually representing the patients atrial structures.
- By successive inclusion of intra-atrial electrophysiological measurements, the computer model will not only be parameterized by the individual anatomy but also based on the patients individual patho-physiology.
- The computer simulation of AF will be extended to include fibre orientation in the atria especially with respect to the pulmonary vein - left atrial junction, the crista terminalis, pectinate muscles, Bachmanns bundle and coronary sinus.
- Fibrosis of atrial tissue will be simulated since it contributes in the initiation of AF in the elderly.

- The computer model will also be extended to include the influence of the autonomous nervous system to be able to investigate its influence in AF initiation and termination.
- The atrium that is already fibrillating for some days is not equal to a heart before fibrillation. Therefore, the integration of remodelling in cell models has to be improved and carried forward to the cellular automaton.
- Virtual drug delivery will be first tested on a virtual patch of atrial tissue that incorporates mathematical model of cardiac cells including specific ion channels. Then, the results will be transferred to the patient model to investigate the effect of drug delivery with respect to different AF initiating mechanisms like ectopic beats at different pulmonary veins.
- Virtual ablation strategies will be carried out to investigate the effect of circumferential lesions and additional linear lesions in the prevention and termination of AF. The influence of transmural lesions will be evaluated as well as epicardially versus endocardially set lesions.
- Intelligent antitachycardial pacing algorithms will be developed with regard to electrode positioning and timing of the stimuli with respect to the electrophysiological behaviour of the patient.

Following this methodology, a tool for off-line optimization of curative treatment of AF will be created to investigate prevalent mechanism of AF in the individual patient on which a patient specific therapy can be planned.

The perspective of the optimisation of cardiac resynchronization therapy has a similar objective:

*to create a computer model of congestive heart failure to support the cardiologist during therapy planning and post-operative optimisation of the pacing parameters.*

The issues concerning the realisation of this objective target fundamental questions both clinically and in modelling:

- As with the AF computer model, high quality imaging modalities will be used to create a virtual anatomical model of a patient. It will be created individually representing the structures of the ventricles in detail.
- ECG measurements will have to be carried out to non-invasively measure the hearts activity by means of body surface potential maps. These will be then used to solve the inverse problem of electrocardiology to gain the patient specific cardiac excitation. This will lead to an ideal parameterization of the computer model with respect to patho-physiology.
- Time series of MRI od CT images could be segmented to determine delayed contraction and to validate the computer model.
- Tissue doppler imaging will have to be used to identify areas of asynchronous contraction according to the American Heart Association classification. These measurements will then be used to further parameterize the computer model.

- A validation of the optimisation strategy will have to be carried out in experimental as well as clinical studies. Different optimisation parameters such as peak blood pressure, cardiac output measurement using ultrasound imaging and invasive measurement using a conductance catheter will have to be evaluated and compared. These clinical measurements will form the basis to which the optimisation strategy of this work can be compared.
- The final step would be to include cardiac contraction into the computer model for the optimisation. This way, the optimisation parameter of the root mean square error could be replaced by calculating the cardiac output in the computer simulations.

These issues will lead to an off-line tool for the automatic optimization of cardiac resynchronization therapy. The optimisation will be based on individual patient data which leads to a tailor made therapy for each patient.

## 15.2 Final Remark

“Considering how major advances have been achieved since the first clinical application of CRT in 1994, one can be optimistic about the future of the electrotherapeutic management of heart failure [249].” With the help of modelling and computer simulations this advance will be further supported. Not only in CRT but also in AF and other cardiac diseases computer models will contribute to an in-depth understanding of the mechanisms behind cardiac diseases. With the integration of clinical measurements on the patient the models will also advance therapy planning with respect to the individual patient.



## Postscript - a personal note

*“Das schönste Glück des denkenden Menschen ist, das Erforschliche erforscht zu haben und das Unerforschliche ruhig zu verehren.”*

The greatest happiness of thinking man is to have explored the explorable and restfully honor the unexplorable.

Johann Wolfgang von Goethe

German dramatist, novelist, poet and scientist (1749 - 1832)

I find the above quote suitable for the end of a PhD thesis. It has been three and a half years now that I was working at the Institute of Biomedical Engineering at the Universität Karlsruhe (TH). Especially 2006 has been a year full of academic highlights. Many results, especially concerning atrial fibrillation, have been presented at both clinical and biomedical engineering conferences. The feedback I received was overwhelming. On these conferences and symposia, it was possible to raise the interest of the medical community for our models. The interest from industry is such that future projects which continue the presented work are already funded. “... and restfully honour the unexplorable.” - often, this part of the quote marks the end of a PhD thesis - at least for the person who has done its work. It is nice to see that my work will be continued and future projects will be started to improve the methods presented. From what I have seen and done, I believe that computer models will at some point support the clinician in their daily routine, improve diagnosis and therapy planning. Therefore I would be very happy, if my work has contributed - in the smallest part at least - to achieve this goal.



---

## List of Figures

3.1	The oxygenated blood flows into the left atrium through the pulmonary veins, and fills the left ventricle. The left ventricle ejects the blood through the aorta to the body. The deoxygenated blood reaches the heart through the venous system back into the right atrium through the venae cavae. The right ventricle propels the blood to the lungs through the pulmonary arteries. Figure downloaded from <a href="http://www.childrenscentralcal.org/images/healthimages/ei175.gif">http://www.childrenscentralcal.org/images/healthimages/ei175.gif</a> (accessed 18.12.2006). . . . .	10
3.2	This figure shows a schematic view of the valve plane [144]. It shows the mitral valve and the tricuspid valve which connect the left and right atrium to the ventricles. The atrio-ventricular (AV) node is situated between these two valves and the aorta. The AV node is surrounded by fibrous tissue and is the only electrophysiologic connection between the atria and the ventricles. . . . .	11
3.3	This figure shows the hearts excitation-conduction system and the pathways of excitation [279]. The excitation of the heart will be initiated by the sino-atrial (SA) node and spreads across the atria. The atrio-ventricular (AV) node delays the excitation before initiating the excitation of the ventricles which is carried forward through the bundle branches to the Purkinje fibres. Only at the end of the Purkinje fibres the working myocardium is excited. . . . .	13
3.4	This figure shows the atrial anatomy looking onto and into the right atrium. Figure adapted from Netter [203]. . . . .	14
3.5	This figure shows the ventricular anatomy looking into the left ventricle. Figure adapted from Netter [203]. . . . .	15
3.6	The figure shows a schematic drawing of the heart and its coronary vessels by H. J. Kretschmann and M. Kaltenbach [246] looking onto the right ventricle. . . . .	17

3.7	The figure shows a microscopic image of myocardial cells (top) [195]. The branching fibres are clearly visible. The laminar structure can be recognized, also. The bottom figure is a schematic drawing of a part of skeletal muscle fibre showing the structures responsible for the contraction of a muscle cell [279]. . . . .	18
3.8	The figure shows the principle components of a cell membrane including a potassium ( $K^+$ ) channel, a sodium ( $Na^+$ ) - potassium pump and the ion channel concentrations with their respective gradients [70]. The voltage gradient points from the intracellular space to the extracellular space making the transmembrane voltage $V$ negative in the resting phase. . . . .	19
3.9	This figure shows the structure of a voltage gated $K^+$ channel. Figure from [10]. . .	20
3.10	Schematic description of a $Na^+ / K^+$ pump [70]. Three $Na^+$ ions are pumped against the chemical gradient to the outside of the cell in one cycle. At the same time, two $K^+$ ions will be transported from the extracellular space into the cell against the $K^+$ ion concentration gradient. The pumping process requires energy which is gained by the hydrolysis of ATP (adenosine triphosphate) into ADP (adenosine diphosphate) and phosphate ions $P$ . . . . .	21
3.11	Schematic description of an ion exchanger [70]. The $Na^+ / Ca^{2+}$ exchanger swaps as an antiport three $Na^+$ for one $Ca^{2+}$ ion from extracellular to intracellular space and vice versa. The $Na^+$ -glucose exchanger transports a glucose molecule against its electrochemical gradient into the cell as the inflowing $Na^+$ ions delivers the energy for this transport. . . . .	21
3.12	Schematic drawing of gap junctions [103]. Gap junctions form an electromechanical interconnection between cardiac cells. A gap junction is barrel shaped and made up of two connexons which is a hexamer of six connexins. . . . .	22
3.13	This figure depicts the elements of an action potential [258]. The sum of different transmembrane currents (left) make up the action potential (right). . . . .	26
3.14	This figure shows the action potentials for different atrial myocytes: the crista terminalis (CT) the pectinate muscles (PM), the atrial appendage (APG) and the atrio-ventricular ring (AVR) [81]. . . . .	27
3.15	Different action potential morphologies are shown for ventricular myocytes that were stimulated with different frequencies. The action potentials were measured on isolated cells from the subendocardium (left), the midmyocardium (middle) and the subepicardium (right) [162]. . . . .	27
3.16	The excitation of the myocardial cells give rise to different action potential shapes at different times in the cardiac cycle (left). They contribute to the morphology of the electrocardiogram (right) [202]. . . . .	28



- 4.1 The figure shows a possible site of cardiac infarction [45]. The top figure shows the heart with a blockage in the left anterior descending coronary artery. The dashed circle at the apex around the artery indicates the area at risk where an infarction could develop due to lack of oxygen. The bottom three drawings show the effect of an obstructed artery: The necrotic area gets larger the longer the obstruction lasts. The result is an infarction leading to ischemic heart disease. .... 36
- 4.2 The left schematic drawing shows the excitation propagation in an atrio-ventricular (AV) block III [74]. The conduction block is right at the AV node which leads to no excitation of the ventricles through atrial excitation. The right figure shows a left bundle branch block. The atrial excitation gets propagated via the AV node to the right ventricular myocardium. The left ventricle will not be excited by physiological conduction but through the right ventricular excitation. .... 37
- 4.3 Figure A shows the ventricular remodelling process after an apical infarction. The initial infarct will not show clinically significant changes in the geometry. However, within days to month, the area affected becomes thinner and expands ending in global remodelling and dilatation. Figure B shows the remodelling process in classical diastolic and systolic heart failure. The myocardial wall thickens in diastolic heart failure while the dilatation occurs in systolic heart failure. A change in anatomical shape is clearly visible in any of these pathologies. Figure from Jessup et al. [140]. .... 38
- 5.1 The diagramm on the left shows the five left atrial lesions of the standard Cox-Maze-III surgical procedure of AF. With new technology it has been reduced to the Mini-Maze procedure where less incisions are made and two circumferential lesions around the left and the right pulmonary veins (PVs) are made instead of encircling all four PVs. Reproduced with permission of the author [47]. .... 46
- 5.2 The figure on the left shows the left atrial ablation strategy by Sueda et al. [274]. The four pulmonary veins (PVs) were isolated and the left atrial appendage (LAA) was excised. Further lesions were set to the posterior wall of the left atrium, between the superior and posterior edges of the LAA (IVC = inferior vena cava; MV = mitral valve; RAA = right atrial appendage; SN = sinus node; SVC = superior vena cava; TV = tricuspid valve). Figure adapted from [274]. The figure on the right shows the anatomical reconstruction of the left atrium with intended ablation lines (pale dots) carried out by Ernst et al. [76]. All four PVs were isolated by one circumferential lesion and a linear lesion (PVMA) was added to connect the latter lesion to the mitral annulus (MA) indicated by the dark red ring. Inf indicates inferior; lat, lateral; PV, pulmonary vein; sup, superior, and sept, septal. Figure adapted from [76] and reproduced with permission from the authors. .... 47

- 5.3 The ablation strategy pursued by Oral et al. [213] is shown here. The ablation lines (red marks) were created during left atrial radiofrequency ablation. A three-dimensional representation of left atrium and the pulmonary veins (PVs) was constructed with an electroanatomic mapping system. Left- and right-sided PVs are encircled. Also shown are ablation lines in mitral isthmus and posterior left atrium. A, Left posterior oblique projection; B, posteroanterior projection. LS indicates left superior; LI, left inferior; RS, right superior; RI, right inferior; and LA, left atrium. Figure adopted from [213]. The ablation strategy by Melo et al. [180, 181] which was also carried out by Ouyang et al. [215] includes the same circumferential lines but the linear lesions will not be included. . . . . 48
- 5.4 Shown is the posteroanterior view of a preablation (A) and postablation (B) voltage map of the left atrium depicting peak-to-peak bipolar electrogram amplitude. Red represents lowest voltage. The red dots indicate radiofrequency ablation lesions. Each pulmonary vein is isolated separately. Figure adopted from [228, 226]. . . . . 49
- 5.5 The circumferential ablation strategy of left atrial tissue surrounding the four pulmonary vein ostia. The electrical voltage inside the ablation line decreased significantly after ablation. Each pulmonary vein (PV) is isolated with two circumferential lesions around the left and right pulmonary veins and a linear lesion to separate the inferior and the superior PVs (Modified from J Am Coll Cardiol. 2003;42:185-197). Figure from [40]. . . . . 50
- 5.6 This figure shows the three-dimensional left atrial voltage maps (postero-anterior view: left, pre-ablation; right, post-ablation). The strategy applied by Pappone et al. includes circumferential lesions as well as linear lesions across the atrial roof and to the mitral valve (LIPV = left inferior pulmonary vein; LSPV = left superior pulmonary vein; MV = mitral valve; RIPV = right inferior pulmonary vein; RSPV = right superior pulmonary vein) [223]. . . . . 50
- 5.7 This schematic drawing shows the linear ablation approach by Gaita (left) and Kottkamp (right). The lesion leads from the mitral annulus inside the pulmonary veins to the right inferior pulmonary vein. Figure from [136]. . . . . 51

5.8	Four standard preventive atrial pacing algorithms applied are illustrated: (A) Pace Conditioning: On detection of a sinus beat the algorithm increases the pacing rate by 15 beats/min above the underlying heart rate; the atrium is paced for about 95 % of the time. Following an increase in rate there is a gradual decay. With this algorithm there is no increase in rate in response to a premature atrial beat (PAC). (B) PAC Suppression: On detection of a PAC, the atrial rate is increased by 15 beats/min above the physiological rate. Because multiple PACs often occur, this increase in rate is maintained for 600 beats after which it decreases gradually. Should an additional PAC occur during the 600-beat period, no additional rate increase occurs. (C) Post-PAC Response: This algorithm eliminates the compensatory pause that occurs after a PAC, by controlling the atrial rate for 2 beats. This corrects the interval and returns the heart to a normal sinus rhythm. (D) Post-Exercise Response: This aims to avoid the rapid fall in heart rate that normally occurs postexercise. The pacing algorithm intervenes and permits the rate to slow more gradually. Figure and text modified from [161]. . . . .	58
7.1	Digital cryosection image of the Visible Man, National Library of Medicine, Bethesda, USA, showing a transversal view through the heart. . . . .	74
7.2	This figure shows the different definitions of the neighbourhood of a cubic voxel: (a) 6er neighbourhood, (b) 18er neighbourhood and (c) 26er neighbourhood. . . . .	75
8.1	Electrical equivalent circuit of the Hodgkin-Huxley model . . . . .	78
8.2	Voltage dependent rate constants of sodium channel . . . . .	81
8.3	Schematic description of Priebe Beuckelmann model . . . . .	82
8.4	This figure shows nine different action potentials for nine different rates which are stored for the computation of the excitation propagation for the cellular automaton (a). The morphology also changes with respect to excitation at different levels in the action potential (b). Overall, for nine different frequencies a stimulation at four different times in the action potential cycle are computed with the cell model by Courtemanche et al. [46] for the simulation of the excitation propagation in the atria. . . . .	85
8.5	Neighbour propagation of a cellular automaton on a surface. Empty squares represent resting cells. Each excited cell (green), communicates the excitation to its eight neighbours (green arrow)(a,b). After an explicit time interval the cell switches to an unexcitable state (red)(c, d). Finally, the cell returns back to an excitable cell (e, f). This process proceeds along the given geometry. Figure from [263]. . . . .	86

8.6	Modified morphologies included in the electrophysiological parameters of the cellular automaton to model the heterogeneous ventricular wall with endocardial, midmyocardial and epicardial cells. The action potentials for the midmyocardial cells show the longest action potential durations. (a) Priebe-Beukelmann model of human ventricular myocytes (B) tenTuscher model of human ventricular myocytes. Figure by D. Farina. ....	86
9.1	Schematic description of a unidirectional conduction block created by two stimuli $s$ and $s$ . Both stimuli are set apart spatially and temporally. The distance of the centers was the radius of the first stimulus. The temporal delay between stimulus $s$ and $s$ was 34 ms. While stimulus $s$ will propagate concentrically, stimulus $s$ falls partly in an area of absolute refractoriness and partly in an area where the cells are re-excitabile. Thus, the excitation will not propagate to the right (A) or to the left (B), respectively. Since some areas of the second stimulus falls into a region or tissue that is re-excitabile again, the excitation will be spread into the excitable area (indicated by the arrows). This way, a unidirectional block is created. ....	91
9.2	Location of stimuli to create AF. (a) The positions of the ectopic foci (blue) were placed equidistant around all four pulmonary veins (green) (only a selection is shown). (b) The two stimuli to create atrial fibrillation had a diameter of about 6.5 mm. The center of the second stimulus (yellow) had a spatial offset of about 6.5 mm to the center of the first stimulus (green). ....	91
9.3	Four different excitation pattern which occur in AF: (a) broad wave fronts as in atrial flutter; (b) streak-like excitation called snakes; (c) rotor waves; (d) multiple wavelets. ....	92
9.4	AF Patterns to test classification methods. (a) The regular pattern shows broad wave fronts only while (b) shows an excitation state of the atria which has broad wave fronts, rotors, snakes and wavelets. ....	93
10.1	Schematic diagramm of the ablation lesion set carried out by Kottkamp et al. [154]. The epicardial view shows the left orifice (LO) at the top behind the left superior pulmonary vein. At the bottom left, the mitral annulus (MA) is shown. The pulmonary veins (PVs) are indicated by the circles with the right PVs on the right side. The dotted lines indicate the ablation lesion. ....	100

- 10.2 Schematic diagram of the ablation lesion set described by (a) Pappone et al. 1999 [225], (b) Chen et al. 2005 [40], (c) Melo et al. 1999 [180], (d) Benussi et al. 2000 [16], (e) Pappone et al. 2005 [223], (f) Pappone et al. 2004 [224], (g) Ernst et al. 1999 [76], (h) Sueda et al. 1997 [273] and (i) Cox 2004 [47]. The epicardial view shows the left orifice (LO) at the top behind the left superior pulmonary vein. At the bottom left, the mitral annulus (MA) is shown. The pulmonary veins (PVs) are indicated by the circles with the right PVs on the right side. The dotted lines indicate the ablation lesion. . . . . 101
- 10.3 This figure shows the 72 equally spaced electrodes on the right atrium to investigate the influence of the electrode position on the outcome of atrial antitachycardial pacing. The blue dots indicate the electrodes position, atrial tissue is brown and the pulmonary veins are indicated by the yellow structures. . . . . 102
- 10.4 This schematic diagram illustrates the timing of the pacing stimulus with respect to the sinus beat and the premature atrial activation (pa) for the post-PAC (premature atrial complex) response algorithm simulated. The premature atrial activation is achieved by triggering action potentials simultaneously at the sinus node and the location of the ectopic beat. The pacing stimulus  $p$  is set between the premature beat and the stimuli  $s$  and  $s$  with a time offset of  $\Delta t$ . The stimuli  $s$  and  $s$  are supposed to be suppressed by the pacing stimulus. If they are not suppressed, they lead to atrial fibrillation. . . . . 103
- 10.5 This schematic diagram illustrates the timing of the pacing stimuli with respect to the sinus beat and the premature atrial activation (pa) for the PAC (premature atrial complex) suppression algorithm simulated. The premature atrial activation is achieved by triggering action potentials simultaneously at the sinus node and the location of the ectopic beat. The pacing stimuli follow the premature beat (pa) with a set frequency. The timing between two successive pacing stimuli is set to  $\Delta t$ . The stimuli  $s$  and  $s$  are supposed to be suppressed by the pacing stimuli. . . . . 103
- 10.6 This schematic diagram illustrates the timing of the burst pacing strategy with respect to the sinus beat and the premature atrial activation (pa). The premature atrial activation is achieved by triggering action potentials simultaneously at the sinus node and the location of the ectopic beat. The stimuli  $s$  and  $s$  lead to atrial fibrillation. The first pacing stimulus  $p$  is set 1800 ms after the stimulus  $s$ . The consecutive pacing stimuli follow with a set frequency of  $1/\Delta t$ . . . . . 104
- 10.7 This figure shows the electrode positions of the pacing leads for the evaluation of electrode position in cardiac resynchronization therapy in the Visible Man data set in anterior view (left) and posterior view (right). . . . . 106

- 10.8 This figure shows the electrode positions of the pacing leads for the evaluation of electrode position in cardiac resynchronization therapy in the patient data set in anterior view (left) and posterior view (right)..... 107
- 10.9 Possible outcomes for an iteration step of the Downhill Simplex Algorithm [238]:  
 (a) The initial simplex defines a triangle in two dimensions. The vertices define the parameters, i. e. the AV and VV delay for the three initial simulations. The resulting  $E$  are sorted from lowest to highest value. The vertex of the highest value  $maxE$  will be reflected to find a new parameter set for the next simulation (b). If the new value is below the the previous  $maxE$ , the reflection is extended by factor two (c). If it is higher, the simplex will be compressed in one dimension (d). The last step in the iteration is a contraction in multiple dimension (e) before the algorithm starts the next iteration step. The points indicate the vertices, the lines the sides of the simplex. The dashed lines indicate the position of the previous simplex and the dashed arrows show the direction in which the vertices move. .... 109
- 11.1 Latero-dorsal view on the left atrium at 138 ms (A) after the initiating trigger. The rotor wave is situated at the left superior pulmonary vein (A) with its center around the initial ectopic focus. The stable excitation pattern is characteristic for atrial flutter. The initial rotor is self-terminating and flutter is maintained due to a second macro re-entrant circuit after 660 ms (B). The transmembrane voltage is shown. The dark lines on the atrial surface indicate the excitation wave fronts. .... 114
- 11.2 (A): Latero-dorsal view on the left atrium at 184 ms after the initiating trigger. The rotor wave is situated at the left inferior pulmonary vein with the center around the initial trigger. The stable excitation pattern is characteristic for atrial flutter. (B): View on the valve plane (the ventricles are hidden for visualization) at 716 ms after the initial trigger. A new dominant rotor wave with center between the mitral and tricuspidal valve has replaced the rotor wave around the initial trigger at the left inferior pulmonary vein. The transmembrane voltage is shown. The dark lines on the atrial surface indicate the excitation wave fronts..... 115
- 11.3 Latero-dorsal view of the left atrium. Figures (A) - (F) depict the time instances at 898 ms, 958 ms, 1000 ms, 1096 ms, 1192 ms, 1288 ms, respectively, of a simulation where the ectopic focus was set at the proximal left superior PV. The break-up of wave fronts can be clearly seen on the left atrial roof. Different cycle length and excitation pattern in different areas of the atria result from this break up. The transmembrane voltage is shown. The dark lines on the atrial surface indicate the excitation wave fronts. .... 116

- 11.4 Latero-dorsal view of the left atrium showing the excitation pattern at 884 ms (A) and 1670 ms (B) after the initial trigger. The ectopic focus was set in the left superior pulmonary vein. The excitation pattern differs in separate regions of the atria. The break-up of wave fronts is clearly visible between the left and right superior pulmonary vein (A). Also, a shorter cycle length can be recognized in the left inferior pulmonary vein than in the right atrium. At a later instance (B), the excitation pattern has changed. Now, the atrial roof is dominated by wavelets, i.e. short cycle length can be observed. A stable pattern can be seen at the right pulmonary veins with longer cycle length. The transmembrane voltage is shown. The dark lines on the atrial surface indicate the excitation wave fronts. . . . . 117
- 11.5 Excitation of the atria at 1658 ms after the initial trigger. The ectopic focus was set in the left superior pulmonary vein. The excitation pattern differs in separate regions of the atria. While the excitation is dominated by multiple wavelets at the roof of the right atrium (right), stable wave fronts can be observed at the right pulmonary veins (left). The transmembrane voltage is shown. The dark lines on the atrial surface indicate the excitation wave fronts. . . . . 118
- 11.6 View onto the right atrium at 1326 ms after the initial trigger at the left superior pulmonary vein. Multiple wavelets (A) and rotor waves (B) can be observed at smooth areas of the atrial roof. Streak-like excitation pattern similar to snakes occur at the same time (C). The snakes are caused by the break-up of the stable excitation wave fronts in areas of the atria where the anatomical structures are not smooth. The transmembrane voltage is shown. The dark lines on the atrial surface indicate the excitation wave fronts. . . . . 118
- 11.7 View onto the right atrium at 17266 ms after the initial trigger at the left inferior pulmonary vein (see figure 11.2). The chaotic excitation pattern can be classified as atrial fibrillation. The transmembrane voltage is shown. The dark lines on the atrial surface indicate the excitation wave fronts. . . . . 119
- 11.8 The ectopic focus was set at the left superior pulmonary vein near the left atrial appendage and the atrial septum. The unidirectional conduction block was set either deeper into the left superiorpulmonary vein (A) or distal, close to the ostia (B). Both set-ups produce atrial fibrillation although a different excitation pattern can be recognized at 700 *ms* after the first stimulus of the ectopic beat. The excitation pattern between the two respective set-ups, however, differs. The transmembrane voltage is shown (latero-dorsal view). The dark lines on the atrial surface indicate the excitation wave fronts. . . . . 120

11.9	The ectopic focus was set at the left superior pulmonary vein near the atrial roof. The unidirectional conduction block was set either deeper into the left superiorpulmonary vein (A) or distal, close to the ostia (B). Both set-ups produce atrial fibrillation although a different excitation pattern can be recognized at 700 <i>ms</i> after the first stimulus of the ectopic beat. The excitation pattern between the two respective set-ups, however, differs. The transmembrane voltage is shown (latero-dorsal view). The dark lines on the atrial surface indicate the excitation wave fronts. ....	120
11.10	The ectopic focus was set at the left superior pulmonary vein on the far side of the vein opposite the atrial roof. The unidirectional conduction block was set either deeper into the left superiorpulmonary vein (A) or distal, close to the ostia (B). Both set-ups did not produce atrial fibrillation. The excitation pattern therefore does not differ at 700 <i>ms</i> after the first stimulus of the ectopic beat. The transmembrane voltage is shown (latero-dorsal view). The dark lines on the atrial surface indicate the excitation wave fronts. ....	121
11.11	The ectopic focus was set at the left inferior pulmonary vein between both left pulmonary veins. The unidirectional conduction block was set either deeper into the left superiorpulmonary vein (A) or distal, close to the ostia (B). Both set-ups produce atrial fibrillation although a different excitation pattern can be recognized at 700 <i>ms</i> after the first stimulus of the ectopic beat. The excitation pattern between the two respective set-ups, however, differs. The transmembrane voltage is shown (latero-dorsal view). The dark lines on the atrial surface indicate the excitation wave fronts. ....	121
11.12	The figures on the left show the magnitude of the gradient (a), the divergence (c) and the magnitude of the rotation operator (e) for excitation pattern A. On the right is displayed the respective figures for the magnitude of the gradient (b), the divergence (d) and the magnitude of the rotation operator (f) for excitation pattern B. The view is onto the right epicardial surface with the left atrium on the left. The blue colors indicate small values, the bright colors indicate large values. ...	123
11.13	This figure shows the magnitude of the gradient of all voxels which had a positive transmembrane voltage of excitation pattern A (a) and B (b).....	124
11.14	A cross-section through the atria is shown. Figure (a) displays the gradient for the voxel with positive transmembrane voltage. Figure (b) shows the same cross-section for the excitation pattern with gradients of a magnitude larger than 50 000. ....	124
11.15	A cross-section through the atria is shown. This figure shows the same cross-section for the excitation pattern as in figure 11.14 with gradients of a magnitude larger than 70 000 (a) and 100 000 (b) .....	125



11.16	A cross-section through the atria is shown. This figure shows the same cross-section for the excitation pattern as in figure 11.14 with gradients of a magnitude larger than 150 000 (a) and 200 000 (b) . . . . .	125
11.17	Based on the preprocessed gradient results of excitation pattern A, the divergence (middle column) and rotation (right column) operator were computed for thresholded gradients (left column) with thresholds 50 000 (top), 70 000 (middle) and 100 000 (bottom). . . . .	126
11.18	Based on the preprocessed gradient results of excitation pattern B, the divergence (middle column) and rotation (right column) operator were computed for thresholded gradients (left column) with thresholds 50 000 (top), 70 000 (middle) and 100 000 (bottom). . . . .	127
11.19	This figure shows the segmented wave fronts by means of the Positive Potential Method. (a) shows the result for excitation pattern A in right atrial epicardial view, (b) shows the results for excitation pattern B in the same view. (c) and (d) also display the results for excitation pattern B with a view onto the right atrial appendage (c) and the left atrium in a latero-dorsal view (d). . . . .	129
11.20	Figure (a) - (c) display the same results with a different resolution. In blue are shown the wave fronts detected in excitation pattern A with respect to their surface over their volume. In red are shown the wave fronts detected in excitation pattern B with respect to their surface over their volume. . . . .	130
11.21	This figure shows the virtual wedge preparations from excitation pattern B to analyse (a) broad wave fronts (b) rotors (c) snakes and (d) wavelets. . . . .	131
11.22	This graph displays the results of the relative volume of a detected wave front to the volume of the wedge preparation. . . . .	131
11.23	This figure shows the effect of reducing ventricular conduction velocity in a left bundle branch block: Visible Man data set at 250 <i>ms</i> (a) and patient data set at 350 <i>ms</i> (b) with 100 % conduction velocity, Visible Man data set at 250 <i>ms</i> (c) and patient data set at 350 <i>ms</i> (d) with 80 % conduction velocity, Visible Man data set at 250 <i>ms</i> (e) and patient data set at 350 <i>ms</i> (f) with 60 % conduction velocity. The red color indicates excited tissue. The anterior view is shown. . . . .	133
12.1	Different views on the left atrium show whether the lesions created around the pulmonary veins were not transmural (a) after the first procedure or whether they were transmural (b). A second procedure was carried out for all ablation strategies with transmural lesions (c - d). . . . .	136

- 12.2 Summary of simulation of ablation strategies: Results of ablation strategies at 900 ms. The initial trigger was set at the left superior pulmonary vein. (A) The ablation strategy by Benussi et al. yielded the highest success rate in the first procedure with non-transmural lesions. The same ectopic trigger still caused fibrillatory conduction if the linear lesions were left out (B). If transmuralitity was achieved, the success rate was increased (C). However, fibrillation was observed in the isolated regions (C - D). The transmembrane voltage is shown. The dark lines on the atrial surface indicate the excitation wave fronts. .... 137
- 12.3 This figure illustrates the transfer of the schematic description of the linear ablation strategy (A) onto the anatomical model (B). A: The epicardial view shows the left orifice (LO) at the top behind the left superior pulmonary vein. At the bottom left, the mitral annulus (MA) is shown. The pulmonary veins (PVs) are indicated by the circles with the right PVs on the right side. The dotted lines indicate the ablation lesion. B: The latero-dorsal view of the left atrium shows the pulmonary veins in yellow, the cardiac tissue in brown and the created lesion in white. .... 140
- 12.4 The ablation strategy described by Kottkamp et al. [154] showed successful mostly at the left inferior pulmonary vein. However, only in four out of 23 simulations, atrial fibrillation was prevented (A). The success was achieved when the ablation lesion was set on top the ectopic focus (B). Otherwise (D) the atria were fibrillating after 900 ms if the ectopic focus was not infringed by the lesion (C). The transmembrane voltage at (A) 900 ms, (B) 240 ms, (C) 900 ms and (D) 240 ms is shown. The narrow dark lines on the atrial surface indicate the excitation wave fronts. The broad dark lines indicate no electrical activity, i. e. the location of the ablation lesions. .... 140
- 12.5 This figure illustrates the transfer of the schematic description of the ablation strategy with four single circumferential lesions (A) onto the anatomical model (B). A: The epicardial view shows the left orifice (LO) at the top behind the left superior pulmonary vein. At the bottom left, the mitral annulus (MA) is shown. The pulmonary veins (PVs) are indicated by the circles with the right PVs on the right side. The dotted lines indicate the ablation lesion. B: The latero-dorsal view of the left atrium shows the pulmonary veins in yellow, the cardiac tissue in brown and the created lesion in white. .... 142

- 12.6 Exemplary results of the circumferential ablation strategy described by Pappone et al. 1999 [225]: (A) demonstrates the successful prevention of atrial fibrillation provoked by an ectopic beat at the left superior pulmonary vein. The ablation lesions, however, were also leading across the position of the ectopic beat (here at the distal part of the left superior pulmonary vein) which suppressed the generation of the initial rotor (B). But atrial fibrillation occurred in almost 50 % of cases (C) because the ectopic focus was situated closer, i. e. proximal, to the atrial roof (D) and thus was not isolated by the lesions. The transmembrane voltage at (A) 900 *ms*, (B) 240 *ms*, (C) 900 *ms* and (D) 240 *ms* is shown. The narrow dark lines on the atrial surface indicate the excitation wave fronts. The broad dark lines indicate no electrical activity, i. e. the location of the ablation lesions. . . . . 142
- 12.7 This figure illustrates the transfer of the schematic description of the ablation strategy with two single circumferential lesions (A) onto the anatomical model (B). A: The epicardial view shows the left orifice (LO) at the top behind the left superior pulmonary vein. At the bottom left, the mitral annulus (MA) is shown. The pulmonary veins (PVs) are indicated by the circles with the right PVs on the right side. The dotted lines indicate the ablation lesion. B: The latero-dorsal view of the left atrium shows the pulmonary veins in yellow, the cardiac tissue in brown and the created lesion in white. . . . . 143
- 12.8 Exemplary results of the circumferential ablation strategy described by Melo et al. 1999 [180]: (A) demonstrates the successful prevention of atrial fibrillation provoked by an ectopic beat at the distal part of the left superior pulmonary vein. Fibrillation in the pulmonary veins caused atrial fibrillation in the atria if the ablation lesion was not transmural (B) Here, the stimulus was set at the left superior pulmonary vein close to the atrial roof. The same ectopic beat was prevented to cause atrial fibrillation, if the ablation lines were transmural (C). Fibrillation in the pulmonary veins was observed in some simulations while sinus rhythm was achieved in others (C - D). The transmembrane voltage at 900 *ms* is shown. The narrow dark lines on the atrial surface indicate the excitation wave fronts. The broad dark lines indicate no electrical activity, i. e. the location of the ablation lesions. . . . . 144

- 12.9 This figure illustrates the transfer of the schematic description of the ablation strategy with two circumferential lesions and two linear lesions at the atrial roof and to the mitral annulus (A) onto the anatomical model (B). A: The epicardial view shows the left orifice (LO) at the top behind the left superior pulmonary vein. At the bottom left, the mitral annulus (MA) is shown. The pulmonary veins (PVs) are indicated by the circles with the right PVs on the right side. The dotted lines indicate the ablation lesion. B: The latero-dorsal view of the left atrium shows the pulmonary veins in yellow, the cardiac tissue in brown and the created lesion in white. .... 145
- 12.10 Exemplary results of the circumferential ablation strategy described by Benussi et al. [16]: (A) demonstrates the successful prevention of atrial fibrillation provoked by an ectopic beat at the distal part of the left superior pulmonary vein. The additional linear lesion lead to a higher success rate than the circumferential ablation strategy. Figure B shows the same simulation set-up as in figure 12.8 B. Here, however, sinus rhythm was established and atrial fibrillation was prevented. With transmural lesions, the result of both ablation strategies is similar (C - D): Fibrillation in the isolated pulmonary veins was observed. The transmembrane voltage at 900 *ms* is shown. The narrow dark lines on the atrial surface indicate the excitation wave fronts. The broad dark lines indicate no electrical activity, i. e. the location of the ablation lesions. .... 146
- 12.11 This figure illustrates the transfer of the schematic description of the ablation strategy with two circumferential lesions and a separate isolation of the inferior and superior pulmonary veins (A) onto the anatomical model (B). A: The epicardial view shows the left orifice (LO) at the top behind the left superior pulmonary vein. At the bottom left, the mitral annulus (MA) is shown. The pulmonary veins (PVs) are indicated by the circles with the right PVs on the right side. The dotted lines indicate the ablation lesion. B: The latero-dorsal view of the left atrium shows the pulmonary veins in yellow, the cardiac tissue in brown and the created lesion in white. .... 147

- 12.12 Exemplary results of the circumferential ablation strategy described by Chen et al. [40]: (A) demonstrates the successful prevention of atrial fibrillation provoked by an ectopic beat at the left inferior pulmonary vein. In this case, the second stimulus of the ectopic beat was situated ostially. The same position of this ectopic focus caused fibrillation if the second stimulus was placed closer to the pulmonary vein (B). The additional isolation of the inferior and superior pulmonary vein did not lead to an improvement in the success rate compared to the simpler circumferential ablation strategy (C). However, transmural lesions also lead to a 100 % success rate in all simulations (D). Fibrillation in the isolated pulmonary veins was observed as in other ablation strategies (E - F). The transmembrane voltage at 900 *ms* is shown. The narrow dark lines on the atrial surface indicate the excitation wave fronts. The broad dark lines indicate no electrical activity, i. e. the location of the ablation lesions. . . . . 148
- 12.13 This figure illustrates the transfer of the schematic description of the ablation strategy of isolating each pulmonary vein with additional atrial roof lesion and a lesion to the mitral annulus (A) onto the anatomical model (B). A: The epicardial view shows the left orifice (LO) at the top behind the left superior pulmonary vein. At the bottom left, the mitral annulus (MA) is shown. The pulmonary veins (PVs) are indicated by the circles with the right PVs on the right side. The dotted lines indicate the ablation lesion. B: The latero-dorsal view of the left atrium shows the pulmonary veins in yellow, the cardiac tissue in brown and the created lesion in white. . . . . 149
- 12.14 Exemplary results of the circumferential ablation strategy described by Pappone et al. 2005 [223]: (A) demonstrates the successful prevention of atrial fibrillation provoked by an ectopic beat at the the right superior pulmonary vein. Figures B and C demonstrate that the additional isolation of the inferior and superior pulmonary vein did not lead to an improvement in the success rate compared to the simpler circumferential ablation strategy (compare figure 12.10). Fibrillation in the isolated pulmonary veins was observed as in other ablation strategies (D). The transmembrane voltage at 900 *ms* is shown. The narrow dark lines on the atrial surface indicate the excitation wave fronts. The broad dark lines indicate no electrical activity, i. e. the location of the ablation lesions. . . . . 150

- 12.15 This figure illustrates the transfer of the schematic description of the ablation strategy of isolating each pulmonary vein with two additional atrial roof lesion and a lesion to the mitral annulus (A) onto the anatomical model (B). A: The epicardial view shows the left orifice (LO) at the top behind the left superior pulmonary vein. At the bottom left, the mitral annulus (MA) is shown. The pulmonary veins (PVs) are indicated by the circles with the right PVs on the right side. The dotted lines indicate the ablation lesion. B: The latero-dorsal view of the left atrium shows the pulmonary veins in yellow, the cardiac tissue in brown and the created lesion in white. .... 151
- 12.16 Exemplary results of the circumferential ablation strategy described by Pappone et al. 2004 [224]: (A) demonstrates the successful prevention of atrial fibrillation provoked by an ectopic beat at the right superior pulmonary vein. Figures B and C demonstrate that the additional isolation of the inferior and superior pulmonary vein did not lead to an improvement in the success rate compared to the simpler circumferential ablation strategy (compare figure 12.10). The additional third linear lesion did only improve the success rate by one simulation compared to the same procedure with only one lesion on the atrial roof. Fibrillation in the isolated pulmonary veins was observed as in other ablation strategies (D). The transmembrane voltage at 900 *ms* is shown. The narrow dark lines on the atrial surface indicate the excitation wave fronts. The broad dark lines indicate no electrical activity, i. e. the location of the ablation lesions. .... 152
- 12.17 This figure illustrates the transfer of the schematic description of the ablation strategy a single circumferential lesion and a lesion to the mitral annulus (A) onto the anatomical model (B). A: The epicardial view shows the left orifice (LO) at the top behind the left superior pulmonary vein. At the bottom left, the mitral annulus (MA) is shown. The pulmonary veins (PVs) are indicated by the circles with the right PVs on the right side. The dotted lines indicate the ablation lesion. B: The latero-dorsal view of the left atrium shows the pulmonary veins in yellow, the cardiac tissue in brown and the created lesion in white. .... 153

- 12.18 Exemplary results of the circumferential ablation strategy described by Ernst et al. [76]: (A) demonstrates the successful prevention of atrial fibrillation provoked by an ectopic beat at the left superior pulmonary vein. Transmural lesions did not improve the overall success rate of the ablation strategy (B - F). Fibrillation and a break-up of wave fronts was observed in either both (B) or the left atrium (C). The left atrium remained fibrillating in some simulations while the right atrium regained sinus rhythm (D). Also, macro re-entrant circuits were observed (E) with wave fronts travelling in seemingly opposite directions in the atria (F). The transmembrane voltage at 900 *ms* is shown. The narrow dark lines on the atrial surface indicate the excitation wave fronts. The broad dark lines indicate no electrical activity, i. e. the location of the ablation lesions. .... 154
- 12.19 This figure illustrates the transfer of the schematic description of the ablation strategy a single circumferential lesion and two lesion to the mitral annulus (A) onto the anatomical model (B). A: The epicardial view shows the left orifice (LO) at the top behind the left superior pulmonary vein. At the bottom left, the mitral annulus (MA) is shown. The pulmonary veins (PVs) are indicated by the circles with the right PVs on the right side. The dotted lines indicate the ablation lesion. B: The latero-dorsal view of the left atrium shows the pulmonary veins in yellow, the cardiac tissue in brown and the created lesion in white. .... 155
- 12.20 Exemplary results of the circumferential ablation strategy described by Sueda et al. [273] which are similar to those described in the last section (compare with figure 12.18): (A) demonstrates the successful prevention of atrial fibrillation provoked by an ectopic beat at the left superior pulmonary vein. Transmural lesions did not improve the overall success rate of the ablation strategy (B - F). Fibrillation and a break-up of wave fronts was observed in either both (B) or the left atrium (C). The left atrium remained fibrillating in some simulations while the right atrium regained sinus rhythm (D). Also, macro re-entrant circuits were observed (E) with wave fronts travelling in seemingly opposite directions in the atria (F). The transmembrane voltage at 900 *ms* is shown. The narrow dark lines on the atrial surface indicate the excitation wave fronts. The broad dark lines indicate no electrical activity, i. e. the location of the ablation lesions. .... 156

- 12.21 This figure illustrates the transfer of the schematic description of the ablation strategy a single circumferential lesion and a lesion to the mitral annulus and to the left atrial orifice (A) onto the anatomical model (B). A: The epicardial view shows the left orifice (LO) at the top behind the left superior pulmonary vein. At the bottom left, the mitral annulus (MA) is shown. The pulmonary veins (PVs) are indicated by the circles with the right PVs on the right side. The dotted lines indicate the ablation lesion. B: The latero-dorsal view of the left atrium shows the pulmonary veins in yellow, the cardiac tissue in brown and the created lesion in white. .... 157
- 12.22 Exemplary results of the circumferential ablation strategy described by Cox [47]: (A) demonstrates the successful prevention of atrial fibrillation provoked by an ectopic beat at the left superior pulmonary vein. Transmural lesions did improve the overall success rate of the ablation strategy to 100 % (B - D). However, macro re-entrant circuits (B) and left atrial fibrillation (C - D) with break-ups of wave fronts were observed. The transmembrane voltage at 900 *ms* is shown. The narrow dark lines on the atrial surface indicate the excitation wave fronts. The broad dark lines indicate no electrical activity, i. e. the location of the ablation lesions. .... 158
- 12.23 The post-PAC response algorithm was not able to suppress the ectopic beat in the pulmonary veins in all simulations. The excitation pattern was changed however: Figure (a) shows the excitation pattern without pacing stimulus. Figure (b) shows the same pathological set-up but with a pacing stimulus at 200 *ms* before the ectopic beat right in the middle of the right atrial roof. Two rotor waves can be clearly distinguished to drive the excitation together with another focus in the left atrium. The transmembrane voltage at 900 *ms* is shown in both figures. The narrow dark lines on the atrial surface indicate the excitation wave fronts. .... 159
- 12.24 The PAC suppression algorithm also did not yield a successful suppression of the ectopic beats. Figure (a) shows the stimulation of the right atrial roof at 600 beats per minute (bpm). The pacing frequency is too slow to dominate any of the atrial area. It is overridden by the fast excitation wave fronts of the driving circuit. An increase in pacing frequency to 800 bpm leads to a break-up of wave fronts (b). A further increase to 1000 bpm (c) and 1200 bpm (d) shows that the right atrial excitation is dominated by the pacing stimuli but does not spread over the whole atrium. The transmembrane voltage is shown. The narrow dark lines on the atrial surface indicate the excitation wave fronts. .... 160



12.25	Figure (a) and (d) shows the isochrones of the simulation of the sinus rhythm in the Visible Man data set. The blue colour shows early activation and the bright yellow shows late activation. Figure (b) shows the isochrones for the simulation of the AV block III. Figure (e) shows the isochrones of the same pathology, only paced by two stimuli at the ventricles. Figure (c) and (f) show the square error between the isochrones of the sinus rhythm and the pathology or therapy, respectively. In both cases, the error is zero in the atria (blue) since they are activated physiologically. The error is large for the pathological simulation (yellow) since the ventricles are not excited at all (c). For the simulation of the therapy, the error is small and can only be recognized around the location of the pacing electrodes (f). . . . .	162
12.26	This figure shows the electrode positions of the pacing leads for the evaluation of electrode position in cardiac resynchronization therapy in the Visible Man data set in anterior view (left) and posterior view (right). . . . .	163
12.27	This figure shows the electrode positions of the pacing leads for the evaluation of electrode position in cardiac resynchronization therapy in the patient data set in anterior view (left) and posterior view (right). . . . .	164
12.28	This figure shows the mean root mean square error with respect to the simulated pathology of an AV block III (AVB) and reduced conduction velocity in the Visible Man data set using a sequential search of the minimum values. The connecting lines are for visualization only. . . . .	169
12.29	The root mean square error is shown in $[ms]$ with respect to AV- and VV-delay for the best electrode position in the simulations of the AV block on the Visible Man data set using the sequential search algorithm. . . . .	170
12.30	This figure shows the mean root mean square error with respect to the simulated pathology of a left bundle branch block (LBBB) and reduced conduction velocity in the Visible Man data set using a sequential search of the minimum values. The connecting lines are for visualization only. . . . .	171
12.31	The root mean square error is shown in $[ms]$ with respect to AV- and VV-delay for the best electrode position in the simulations of the left bundle branch block on the Visible Man data set using the sequential search algorithm. . . . .	172
12.32	The root mean square error is shown in $[ms]$ with respect to AV- and VV-delay for the best electrode position in the simulations of the AV block on the patient data set using the sequential search algorithm. . . . .	175
12.33	This figure shows the mean root mean square error with respect to the simulated pathology of an AV block III (AVB) and reduced conduction velocity in the patient data set using a sequential search of the minimum values. The connecting lines are for visualization only. . . . .	176

12.34	This figure shows the mean root mean square error with respect to the simulated pathology of an left bundle branch block (LBBB) and reduced conduction velocity in the patient data set using a sequential search of the minimum values. The connecting lines are for visualization only. ....	176
12.35	The root mean square error is shown in $[ms]$ with respect to AV- and VV-delay for the best electrode position in the simulations of the left bundle branch block on the patient data set using the sequential search algorithm. ....	177
12.36	This figure shows the mean root mean square error with respect to the simulated pathology of an AV block III (AVB) and reduced conduction velocity in the Visible Man data set using the downhill simplex algorithm. Also shown is the number of simulations which were carried out to achieve the results. The connecting lines are for visualization only. ....	181
12.37	This figure shows the mean root mean square error with respect to the simulated pathology of an left bundle branch block (LBBB) and reduced conduction velocity in the Visible Man data set using the downhill simplex algorithm. Also shown is the number of simulations which were carried out to achieve the results. The connecting lines are for visualization only. ....	183
12.38	This figure shows the mean root mean square error with respect to the simulated pathology of an AV block III (AVB) and reduced conduction velocity in the patient data set using the downhill simplex algorithm. Also shown is the number of simulations which were carried out to achieve the results. The connecting lines are for visualization only. ....	186
12.39	This figure shows the mean root mean square error with respect to the simulated pathology of an AV block III (AVB) and reduced conduction velocity in the patient data set using the downhill simplex algorithm. Also shown is the number of simulations which were carried out to achieve the results. The connecting lines are for visualization only. ....	189

---

## List of Tables

3.1	Typical ion concentration and their associated Nernst voltages of skeletal muscle [266]. . . . .	24
8.1	Electrophysiological models of cardiac cells . . . . .	79
9.1	Patho-physiology included in this work for the simulation of cardiac resynchronization therapy. vRV - right ventricular conduction velocity; vLV - right ventricular conduction velocity; AV block III - atrio-ventricular block third degree; LBBB - left bundle branch block; . . . . .	98
11.1	This table shows the distribution of ectopic foci simulated. Atrial fibrillation could be initiated at all pulmonary veins. LSPV - left superior pulmonary vein; RSPV - right superior pulmonary vein; LIPV - left inferior pulmonary vein; RIPV - right inferior pulmonary vein; AF - atrial fibrillation . . . . .	113
11.2	This table shows the results of the detection of wave fronts in the virtual wedge preparations. . . . .	128
12.1	Results of ablation strategies. The first procedure indicates lesions set epicardially with a set tissue depth leading to non-transmural lesions at some positions. Transmurality was ensured in the second procedure. . . . .	138
12.2	Sustained atrial fibrillation and successful therapy after the first procedure of the linear ablation lesion strategy only reported by Kottkamp et al. [154]. A second procedure was not carried out. . . . .	139
12.3	Sustained atrial fibrillation and successful therapy after the first procedure of the circumferential ablation of each pulmonary vein strategy reported by Pappone et al. 1999 [225]. The lesions were all transmural in the first procedure and therefore, a second procedure was not carried out. . . . .	141

12.4 Sustained atrial fibrillation and successful therapy after the first procedure of the circumferential ablation strategy reported by Melo et al. [180]. The second procedure with complete transmural lesions lead to a prevention of atrial fibrillation in all simulations. ....	143
12.5 Sustained atrial fibrillation and successful therapy after the first procedure of the circumferential ablation with two additional linear lesions reported by Benussi et al. [16]. The second procedure with complete transmural lesions lead to a prevention of atrial fibrillation in all simulations. ....	145
12.6 Sustained atrial fibrillation and successful therapy after the first procedure of the circumferential ablation strategy described by Chen et al. [40]. The second procedure with complete transmural lesions lead to a prevention of atrial fibrillation in all simulations. ....	147
12.7 Sustained atrial fibrillation and successful therapy after the first procedure of the linear ablation lesion strategy only reported by Pappone et al. 2005 [223]. The second procedure with complete transmural lesions lead to a prevention of atrial fibrillation in all simulations. ....	149
12.8 Sustained atrial fibrillation and successful therapy after the first procedure of the linear ablation lesion strategy only reported by Pappone et al. 2004 [224]. The second procedure with complete transmural lesions lead to a prevention of atrial fibrillation in all simulations. ....	151
12.9 Sustained atrial fibrillation and successful therapy after the first and second procedure of the linear ablation lesion strategy only reported by Ernst et al. [76]. ...	153
12.10 Sustained atrial fibrillation and successful therapy after the first procedure of the linear ablation lesion strategy only reported by Sueda et al. [273]. ....	155
12.11 Sustained atrial fibrillation and successful therapy after the first procedure of the linear ablation lesion strategy only described by Cox [47]. The second procedure with complete transmural lesions lead to a prevention of atrial fibrillation in all simulations. ....	157
12.12 Summary of CRT optimisation on the Visible Man data set. ....	163
12.13 Summary of CRT optimisation on the patient data set. ....	164
12.14 The minimal $E$ in $[ms]$ in different electrode positioning for the conduction velocity set to 100% of the physiological values is shown for the Visible Man data set. The corresponding AV and VV-delays are shown, also, together with the respective electrode set-up. The optimisation was carried out by the sequential search algorithm. ....	166
12.15 The minimal $E$ in $[ms]$ in different electrode positioning for the conduction velocity set to 80% of the physiological values is shown for the Visible Man data set. The corresponding AV and VV-delays are shown, also, together with the respective electrode set-up. The optimisation was carried out by the sequential search algorithm. ....	167

12.16	The minimal $E$ in $[ms]$ in different electrode positioning for the conduction velocity set to 60% of the physiological values is shown for the Visible Man data. The corresponding AV and VV-delays are shown, also, together with the respective electrode set-up. The optimisation was carried out by the sequential search algorithm. ....	167
12.17	The minimal $E$ in $[ms]$ in different electrode positioning for the conduction velocity set to 100% of the physiological values is shown for the patient data. The corresponding AV and VV-delays are shown, also, together with the respective electrode set-up. The optimisation was carried out by the sequential search algorithm. ....	173
12.18	The minimal $E$ in $[ms]$ in different electrode positioning for the conduction velocity set to 80% of the physiological values is shown for the patient data. The corresponding AV and VV-delays are shown, also, together with the respective electrode set-up. The optimisation was carried out by the sequential search algorithm. ....	173
12.19	The minimal $E$ in $[ms]$ in different electrode positioning for the conduction velocity set to 60% of the physiological values is shown for the patient data. The corresponding AV and VV-delays are shown, also, together with the respective electrode set-up. The optimisation was carried out by the sequential search algorithm. ....	174
12.20	The minimal $E$ in different electrode positioning for the conduction velocity set to 100% of the physiological value in the Visible Man data set. The corresponding AV and VV-delays are shown, also, together with the respective electrode set-up. The results were computed by the downhill simplex search algorithm ....	179
12.21	The minimal $E$ in different electrode positioning for the conduction velocity set to 80% of the physiological value in the Visible Man data set. The corresponding AV and VV-delays are shown, also, together with the respective electrode set-up. The results were computed by the downhill simplex search algorithm ....	180
12.22	The minimal $E$ in different electrode positioning for the conduction velocity set to 60% of the physiological value in the Visible Man data set. The corresponding AV and VV-delays are shown, also, together with the respective electrode set-up. The results were computed by the downhill simplex search algorithm ....	180
12.23	The minimal $E$ in different electrode positioning for the conduction velocity set to 100% of the physiological value in the Visible Man data set. The corresponding AV and VV-delays are shown, also, together with the respective electrode set-up. The results were computed by the downhill simplex search algorithm ....	181
12.24	The minimal $E$ in different electrode positioning for the conduction velocity set to 80% of the physiological value in the Visible Man data set. The corresponding AV and VV-delays are shown, also, together with the respective electrode set-up. The results were computed by the downhill simplex search algorithm ....	182

12.25	The minimal $E$ in different electrode positioning for the conduction velocity set to 60% of the physiological value in the Visible Man data set. The corresponding AV and VV-delays are shown, also, together with the respective electrode set-up. The results were computed by the downhill simplex search algorithm . . . . .	182
12.26	The minimal $E$ in different electrode positioning for the conduction velocity set to 100% of the physiological value in the patient data set. The corresponding AV and VV-delays are shown, also, together with the respective electrode set-up. The results were computed by the downhill simplex search algorithm . . . . .	184
12.27	The minimal $E$ in different electrode positioning for the conduction velocity set to 80% of the physiological value in the patient data set. The corresponding AV and VV-delays are shown, also, together with the respective electrode set-up. The results were computed by the downhill simplex search algorithm . . . . .	185
12.28	The minimal $E$ in different electrode positioning for the conduction velocity set to 60% of the physiological value in the patient data set. The corresponding AV and VV-delays are shown, also, together with the respective electrode set-up. The results were computed by the downhill simplex search algorithm . . . . .	185
12.29	The minimal $E$ in different electrode positioning for the conduction velocity set to 100% of the physiological value in the patient data set. The corresponding AV and VV-delays are shown, also, together with the respective electrode set-up. The results were computed by the downhill simplex search algorithm . . . . .	187
12.30	The minimal $E$ in different electrode positioning for the conduction velocity set to 80% of the physiological value in the patient data set. The corresponding AV and VV-delays are shown, also, together with the respective electrode set-up. The results were computed by the downhill simplex search algorithm . . . . .	188
12.31	The minimal $E$ in different electrode positioning for the conduction velocity set to 60% of the physiological value in the patient data set. The corresponding AV and VV-delays are shown, also, together with the respective electrode set-up. The results were computed by the downhill simplex search algorithm . . . . .	188

---

## References

1. W. T. Abraham, W. G. Fisher, A. L. Smith, D. B. Delurgio, A. R. Leon, E. Loh, D. Z. Kocovic, M. Packer, A. L. Clavell, D. L. Hayes, M. Ellestad, R. J. Trupp, J. Underwood, F. Pickering, C. Truex, P. McAtee, and J. Messenger for the MIRACLE Study Group. Multicenter InSync Randomized Clinical Evaluation. Cardiac resynchronization in chronic heart failure. *N Engl J Med*, 346:1845 – 1853, 2002.
2. S. W. Adler II, C. Wolpert, E. N. Warman, S. K. Musley, J. K. Koehler, and D. E. Euler. Efficacy of pacing therapies for treating atrial tachyarrhythmias in patients with ventricular arrhythmias receiving a dual-chamber implantable cardioverter defibrillator. *Circulation*, 104(8):887–892, 2001.
3. A. Agarwal, M. York, B. K. Kantharia, and M. Ezekowitz. Atrial fibrillation: modern concepts and management. *Annu Rev Med*, 56:475–494, 2005.
4. M. Allessie and U. Schotten. Paroxysmal atrial fibrillation: just a matter of nerves? *Heart Rhythm*, 3(2):209–211, 2006.
5. R. Arora, S. Verheule, and L. Scott. Arrhythmogenic substrate of the pulmonary veins assessed by high-resolution optical mapping. *Circulation*, 107:1816–1821, 2003.
6. P. Attuel, D. Danilovic, K.-H. Konz, J. Brachmann, D. el Allaf, S. Löscher, C. Gomes, T. Scheibner, V. Schibgilla, I. Szendey, and A. Hartmann. Relationship between selected overdrive parameters and the therapeutic outcome and tolerance of atrial overdrive pacing. *PACE*, 26(II):2257–263, Jan 2003.
7. W. Auerwald. *Lehrbuch der Medizinischen Physiologie*. Springer Verlag, Berlin, Heidelberg, New York, 1974.
8. A. Auricchio and C. Fantoni. Cardiac resynchronization therapy in heart failure. *Ital Heart J*, 6(3):256–260, 2005.
9. A. Auricchio, C. Stellbrink, M. Block, S. Sack, J. Vogt, P. Bakker, Klein, A. Kramer, J. Ding, R. Salo, Tockman, T. Pochet, and J. Spinelli. Effect of pacing chamber and atrioventricular delay on acute systolic function of paced patients with congestive heart failure. *Circulation*, 99:2993–3001, 1999.
10. C. W. Balke, E. Marbán, and B. O’Rourke. Calcium channels: Structure, function, and regulation. In D. P. Zipes and J. Jalife, editors, *Cardiac Electrophysiology. From Cell to Bedside*, chapter 2, pages 8–21. W. B. Saunders Company, Philadelphia, 3 edition, 1999.
11. J. J. Bax, G. Ansalone, O. A. Breithardt, G. Derumeaux, C. Leclercq, M. J. Schalij, P. Sogaard, M. St. John Sutton, and P. Nihoyannopoulos. Echocardiographic evaluation of cardiac resynchronization therapy: ready for routine clinical use? *J Am Coll Cardiol*, 44:1–9, 2004.

12. R. C. Becker. Biomarkers in atrial fibrillation: investigating biologic plausibility, cause, and effect. *J Thromb Thrombolysis*, 19(1):71–75, Feb 2005.
13. G. W. Beeler and H. Reuter. Reconstruction of the action potential of ventricular myocardial fibres. *J. Physiol.*, 268:177–210, 1977.
14. S. Benussi. Treatment of atrial fibrillation. *Eur J Cardiothorac Surg*, 26 Suppl 1:S39–S41, Dec 2004. discussion S41.
15. S. Benussi, S. Nascimbene, S. Calvi, and O. Alfieri. A tailored anatomical approach to prevent complications during left atrial ablation. *Ann Thorac Surg*, 75:1979–1981, 2003.
16. S. Benussi, C. Pappone, S. Nascimbene, G. Oreto, A. Caldarola, P. L. Stefano, V. Casati, and O. Alfieri. A simple way to treat chronic atrial fibrillation during mitral valve surgery: the epicardial radiofrequency approach. *Eur J Cardiothorac Surg*, 17:524–529, 2000.
17. O. Bernus, R. Wilders, C. W. Zemlin, H. Verschelde, and A. V. Panfilov. A computationally efficient electrophysiological model of human ventricular cells. *Am. J. Physiol.*, 282:H2296–H2308, 2002.
18. D. M. Beyerbach and D. P. Zipes. Mortality as an endpoint in atrial fibrillation. *Heart Rhythm*, 1(2 Suppl):B8–B18, discussion B18–B19, Jul 2004.
19. J. J. Blanc. Pacing to prevent atrial fibrillation: utility or futility? *J Cardiovasc Electrophysiol*, 16(7):724–726, Jul 2005. Comment on: *J Cardiovasc Electrophysiol*. 2005 Jul;16(7):714–23.
20. O. Blanc, N. Virag, J. M. Vesin, and L. Kappenberger. Virtual rf ablation in a 3d computer model of atrial arrhythmias. In *Proceedings of The First Joint BMES/EMBS Conference Serving Humanity, Advancing Technology, Oct 13-16. 1999, Atlanta, GA, USA*, page 1198. IEEE, 1999.
21. O. Blanc, N. Virag, J. M. Vesin, and L. Kappenberger. A computer model of human atria with reasonable computational load and realistic anatomical properties. *IEEE Transactions on Biomedical Engineering*, 48(11):1229–1237, 2001.
22. G. B. Bleeker, M. J. Schalij, S. G. Molhoek, H. F. Verwey, E. R. Holman, E. Boersma, P. Steendijk, E. E. Van der Wall, and J. J. Bax. Relationship between qrs duration and left ventricular dyssynchrony in patients with end-stage heart failure. *Journal of Cardiovascular Electrophysiology*, 15(5):544–549, May 2004.
23. D. Blommaert, M. Gonzalez, J. Mucumbitsi, O. Gurne, P. Evrard, M. Buche, Y. Louagie, P. Eucher, J. Jamart, E. Installe, and L. D. Roy. Effective prevention of atrial fibrillation by continuous atrial overdrive pacing after coronary artery bypass surgery. *J Am Coll Cardiol*, 35:1411–1415, 2000.
24. H. L. Bloom. Concise review of atrial fibrillation: treatment update considerations in light of affirm and race. *Clin Cardiol*, 27(9):495–500, Sep 2004.
25. D. Bocker and R. Gradaus. Cardiac resynchronization therapy and arrhythmias. *Herzschrittmacherther Elektrophysiol*, 16(1):28–31, Mar 2005. Article in German.
26. A. Bollmann, D. Husser, and D. S. Cannom. Antiarrhythmic drugs in patients with implantable cardioverter-defibrillators. *Am J Cardiovasc Drugs*, 5(6):371–378, 2005.
27. P. Bordachar, S. Lafitte, S. Reuter, P. Sanders, P. Jais, M. Haissaguerre, R. Roudaut, S. Garrigue, and J. Clementy. Echocardiographic parameters of ventricular dyssynchrony validation in patients with heart failure using sequential biventricular pacing. *J Am Coll Cardiol*, 44:2157–2165, 2004.
28. D. Bottino, C. Penland, A. Stamps, M. Traebert, B. Dumotier, A. Georgieva, G. Helmlinger, and G. Scott Lett. Preclinical cardiac safety assessment of pharmaceutical compounds using an integrated systems-based computer model of the heart. Technical report, CAMS Report 0405-23, [Fall 2004/Spring 2005], 2005.



29. M. R. Bristow, L. A. Saxon, J. Boehmer, S. Krueger, D. A. Kass, T. De Marco, P. Carson, L. DiCarlo, D. DeMets, B. G. White, and et al. Comparison of medical therapy, pacing and defibrillation in heart failure (companion) investigators. cardiac resynchronization therapy with or without an implantable defibrillator in advanced chronic heart failure. *N Engl J Med*, 250:2140–2150, 2004.
30. R. Brugada. Is atrial fibrillation a genetic disease? *J Cardiovasc Electrophysiol*, 16(5):553–556, May 2005.
31. G. E. Burch and R. B. Romney. Functional anatomy and “throttle valve” action of the pulmonary veins. *Am Heart J*, 47:58–66, 1954.
32. L. Calo, F. Lamberti, M. L. Loricchio, E. De Ruvo, L. Bianconi, C. Pandozi, and M. Santini. Atrial flutter and atrial fibrillation: which relationship? new insights into the electrophysiological mechanisms and catheter ablation treatment. *Ital Heart J*, 6(5):368–373, May 2005.
33. R. Cappato, H. Calkins, S.-A. Chen, W. Davies, Y. Iesaka, J. Kalman, Y.-H. Kim, G. Klein, D. Packer, and A. Skanes. Worldwide survey on the methods, efficacy, and safety of catheter ablation for human atrial fibrillation. *Circulation*, 111(9):1100–1105, 2005.
34. J. Carlson, J. Neuzner, and Y. D. Rosenberg. Therapy of atrial fibrillation: Rhythm control versus rate control. *PACE*, 23:891–903, 2000.
35. M. D. Carlson, J. Ip, J. Messenger, and et al. A new pacemaker algorithm for the treatment of atrial fibrillation: results of the atrial dynamic overdrive pacing trial (adopt). *J Am Coll Cardiol*, 42:627–633, 2003.
36. S. Cazeau, C. Alonso, G. Jauvert, A. Lazarus, and P. Ritter. Cardiac resynchronization therapy. *Europace*, 5 Suppl1:S42–S48, Sep 2004.
37. S. Cazeau, C. Leclercq, T. Lavergne, S. Walker, C. Varma, C. Linde, S. Garrigue, L. Kappnberger, G. A. Haywood, M. Santini, and et al. Multisite stimulation in cardiomyopathies (mistic) study investigators. effects of multisite biventricular pacing in patients with heart failure and intraventricular conduction delay. *N Engl J Med*, 344:873–880, 2001.
38. M. C. Chen, G. B. Guo, J. P. Chang, and et al. Radiofrequency and cryoablation of atrial fibrillation in undergoing valvular operations. *Ann Thorac Surg*, 65:1666– 1672, 1998. check this literature again!!!
39. S. A. Chen and C. T. Tai. Catheter ablation of atrial fibrillation originating from the non-pulmonary vein foci. *J Cardiovasc Electrophysiol*, 16(2):229–232, Feb 2005.
40. S. A. Chen and C. T. Tai. Catheter ablation of paroxysmal atrial fibrillation. *Cardiol Rev*, 13(2):87–94, Mar-Apr 2005.
41. E. M. Cherry, F. Xie, Z. Feliciano, and A. Garfinkel. Computer modeling of atrial fibrillation. *Cardiac Electrophysiology Review*, 5:271–276, 2001.
42. M. K. Chung, R. S. Augostini, C. R. Asher, D. P. Pool, T. A. Grady, M. Zikri, S. m Buehner, M. Weinstock, and P. M. McCarthy. Ineffectiveness and potential proarrhythmia of atrial pacing for atrial fibrillation prevention after coronary artery bypass grafting. *Ann Thorac Surg*, 69:1057–1063, 2000.
43. G. Ciaramitaro, G. Sgarito, M. Farinella, P. Prestifilippo, P. Assennato, and S. Novo. Right ventricular pacing: a resource or a threat? *Ital Heart J Suppl*, 6(10):627–634, Oct 2005. Article in Italian.
44. J. G. F. Cleland, J. C. Daubert, E. Erdmann, N. Freemantle, D. Gras, L. Kappenberger, and L. Tavazzi for the Cardiac Resynchronization-Heart Failure (CARE-HF) Study Investigators. The effect of

- cardiac resynchronization on morbidity and mortality in heart failure. *N Engl J Med*, 352:1539–1549, 2005.
45. R. S. Cotran, V. Kumar, and T. Collins. *Robbins Pathologic Basis of Disease*. W. B. Saunders Company, 6 edition, 1999.
  46. M. Courtemanche, R. J. Ramirez, and S. Nattel. Ionic mechanisms underlying human atrial action potential properties: Insights from a mathematical model. *Am. J. Physiol.*, 275(44):H301–H321, 1998.
  47. J. L. Cox. Surgical treatment of atrial fibrillation: a review. *Europace*, 5 Suppl1:S20–S29, Sep 2004.
  48. J. L. Cox and N. Ad. The importance of cryoablation of the coronary sinus during the maze procedure. *Semin Thorac Cardiovasc Surg*, 12:20–24, 2000.
  49. J. L. Cox, N. Ad, T. Palazz, S. Fitzpatrick, J. P. Suyderhoud, K. W. DeGroot, E. A. Pirovic, H. C. Lou, W. Z. Duvall, and Y. D. Kim. Current status of the maze procedure for the treatment of atrial fibrillation. *Semin Thorac Cardiovascular Surg*, 12:15–19, 2000.
  50. J. L. Cox, J. P. Boineau, R. B. Schuessler, K. M. Kater, and D. G. Lappas DG. Five-year experience with the maze procedure for atrial fibrillation. *Ann Thorac Surg*, 56:814–824, 1994.
  51. J. L. Cox, R. B. Schuessler, and J. P. Boineau. The development of the maze procedure for the treatment of atrial fibrillation. *Semin Thorac Cardiovascular Surg*, 12:2–14, 2000.
  52. D. Cozma, J. Kalifa, D. Lighezan, S. Pescariu, J.-C. Deharo, C. Mornos, P. Djiane, and S.-I. Dragulescu. Mechanism of atrial fibrillation: Decremental conduction, fragmentation, and ectopic activity in patients with drug resistant paroxysmal atrial fibrillation and structurally normal heart. *PACE*, 28:S115–S119, 2005.
  53. L. L. Creswell, J. C. Alexander Jr., T. B. Ferguson Jr., A. Lisbon, L. A. Fleisher, and American College of Chest Physicians. Intraoperative interventions: American college of chest physicians guidelines for the prevention and management of postoperative atrial fibrillation after cardiac surgery. *Chest*, 128(2 Suppl):28S–35S, Aug 2005.
  54. H.J. Crijns. Rate versus rhythm control in patients with atrial fibrillation: what the trials really say. *Drugs*, 65(12):1651–1667, 2005.
  55. E. Crystal, M. S. Garfinkle, S. S. Connolly, T. T. Ginger, K. Sleik, and S. S. Yusuf. Interventions for preventing post-operative atrial fibrillation in patients undergoing heart surgery. *Cochrane Database Syst Rev*, 4:CD003611, Oct 2004.
  56. J. Cummings, A. Pacifico, J. L. Drago, F. Kilicaslan, and A. Natale. Alternative energy sources for the ablation of arrhythmias. *PACE*, 28:434–443, 2005.
  57. A. Dabrowska-Kugacka, E. Lewicka-Nowak, A. Kutarski, P. Zagodzdon, and G. Swiatecka. Hemodynamic effects of alternative atrial pacing sites in patients with paroxysmal atrial fibrillation. *PACE*, 26(Pt. II):278–283, 2003.
  58. L. Dang, N. Virag, Z. Ihara, and et al. Evaluation of ablation patterns using a biophysical model of atrial fibrillation. *Ann Biomed Eng*, 33(4):465–474, 2005.
  59. E. G. Daoud, R. Dabir, M. Archambeau, and F. Morady and S. A. Strickberger. Randomized, double-blind trial of simultaneous right and left atrial epicardial pacing for prevention of post-open heart surgery atrial fibrillation. *Circulation*, 102:761–765, 2000.
  60. E. G. Daoud, R. Snow, J. D. Hummel, S. J. Kalbfleisch, R. Weiss, and R. Augostini. Temporary atrial epicardial pacing as prophylaxis against atrial fibrillation after heart surgery: A meta-analysis. *J Cardiovasc Electrophysiol*, 14:127–132, 2003.

61. J. J. A. M. T. Defauw, G. M. Guiraudon, N. M. Van Hemel, and et al. Surgical therapy of paroxysmal atrial fibrillation with the corridor operation. *Ann Thorac Surg*, 53:564–571, 1992.
62. S. S. Demir, J. W. Clark, C. R. Murphey, and W. R. Giles. A mathematical model of a rabbit sinoatrial node cell. *Am. J. Physiol.*, 35:832–852, 1994.
63. S. S. Demir, B. O'Rourke, G. F. Tomaselli, E. Marbán, and R. L. Winslow. Action potential variation in canine ventricle: A modeling study. In *Proc. Computers in Cardiology*, volume 23, pages 221–224, 1996.
64. D. DiFrancesco and D. Noble. A model of cardiac electrical activity incorporating ionic pumps and concentration changes. *Phil. Trans. R. Soc. Lond.*, 307:353–398, 1985.
65. C. Dimmer, T. Szili-Torok, R. Tavernier, T. Verstraten, and L. J. Jordaens. Initiating mechanisms of paroxysmal atrial fibrillation. *Europace*, 5:1–9, 2003.
66. N. H. Dinh and H. J. Crijns. Stroke and bleeding as an endpoint in atrial fibrillation studies. *Heart Rhythm*, 1(2 Suppl):B27–30, Jul 2004.
67. S. Dokos, B. G. Celler, and N. H. Lovell. Vagal control of sinoatrial rhythm: A mathematical model. *J. Theor. Biol.*, 182:21–44, Sep. 1996.
68. J. Dong and H. Calkins. Technology insight: catheter ablation of the pulmonary veins in the treatment of atrial fibrillation. *Nat Clin Pract Cardiovasc Med*, 2(3):159–166, Mar 2005.
69. P. Dorian, I. Mangat, A. Pinter, and V. Korley. The burden of atrial fibrillation: should we abandon antiarrhythmic drug therapy? *J Cardiovasc Pharmacol Ther*, 9(4):257–262, Dec 2004. Comment in: *J Cardiovasc Pharmacol Ther*. 2004 Dec;9(4):219–21.
70. J. Dudel. Grundlagen der Zellphysiologie. In R. F. Schmidt, G. Thews, and F. Lang, editors, *Physiologie des Menschen*, chapter 1, pages 3–19. Springer, Berlin, Heidelberg, New York, 2000.
71. G. D.Veenhuizen, C. S. Simpson, and H. Abdollah. Atrial fibrillation. *CMAJ*, 171(7):755–760, Sep 2004.
72. M. J. Earley and R. J Schilling. Catheter and surgical ablation of atrial fibrillation. *Heart*, 92(2):266–274, Feb 2006.
73. Y. E. Earm and D. Noble. A model of single atrial cell: Relation between calcium current and calcium release. *Proc. R. Soc. Lond.*, 240:83–96, 1990.
74. H.-H. Ebert. *Der EKG Lotse*. Georg Thieme Verlag, 2001.
75. S. Ernst, F. Ouyang, F. Löber, M. Antz, and K.-H. Kuck. Catheter-induced linear lesions in the left atrium in patients with atrial fibrillation: an electroanatomic study. *J Am Coll Cardiol*, 42:1271–1282, 2003.
76. S. Ernst, M. Shluter, F. Ouyang, A. Khanedani, R. Cappato, J. Hebe, M. Volkmer, M. Antz, and K.-H. Kuck. Modification of the substrate for maintenance of idiopathic human atrial fibrillation: efficacy of radiofrequency ablation using nonfluoroscopic catheter guidance. *Circulation*, 100:2085–2092, 1999.
77. K. Fan, K. Lee, and C.-P. Lau. Mechanisms of biatrial pacing for prevention of postoperative atrial fibrillation-insights from a clinical trial. *Cardiac Electrophysiology Review*, 7:147–152, 2003.
78. K. Fan, K. L. Lee, C. S. W. Chiu, J. W. Lee, G. W. He, D. Cheing, M. P. Sun, and C. P. Lau. Effects of biatrial pacing in prevention of postoperative atrial fibrillation after coronary artery bypass surgery. *Circulation*, 102:755–760, 2000.
79. D. Farina and O. Dössel. Influence of cardiac activity in midmyocardial cells on resulting ecg: Simulation study. In *Biomedizinische Technik*, 2006.

80. L. Fauchier, O. Marie, D. Casset-Senon, D. Babuty, P. Cosnay, and J. P. Fauchier. Interventricular and intraventricular dyssynchrony in idiopathic dilated cardiomyopathy: a prognostic study with fourier phase analysis of radionuclide angioscintigraphy. *J Am Coll Cardiol*, 40(11):2022–2030, 2002.
81. J. Feng, L. Yue, Z. Wang, and S. Nattel. Ionic mechanisms of regional action potential heterogeneity in the canine right atrium. *Circ. Res.*, 83:541–551, 1998.
82. N. M. Fried, A. C. Larado, R. D. Berger, H. Calkins, and H. R. Halperin. Linear lesions in myocardium created by nd:yag laser using diffusing optical fibres: In vitro and in vivo results. *Lasers Surg Med*, 27:295–304, 2000.
83. S. P. Fynn and J. M. Kalman. Pulmonary veins: anatomy, electrophysiology, tachycardia, and fibrillation. *Pacing Clin Electrophysiol*, 27(11):1547–1559, Nov 2004.
84. F. Gaita, R. Gallotti, L. Calo, E. Manasse, R. Riccardi, L. Garberoglio, M. Nicolini, M. Scaglione, P. Fi Donna, M. Caponi, and G. Franciosi. Limited posterior left atrial cryoablation in patients with chronic atrial fibrillation undergoing valvular heart surgery. *J Am Coll Cardiol*, 36:159–166, 2000.
85. F. Gaita, R. Gallotti, R. Riccardi, E. Manasse, L. Garberoglio, D. Caponi M. Scaglione, M. Nicolini, and M. Gasparini. Follow-up of three different patterns of cryolesions limited to posterior left atrium in patients with chronic atrial fibrillations and valvular disease. *PACE*, 23(4 part II):599, 2000.
86. F. Gaita, R. Riccardi, L. Calo, M. Scaglione, L. Garberoglio, R. Antolini, M. Kirchner, F. Lamberti, and E. Richiardi. Atrial mapping and radiofrequency catheter ablation in patients with idiopathic atrial fibrillation. Electrophysiological findings and ablation results. *Circulation*, 97:2136–2145, 1998.
87. F. Gaita, R. Riccardi, and R. Gallotti. Surgical approaches to atrial fibrillation. *Cardiac Electrophysiology Review*, 6:401–405, 2002.
88. C. T.-J. Gan, J.-W. Lankhaar, J. T. Marcus, N. Westerhof, K. M. Marques, J. G. F. Bronzwaer, A. Boonstra, P. E. Postmus, and A. Vonk-Noordegraaf. Impaired left ventricular filling due to right-to-left ventricular interaction in patients with pulmonary arterial hypertension. *Am J Physiol Heart Circ Physiol*, 260:1528–1533, 2006. First published Nov 11, 2005;.
89. L. F. Garnier, P. Rouesnel, and F. Espitalier. Atrial fibrillation and anticoagulation. *Arch Mal Coeur Vaiss*, 97(10):1001–1005, Oct 2004.
90. E. P. Gerstenfeld, D. J. Callans, S. Dixit, and et al. Mechanisms of organized left atrial tachycardias occurring after pulmonary vein isolation. *Circulation*, 110:1351–1357, 2004.
91. E. P. Gerstenfeld, M. R. S. Hill, S. N. French, R. Mehra, K. Rofino, T. J. Van der Salm, and R. S. Mittleman. Evaluation of right atrial and biatrial temporary pacng for the prevention of atrial fibrillation after coronary atery bypass surgery. *J Am Coll Cardiol*, 33:1981–1988, 1999.
92. H. Ghanbari, B. Hassunizadeh, and C. Machado. Expanding cardiac resynchronization for systolic heart failure to patients with mechanical dyssynchrony and atrial fibrillation. *Rev Cardiovasc Med*, 6(3):140–151, 2005.
93. A. M. Gillinov. Ablation of atrial fibrillation with mitral valve surgery. *Curr Opin Cardiol*, 20(2):107–114, Mar 2005.
94. A. M. Gillinov and R. K. Wolf. Surgical ablation of atrial fibrillation. *Prog Cardiovasc Dis*, 48(3):169–177, Nov-Dec 2005.
95. M. A. Gillinov, E. H. Blackstone, , and P. M. McCarthy. Atrial fibrillation: Current surgical options and their assessment. *Ann Thorac Surg*, 74:2210–2217, 2002.
96. M. A. Gillinov and P. M. McCarthy. Atricure bipolar radiofrequency clamp for intraoperative ablation of atrial fibrillation. *Ann Thorac Surg*, 74:2165–2168, 2002.

97. M. A. Gillinov, P. M. McCarthy, N. Marrouche, and et al. Contemporary surgical treatment for atrial fibrillation. *Pacing Clin Electrophysiol*, 26:1–4, 2003.
98. Gillis. Rhythm control in atrial fibrillation: endpoints for device-based trials. *Heart Rhythm*, 1(2 Suppl):B52–B57, discussion B57, Jul 2004.
99. I. Giorgberidze, S. Saksena, L. Mongeon, R. Mehra, R. B. Krol, A. N. Munsif, and P. Mathew. Effects of high-frequency atrial pacing in atypical atrial flutter and atrial fibrillation. *J Interv Cardiac Electrophysiol*, 1:111–123, 1997.
100. A. S. Go, M. C. Fang, and D. E. Singer. Antithrombotic therapy for stroke prevention in atrial fibrillation. *Prog Cardiovasc Dis*, 48(2):108–124, Sep-Oct 2005.
101. M. R. Gold, R. B. Leman, and D. E. Euler. Effectiveness of rapid atrial pacing for termination of drug refractory atrial fibrillation: Results of a dual chamber implantable cardioverter defibrillator trial. *Cardiac Electrophysiology Review*, 7:341–344, 2003.
102. Y. Gong and D. J. Christini. Antispiral waves in reaction-diffusion systems. *Physical Review Letters*, 90(8):088302–1, 2003.
103. D. A. Goodenough and D. L. Paul. Beyond the gap: Functions of unpaired connexon channels. *Nature Reviews Molecular Cell Biology*, 4:285–295, 2003.
104. J. Gorscan, H. Kanzaki, R. Bazaz, K. Dohi, and D. Schwartzman. Usefulness of echocardiographic tissue synchronization imaging to predict acute response to cardiac resynchronization therapy. *Am J Cardiol*, 93:1178–1181, 2004.
105. A. Graffigna, F. Pagani, G. Minzioni, J. Salerno, and M. Vigano. Left atrial isolation associated with mitral valve operations. *Ann Thorac Surg*, 54:1093–1097, 1992.
106. M. D. Greenberg, N. M. Katz, S. Iuliano, B. J. Tempesta, and A. J. Solomon. Atrial pacing for the prevention of atrial fibrillation after cardiovascular surgery. *J Am Coll Cardiol*, 35:1416–1422, 2000.
107. Y. Guyomar, O. Thomas, C. Marquie, and et al. Mechanisms of onset of atrial fibrillation: a multicenter, prospective, pacemaker-based study. *Pacing Clin Electrophysiol*, 26:1336–1341, 2003.
108. M. Haïssaguerre, P. Jaïs, D. C. Shah, A. Takahashi, M. Hocini, G. Quiniou, S. Garrigue, A. Le Mouroux, P. Le Metayer, and J. Clementy. Spontaneous initiation of atrial fibrillation by ectopic beats originating in the pulmonary veins. *N Engl Med*, 339:659–666, 1998.
109. M. Haïssaguerre, D. C. Shah, and P. Jais. Electrophysiological breakthroughs from the left atrium to the pulmonary veins. *Circulation*, 102:2463–2465, 2000.
110. A. Hamabe, Y. Okuyama, and Y. Miyauchi. Correlation between anatomy and electrical activation in canine pulmonary veins. *Circulation*, 107:1550–1555, 2003.
111. A. Harada, T. Konishi, M. Fikata, K. Higuchi, T. Sugimoto, and K. Sasaki. Intraoperative map guided operation for atrial fibrillation due to mitral valve disease. *Ann Thorac Surg*, 69:446–450, 2000.
112. D. M. Harrild and C. S. Henriquez. A computer model of normal conduction in the human atria. *Circ. Res.*, 87(7):e25–e36, 2000.
113. J.-S. Hermida, C. Carpentier, M. Kubala, A. Otmani, J. Delonca, G. Jarry, and J.-L. Rey. Atrial septal versus atrial appendage pacing; feasibility and effects on atrial conduction, interatrial synchronization, and atrioventricular sequence. *PACE*, 26(Pt. I):26–35, 2003.
114. A. Hersi and D. G. Wyse. Management of atrial fibrillation. *Curr Probl Cardiol*, 30(4):175–233, Apr 2005.
115. S. L. Higgins, H. D. Hummel, I. K. Niazi, M. C. Guidici, S. J. Worley, L. A. Saxon, J. P. Boehmer, M. B. Higginbotham, T. De Marco, E. Foster, and et al. Cardiac resynchronization therapy for

- the treatment of heart failure in patients with intraventricular conduction delay and malignant ventricular tachyarrhythmias. *J Am Coll Cardiol*, 42:1454–1459, 2003.
116. J. T. Hii, B. Mitchell, H. J. Duff, D. G. Wyse, and A. M. Gillis. Comparison of atrial overdrive pacing with and without extrastimuli for termination of atrial flutter. *Am J Cardiol*, 70:463–467, 1992.
  117. D. W. Hilgemann and D. Noble. Excitation-contraction coupling and extracellular calcium transients in rabbit atrium: Reconstruction of basic cellular mechanisms. *Proc. R. Soc. Lond.*, 230:163–205, 1987.
  118. S. Y. Ho, J. A. Cabrera, and V. H. Tran. Architecture of the pulmonary veins: Relevance to radiofrequency ablation. *Heart*, 86:265–270, 2001.
  119. S. Y. Ho, D. Sanchez-Quintana, and J. A. Cabrera. Anatomy of the left atrium: Implications for radiofrequency ablation of atrial fibrillation. *J cardiovasc Electrophysiol*, 10:1525–1533, 1999.
  120. M. Hocini, M. Haissaguerre, D. Shah, and et al. Multiple sources initiating atrial fibrillation from a single pulmonary vein identified by a circumferential catheter. *Pacing Clin Electrophysiol*, 23:1828–1831, 2000.
  121. M. Hocini, S. Y. Ho, and T. Kawara. Electrical conduction in canine pulmonary veins: Electrophysiological and anatomic correlation. *Circulation*, 105:2442–2448, 2002.
  122. A. L. Hodgkin and A. F. Huxley. A quantitative description of membrane current and its application to conduction and excitation in nerve. *J. Physiol.*, 177:500–544, 1952.
  123. E. Hoffman, S. Janko, G. Steinbeck, N. Edvardsson, and A. J. Camm. Analysis of onset mechanisms of atrial fibrillation in pacemaker patients. *Heart*, 83(Suppl. 1):19, 2001. Abstract.
  124. C. W. Hogue Jr., L. L. Creswell, D. D. Gutterman, L. A. Fleisher, and American College of Chest Physicians. Epidemiology, mechanisms, and risks: American college of chest physicians guidelines for the prevention and management of postoperative atrial fibrillation after cardiac surgery. *Chest*, 128(2 Suppl):9S–16S, Aug 2005.
  125. B. Hugel, C. W. Israel, C. Unterberg, T. Lawo, J. C. Geller, I. M. Kennis, D. E. Euler, J. L. Koehler, and D. A. Hettrick. Incremental programming of atrial anti-tachycardia pacing therapies in bradycardia-indicated patients: effects on therapy efficacy and atrial tachyarrhythmia burden. *Europace*, 5:403–409, 2003.
  126. K. Imai, T. Sueda, K. Orihashi, and et al. Clinical analysis of results of a simple left atrial procedure for chronic atrial fibrillation. *Ann Thorac Surg*, 71:577–581, 2001.
  127. M. E. Irwin. Cardiac pacing device therapy for atrial dysrhythmias: how does it work? *AACN Clin Issues*, 15(3):377–390, Jul-Sep 2004.
  128. C. W. Israel and S. H. Hohnloser. Pacing to prevent atrial fibrillation. *J Cardiovasc Electrophysiol*, 14:S20–S26, Sep 2003.
  129. C. W. Israel, B. Hugel, C. Unterberg, and et al. Pace-termination and pacing for prevention of atrial tachyarrhythmias: results from a multicenter study with an implantable device for atrial therapy. *J Cardiovasc Electrophysiol*, 12:1121–1128, Oct 2001.
  130. C. W. Israel, T. Lawo, B. Lemke, G. Gronefeld, and S. H. Hohnloser. Atrial pacing in the prevention of paroxysmal atrial fibrillation: first results of a new combined algorithm. *Pacing Clin Electrophysiol*, 23:1888–1890, 2000.
  131. V. Iyer, R. Mazhari, and R. L. Winslow. A computational model of the human left-ventricular epicardial myocyte. *Biophys. J.*, 87(3):1507–1525, 2004.

132. M. S. Jafri, J. J. Rice, and R. L. Winslow. Cardiac  $Ca^{2+}$  dynamics: The roles of ryanodine receptor adaptation and sarcoplasmic reticulum load. *Biophysical J.*, 74:1149–1168, Mar. 1998.
133. P. Jaïs, M. Haïssaguerre, and D. C. Shah. A focal source of atrial fibrillation treated by discrete radiofrequency ablation. *Circulation*, 95:572–576, 1997.
134. P. Jaïs, M. Hocini, and L. Macle. Distinctive electrophysiological properties of pulmonary veins in patients with atrial fibrillation. *Circulation*, 106:2479–2485, 2002.
135. P. Jaïs, D. C. Shah, M. Haïssaguerre, and et al. Efficacy and safety of septal and left atrial linear ablation for atrial fibrillation. *Am J Cardiol*, 84:139R–146R, 1999.
136. P. Jaïs, R. Weerasooriya, D. C. Shah, M. Hocini, L. Macle, K.-J. Choi, C. Scavee, M. Haïssaguerre, and J. Clementy. Ablation therapy for atrial fibrillation (af): Past, present and future. *Cardiovascular Research*, 54:337–346, 2002. Accent sur Clementy!!!
137. J. Jalife, O. Berenfield, and M. Mansour. Mother rotors and fibrillatory conduction: A mechanism of atrial fibrillation. *Cardiovasc Res*, 54:204–216, 2002.
138. V. Jaquemet, N. Virag, Z. Ihara, L. Dang, O. Blanc, J. M. Vesin, C. S. Henriquez, and L. Kappenberger. A computer model of sustained atrial fibrillation to study atrial electrograms. *International Journal of Bioelectromagnetism*, 5(1):181–182, 2003.
139. V. Jaquemet, N. Virag, and L. Kappenberger. Wavelength and vulnerability to atrial fibrillation: Insights from a computer model of human atria. *Europace*, 7:S83–S92, 2005.
140. M. Jessup and S. Brozena. Heart failure. *N Engl J Med*, 348:2007–2018, May 2003.
141. J. Johnson and K. T. Napier. Atrial fibrillation: new theories, emerging treatments. *JAAPA*, 18(6):36–41, Jun 2005. quiz 43-4.
142. J. Kalifa, J. Jalife, and A. V. Zaitsev. Intra-atrial pressure increases rate and organization of waves emanating from the superior pulmonary veins during atrial fibrillation. *Circulation*, 108:668–671, 2003.
143. D. A. Kass, C. H. Chen, C. Curry, M. Talbot, R. Berger, B. Fetics, and E. Nevo. Improved left ventricular mechanics from acute vdd pacing in patients with dilated cardiomyopathy and ventricular conduction delay. *Circulation*, 99:1567–1573, 1999.
144. A. M. Katz. *Physiology of the Heart*, chapter 1. Structure of the heart and cardiac muscle, pages 1–36. Raven Press, New York, 2nd edition, 1992. ISBN: 0-88167-838-4.
145. W. F. Kerwin and O. Paz. Cardiac resynchronisation therapy: Overcoming ventricular dyssynchrony in dilated heart failure. *Cardiology in Review*, 11(4):221–239, July/Aug. 2003.
146. A. Khaja and G. Flaker. Bachmann’s bundle: does it play a role in atrial fibrillation? *Pacing Clin Electrophysiol*, 28(8):855–863, Aug 2005. Erratum in: *Pacing Clin Electrophysiol*. 2005 Sep;28(9):1012.
147. R. Khan. Identifying and understanding the role of pulmonary vein activity in atrial fibrillation. *Cardiovasc Res*, 64(3):387–394, Dec 2004.
148. K. Khargi, B. A. Hutten, B. Lemke, and T. Deneke. Surgical treatment of atrial fibrillation; a systematic review. *Eur J Cardiothorac Surg*, 27(2):258–265, Feb 2005. Comment in: *Eur J Cardiothorac Surg*. 2005 Jul;28(1):183; author reply 183-4. Evid Based Cardiovasc Med. 2005 Jun;9(2):120-2.
149. P. M. Kistler, P. Sanders, and S. P. Fynn et al. Electrophysiological and electrocardiographic characteristics of focal atrial tachycardia originating from the pulmonary veins: Acute and long-term outcomes of radiofrequency ablation. *Circulation*, 108:1968–1975, 2003.
150. R. Klinke and S. Silbernagl. *Taschenatlas der Physiologie*. Georg Thieme Verlag, Stuttgart; New York, 5 edition, 2001.

151. J. Kneller, J. Kalifa, R. Zou, A. V. Zaitsev, M. Warren, O. Berenfeld, E. J. Vigmond, L. J. Leon, S. Nattel, and J. Jalife. Mechanisms of atrial fibrillation termination by pure sodium channel blockade in an ionically-realistic mathematical model. *Circ Res*, 96:e35–e47, 2005.
152. J. Kneller, R. Zou, E. J. Vigmond, Z. Wang, L. J. Leon, and S. Nattel. Cholinergic atrial fibrillation in a computer model of a two-dimensional sheet of canine atrial cells with realistic ionic properties. *Circ Res*, 90:e73–e87, 2002.
153. B. P. Knight, B. J. Gersh, M. D. Carlson, P. A. Friedman, R. L. McNamara, S. A. Strickberger, H. F. Tse, A. L. Waldo, American Heart Association Council on Clinical Cardiology (Subcommittee on Electrocardiography and Arrhythmias), Quality of Care and Outcomes Research Interdisciplinary Working Group, Heart Rhythm Society, and AHA Writing Group. Role of permanent pacing to prevent atrial fibrillation: science advisory from the american heart association council on clinical cardiology (subcommittee on electrocardiography and arrhythmias) and the quality of care and outcomes research interdisciplinary working group, in collaboration with the heart rhythm society. *Circulation*, 111(2):240–243, Jan 2005.
154. H. Kottkamp, G. Hindricks, D. Hammel, R. Autschbach, J. Mergenthaler, M. Borggrefe, G. Breithardt, F. W. Mohr, and H. H. Scheld. Intraoperative radiofrequency ablation of chronic atrial fibrillation: a left atrial curative approach by elimination of anatomic ‘anchor’ reentrant circuits. *J Cardiovasc Electrophysiol*, 10:772–780, 1999.
155. K. Kumagai, T. Yasuda, and H. Tojo. Role of rapid focal activation in the maintenance of atrial fibrillation originating from the pulmonary veins. *PACE*, 23:1823–1827, 2000.
156. D. J. Kurz, B. Naegeli, M. Kunz, M. Genoni, U. Niederhauser, and O. Bertel. Epicardial, biatrial synchronous pacing for prevention of atrial fibrillation after cardiac surgery. *Pacing Clin Electrophysiol*, 22:721–726, 1999.
157. B. I. Lee, J. S. Gottdiener, R. D. Fletcher, E. R. Rodriguez, and V. J. Ferrans. Transcatheter ablation: Comparison between laser photoablation and electrode shock ablation in the dog. *Circulation*, 71:579–589, 1985.
158. M. A. Lee, R. Weachter, S. Pollak, and et al. The effect of atrial pacing therapies on atrial tachyarrhythmia burden and frequency: results of a randomized trial in patients with bradycardia and atrial tachyarrhythmias. *J Am Coll Cardiol*, 41:1926–1932, 2003.
159. M. Leonardi and J. Bissett. Prevention of atrial fibrillation. *Curr Opin Cardiol*, 20(5):417–423, Sep 2005.
160. T. Levy, G. Fotopoulos, S. Walker, S. Rex, M. Octave, V. Paul, and M. Amrani. Randomized controlled study investigating the effect of biatrial pacing in prevention of atrial fibrillation after coronary artery bypass grafting. *Circulation*, 102:1382–1387, 2000.
161. T. Lewalter, A. Yang, D. Pfeiffer, J. Ruiter, G. Schnitzler, T. Markert, M. Asklund, O. Przibille, A. Welz, B. Esmailzadeh, M. Linhart, and B. Lüderitz. Individualized selection of pacing algorithms for the prevention of recurrent atrial fibrillation: Results from the vip registry. *PACE*, 29:124–134, 2006.
162. G.-R. Li, J. Feng, L. Yue, and M. Carrier. Transmural heterogeneity of action potentials and  $I_{to1}$  in myocytes isolated from the human right ventricle. *Am. J. Physiol.*, 275:H369–H377, 1998.
163. R. Lieberman, D. Grenz, H. G. Mond, and M. D. Gammage. Selective site pacing: Defining and reaching the selected site. *PACE*, 27:883–886, 2004.



164. G. Y. Lip and C. J. Boos. Antithrombotic treatment in atrial fibrillation. *Heart*, 92(2):155–161, Feb 2006.
165. I. F. Lozano, A. Vincent, J. Roda, and et al. Paroxysmal atrial fibrillation prevention by pacing in patients with pacemaker indication. *Europace*, 5:267–273, 2003.
166. M. Lunati, M. Paolucci, G. Cattafi, G. Magenta, M. R. Vecchi, M. Schirru, M. Lanfranconi, and E. Vitali. Surgical ablation of arrhythmias. *Ital Heart J*, 6(3):231–240, Mar 2005.
167. C.-H. Luo and Y. Rudy. A model of the ventricular cardiac action potential. *Circ. Res.*, 68(6):1501–1526, 1991.
168. C.-H. Luo and Y. Rudy. A dynamic model of the ventricular cardiac action potential: I. Simulations of ionic currents and concentration changes. *Circ. Res.*, 74(6):1071–1096, 1994.
169. C.-H. Luo and Y. Rudy. A dynamic model of the ventricular cardiac action potential: II. afterdepolarizations, triggered activity, and potentiation. *Circ. Res.*, 74(6):1097–1113, 1994.
170. P. Mabo, D. Pavin, C. Crocq, and J. C. Daubert. The role of cardiac pacing in the treatment of atrial arrhythmias. *Arch Mal Coeur Vaiss*, 97(11):1063–1070, Nov 2004. [Article in French].
171. W. H. Maisel, A. E. Epstein, and American College of Chest Physicians. The role of cardiac pacing: American college of chest physicians guidelines for the prevention and management of postoperative atrial fibrillation after cardiac surgery. *Chest*, 128(2 Suppl):36S–38S, Aug 2005.
172. R. Mandrapati, A. Skanes, and J. Chen. Stable microreentrant sources as a mechanism of atrial fibrillation in the isolated sheep heart. *Circulation*, 101:194–199, 2000.
173. M. Mansour, R. Mandapati, and O. Berenfeld. Left-to-right gradient of atrial frequencies during acute atrial fibrillation in the isolated sheep heart. *Circulation*, 103:2631–2636, 2001.
174. J. Mansourati, C. Barnay, J. L. Marcon, and et al. Assessment of pacing algorithms in prevention of atrial fibrillation. *J Am Coll Cardiol*, 39:107, 2002. Abstract.
175. J A Mariani, P A Gould, A Broughton, and D M Kaye. Cardiac resynchronisation therapy for heart failure. *Intern Med J*, 36(2):114–123, Feb 2006.
176. J. E. Marine, J. Dong, and H. Calkins. Catheter ablation therapy for atrial fibrillation. *Prog Cardiovasc Dis*, 48(3):178–192, Nov-Dec 2005.
177. F. A. McAlister, J. A. Ezekowitz, N. Wiebe, B. Rowe, C. Spooner, E. Crumley, L. Hartling, T. Klassen, and W. Abraham. Systematic review: cardiac resynchronization in patients with symptomatic heart failure. *Ann Intern Med*, 141(5):381–390, Sep 2004. Erratum in: *Ann Intern Med*. 2005 Feb 15;142(4):311. Comment in: *ACP J Club*. 2005 Mar-Apr;142(2):35. *Ann Intern Med*. 2004 Sep 7;141(5):399-400. *Ann Intern Med*. 2004 Sep 7;141(5):I64. *Ann Intern Med*. 2005 Feb 15;142(4):305-7; author reply 307-8. *Ann Intern Med*. 2005 Feb 15;142(4):305; author reply 307-8.
178. R. E. McAllister, D. Noble, and R. W. Tsien. Reconstruction of the electrical activity of cardiac purkinje fibres. *J. Physiol.*, 251:1–59, 1975.
179. G. E. Mead, A. T. Elder, A. D. Flapan, and A. Kelman. Electrical cardioversion for atrial fibrillation and flutter. *Cochrane Database Syst Rev*, 20(3):CD002903, Jul 2005. Update of: *Cochrane Database Syst Rev*. 2002;(1):CD002903.
180. J. Melo, P. Adragao, J. Neves, M. M. Ferreira, M. M. Pinto, M. J. Rebocho, L. Parreira, and T. Ramos. Surgery for atrial fibrillation using radiofrequency catheter ablation: Assessment of results at one year. *Eur J Cardiothorac Surg*, 15:851–855, 1999.

181. J. Melo, P. Adragao, J. Neves, M. M. Ferreira, A. Timoteo, Santiago, R. Ribeiras, and M. Canada. Endocardial and epicardial radiofrequency ablation in the treatment of atrial fibrillation with a new intra-operative device. *Eur J Cardiothorac Surg*, 18:182–186, 2000.
182. R. Miri, M. Reumann, D. Farina, B. Osswald, and O Dössel. Optimizing A-V and V-V delay in cardiac resynchronization therapy in simulations including ventricle heterogeneity. In J. W. Gardner, editor, *Proceedings of the fifth IASTED International Conference on Biomedical Engineering*, 2007. ISBN: 978-0-88986-648-5.
183. T. Misaki and K. Fukahara. Recent topics on the surgical treatment for atrial fibrillation. *Ann Thorac Cardiovasc Surg*, 10(5):277–280, Oct 2004.
184. A. R. R. Misier, W. P. Beukema, and H. A. Oude Luttikhuis. Multisite or alternate site pacing for the prevention of atrial fibrillation. *Am J Cardiol*, 83:237D–240D, 1999.
185. G. Miske, C. Acevedo, T. W. Goodlive, C. M. Brown, and T. B. Levine. Cardiac resynchronization therapy and tools to identify responders. *Congestive Heart Failure*, 11(4):199–206, 2005.
186. A. R. Mitchell. Will this be the end of the anticoagulation clinic for patients with atrial fibrillation? *Curr Drug Targets Cardiovasc Haematol Disord*, 5(5):405–408, Oct 2005.
187. A. R. Mitchell and N. Sulke. How do atrial pacing algorithms prevent atrial arrhythmias? *Europace*, 6(4):351–362, Jul 2004.
188. G. K. Moe. On the multiple wavelet hypothesis of atrial fibrillation. *Arch Int Pharmacodyn Ther*, 140:183–188, 1962.
189. G. K. Moe, W. C: Rheinboldt, and J. A: Abidskov. A computer model of atrial fibrillation. *Am Heart J*, 67(2):200–220, 1964.
190. C. A. Morillo, G. J Klein, and D. L. Jones. Chronic rapid atrial pacing. structural, functional, and electrophysiological characteristics of a new model of sustained atrial fibrillation. *Circulation*, 91:1588–1595, 1995.
191. A. D. Waggoner N. S. Sawhney, S. Garhwal, M. K. Chawla, J. Osborn, and M. N. Faddis. Randomized prospective trial of atrioventricular delay programming for cardiac resynchronization therapy. *Heart Rhythm*, 5:562–567, 2004.
192. K. Nademane, J. McKenzie, E. Kosar, and et al. A new approach for catheter ablation of atrial fibrillation: Mapping of the electrophysiologic substrate. *J Am Coll Cardiol*, 43:2044–2053, 2004.
193. H. Nakagawa, R. Lazzara, T. Khastgir, and et al. Role of the tricuspid annulus and the eustachian valve/ridge in atrial flutter. relevance to catheter ablation of the septal isthmus and a new technique for rapid identification of ablation success. *Circulation*, 94:407–424, 1996.
194. K. Nanthakumar, Y. R. Lau, V. J. Plump, A. E. Epstein, and G. N. Kay. Electrophysiological findings in adolescents with atrial fibrillation who have structurally normal hearts. *Circulation*, 110:117–123, 2004.
195. M. Nash. *Mechanics and Material Properties of the Heart using an Anatomically Accurate Mathematical Model*. PhD thesis, University of Auckland, Dep. of Engineering Science, New Zealand, 1998.
196. H. Nathan and M. Eliakim. The junction between the left atrium and the pulmonary veins. an anatomic study of human hearts. *Circulation*, 34:412–422, 1966.
197. S. Nattel and L. H. Opie. Controversies in atrial fibrillation. *Lancet.*, 367(9506):262–272, Jan 2006.
198. S. Nattel, A. Shiroshita-Takeshita, B. J. Brundel, and L. Rivard. Mechanisms of atrial fibrillation: lessons from animal models. *Prog Cardiovasc Dis*, 48(1):9–28, Jul-Aug 2005.

199. S. Nattel, A. Shiroshita-Takeshita, S. Cardin, and P. Pelletier. Mechanisms of atrial remodeling and clinical relevance. *Curr Opin Cardiol*, 20(1):21–25, Jan 2005.
200. G. Ndrepepa, M. A. Schneider, and M. R. Karch. Pulmonary vein internal electrical activity does not contribute to the maintenance of atrial fibrillation. *PACE*, 26:1356–1362, 2003.
201. J. A. Nelder and R. Mead. A simplex method for function minimization. *Computer Journal*, 7:308–313, 1965.
202. F. H. Netter. *Farbatlanten der Medizin*, volume 1. Thieme, Stuttgart; New York, 3 edition, 1990.
203. F. H. Netter. *Atlas der Anatomie des Menschen*. Novartis, 1995.
204. D. Newman. Quality of life as an endpoint for atrial fibrillation research: pitfalls and practice. *Heart Rhythm*, 1(2 Suppl):B20–B25, discussion B25–B26, Jul 2004.
205. T. Nitta. Surgery for atrial fibrillation. *Ann Thorac Cardiovasc Surg*, 11(3):154, 158 2005.
206. T. Nitta, Y. Ishii, H. Ogasawara, and et al. Initial experience with the radial incision approach for atrial fibrillation. ii. electrophysiologic effects and atrial contribution to ventricular filling. *Ann Thorac Surg*, 67(1):36–50, 1999.
207. D. Noble. A modification of the Hodgkin-Huxley equation applicable to Purkinje fibre action and pacemaker potentials. *J. Physiol.*, 160:317–352, 1962.
208. D. Noble, A. Varghese, P. Kohl, and P. Noble. Improved guinea-pig ventricular cell model incorporating a diadic space,  $I_{Kr}$  and  $I_{Ks}$ , and length- and tension-dependend processes. *Can. J. Cardiol.*, 14(1):123–134, Jan. 1998.
209. A. Nygren, C. Fiset, L. Firek, J. W. Clark, D. S. Lindblad, R. B. Clark, and W. R. Giles. Mathematical model of an adult human atrial cell. *Circ. Res.*, 82:63–81, 1998.
210. B. Olshansky. Interrelationships between the autonomic nervous system and atrial fibrillation. *Prog Cardiovasc Dis*, 48(1):57–78, Jul-Aug 2005.
211. H. Oral. Mechanisms of atrial fibrillation: lessons from studies in patients. *Prog Cardiovasc Dis*, 48(1):29–40, Jul-Aug 2005.
212. H. Oral, B. P. Knight, and M. Ozaydin. Segmental ostial ablation to isolate the pulmonary veins during atrial fibrillation: Feasibility and mechanistic insights. *Circulation*, 106:1256–1262, 2002.
213. H. Oral, C. Scharf, A. Chugh, B. Hall, P. Cheung, E. Good, S. Veerareddy, F. Pelosi, and F. Morady. Catheter ablation for paroxysmal atrial fibrillation segmental pulmonary vein ostial ablation versus left atrial ablation. *Circulation*, 108:2355–2360, 2003.
214. B. O'Rourke, D. A. Kass, G. F. Tomaselli, S. Kaab, R. Tunin, and E. Marbán. Mechanisms of altered excitation-contraction coupling in canine tachycardia-induced heart groups = cardiac measurement, failure, I experimental studies. *Circ. Res.*, 84(5):562–570, 1999.
215. F. Ouyang, D. Bänsch, S. Ernst, A. Schaumann, H. Hachiya, M. Chen An J. Chhun, P. Falk, A. Khanedani, M. Antz, and K.-H. Kuck. Complete isolation of left atrium surrounding the pulmonary veins - new insights from the double-lasso technique in paroxysmal atrial fibrillation. *Circulation*, 110:2090–2096, 2004.
216. I. E. Ovsyshcher and S. S. Barold. Drug induced bradycardia: to pace or not to pace. *PACE*, 27(8):1144–1147, 2004.
217. L. Padeletti, A. Michelucci, P. Pieragnoli, A. Colella, and N. Musilli. Atrial septal pacing: a new approach to prevent atrial fibrillation. *Pacing Clin Electrophysiol*, 27(6 Pt 2):850–854, Jun 2004.

218. L. Padeletti, P. Pieragnoli, C. Ciapetti, and et al. Randomized crossover comparison of right atrial appendage pacing versus interatrial septum pacing for prevention of paroxysmal atrial fibrillation in patients with sinus bradycardia. *Am Heart J*, 142:1047–1055, 2001.
219. L. Padeletti, H. Purerfellner, S. W. Adler, and et al. Combined efficacy of atrial septal lead placement and atrial pacing algorithms for prevention of paroxysmal atrial tachyarrhythmia. *J Cardiovasc Electrophysiol*, 14:1189–1195, 2003.
220. W. Paladino, M. Bahu, B. P. Knight, R. Weiss, J. Sousa, A. Zivin, R. Goyal, E. Daoud, K. K. Ching Man, A. Strickberger, and F. Morady. Failure of single-and multisite high-frequency atrial pacing to terminate atrial fibrillation. *Am J Cardiol*, 80:226–227, 1997.
221. C. A. Palin, R. Kailasam, and C. W. Hogue Jr. Atrial fibrillation after cardiac surgery: pathophysiology and treatment. *Semin Cardiothorac Vasc Anesth*, 8(3):175–183, Sep 2004.
222. S. V. Pandit, R. B. Clark, W. R. Giles, and S. S. Demir. A mathematical model of action potential heterogeneity in adult left ventricular myocytes. *Biophys. J.*, 81:3029–3051, 2001.
223. C. Pappone, G. Augello, and V. Santinelli. Atrial fibrillation ablation. *Ital Heart J*, 6(3):190–199, Mar 2005.
224. C. Pappone, F. Manguso, G. Vicedomini, F. Gugliotta, O. Santinelli, A. Ferro, S. Gulletta, S. Sala, N. Sora, G. Paglino, G. Augello, E. Agricola, A. Zangrillo, O. Alfieri, and Vincenzo Santinelli. Prevention of iatrogenic atrial tachycardia after ablation of atrial fibrillation: A prospective randomized study comparing circumferential pulmonary vein ablation with a modified approach. *Circulation*, 110:3036–3042, 2004.
225. C. Pappone, G. Oreto, and F. Lambertini et al. Catheter ablation of paroxysmal atrial fibrillation using a 3d mapping system. *Circulation*, 100:1203–1208, 1999.
226. C. Pappone, G. Oreto, S. Rosanio, G. Vicedomini, M. Tocchi, F. Gugliotta, A. Salvati, C. Dicandia, M. P. Calabro, P. Mazzone, E. Ficarra, C. Di Gioia, S. Gulletta, S. Nardi, V. Santinelli, S. Benussi, and O. Alfieri. Atrial electroanatomic remodeling after circumferential radiofrequency pulmonary vein ablation: efficacy of an anatomic approach in a large cohort of patients with atrial fibrillation. *Circulation*, 104:2539–2544, 2001.
227. C. Pappone, S. Rosanio, G. Augello, and et al. Mortality, morbidity, and quality of life after circumferential pulmonary vein ablation for atrial fibrillation: outcomes from a controlled nonrandomized long-term study. *J Am Coll Cardiol*, 42:185–197, 2003.
228. C. Pappone, S. Rosanio, G. Oreto, M. Tocchi, F. Gugliotta, G. Vicedomini, A. Salvati, C. Dicandia, P. Mazzone, V. Santinelli, S. Gulletta, and S. Chierchia. Circumferential radiofrequency ablation of pulmonary vein ostia: a new anatomic approach for curing atrial fibrillation. *Circulation*, 102:2619–2628, 2000.
229. C. Pappone, V. Santinelli, F. Maguso, G. Vicedomini, F. Gugliotta, G. Augello, P. Mazzone, V. Tortorelli, G. Landoni, A. Zangrillo, C. Lang, T. Tomita, C. Mesas, E. Mastella, and O. Alfieri. Pulmonary vein denervation enhances long-term benefit after circumferential ablation for paroxysmal atrial fibrillation. *Circulation*, 109:327–334, 2004.
230. M. Pasic, P. Bergs, P. Muller, and et al. Intraoperative radiofrequency maze ablation for atrial fibrillation: Berlin modification. *Ann Thorac Surg*, 72:1484–1491, 2001.
231. M. Penicka, J. Bartunek, B. De Bynne, M. Vanderheyden, M. Goethals, M. De Zutter, P. Brugada, and P. Geelen. Improvement of left ventricular function after cardiac resynchronization therapy is predicted by tissue doppler imaging echocardiography. *Circulation*, 109:978–983, 2004.

232. G. B. Perego, R. Chianca, M. Facchini, A. Frattola, E. Balla, S. Zucchi, S. Cavaglia, I. Vicini, M. Negretto, and G. Osculati. Simultaneous vs sequential biventricular pacing in dilated cardiomyopathy: an acute hemodynamic study. *Eur J Heart Fail*, 5(3):305–313, 2003.
233. N. S. Peters, C. Cabo, and A. L. Wit. Arrhythmogenic mechanisms: Automaticity, triggered activity, and reentry. In D. P. Zipes and J. Jalife, editors, *Cardiac Electrophysiology. From Cell to Bedside*, chapter 40, pages 345–355. W. B. Saunders Company, Philadelphia, 3 edition, 1999.
234. D. Pfeiffer, R. Moosdorf, R. H. Svenson, and et al. Epicardial neodymium. yag laser photocoagulation of ventricular tachycardia without ventriculotomy in patients after myocardial infarction. *Circulation*, 94:3221–3225, 1996.
235. F. Philippon. Cardiac resynchronization therapy: Device-based medicine for heart failure. *J Card Surg*, 19:270–274, 2004.
236. M. V. Pitzales, M. Iacoviello, R. Romito, P. Guida, E. De Tommasi, G. Luzzi, M. Anaclerio, C. Forleo, and P. Rizzon. Ventricular asynchrony predicts better outcome in patients with chronic heart failure receiving cardiac resynchronization therapy. *J Am Coll Cardiol*, 45:65–69, 2005.
237. M. C. Porciani, C. Dondina, R. Macioce, G. Demarchi, P. Pieragnoli, N. Musilli, A. Colella, G. Ricciardi, A. Michelucci, and L. Padeletti. Echocardiographic examination of atrioventricular and interventricular delay optimization in cardiac resynchronization therapy. *Am J Cardiol*, 95:1108–1110, 2005.
238. W. H. Press, S. A. Teukolsky, W. T. Vetterling, and B. P. Flannery. *Numerical Recipes in C. The art of scientific computing*. Cambridge University Press, 2 edition, 2002.
239. L. Priebe and D. J. Beuckelmann. Simulation study of cellular electric properties in heart failure. *Circ. Res.*, 82:1206–1223, 1998.
240. J. L. Puglisi and D. M. Bers. LabHEART: An interactive computer model of rabbit ventricular myocyte ion channels and Ca transport. *Am. J. Physiol.*, 281:C2049–C2060, 2001.
241. I. B. Ray and E. K. Heist. Treating atrial fibrillation. what is the consensus now? *Postgrad Med*, 118(4):47–48, 51–54, 58, Oct 2005.
242. R. W. Rho and R. L. Page. Asymptomatic atrial fibrillation. *Prog Cardiovasc Dis*, 48(2):79–87, Sep-Oct 2005.
243. R. P. Ricci. Atrial tachyarrhythmia prevention and treatment by means of special pacing algorithms. *Ital Heart J*, 6(3):200–205, Mar 2005.
244. L. Riedlbauchova, J. Kautzner, and P. Frodl. Is right ventricular outflow tract pacing an alternative to left ventricular/biventricular pacing? *PACE*, 28:S19–S23, 2005.
245. L. Riedlbauchova, J. Kautzner, R. Hatala, and T. A. Buckingham. Is right ventricular outflow tract pacing an alternative to left ventricular/biventricular pacing? *PACE*, 27:871–877, 2004.
246. J. W. Rohen. *Topographische Anatomie: Kurzlehrbuch für Studierende und Ärzte*. F. K. Schattauer Verlag, 9 edition, 1992.
247. K. Rohlf, L. Glass, and R. Kapral. Spiral wave dynamics in excitable media with spherical geometries. *Chaos*, 16:037115, Sep 2006. published online.
248. R. Rom, J. Erel, M. Glikson, K. Rosenblum, R. Ginosar, and D. L. Hayes. Adaptive cardiac resynchronization therapy device: A simulation report. *PACE*, 28:1168–1173, 2005.
249. S. Rosanio, E. R. Schwarz, M. Ahmad, P. Jammula, A. Vitarelli, B. F. Uretsky, Y. Birnbaum, D. L. Ware, S. Atar, and M. Saeed. Benefits, unresolved questions, and technical issues of cardiac resynchronization therapy for heart failure. *Am J Cardiol*, 96(5):710–717, Sep 2005.

250. S. Rosanio, D. L. Ware, and M. Saeed. Pulmonary vein ablation of atrial fibrillation: beyond the traditional. *Am J Med Sci*, 328(6):323–329, Dec 2004.
251. L. E. Rosenfeld. Bradyarrhythmias, abnormalities of conduction, and indications for pacing in acute myocardial infarction. *Cardiol Clin*, 6(1):49–61, 1988.
252. F. B. Sachse, C. D. Werner, and G. Seemann. Anatomical models of the heart for the simulation of excitation propagation and force development. In *Annals of Biomedical Engineering*, page 48, Oct. 2001.
253. S. Saksena, I. Gielschinsky, and N. G. Tullo. Argon laser ablation of malignant ventricular tachycardia associated with coronary artery disease. *Am J Cardiol*, 64:1298–1304, 1989.
254. M. Santini. The role of the implantable atrial cardioverter-defibrillator. *Ital Heart J*, 6(3):206–209, Mar 2005.
255. I. Savelieva and A. John Camm. Atrial fibrillation and heart failure: natural history and pharmacological treatment. *Europace*, 5 Suppl1:S5–S19, Sep 2004.
256. C. Scharf. Atrial flutter and fibrillation. *Schweiz Rundsch Med Prax*, 94(45):1753–1759, Nov 2005. Article in German.
257. B. J. Scherlag, E. Patterson, and S. S. Po. The neural basis of atrial fibrillation. *J Electrocardiol*, 39:S180–S183, 2006.
258. R. F. Schmidt. Erregungsphysiologie des Herzens. In *Physiologie kompakt*, chapter 23, pages 197–204. Springer, Berlin, Heidelberg, New York, 1999.
259. M. A. Schneider. Nature of rapid pulmonary vein tachycardias: Reentry or not reentry? *J Cardiovasc Electrophysiol*, 14:933–934, 2003.
260. B.A. Schoonderwoerd, I. C. Van Gelder, D. J. Van Veldhuisen, M. P. Van den Berg, and H. J. Crijns. Electrical and structural remodeling: role in the genesis and maintenance of atrial fibrillation. *Prog Cardiovasc Dis*, 48(3):153–168, Nov-Dec 2005.
261. A. Schuchert. Contributions of permanent cardiac pacing in the treatment of atrial fibrillation. *Europace*, 5 Suppl1:S35–S41, Sep 2004.
262. G. Seemann, C. Höper, F. B. Sachse, O. Dössel, A. V. Holden, and H. Zhang. 3d anatomical and electrophysiological model of human sinoatrial node and atria. *Phil. Trans. Roy. Soc.*, 2006. accepted.
263. G. Seemann, D. L. Weiß, F. B. Sachse, and O. Dössel. Electrophysiology and tension development in a transmural heterogeneous model of the visible female left ventricle. In A. F. Franji, P. I. Radeva, A. Santos, and M. Hernandez, editors, *LNCS*, volume 3504, pages 172–182, 2005.
264. Gunnar Seemann. *Modeling of electrophysiology and tension development in the human heart*. PhD thesis, Institut für Biomedizinische Technik, Universitätsverlag Karlsruhe ISBN 3-937300-66-X, 2005.
265. D. Shah. Catheter ablation for atrial fibrillation: mechanism-based curative treatment. *Expert Rev Cardiovasc Ther*, 2(6):925–933, Nov 2004.
266. S. Silbernagl and A. Despopoulos. Grundlagen, Zellphysiologie. In *Taschenatlas der Physiologie*, chapter 1, pages 2–41. Georg Thieme Verlag, Stuttgart, 2001.
267. G. Sleilaty, A. Sarkis, P. Achouh, V. Jebara, and J.N. Fabiani. Prevention and treatment of atrial fibrillation after cardiac surgery. *Arch Mal Coeur Vaiss*, 98(9):894–898, Sep 2005. Article in French.
268. P. Sogaard, H. Egeblad, A. K. Pedersen, W. Y. Kim, B. O. Kristensen, P. S. Hansen, and P. T. Mortensen PT. Sequential versus simultaneous biventricular resynchronization for severe heart failure: evaluation by tissue doppler imaging. *Circulation*, 106:2078–2084, 2002.

269. S. G. Spitzer, S. Gazarek, P. Wacker, K. Malinowski, and V. Schibgilla. Pacing of the atria in sick sinus syndrome trial: preventive strategies for atrial fibrillation. *Pacing Clin Electrophysiol*, 26:268–271, 2003.
270. W. G. Stevenson and M. O. Sweeney. Single site left ventricular pacing for cardiac resynchronization. *Circulation*, 109:1694–1696, 2004.
271. B. Strohmer, M. Pilcher, M. Froemmel, M. Migschitz, and F. Hinteringer. Evaluation of atrial conduction time at various sites of right atrial pacing and influence on atrioventricular delay optimization by surface electrocardiography. *PACE*, 27:468–474, 2004.
272. M. L. Sturmer, M. Talajic, B. Thibault, P. G. Guerra, M. Dubuc P. Novak, and D. Roy. Management of atrial fibrillation in patients with congestive heart failure. *Am J Geriatr Cardiol*, 14(2):91–94, Mar-Apr 2005.
273. T. Sueda, H. Nagata, K. Orihashi, S. Morita, K. Okada, and M. Sueshiro. Efficacy of a simple left atrial procedure for chronic atrial fibrillation in mitral valve operations. *Ann Thorac Surg*, 63:1070–1075, 1997.
274. T. Sueda, H. Nagata, and H. Shikata. Simple left atrial procedure for chronic atrial fibrillation associated with mitral valve disease. *Ann Thorac Surg*, 62:1796–1800, 1996.
275. Y. Takahashi, Y. Iesaka, and A. Takahashi. Reentrant tachycardia in pulmonary veins of patients with paroxysmal atrial fibrillation. *Cardiovasc Electrophysiol*, 14:927–932, 2003.
276. K. H. W. J. ten Tusscher, D. Noble, P. J. Noble, and A. V. Panfilov. A model for human ventricular tissue. *Am. J. Physiol.*, 286:H1573–H1589, 2004.
277. B. Thiebault. Optimizing algorithms for crt devices. a critical overview. *Cardiostim 2006*, Nice, 2006.
278. M. S. Turner, R. A. Bleasdale, D. Vinereanu, C. E. Mumford, V. Paul, A. G. Fraser, and M. P. Frenneaux. Electrical and mechanical components of dyssynchrony in heart failure patients with normal qrs duration and left bundle-branch block. *Circulation*, 109:2544–2549, 2004.
279. unknown. Conduction system of the heart, 2003. Pearson Education, Inc., publishing as Benjamin Cummings.
280. L. C. M. van Campen, F. C. Visser, C. C. de Cock, D. h. S. Vos, O. Kamp, and C. A. Visser. Comparison of the hemodynamics of different pacing sites in patients undergoing resynchronization therapy: need for individualization an optimal lead localization. *Heart*, published online, Jun 2006.
281. B. M. Van Gelder, F. A. Bracke, A. Meijer, L. J. Lakerveld, and N. H. Pijls. Effect of optimizing the vv interval on left ventricular contractility in cardiac resynchronisation therapy. *Am J Cardiol*, 93:1500–1503, 2004.
282. X. A. A. M. Verbeek, Auricchio A, Y. Yu, J. Ding, T. Pochet, K. Vernoooy, A. Kramer, J. Spinelli, and F. W. Prinzen. Tailoring cardiac resynchronization therapy using interventricular asynchrony. validation of a simple model. *Am J Physiol Heart Circ Physiol*, 290:H968–H977, 2006.
283. X. A. A. M. Verbeek, K. Vernoooy, M. Peschar, R. N. M. Cornelussen, and F. W. Prinzen. Intra-ventricular resynchrony for optimal left ventricular function during pacing in experimental left bundle branch block. *J Am Coll Cardiol*, 42:558–567, 2003.
284. H. J. Vidaillet. Rate control vs. rhythm control in the management of atrial fibrillation in elderly persons. *Am J Geriatr Cardiol*, 14(2):73–78, Mar-Apr 2005. quiz 79-80.
285. E. J. Vigmond, R. Ruckdeschel, and N. Trayanova. Reentry in a morphologically realistic atrial model. *J Cardiovasc Electrophys*, 12(9):1046–1054, 2001.

286. E. J. Vigmond, V. Tsoi, S. Kuo, H. Arevalo, J. Kneller, S. Nattel, and N. Trayanova. The effect of vagally induced dispersion of action potential duration on atrial arrhythmogenesis. *Heart Rhythm*, 1(3):334–344, 2004.
287. N. Virag, O. Blanc, J. M. Vesin, and L. Kappenberger. 3d computer model of atrial arrhythmias. In *Proceedings of The First Joint BMES/EMBS Conference Serving Humanity, Advancing Technology, Oct 13-16. 1999, Atlanta, GA, USA*, page 1198. IEEE, 1999.
288. N. Virag, V. Jacquement, C. S. Henriquez, and et al. Reentry in a morphologically realistic atrial model. *Chaos*, 12:754–763, 2002.
289. N. Virag, J. M. Vesin, and L. Kappenberger. A computer model of cardiac electrical activity for the simulation of arrhythmias. *PACE*, 21[Pt. II]:2366–2371, 1998.
290. A. L. Waldo. The interrelationship between atrial fibrillation and atrial flutter. *Prog Cardiovasc Dis*, 48(1):41–56, Jul-Aug 2005.
291. D. L. Ware, P. Boor, C. Yang, A. Gowda, J. J. Grady, and M. Motamedi. Slow intramural heating with diffused laser light: A unique method for deep myocardial coagulation. *Circulation*, 99:1630–1636, 1999.
292. O. M. Wazni, N. F. Marouche, D. O. Martin, and et al. Radiofrequency ablation vs antiarrhythmic drugs as first-line treatment of symptomatic atrial fibrillation: a randomized trial. *JAMA*, 293:2634–2640, 2005.
293. H. P. Weber and A. Henze. Laser catheter ablation of atrial flutter and of atrioventricular nodal reentrant tachycardia in a single session. *European Heart Journal*, 15:1147–1149, 1994.
294. D. L. Weiß. Vergleich des Verhaltens eines Elektrophysiologischen Zellmodells mit einem Zellulären Automaten bei Simulierten Atrialen Fibrillationen. Master’s thesis, Universität Karlsruhe (TH), Institut für Biomedizinische Technik, 2002. Student Research Project.
295. E. M. Weiss and T. Buescher. Atrial fibrillation: treatment options and caveats. *AACN Clin Issues*, 15(3):362–376, Jul-Sep 2004.
296. C. Werner. *Simulation der elektrischen Erregungsausbreitung in anatomischen Herzmodellen mit adaptiven Zellulären Automaten*. Tenea, Berlin, 2001. Dissertation.
297. C. D. Werner. *Simulation der elektrischen Erregungsausbreitung in anatomischen Herzmodellen mit adaptiven zellulären Automaten*. PhD thesis, Universität Karlsruhe (TH), Institut für Biomedizinische Technik, 2001.
298. C. D. Werner, F. B. Sachse, and O. Dössel. Electrical excitation propagation in the human heart. *Int. J. Bioelectromagnetism*, 2(2), 2000.
299. Z. I. Whinnett, J. E. R. Davies, K. Willson, C. H. Manisty, A. W. Chow, R. A. Foale, D. W. Davies, A. D. Hughes, J. Mayet, and D. P. Francis. Haemodynamic effects of changes in av and vv delay in cardiac resynchronisation therapy show a consistent pattern: analysis of shape, magnitude and relative importance of av and vv delay. *Heart*, published online, May 2006.
300. M. C. E. F. Wijffels, C. J. H. J. Kirchhof, R. Dorland, and M. A. Allesie. Atrial fibrillation begets atrial fibrillation. *Circ.*, 92:1954–1968, 1995.
301. M. R. Williams, J. R. Stewart, S. F. Bolling, and et al. Surgical treatment of atrial fibrillation using radiofrequency energy. *Ann Thorac Surg*, 71:1939–1944, 2001.
302. R. L. Winslow, J. J. Rice, S. Jafri, E. Marbán, and B. O’Rourke. Mechanisms of altered excitation-contraction coupling in canine tachycardia-induced heart failure, II model studies. *Circ. Res.*, 84:571–586, 1999.



303. D. G. Wyse. Are there alternatives to mortality as an endpoint in clinical trials of atrial fibrillation? *Heart Rhythm*, 1(2 Suppl):B41–B44, discussion B44, Jul 2004.
304. D. G. Wyse. Rate control vs rhythm control strategies in atrial fibrillation. *Prog Cardiovasc Dis*, 48(2):125–138, Sep-Oct 2005.
305. A. Yang, M. Hochhausler, J. Schrickel, and et al. Advanced pacemaker diagnostic features in the characterization of atrial fibrillation: impact on preventive pacing algorithms. *Pacing Clin Electrophysiol*, 26:310–313, 2003.
306. A. Yang, B. Luderitz, and T. Lewalter. Atrial fibrillation: profit from cardiac pacing? *Z Kardiol*, 94(3):141–151, Mar 2005.
307. J. B. Young, W. T. Abraham, A. L. Smith, A. R. Leon, R. Lieberman, B. Wilkoff, R. C. Canby, J. S. Schroeder, L. B. Liem, S. Hall, and et al. Multicenter insync icd randomized clinical evaluation (miracle icd) trial investigators. combined cardiac resynchronization and implantable cardioversion defibrillation in advanced chronic heart failure. *JAMA*, 289:2685–2694, 2003.
308. C. M. Yu, J. W. Fung, Q. Zhang, C. K. Chan, Y. S. Chan, H. Lin, L. C. Kum and S. L. Kong, Y. Zhang, and J. E. Sanderson. Tissue doppler imaging is superior to strain rate imaging and postsystolic shortening on the prediction of reverse remodeling in both ischemic and nonischemic heart failure after cardiac resynchronization therapy. *Circulation*, 110:66–73, 2004.
309. C.-M. Yu, J. W.-H. Fung, Q. Zhang, and J. E. Sanderson. Understanding nonresponders of cardiac resynchronization therapy - current and future perspectives. *J Cardiovasc Electrophysiol*, 16:1117–1124, Oct 2005.
310. C. M. Yu, H. Lin, Q. Zhang, and J. E. Sanderson. High prevalence of left ventricular systolic and diastolic asynchrony in patients with congestive heart failure and normal qrs duration. *Heart*, 89:54–60, 2003.
311. H. Zhang, A. V. Holden, I. Kodama, H. Honjo, M. Lei, T. Varghese, and M. R. Boyett. Mathematical models of action potentials in the periphery and center of the rabbit sinoatrial node. *Am. J. Physiol.*, 279(1):397–421, 2000.





## Curriculum Vitae – Matthias Reumann

Date/Place of birth	January 6th, 1978 - Frankfurt/Main, Germany
Nationality	German
Address	Hauptstrasse 115 68259 Mannheim, Germany
Telephone	+49 - 1 77 - 6 72 77 31
e-mail	mreumann@ieee.org
Education	<p>Certificate for Higher Education “Baden-Württemberg Certificate” (2005)</p> <p>First Class Honours - Masters of Engineering in Electronics with the Tripartite Diploma Department of Electronics and Computer Science - University of Southampton, UK (1998 - Juni 2003)</p> <p>European Masters Programm at the Universities:</p> <ul style="list-style-type: none"> <li>– University of Southampton, UK (1998 - 2001)</li> <li>– Universität Karlsruhe (TH), Germany (2001/02)</li> <li>– ESIEE in Paris, France (2002/03)</li> </ul> <p>Student projects:</p> <ul style="list-style-type: none"> <li>– Breast Reconstruction Using Ultrasound Scans, Southampton, UK (2001)</li> <li>– Klassifizierung von Geräuschquellen (Classification of Sound Sources), Karlsruhe, Germany (2002)</li> <li>– Algorithmes pour un Reseau de Haut-Parleurs Fortement Directionnels (Algorithms for Parametric Acoustic Arrays), Ulm, Germany (2003)</li> </ul> <p>German Abitur: 1.5 (second best result in the year) Liebigschule, Frankfurt/Main, Germany (1988 - 1997)</p>
Languages	German (maternal language), English (excellent), French (very good), Spanish (poor)

## Professional Experience

Research assistant at the Institute of Biomedical Engineering, Universität Karlsruhe (TH) (since July 2003)

Research Interests: Development of optimization strategies for therapy planning and evaluation of cardiac resynchronization therapy and non-pharmacological strategies in the treatment of supraventricular arrhythmia in a computer model.

Teaching: Responsible for the organization of the 1st year course on "Linear circuit analysis" (Exercise classes, tutorials, supervision and education of tutors, exams)

Projects:

- MedidaPrix 2006: "iLME-coleG" Interactive teaching in Electronics - cooperate learning in large groups of students
- SULKA - Online admission system for foreign students (since 2005)
- Governmental Survey (2004-2005): "Situation of Biomedical Engineering in Germany in an International Context"
- Large Research Project (SFB 414) "Information Technology in Medicine" (2003 - 2005)

Master Thesis at Daimler Chrysler AG, Research and Technology, Ulm, Germany (01.12.02 - 31.05.03)

- Development of algorithms for the simulation of a parametric acoustic array to generate an audio spotlight. Digital signal processing algorithms were developed in Matlab.

Part time work at the Institute of Biomedical Engineering, Universität Karlsruhe (TH) (01.03.02 - 31.07.02)

- Supervision of Laboratory session in the field of biomedical technology
- Help in organising of the BMT 2002 conference in Karlsruhe, Germany

Internship with Imagination Technologies Group, VideoLogic Systems Division (02.07.01 - 14.09.01)

- User Interface Development and responsible for the solving of reported problems with the User Interface and Installation software, using Microsoft Visual C++, MFCC, InstallShield script.

## Professional Experience cont.

Internship with Finatec Financial Software Solutions AG (12.06.00 - 15.09.00)

– Developing algorithms for the automatic calculation of calendar dates such as Easter, a corresponding web application to parameterise and maintain the generated dates. The system was realised in HTML, Java, Java Script, JSP, SQL and is now included in the Software Product that is being sold.

Internship with Brandeis, Hauck & Partner GmbH (02.08.99 - 24.09.99)

– Working in the Accounting Department, clearing and booking accounts, helping the head of the department on the annual statement of accounts

Full time work for Samson AG, Frankfurt (22.03.99 - 05.04.99)

– Factory work (painting circuit boards)

Military Training as Paramedic (01.09.97 - 30.06.98)

Part time work for Infratest Burke int., Frankfurt (1997 - 1998)

– Interviewer, Recruiter, Study Supervisor in market research

Part time work in a supermarket (1994 - 1997)

## Selected Awards/Societies

Kenichi Harumi Young Investigators Award (2. Place) “The role of conduction delay and complex anatomical structures in the initiation and maintenance of atrial fibrillation” at the 33rd International Congress on Electrophysiology 2006

1. Prize at the student competition of the International Conference on Medical Physics and the annual meeting of the German Society of Biomedical Engineering ICMP - BMT 2006 - “Computer-Aided Evaluation and Optimisation of Biventricular Pacing for Patients with Congestive Heart Failure” K. Albrecht, M. Reumann, G. Seemann, G. Reinerth, C. F. Vahl, O. Dössel

Liebig Prize 1997 for the best academic achievement and social commitment in High School

Proposed for a scholarship of the “Studienstiftung des deutschen Volkes”

Task Force “Key Competences” Universität Karlsruhe (TH)

Student member - Staff and Student Liaison Committee (1998 - 2001)

Student member - MEng Faculty Board (2000/01)

Professional Societies: IEEE EMBS, VDE DGBMT, The IET

## Hobbies &amp; Interests

Literature, Traveling/meeting other cultures, Music (bassoon)

Dancing (latin formation) - Teamleader since 2006

Sailing - several licences, Skipper since 1996

Golf

## Publications

### *First Author*

- M. Reumann, J. Bohnert, G. Seemann, B. Osswald and O. Dössel. Preventive Ablation Strategies in a Biophysical Model of Atrial Fibrillation Based on Realistic Anatomical Data. *IEEE Transactions on Biomedical Engineering*. submitted October 2006
- M. Reumann, J. Bohnert, B. Osswald, S. Hagl, O. Dössel. Multiple wavelets, rotors and snakes in atrial fibrillation - a computer simulation study. *International Journal of Electrophysiology* 2007 in press
- M. Reumann, M. Mohr, O. Dössel, A. Diez. Vorlesung, Übung und Tutorium im koordinierten Zusammenspiel. Ein Lehr-/Lernpaket schnüren - Grundlagenveranstaltung. *Neues Handbuch Hochschullehre*. 2006
- M. Reumann, J. Bohnert, O. Dössel. Simulating pulmonary vein activity leading to atrial fibrillation using a rule-based approach on realistic anatomical data. *Proceedings of the 28th IEEE EMBS Annual International Conference, New York City, USA*. pp. 3943-3946, 2006
- M. Reumann, B. Osswald, S. Hagl, Olaf Dössel. Computer-based evaluation of atrial antitachycardial pacing to prevent atrial fibrillation on realistic anatomical data. *In Biomedizinische Technik*. 2006
- M. Reumann, J. Bohnert, B. Osswald, S. Hagl, O. Dössel. The role of conduction delay and complex anatomical structures in the initiation and maintenance of atrial fibrillation. *In 33rd International Congress on Electrophysiology* 2006
- M. Reumann, B. Osswald, S. Hagl, O. Dössel. Computer model of terminating atrial fibrillation through atrial antitachycardial pacing. *In 33rd International Congress on Electrophysiology* 2006
- M. Reumann, K. Nissen, G. Reinerth, G. Seemann, C. F. Vahl, S. Hagl, O. Dössel. Computer aided optimization of cardiac resynchronization therapy. *Europace*. 8(Supplement 1):231/1, 2006
- M. Reumann, B. Osswald, S. Hagl, O. Dössel. Computer aided evaluation of preventive atrial antitachycardial pacing. *Europace*. 1(Supp. 1):213/6, 2006
- M. Reumann, J. Bohnert, G. Seemann, B. Osswald, S. Hagl, O. Dössel. Atrial fibrillation in a computer model of the visible female heart for planning of surgical intervention. *Biomedizinische Technik* 50(1):699-700, 2005
- M. Reumann, G. Reinerth, G. Seemann, C. F. Vahl, S. Hagl, O. Dössel. Modelling intraventricular conduction delay in cardiac resynchronisation therapy. *Biomedizinische Technik* 49-2/1:358-359, 2004
- M. Reumann, G. Reinerth, G. Seemann, C. F. Vahl, S. Hagl, O. Dössel. Simulating biventricular pacing on an individual heart model with respect to stimuli delay. *In Proc. MEDICON 2004*. 2004
- M. Reumann, G. Reinerth, G. Seemann, C. F. Vahl, S. Hagl, O. Dössel. Computer assisted electrode positioning in biventricular pacing. *In Proc. CARS 2004*. 2004

### *Co-author*

- O. Dössel, D. Farina, M. Mohr, M. Reumann, G. Seemann, D. L. Weiss. Computer-assisted planning of cardiac interventions and heart surgery. *In Informatik 2006 - Informatik für Menschen*. pp. 499-506. Gesellschaft für Informatik e.V. (GI), Köllen Druck+Verlag GmbH, Bonn, Okt. 2006.
- O. Dössel, M. Reumann, G. Seemann, D. Weiss. The Missing Link between Cardiovascular Rhythm Control and Myocardial Cell Modeling. *Biomedizinische Technik* 2006;51(4):205-209



- J. Bohnert, M. Reumann, T. Faber, O. Dössel. Investigation of curative ablation techniques for atrial fibrillation in a computer model. *In Biomedizinische Technik*. 2006
- O. Krawczyk, B. Gehrke, H. Leger, M. Leidmann, C. Fricke, C. Schulz, C. Rammner, M. Feldmann, O. Dössel, M. Reumann, T. Becks, A. Gillner, E. Bremus-Köbberling, H. Leschner, C. Rosier, M. Hilgers, S. Hillenbach, T. Schmitz-Rode, M. G. Floren, M. Baumann, R. Farkas, C. Monfred, J. v. Zahn, H. Gothe, B. Häussler, M. Schneider, U. Hofmann. Studie zur Situation der Medizintechnik in Deutschland im internationalen Vergleich. Im Auftrag des Bundesministerium für Bildung und Forschung erstellt. 2005
- K. Albrecht, M. Reumann, G. Seemann, G. Reinerth, C. F. Vahl, O. Dössel. Computer-aided evaluation and optimisation of biventricular pacing for patients with congestive heart failure. *Biomedizinische Technik*. 50(1):701-702, 2005.
- J. Qin, M. Reumann, D. L. Weiss, G. Seemann, B. Osswald, S. Hagl, O. Dössel. Developing algorithms for the optimization of overdrive pacing strategies in patients with atrial fibrillation. *In Biomedizinische Technik* 2005
- G. Reinerth, M. Reumann, G. Seemann, N. Kayhan, J. Albers, O. Dössel, S. Hagl, C.-F. Vahl. Electrophysiological computer models and individualisation of antiarrhythmic cardiac surgery *In Biomedizinische Technik*. 49:368-369, 2004
- G. Reinerth, M. Reumann, G. Seemann, N. Kayhan, J. Albers, O. Dössel, S. Hagl, C.-F. Vahl. A porcine model to evaluate electrophysiological simulations in cardiac tissue *In Biomedizinische Technik*. 49:388-389, 2004
- G. Reinerth, M. Reumann, G. Seemann, N. Kayhan, J. Albers, O. Dössel, S. Hagl, C.-F. Vahl. Three-dimensional electrophysiological and morphological computer models for individualisation of antiarrhythmic cardiac surgery. *In Proc. CARS 2004*. 2004
- G. Reinerth, G. Seemann, M. Reumann, T. Schmidt, O. Dössel, C.-F. Vahl. Simulation der elektrischen Aktivität der Ventrikel bei biventrikulärer Stimulation. *Z. Kardiologie* 2004
- G. Seemann, G. Reinerth, T. Schmidt, M. Reumann, O. Dössel, C. F. Vahl, S. Hagl. Simulation of ventricular activity in ventricular pacing using mathematical models in a porcine model based on 3D-echocardiographic images. *In Proc. CURAC 03* 2003

#### *Invited Talks*

- M. Reumann, J. Bohnert, K. Nissen, B. Osswald, S. Hagl, O. Dössel. Computer Assisted Optimisation of Non-Pharmacological Treatment of Congestive Heart Failure and Supraventricular Arrhythmia Beth Isreal Diaconess Medical Centre, Boston, USA, August 2006
- M. Reumann, G. Seemann, D. Weiss, M. Mohr, D. Farina, O. Dössel. Modelling Cardiac Pathophysiology IBM Watson Research Laboratory, New York, USA, August 2006

### **Supervised diploma theses and student research projects**

- S. Lurz, “Optimierungsstrategien bei kardialer Resynchronisationstherapie,” Student Project, Institut für Biomedizinische Technik, Universität Karlsruhe (TH), 2007. in writing
- J. Bohnert, “Untersuchung von Ablationslinienführungen zur Therapie von Vorhofflimmern am Computermodell,” Student Project, Institut für Biomedizinische Technik, Universität Karlsruhe (TH), 2006.
- K. Albrecht, “Computerunterstützte Evaluation und Optimierung der biventrikulären Schrittmacher-Therapie bei Patienten mit Herzinsuffizienz,” Diploma Thesis, Institut für Biomedizinische Technik, Universität Karlsruhe (TH), 2005.
- J. Qin, “Developing Algorithms for the Optimization of Overdrive Pacing Strategies in Patients with Atrial Fibrillation,” Master Thesis, Institut für Biomedizinische Technik, Universität Karlsruhe (TH), 2005.



Heart Failure is the most common cardiac disease worldwide; supraventricular arrhythmia the most common cardiac arrhythmia. The understanding of these diseases advances treatment options. Ablation therapy and atrial antitachycardial pacing are non-pharmacological options in the treatment of atrial fibrillation. Cardiac resynchronization therapy with biventricular pacing devices has been shown successful in patients with severe heart failure. However, an optimization or even individual therapy planning is not standard or not even carried out today. These non-pharmacological treatments can be investigated and optimized with the help of computer models of the heart. The simulation of atrial fibrillation with a realistic atrial anatomical model aims at explaining seemingly contradictory results from clinical studies. Different ablation strategies and pacing algorithms are then applied to terminate the arrhythmia in the virtual environment. Thus, a comparison of strategies can be carried out. With respect to cardiac resynchronization therapy, the computer model allows for automatic and non-invasive optimization of electrode positions and timing delays. With clinical validation, the presented computer models and methods have the potential to contribute to individualized therapy planning.